

---

**Modélisation de la propagation des ondes sismiques:  
une méthode multipôle rapide (éléments de frontière)  
et son couplage avec la méthode des éléments finis**

---

**THÈSE DE DOCTORAT  
DE L'UNIVERSITÉ PARIS-EST**

Ecole Doctorale: **SIE - Sciences, Ingénierie et Environnement**  
Spécialité: **Mécanique**

Présentée par

**Eva GRASSO**

pour l'obtention du diplôme de

DOCTEUR DE L'UNIVERSITÉ PARIS EST

Composition du jury

Directeurs de thèse	M. Marc Bonnet	(POems, ENSTA)
	M. Jean-François Semblat	(GER 1, IFSTTAR Paris)
Rapporteurs	M. Geert Degrande	(KU Leuven)
	M. Alan Millard	(CEA)
Examineurs	M. Stéphane Lanteri	(INRIA, NACHOS Project team)
	M. Jean Virieux	(UJF, Lab. ISTerre)
Invité	Mme. Stéphanie Chaillat	(POems, ENSTA)



---

**Modelling visco-elastic seismic wave propagation:  
a fast-multipole boundary element method and  
its coupling with finite elements**

---

**Eva GRASSO**

# Résumé étendu

## CONTEXTE

Cette thèse porte sur la modélisation numérique de la propagation des ondes visco-élastiques dans les milieux étendus et infinis. Cette problématique est pertinente pour plusieurs types d'application, tels que la transmission des vibrations dues au trafic ferroviaire ou la propagation des ondes sismiques dans les sols (idéalisés comme infinis ou semi-infinis), leur interaction avec la géologie de surface (*effets de site*) et avec les structures (*interaction sol-structure*, ISS). Parmi les méthodes numériques qui permettent de résoudre ce type de problème, nous pouvons citer la méthode des éléments de frontière (*Boundary Element Method*, ou BEM [44, 51]) ou la méthode des éléments finis (*Finite Element Method*, ou FEM [159, 330]).

La BEM nécessite uniquement la discrétisation de la frontière du domaine d'intérêt, ce qui réduit d'une unité la dimension spatiale du problème à résoudre. De plus, sa formulation prend implicitement en compte les conditions de rayonnement à l'infini, ce qui permet de modéliser des domaines infinis. Enfin, une fois que la solution sur la frontière est connue, la BEM permet l'évaluation précise de la solution en tous points du domaine, évitant les erreurs liées à la dispersion numérique ou à l'anisotropie du maillage introduites par les discrétisations volumiques. Pour ces raisons, la BEM est une méthode particulièrement bien adaptée pour le calcul de la propagation d'ondes sismiques.

En contrepartie, la BEM est limitée aux milieux linéaires et homogènes par morceaux. De plus, sous sa forme classique, elle amène à résoudre un système linéaire dont la matrice est pleine et (avec l'approche par collocation) non-symétrique. Cela induit pour la BEM classique un coût numérique important et limite la taille des problèmes à  $\mathcal{O}(10^4)$  degrés de liberté (DDLs) de frontière.

Il existe plusieurs stratégies permettant d'augmenter la taille des modèles BEM et d'accélérer la résolution du système linéaire. On peut en particulier citer les méthodes algébriques, qui agissent directement sur le système matriciel (*H*-matrices [149], *Adaptive Cross Approximation* [30]), et la méthode multipôle rapide (*Fast Multipole Method*, ou FMM [260]) qui se base sur une décomposition des solutions fondamentales. En particulier, la FMM appliquée à la BEM et sa version multi-niveau (*Multi Level-FMBEM*, ou ML-FMBEM) autorise, par rapport à la BEM classique, une forte réduction de la complexité en temps de calcul et en mémoire

(de  $\mathcal{O}(N^2)$  à  $\mathcal{O}(N \log N)$ ) [68, 82, 236]. Concernant l'élastodynamique, la ML-FMBEM a été récemment appliquée à la résolution de problèmes de propagation d'ondes sismiques dans des milieux homogènes par morceaux [62, 63].

La FEM, quant à elle, permet de traiter des problèmes à comportement complexe (hétérogène, anisotrope, non-linéaire) et est donc la principale méthode numérique de calcul de structures. De plus, le système linéaire d'équations produit par la FEM fait intervenir une matrice creuse. En revanche, la FEM repose sur une discrétisation volumique du domaine d'intérêt et nécessite des stratégies spécifiques (conditions absorbantes [34], éléments infinis [37]) pour la prise en compte des conditions de rayonnement. Par ailleurs, la dispersion numérique et l'erreur de pollution entachent la précision des calculs de propagation d'ondes. Ces considérations font que les éléments finis ne sont pas toujours adaptés à la propagation des ondes dans des domaines étendus ou à fréquence élevée.

Une alternative intéressante à l'emploi de conditions d'absorption consiste à coupler la FEM avec la BEM. Cela permet à la fois de prendre en compte des structures à comportement complexe et de garantir le rayonnement des ondes à l'infini. Le couplage FEM/BEM permet de résoudre un problème contenant des irrégularités (de géométrie ou comportement, contenues dans une région limitée de l'espace) en champ proche avec les éléments finis, la propagation en champ lointain étant prise en compte par les éléments de frontière.

Ce travail de thèse poursuit deux objectifs principaux. D'une part, la formulation FMBEM pour l'élastodynamique 3-D en domaine fréquentiel, issue de travaux précédents, a été étendue au cas des milieux faiblement amortis. D'autre part, deux méthodes différentes de couplage de la FEM avec la ML-FMBEM ont été proposées et comparées.

Le manuscrit est organisé en trois chapitres. Le premier chapitre, de nature bibliographique, est une introduction aux sujets abordés au cours du travail. Le deuxième chapitre est dédié à l'application de la FMBEM à la visco-élasticité 3-D. Enfin, le troisième chapitre porte sur le couplage FEM/FM-BEM en visco-élastodynamique 3-D.

## **APPLICATION DE LA FMBEM MULTI-NIVEAU À LA VISCO-ÉLASTODYNAMIQUE 3-D**

La formulation ML-FMBEM pour l'élastodynamique 3-D en domaine fréquentiel a été étendue au cas des milieux viscoélastiques faiblement amortis. L'adaptation de la ML-FMBEM aux matériaux amortissants permet de reproduire la décroissance de l'amplitude des ondes due à la dissipation intrinsèque du milieu de propagation, et de décrire l'amplitude limitée et le décalage de phase typiques des systèmes excités près de la résonance [128].

L'introduction de l'atténuation dans la ML-FMBEM influence l'évaluation de la décomposition multipolaire des solutions fondamentales de la visco-élastodynamique. Premièrement, aucune étude mathématique rigoureuse n'a été proposée à ce jour sur la convergence de la formulation FMBEM en nombre d'onde complexe, contrairement à celle en nombre d'onde réel (acoustique, électromagnétisme, élastodynamique) pour laquelle plusieurs études existent [82, 299]. D'autre part, peu de travaux dans la littérature abordent le problème du réglage des paramètres algorithmiques de la FMM pour prendre en compte le nombre d'onde com-



plexe, et ceux-ci n'ont pas été effectués dans le domaine de la visco-élastodynamique (voir [134] en électromagnétisme, [323] en acoustique, [118] pour des problèmes génériques de type Helmholtz avec une formulation FMM adaptée aux basses fréquences).

D'un point de vue formel, la formulation intégrale des éléments de frontière et la méthode multipôle rapide en visco-élastodynamique sont identiques à celles de l'élastodynamique, la seule différence étant qu'en visco-élastodynamique, le nombre d'onde est complexe à cause de l'atténuation.

La première section du chapitre 2 est un rappel de la formulation ML-FMBEM en visco-élastodynamique. La deuxième section rappelle la loi de comportement des milieux visco-élastiques linéaires isotropes pour des sollicitations harmoniques, puis définit le nombre d'onde complexe et son approximation dans le cas des milieux peu amortissants. La section 2.4 présente ensuite la formulation en nombre d'onde complexe pour la méthode FMBEM multi-niveaux.

La section 2.5 détaille les parties de la formulation qui sont particulièrement touchées par l'introduction des paramètres complexes, comme l'évaluation numérique du développement multipôle du noyau de Helmholtz. On met en évidence les erreurs d'évaluation de ce noyau que l'on commet lorsque l'on utilise les réglages numériques utilisés pour la formulation en nombre d'onde réel. L'étude menée pour pouvoir évaluer précisément ce développement est également présentée. On y montre que la série définissant la fonction de transfert doit être tronquée à un ordre plus élevé (comparativement à la formulation en nombre d'onde réel) et on propose une relation permettant d'ajuster le paramètre de troncature selon le niveau d'amortissement.

### COUPLAGE FEM/FMBEM EN VISCO-ÉLASTODYNAMIQUE 3-D

Le chapitre 3 est dédié au couplage FEM/FMBEM, permettant de combiner la flexibilité de la FEM (géométries et comportement complexes) et la capacité de la BEM à traiter les domaines infinis. Ce couplage peut être considéré comme une forme de décomposition du domaine (*Domain Decomposition Methods*, ou DDMs [305]). Contrairement au couplage FEM/BEM classique, pour lequel la littérature est vaste [15, 104], peu de travaux existent sur le couplage FEM/FMBEM [120, 134, 323], et aucun d'entre eux ne concerne la visco-élastodynamique.

Dans cette thèse, deux approches de couplage sont proposées. L'idée est d'associer un sous-domaine spatialement borné contenant des structures complexes ou des fortes hétérogénéités (le problème en champ proche associé, résolu par la FEM) et son complémentaire semi-infini (le problème en champ lointain associé, résolu par la ML-FMBEM) au moyen d'une décomposition de domaine sans recouvrement. Des conditions de transmission (continuité des déplacements et équilibre des tractions) garantissent la continuité à travers l'interface commune. Les deux approches de couplage proposées, l'une de nature séquentielle et l'autre de nature simultanée, ont été mises en œuvre et leur performances évaluées sur des exemples simples.

**Couplage séquentiel :** il s'agit d'un couplage du type *Dirichlet-Neumann* avec une seule relaxation du champ de déplacement sur l'interface. Des codes FEM (CESAR-LCPC) et ML-

FMBEM existants ont été utilisés comme des boîtes noires et sont interfacés par un algorithme externe. La dépendance de la convergence par rapport au paramètre de relaxation, à la géométrie et au contraste de comportement des matériaux (ici linéaires dans les deux sous-domaines) est étudiée à l'aide de plusieurs exemples.

**Couplage simultané :** il repose sur la résolution d'un système global d'équations combiné avec les conditions de transmissions sur l'interface. Une condensation implicite des degrés de liberté FEM est appliquée et le système global, piloté par la ML-FMBEM, est résolu itérativement par l'algorithme GMRES (*Generalized Minimal Residual*). Ici encore, des études paramétriques sont effectuées sur plusieurs exemples.

## CONCLUSIONS ET PERSPECTIVES

L'objectif de cette thèse a été double. D'une part, on a étendu avec succès la formulation FMBEM pour l'élastodynamique 3-D en domaine fréquentiel au cas des milieux faiblement amortis. D'autre part, on a proposé et mis en œuvre deux méthodes différentes permettant de coupler la FEM et la ML-FMBEM. Pour des raisons de temps, les deux approches n'ont pas encore été testées sur des problèmes identiques, ce qui empêche pour l'instant une comparaison rigoureuse de l'efficacité des deux approches de couplage. Ceci constituera l'objectif d'études comparatives ultérieures.

Le couplage FEM/FMBEM a cependant donné des résultats très encourageants et nous paraît être une direction de travail intéressante pour les applications dans les domaines de l'interaction sol-structure (ISS) et la modélisation des vibrations ferroviaires. Plusieurs améliorations sont envisageables à court terme (section 3.7), en particulier l'extension du couplage FEM/FMBEM (i) aux maillages non-conformes, (ii) à des comportements non-linéaires dans le sous-domaine FEM, (iii) aux milieux anisotropes, ou (iv) aux milieux poro-élastiques.

# Abstract

## BACKGROUND

The numerical simulation of elastic wave propagation in unbounded media is a topical issue. This demand arises in a variety of real life engineering problems, from the modelling of railway- or machinery-induced vibrations to the analysis of seismic wave propagation and dynamic soil-structure interaction. Due to the complexity of the involved geometries and materials behavior, modelling such situations requires sophisticated numerical methods.

The most popular methods in the engineering practice are the finite and the spectral element methods. They present known advantages (deal with complex geometries, material nonlinearities, etc) and drawbacks (numerical damping and dispersion, spurious reflections at artificial truncation boundaries). Although various numerical strategies exist to limit spurious reflections (e.g. absorbing boundary conditions or boundary layers), the Boundary Element method (BEM) remains a very effective approach for dynamic problems in spatially-extended regions (idealized as unbounded), especially so since the advent of fast BEMs such as the fast multipole method (FMM) used in this work.

The BEM is based on a boundary integral formulation which requires the discretization of the only domain boundary (i.e. a surface in 3-D) and accounts implicitly for the radiation conditions at infinity. As a main disadvantage, the BEM leads *a priori* to a fully-populated and (using the collocation approach) non-symmetric coefficient matrix, which makes the traditional implementation of this method prohibitive for large problems ( $\mathcal{O}(10^6)$  DoF). Applied to the BEM, the multi-level version of the fast multipole method (ML-FMM) strongly reduces the computational complexity and the memory requirement typical of the classical formulation, making the BEM very competitive in modelling elastic wave propagation. The elastodynamic version of the fast multipole BEM (FMBEM), in a form permitting piecewise-homogeneous media, has for instance been successfully applied to the solution of seismic wave propagation problems.

## SUMMARY OF CONTRIBUTIONS OF THIS THESIS

The present thesis aims at extending the capabilities of the existing frequency-domain elastodynamic FMBEM in two directions:

**Adaptation to viscoelastodynamics.** The time-harmonic elastodynamic ML-FMBEM formulation has been extended to the case of weakly dissipative viscoelastic media. The underlying boundary integral equation and fast multipole formulations are formally identical to that of elastodynamics, except that the wavenumbers are complex-valued due to attenuation. Attention is focused on evaluating the multipole decomposition of the viscoelastodynamic fundamental solution. A damping-dependent modification of the selection rule for the multipole truncation parameter, required by the presence of complex wavenumbers, is proposed. It is empirically adjusted so as to maintain a constant accuracy over the damping range of interest in the approximation of the fundamental solution, and validated on numerical tests focusing on the evaluation of the latter. The proposed modification is then assessed on 3D single-region and multi-region visco-elastodynamic examples for which exact solutions are known. Finally, the multi-region formulation is applied to the problem of a wave propagating in a semi-infinite medium with a lossy semi-spherical inclusion (seismic wave in alluvial basin). These examples involve problem sizes of up to about  $3 \cdot 10^5$  boundary unknowns.

**Coupling of the FMBEM with the finite element method.** FMBEM/FEM coupling approaches take advantage of the versatility of the FEM to model complex geometries and non-linearities and of the exact account for infinite domains, mobile boundaries or unknown boundaries offered by the boundary integral approach. In this thesis, we apply two strategies for coupling the FMBEM and the FEM to solve three-dimensional time-harmonic wave propagation problems in unbounded domains. The main idea is to separate one or more bounded subdomains containing complex structures or strong heterogeneities (solved by the FEM) from the complementary semi-infinite viscoelastic space of propagation (solved by the FMBEM) through a non-overlapping domain decomposition. The two following strategies have been implemented and their performances compared on simple examples.

*First strategy:* it consists in an *iterative Dirichlet-Neuman coupling* with single interface relaxation of the displacement field. Existing FEM (CESAR-LCPC) and FMBEM software are used in black-box fashion and driven by an external interface algorithm. The dependence of the convergence on the relaxation parameter and on the geometrical/material properties of the problem at hand is shown through different examples.

*Second strategy:* it is a *simultaneous coupling* approach based on solving a global system of equations combined with the transmission conditions across the common interface. An implicit condensation for the FEM degrees of freedom is employed and the global system is solved by generalized minimal residual (GMRES).

# Contents

<b>Résumé étendu</b>	<b>iii</b>
<b>Abstract</b>	<b>vii</b>
<b>1 Modelling waves in attenuating media</b>	<b>1</b>
1.1 Overview . . . . .	2
1.2 Wave propagation problems in unbounded domains . . . . .	2
1.2.1 Seismic wave propagation . . . . .	2
1.2.2 Vibrations due to traffic or construction works . . . . .	6
1.3 Wave propagation in a viscoelastic medium . . . . .	9
1.3.1 Elastic wave equation in the time domain . . . . .	9
1.3.2 Elastic wave equation in the spectral-domain . . . . .	10
1.3.3 Low-strain levels and linear viscoelasticity . . . . .	11
1.3.4 Constitutive law for an isotropic linear viscoelastic medium . . . . .	13
1.3.5 Rheological models . . . . .	13
1.4 Simulating wave propagation . . . . .	15
1.4.1 Analytical approaches . . . . .	15
1.4.2 Numerical modelling of wave propagation . . . . .	17
Introduction . . . . .	17
Overview of numerical methods in visco-elastodynamics . . . . .	18
1.4.3 Artificial truncation of unbounded domains . . . . .	21
1.5 Fast Multipole Boundary Element Method . . . . .	23
1.5.1 Boundary Element Method. . . . .	23
1.5.2 Viscoelasticity with BEMs. . . . .	24
1.5.3 Inelasticity with BEMs. . . . .	25
1.5.4 Fast BEMs. . . . .	25
1.5.5 Remark: BEM vs ABCs. . . . .	26
1.6 Outline . . . . .	27

<b>2</b>	<b>Application of the multi-level time-harmonic FM-BEM to 3-D visco-elastodynamics</b>	<b>29</b>
2.1	Introduction . . . . .	30
2.2	Elastodynamic Fast Multipole Boundary Element Method: survey . . . . .	31
2.2.1	Boundary Element Method . . . . .	31
2.2.2	Fast Multipole-Boundary Element Method . . . . .	34
2.2.3	Multi-region FMBEM formulation for seismic wave propagation . . . .	40
2.2.4	Computational aspects . . . . .	43
2.3	Behavior of weakly dissipative media . . . . .	44
2.3.1	Constitutive law for a linear viscoelastic medium . . . . .	44
2.3.2	Complex wavenumbers and mechanical parameters . . . . .	46
2.4	Multi-Level FMBEM formulation for viscoelastodynamics . . . . .	47
2.4.1	Viscoelastodynamic boundary element formulation . . . . .	48
2.4.2	Multi-Level Fast Multipole BEM (ML-FMBEM) . . . . .	50
2.5	Truncation of the transfer function with complex-wavenumber . . . . .	50
2.5.1	Evaluation on the transfer function . . . . .	51
2.5.2	New damping-dependent selection rule for truncation parameter $L$ . . .	52
2.6	Full ML-FMBEM examples in 3-D visco-elastodynamics . . . . .	55
2.7	Multi-domain ML-FMBEM in 3-D visco-elastodynamics . . . . .	60
2.7.1	Verification on a two-region example . . . . .	61
2.7.2	Seismic wave propagation in a damped basin . . . . .	62
2.8	Some remarks on preconditioning . . . . .	65
2.9	Conclusions . . . . .	66
<b>3</b>	<b>FEM / FMBEM coupling in 3D visco-elastodynamics</b>	<b>67</b>
3.1	Introduction . . . . .	68
3.1.1	Contribution of this thesis . . . . .	68
3.1.2	Work choices and constraints . . . . .	69
3.2	FEM / BEM coupling approaches for wave propagation problems: survey . . .	70
3.2.1	Conventional approaches . . . . .	70
3.2.2	Domain decomposition methods: introduction . . . . .	72
3.2.3	Classical non-overlapping domain decomposition methods . . . . .	73
3.2.4	Coupling of FEM with BEM and FMBEM for wave propagation problems	77
3.3	Finite element method for time-harmonic visco-elastodynamics . . . . .	77
3.3.1	Time-harmonic formulation . . . . .	77
3.3.2	The Rayleigh damping matrix . . . . .	79
3.3.3	FEM numerical dissipation and dispersion for wave propagation problems	80
3.3.4	Influence of the mass matrix formulation on numerical dispersion . . .	81
3.4	Domain decomposition and interface problem . . . . .	81
3.4.1	Surface loading and far field excitation . . . . .	81
3.4.2	Interface problem statement . . . . .	82
3.4.3	Assumptions common to the coupling algorithms . . . . .	84

3.5	Iterative FEM/FMBEM coupling . . . . .	85
3.5.1	Introduction . . . . .	85
3.5.2	Interface relaxation algorithm for a surface loading . . . . .	86
3.5.3	Interface relaxation algorithm for a far field excitation . . . . .	87
3.5.4	Implementation . . . . .	89
3.5.5	Verification . . . . .	90
	Example of surface loading: time-harmonic load on a half-space . . . .	90
	Example of surface loading: vibration isolation through semi-circular trenches . . . . .	91
	Example of far field excitation: scattering by a semi-spherical canyon .	93
3.5.6	Conclusions . . . . .	94
3.6	Simultaneous FEM/FMBEM coupling . . . . .	96
3.6.1	Introduction . . . . .	96
3.6.2	Domain decomposition for the simultaneous coupling: notation . . . .	96
3.6.3	The finite element subdomain . . . . .	97
3.6.4	The boundary element subdomain . . . . .	98
3.6.5	Simultaneous algorithm for a BE surface loading . . . . .	99
3.6.6	Remark on GMRES accuracy . . . . .	100
3.6.7	Verification . . . . .	100
	Wave propagation in a homogeneous half-space . . . . .	101
	Wave propagation in a homogeneous half-space containing a soft inclu- sion . . . . .	106
	Wave propagation in a homogeneous half-space containing a soft inclu- sion: contrast at the interface $\Phi$ . . . . .	107
3.6.8	Straightforward improvements . . . . .	109
3.6.9	Conclusions . . . . .	111
3.7	Perspectives . . . . .	111
<b>A</b>	<b>Numerical evaluation of the spherical Hankel functions with complex-argument</b>	<b>115</b>
A.1	Spherical Hankel functions . . . . .	116
A.2	Numerical evaluation of spherical $h_n^{(1)}(z^*)$ with complex argument . . . . .	117
A.3	The Helmholtz Green's function expansion . . . . .	119
A.3.1	The Gegenbauer series . . . . .	119
A.3.2	The spherical harmonics . . . . .	120
A.3.3	Plane wave expansion . . . . .	120
<b>B</b>	<b>Analytical solutions for test problems</b>	<b>123</b>
B.1	Spherical cavity under uniform pressure . . . . .	123
B.2	Spherical cavity under uniform pressure surrounded by a spherical shell . . . .	123
B.3	Scattering of a P-wave by a spherical cavity . . . . .	124

<b>C</b>	<b>Interface relaxation algorithms for non-overlapping domain decomposition</b>	<b>127</b>
C.1	Interface problem statement in elasticity. . . . .	127
C.2	Algorithms. . . . .	128
<b>D</b>	<b>User's guides</b>	<b>131</b>
D.1	COFFEE program . . . . .	131
D.1.1	Introduction . . . . .	131
D.1.2	Installation requirements. . . . .	132
D.1.3	Input files . . . . .	132
D.1.4	Output files . . . . .	135
D.1.5	Post-processing . . . . .	137
D.2	CUSIM program . . . . .	137
D.2.1	Introduction . . . . .	137
D.2.2	Installation requirements. . . . .	138
D.2.3	Input files . . . . .	138
D.2.4	Output files . . . . .	142
D.2.5	Post-processing . . . . .	142
D.3	CUSEQ program . . . . .	144
D.3.1	Introduction . . . . .	144
D.3.2	Installation requirements. . . . .	144
D.3.3	Input data . . . . .	144
D.3.4	Output data and post-processing . . . . .	144
	<b>References</b>	<b>147</b>



Chapter 1

Modelling waves in attenuating media

Contents

---

1.1	Overview . . . . .	2
1.2	Wave propagation problems in unbounded domains . . . . .	2
1.3	Wave propagation in a viscoelastic medium . . . . .	9
1.4	Simulating wave propagation . . . . .	15
1.5	Fast Multipole Boundary Element Method . . . . .	23
1.6	Outline . . . . .	27

---

## 1.1 OVERVIEW

This thesis focuses on the numerical modelling of 3-D elastic wave propagation in unbounded media. Among the existing numerical methods suitable in elastodynamics, the Boundary Element Method (BEM) is very well adapted to deal with propagation in unbounded media because of the built-in, exact satisfaction of radiation conditions. Moreover, the boundary-only discretization required by the formulation allows smaller model sizes w.r.t. volume-based methods such as the FEM. However, the BEM leads to the resolution of a full linear system, which entails high CPU costs and memory requirements that increase with the size of the problem. In case of large domains or high-frequency problems, these requirements become too high, letting the classical BEM loose competitiveness towards other numerical methods such as the Finite Element Method (FEM). In this sense, the BEM has recently known important advances, with the extension of the accelerated version of the Fast Multipole Boundary Element Method (FM-BEM) to 3-D multi-domain elastodynamics [62, 63]. The Fast Multipole algorithm, introduced in 1987 by Leslie Greengard and Vladimir Rokhlin [142], is considered among the ten best algorithms of the computer age [96], and nowadays is hugely employed in fields such as electromagnetism or acoustics. Applied to the classical BEM formulation, the Fast Multipole Method (FMM) allows to overcome its major limitations, namely the CPU costs and memory requirements.

## 1.2 WAVE PROPAGATION PROBLEMS IN UNBOUNDED DOMAINS

Wave propagation in viscoelastic unbounded media is a useful idealization for a variety of real-life engineering problems. In this work we focus on two specific applications, namely the seismic wave propagation and the traffic-induced vibrations. This Section is thus devoted to a brief introduction to these two classes of problems involving wave propagation. We describe their main features and highlight the peculiarities and the challenges of their physical and numerical modelling.

### 1.2.1 Seismic wave propagation

The prediction of seismic ground motions is a crucial step in the evaluation of seismic risk. This task raises the need for the analysis of three different phenomena, sketched in Figure 1.1: the fault rupture mechanism (e.g. rupture initiation, fault size and plane, slip distributions), the elastic wave propagation through the earth's crust and the local site response. On the one hand, the local site response depends on the characteristics of the incident wave field (amplitude, duration and frequency content of the ground motion), which influence the energy content and the spatial variability of the ground motion. On the other hand, it depends on the presence of topography irregularities, of near-surface sedimentary structures or of lateral discontinuities, which cause multiple wave scattering, trapping of specific frequency components and ground motion amplification. In the following, the main issues related to the propagation of seismic waves are briefly presented.

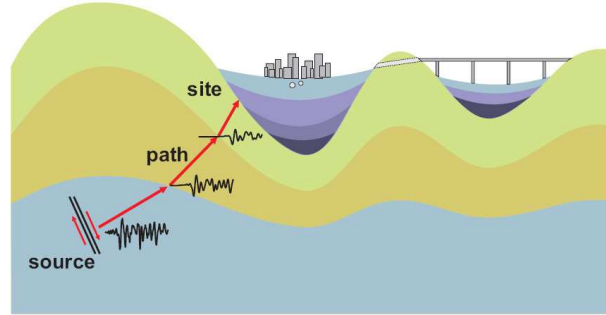


**Figure 1.1:** Seismic wave propagation from the source to an alluvial site [285].

**Effects of surface topography and subsurface heterogeneities.** Historically, anthropic settlements have often risen and developed over alluvial valleys. For example, Mexico City sits on an old lakebed, and it is partially surrounded by mountain ranges. During the earthquakes that struck the city in 1985, a great amplification of the ground motion was measured in different areas of the basin. This amplification was due to the resonance in the lakebed sediments, to the long duration of the shaking, and to the interference of scattered and trapped waves. Also the 1994 Northridge (California) and the 1995 Kobe (Japan) earthquakes, classified as moderate-to-large, have shown an unexpected potential for causing damage due to their local geological features. Other big cities known to lie over alluvial basin are Santa Cruz (California, hit in 1989 by the Loma Prieta earthquake), Caracas (Venezuela), Grenoble (France).

All these observations have shown that the ground motion is influenced by the *vertical heterogeneities* of the medium, i.e. by the horizontal layering of different geological structures. To explain this phenomenon, the simplified model of a stratified medium composed by soft alluvial layers over a rigid bedrock is often used. Using the theory of elastic wave propagation [4], the velocity contrast between a stiffer and a softer medium is shown to cause frequency-dependent amplifications and a trap of the transmitted wave field. The assumption of horizontally stratified medium justifies one-dimensional approaches, allowing for the identification of the site fundamental frequency or the characterization of non-linear seismic response [26, 92].

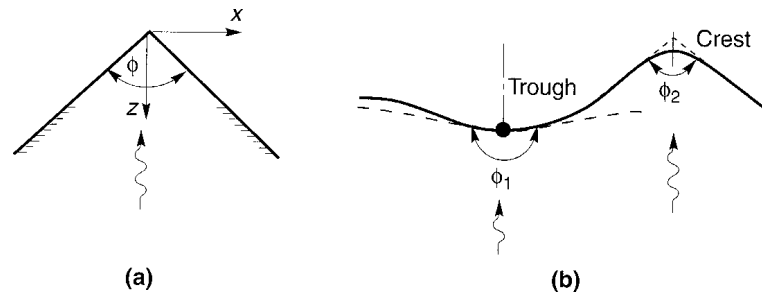


**Figure 1.2:** Simple models to explain topographic effects: (a) triangular infinite wedge model and (b) approximation of the ground surface by trough and wedges [193].



**Figure 1.3:** The Rognes hill after the Lambesc earthquake (1909, France). The effects of amplification induced by the presence of the hill are clearly visible in this picture taken few time after the ground motion.

However, approaches based on 1-D simulations do not account for *horizontal heterogeneities*. Therefore, they cannot satisfactorily estimate the maximum amplification level in realistic media, nor explain the strong amplification and the longer motion duration caused by lateral discontinuities [229]. Such phenomena, due to the horizontal heterogeneities are called *basin effects*. They are relevant for a local hazard assessment, and can be investigated only through two- and three-dimensional simulations [26, 39, 280].

Also the presence of *topographic irregularities* such as ridge or hills affects the ground motion, see e.g. the damages suffered by the french Rognes' city, hit in 1909 by the Lambesc earthquake (see Fig.1.3), or by the Pacoima dam during the 1971 San Francisco earthquake [46]. Simple idealized models such as those shown in Figure 1.2 enable to qualitatively explain the observed amplification phenomena, e.g. the higher amplifications at mountain tops occurring when the wavelengths are comparable with the mountain width. The interaction of incoming and reflected waves produces complicated amplification patterns, whose localisation depends on the type of the wave, its angle of incidence and its frequency content [47, 241, 270]. The amplification at mountain tops generally decreases along the slope or as the angle of incidence increases [25].

Although the analysis of simplified models helps in the understanding of the main amplification phenomena caused by the propagation of seismic waves in irregular topographic profiles, it generally leads to an underestimation of the amplification levels [131].

**Effects of ground motion spatial variability.** The analysis of data recorded at dense instrument arrays shows a difference in seismic time histories recorded in different locations. This phenomenon, called the spatial variability of ground motion, has been studied since the mid

1960's [42]. As the signal characteristics (amplitude, phase, duration, etc) vary at the scale of widely extended areas, the uniform excitation generally used as input for studying the response of single structures is no longer realistic. The response analysis of long (e.g. pipelines, dams) or multi-supported structures (e.g. bridges) need to account for the fact that their supports undergo non-uniform excitation. The physical causes for the spatial variability lie in the wave passage effect (i.e. the differences in the arrival time of seismic waves at various locations) and in the loss of coherency effects, namely in the source position, extent and history of trigger, in the different propagation paths of the incident waves, which travel through a heterogeneous medium, and in the attenuation, see Figure 1.4 [2]. The loss of coherency between signals recorded at various locations is used as stochastic estimation of the spatial variability. Usually, it is estimated through empirical and semi-empirical models. For an exhaustive review on the subject we suggest [326].

**Effects of site-city interaction (SCI).** The study of the basin effects allows the analysis of the free-field response of a given site. However, the presence of a city on the free surface influences the free-field response of the ground motion. In 1970, Jennings investigated the ground motion generated by a vibrating building [165]. Since, the hypothesis that the interaction between the radiating fields induced by multiple adjacent buildings could influence the free-field ground motion has been confirmed by many observations, and several works addressed this topic. An analytical approach has been proposed by Guéguen, based on a superposition of single modal soil-structure interaction analysis [144]. Numerical simulations have been conducted mainly in two dimensions, with the use of simplified models to isolate the buildings interaction from the

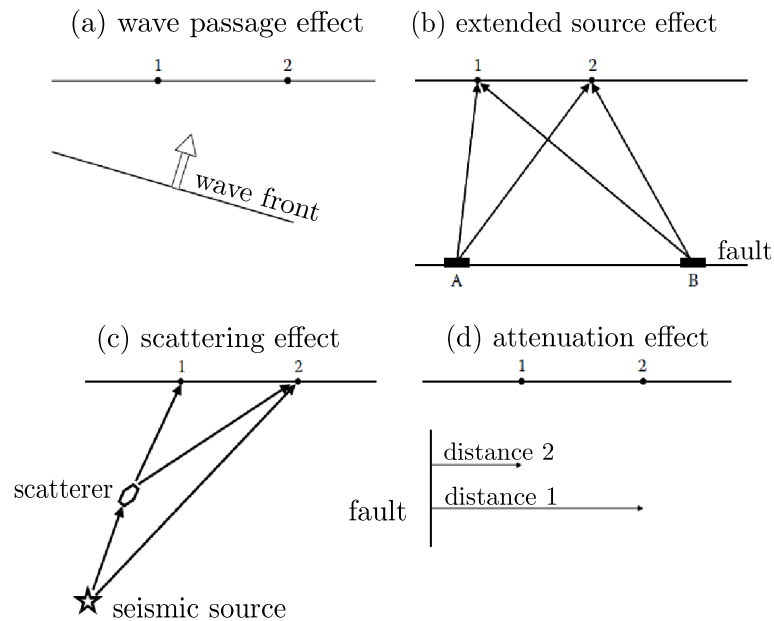


**Figure 1.4:** Physical causes underlying the spatial variability of ground motion (from [326]).

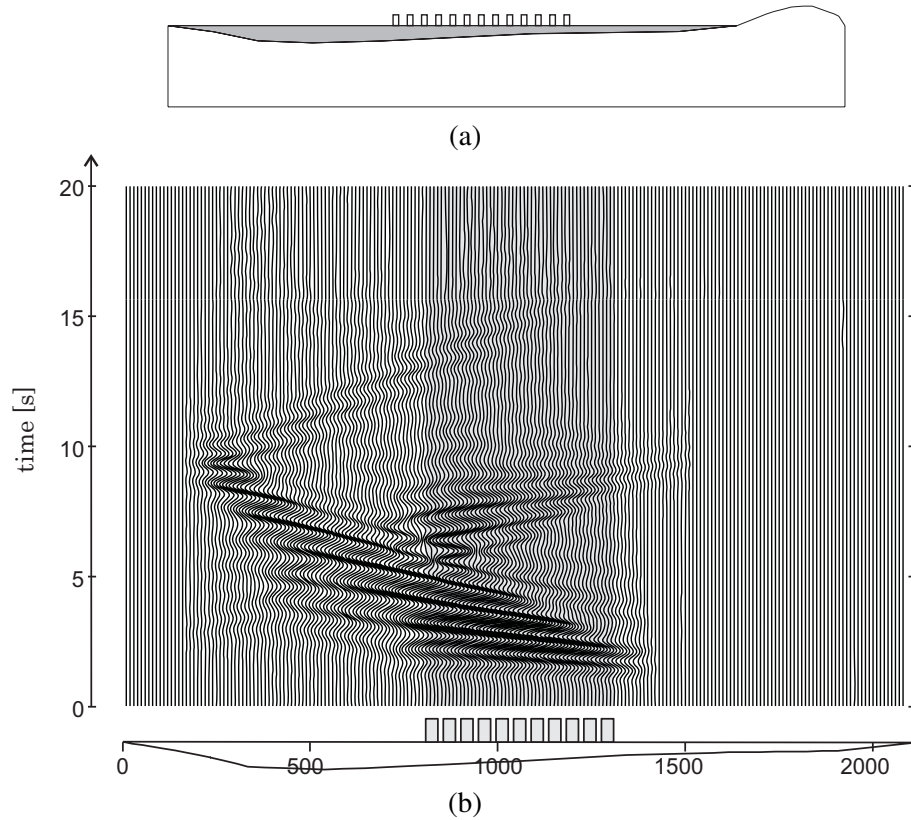


**Figure 1.5:** (a) Model for the analysis of site-city interaction in a shallow alluvial basin ([279]). (b) Influence of site-city interaction on the amplification of the seismic ground motion in a shallow alluvial basin (Nice, France): perturbations  $u_p$  for a given city configuration ([279]).

basin effects, see Figure 1.5 [184, 279]. In regular cities, the band of resonance frequencies of the buildings is narrow. When these frequencies coincide with the resonance frequency of the underlying soft soil layer, resonance occurs for the building group, which exhibit a homogeneous group effect. In this case, inside the city a strong reduction of the ground motion (up to 50%) can be achieved, whereas outside the city an increase of the ground motion around 10% can be observed. The city irregularity modifies this coherency in the buildings response, causing a strong decrease of spatial correlation of the ground motion [27].

### 1.2.2 Vibrations due to traffic or construction works

Ground vibrations may be generated by rotating turbines, vibrating machines, by road or railway traffic (at surface or underground), by pile driving, by excavating machines (see Figure 1.6) or by explosions at construction sites. Some of these sources are transient, e.g. explosions or construction works, and the disturbance they occasion is often small or however limited in time. Some other sources, e.g. road or railway traffic, act in the long term and their propagation in urban areas may produce annoyance to human beings (under the form of building vibration or



of noise), long term structural effects on structures (ancient buildings, historical monuments) or disturbance on technology equipments located close to the source [308]. With the modern development of high speed trains and of metropolitan railways, vibrations have become a major issue. When dealing with a new project, the vibration levels attainable in the surrounding environment should be quantified in advance, to provide adequate isolation countermeasures at the design stage. In existing structures, effective isolation techniques have to be designed a posteriori to mitigate excessive vibration levels. In this perspective, numerical simulations constitute an essential tool of prediction for engineers.

**Railway-induced vibrations.** Modelling the passage of a train is a complicated task. Indeed, it produces a dynamic interaction between the train wheels, the rails, the sleepers and the underlying ballast structure (see Figure 1.7a) which is difficult to reproduce. Moreover, all these parts contain geometrical imperfections that introduce further vibrations in the system. *In situ measurements* allow a realistic evaluation of the propagation phenomena. However, the recorded signals include all incertitudes concerning the local geology, ground heterogeneities and the dynamic train-track-embankment interaction [282]. The *numerical modelling* is a key tool to analyse the in situ measurement and generalize the attenuation law for the ground vibrations [282]. In [288], the track is modelled as a beam structure resting on a layered ground.

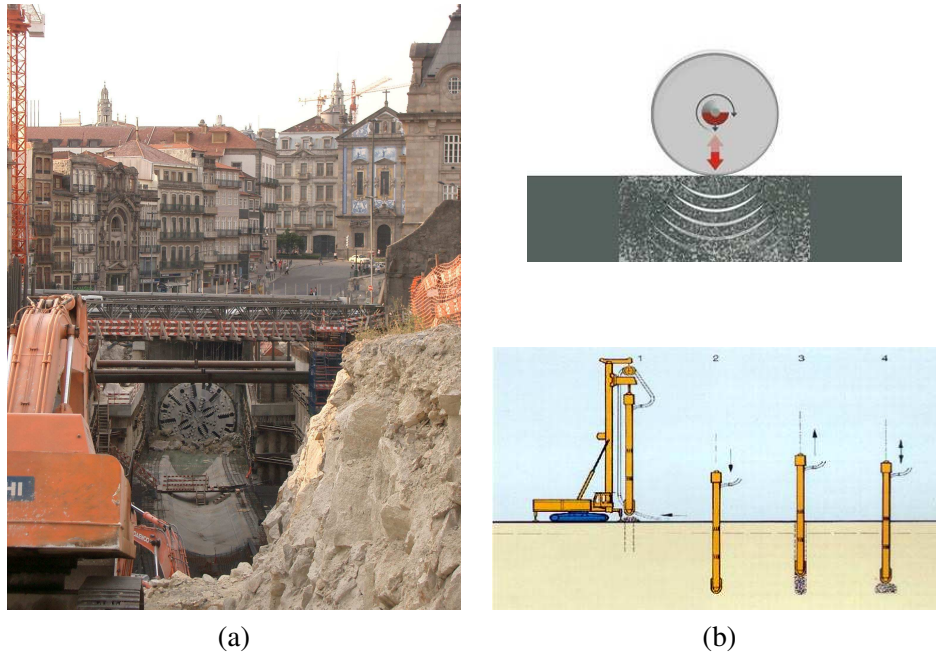


**Figure 1.6:** Vibrations due to construction works: (a) breakthrough of the Herrenknecht Tunnel Boring Machine (TBM) at Sao Bento Station under construction (2003, Porto Metro Line S, Portugal) [145], (b) two examples of soil dynamic compaction that generate ground vibrations. Often civil engineering works in urban areas induce ground vibrations from short- to long-time periods.

To couple the track and the ground, the authors propose to model the sleepers as a continuous mass per unit length of the track and the ballast as a continuous distributed vertical spring stiffness and mass. Train-track-embankment dynamic interactions have been studied for example in [5, 59, 163, 167, 256, 303].

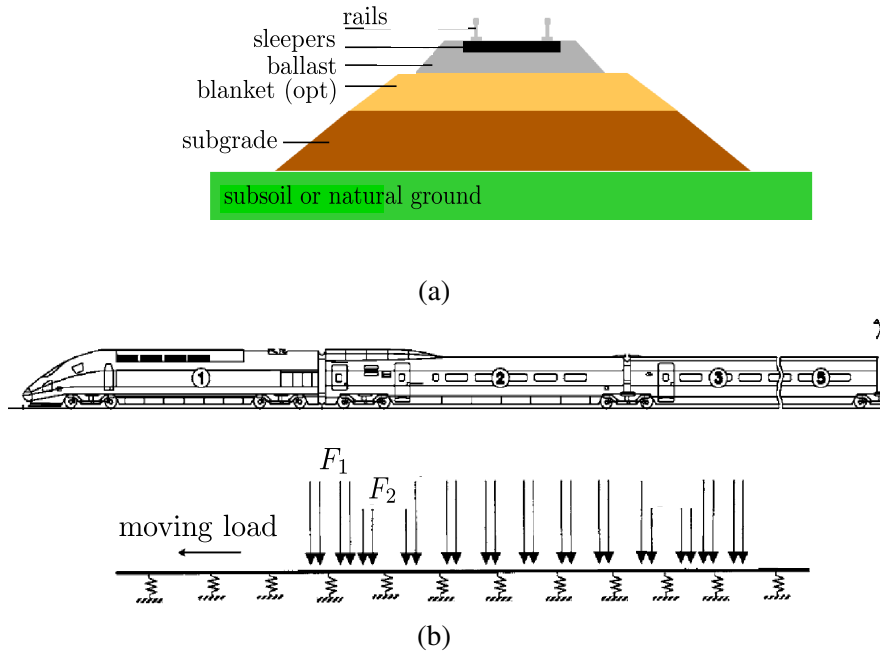


**Figure 1.7:** Railway-induced vibrations modelling: (a) cross section of the track-embankment system and (b) sketch of the Thalys high-speed train used in [240] (top) and the corresponding model used for numerical simulations, consisting in a beam lying on an elastic foundation subjected to the wheel forces transmitted by the train.

**Isolation techniques.** Most of the vibratory energy is carried by the Rayleigh waves [36, 319], a type of waves that propagates close to the soil surface and that decays more slowly with distance than the volume waves do [193]. Therefore, the ground vibration may be reduced by placing a suitable wave barrier in the ground [11, 12, 36, 60, 76, 187]. The trench barriers shield the propagating waves, lead to a complex mechanism of wave reflection, mode alteration and wave transmission, and finally produce a reduction in ground vibration beyond the trench [282]. There exist two techniques of vibration mitigation based on the insertion of barriers. On the one hand, the so called *active isolations* aim at the source isolation; the barriers are thus located near to the source of vibration. On the other hand, the *passive screening* methods provide the "receiver" isolation; the barriers are positioned close to the area to be protected or along the propagation path. In the former case the mechanism mentioned above of waves interaction with the barriers involves both body waves (P and S) and Rayleigh waves, whereas in the latter



case Rayleigh waves are dominant, due to the greater radiation damping of the body waves [193]. Literature on isolation techniques is huge. Numerical evaluation of vibration screening is addressed for example in [6–8, 13, 17, 20, 105, 127, 156, 201, 202, 209, 223, 321].

### 1.3 WAVE PROPAGATION IN A VISCOELASTIC MEDIUM

#### 1.3.1 Elastic wave equation in the time domain

Let  $\Omega \in \mathbb{R}^3$  be an isotropic homogeneous linear elastic solid with boundary  $\partial\Omega$  and characterized by a density  $\rho$ . The description of wave propagation in  $\Omega$  during the time interval  $t \in [0, t^F]$  is based on the balance of momentum (Cauchy first law of motion) combined with the compatibility conditions and the constitutive relation, respectively given by:

$$\nabla \cdot \boldsymbol{\sigma} + \rho \mathbf{F} = \rho \ddot{\mathbf{u}} \quad \text{in } \Omega \times [0, t^F], \quad (1.1a)$$

$$\boldsymbol{\varepsilon}(\mathbf{u}) = \frac{1}{2}(\nabla \mathbf{u} + \nabla \mathbf{u}^T) \quad \text{in } \Omega \times [0, t^F], \quad (1.1b)$$

$$\boldsymbol{\sigma} = \mathcal{A} : \boldsymbol{\varepsilon}, \quad (1.1c)$$

where “ $\nabla$ .” is the divergence operator,  $\boldsymbol{\sigma} = \boldsymbol{\sigma}(\mathbf{x}, t)$  is the stress tensor,  $\boldsymbol{\varepsilon} = \boldsymbol{\varepsilon}(\mathbf{x}, t)$  is the deformation tensor  $\ddot{\mathbf{u}} = \ddot{\mathbf{u}}(\mathbf{x}, t)$  is the second-time derivative of the displacement field  $\mathbf{u}(\mathbf{x}, t)$ ,  $\mathbf{F} = \mathbf{F}(\mathbf{x}, t)$  is a body source distribution and  $\mathcal{A}$  is the fourth-order elasticity tensor. Equation (1.1) can be recast in the following equivalent forms [4]:

$$\rho \ddot{\mathbf{u}} = \mu \nabla^2 \mathbf{u} + (\lambda + \mu) \nabla \nabla \cdot \mathbf{u} + \rho \mathbf{F}, \quad (1.2)$$

$$\rho \ddot{\mathbf{u}} = \frac{\mu}{1 - 2\nu} \nabla (\nabla \cdot \mathbf{u}) + \mu \nabla^2 \mathbf{u} + \rho \mathbf{F}. \quad (1.3)$$

For a well-posed problem, conditions have to be prescribed at the domain boundary (boundary conditions, BCs) and at the initial time  $t = 0$  (initial conditions). Boundary conditions can be of different types, depending if they impose the solution (displacements  $\mathbf{u}$ ) or its derivative (tractions  $\mathbf{t}$ ). Among the others, we cite the Dirichlet BCs ( $\mathbf{u}$ ), Neumann BCs ( $\mathbf{t}$ ), Cauchy BCs (both  $\mathbf{u}$  and  $\mathbf{t}$ ), Robin BCs (linear combination of  $\mathbf{u}$  and  $\mathbf{t}$ ), mixed BCs (different BCs are used on different parts of the boundary). The initial conditions gives the solution at the instant from which the physical system evolves:

$$\mathbf{u}(\mathbf{x}, 0) = \mathbf{u}_0(\mathbf{x}),$$

$$\dot{\mathbf{u}}(\mathbf{x}, 0) = \mathbf{v}_0(\mathbf{x}).$$

The case of vanishing initial conditions (i.e.  $\mathbf{u}_0(\mathbf{x}) = \mathbf{v}_0(\mathbf{x}) = 0$ ) is termed *initial rest* or *quiescent past*.

**Body waves.** As any vectorial field which is sufficiently regular admits the decomposition in an irrotational part and an incompressible part, the elastodynamic displacement field  $\mathbf{u}$  can be

written:

$$\mathbf{u} = \nabla\Phi + \text{rot}\Psi, \quad (1.4)$$

where  $\Phi$  (a scalar potential of dilatation) and  $\Psi$  (a vectorial potential of distortion) satisfy uncoupled wave equations. Substituting the potentials of (1.4) in (1.3) yields

$$\nabla^2\Phi = c_P^2\ddot{\Phi}, \quad \nabla^2\Psi = c_S^2\ddot{\Psi}; \quad (1.5)$$

where

$$c_P^2 = \frac{\mu}{\rho} \frac{2(1-\nu)}{(1-2\nu)}, \quad c_S^2 = \frac{\mu}{\rho}, \quad \gamma = \frac{c_S}{c_P} = \sqrt{\frac{(1-2\nu)}{(2-2\nu)}}.$$

Subscript  $P$  refers to the irrotational primary waves ( $\text{rot}\mathbf{u}_P = \mathbf{0}$ ), that propagate with velocity  $c_P$  involving a particle motion parallel to the direction of wave propagation. Subscript  $S$  indicates the incompressible shear waves ( $\text{div}\mathbf{u}_S = \mathbf{0}$ ), characterized by the velocity  $c_S$ . The particle motion induced by shear waves is constrained in the plane perpendicular to the direction of motion. The S-waves divide in SH (S-horizontal) and SV (S-vertical) depending on the polarization of the particle motion (i.e. in the horizontal or in the vertical plane). The primary and the shear waves are the only two types of waves that can exist in an unbounded elastic solid [193].

**Surface waves.** If a wave propagation problem (1.1) is associated with free-surface boundary conditions, other solutions to the motion equation rise. These solutions are waves that involve a particle motion restricted to a shallow region close to the free surface, and are called *Rayleigh waves*. Rayleigh waves travel slightly more slowly than the shear waves and produce both a vertical and horizontal particle motion that follow a retrograde elliptical pattern. The depth at which Rayleigh waves induce significant motion is inversely proportional to the frequency of the wave. Thus, low-frequency Rayleigh waves can produce particle motion at large depth, whereas high-frequency Rayleigh waves are confined to shallow depths. Noting  $K_{RS}$  the ratio between the wave propagation velocity of the Rayleigh and the shear waves  $K_{RS} = c_R/c_S$ , the following cubic equation in  $K_{RS}^2$  can be defined [193]:

$$K_{RS}^6 - 8K_{RS}^4 + (24 - 16\gamma^2)K_{RS}^2 + 16(\gamma^2 - 1) = 0,$$

Another type of wave rises at the interface between layers having a high contrast of material properties (e.g. soft layer lying on a rigid bedrock). These waves are called *Love waves*. For a detailed description of all body and surface waves we refer the reader to [10, 108, 193].

### 1.3.2 Elastic wave equation in the spectral-domain

Sometimes the variables of the problem have a harmonic dependence in time, at a given frequency  $\omega$ . This can be the case for example of a system submitted to steady forces which have reached a permanent regime in time, or of a transient dynamic problem formulated in the

Fourier domain. In these cases, the initial conditions are negligible (they can be considered as located at  $t = -\infty$ ), and the system of partial differential equations which governs the problem can be formulated in the frequency domain. The unknown field variable is now a complex-valued function which depends on the fixed angular frequency  $\omega$ , related to the time-dependent unknown as follows [44]:

$$\mathbf{u}(\mathbf{r}, t) \longrightarrow \Re[\tilde{\mathbf{u}}(\mathbf{r})e^{-i\omega t}] \quad (1.6)$$

Let consider a linearly elastic homogeneous body  $\Omega$  bounded by a border  $\partial\Omega$ . The equation of motion can be derived in the spectral domain by applying the Fourier transform to the Cauchy first law of motion (1.1) [4]:

$$\nabla \cdot \boldsymbol{\sigma} + \rho\omega^2 \mathbf{u} + \rho \mathbf{F} = 0 \quad \text{in } \Omega. \quad (1.7)$$

### 1.3.3 Low-strain levels and linear viscoelasticity

A stress wave propagating in a viscoelastic medium is subjected to two different attenuation phenomena, namely the geometric and the material damping [193]. The *geometric damping* has purely geometrical origin and is independent of the behaviour of the material. It is also called radiation damping because it results from the spreading of the wave energy at its wave front when travelling away from its source. The *material damping*, or intrinsic damping, is strictly related to the physical properties of the medium and represents different energy dissipation mechanisms, i.e. ground boundary relaxation, thermoelasticity, diffusional motion of dislocations and point defects, etc. Wave propagation through the earth's crust or in the ground presents both attenuation phenomena.

Experimental observations show that the stress-strain path followed during a cyclic excitation process and the magnitude of the deviatoric strain tensor are the most important external variables affecting the dynamic soil response [195]. Depending on the attained strain level, four types of phenomenological soil response to cyclic excitation can be identified (Tab. 1.1). Strains below the so-called *linear cyclic threshold strain*  $\gamma_t^\ell$  correspond to a nearly linear material response, whereas at larger strains non-linear behavior sets in and eventually dominates.

Shear Strain Magnitude	$0 < \gamma \leq \gamma_t^\ell$ Very Small Strain	$\gamma_t^\ell < \gamma \leq \gamma_t^v$ Small Strain	$\gamma_t^\ell < \gamma \leq \gamma_t^v$ Intermediate Strain	$\gamma_t^v < \gamma \leq \gamma_t^{pf}$ Large Strain
Soil Response	Linear Viscoelastic	Non-linear Viscoelastic	Non-linear Elasto-Visco-Plastic	Non-linear Elasto-Visco-Plastic
Type of Non-Linearity	-	Material	Material	Material and Geometric

**Table 1.1:** Phenomenological soil response to cyclic excitation as a function of shear strain level [195]. Below the linear cyclic threshold strain  $\gamma_t^\ell$  the behavior of soil can be accurately described from the phenomenological point of view by the theory of linear viscoelasticity.

The intended applications of this work are weak seismic waves or traffic-induced vibrations, for which shear strain levels are below the linear threshold. In this range, the typical dynamic stiffness reduction of inelastic behaviors is not yet observed, and there are not yet differences between drained or undrained responses, and the behavior of soil can be accurately described from the phenomenological point of view by the theory of linear viscoelasticity [193]. In general, the value of  $\gamma_t^\ell$  varies considerably with the soil type; it is on the order of  $10^{-4}\%$  for sands and of  $10^{-3}\%$  for normally consolidated clays with a plasticity index  $PI = 50$  [195].

The dynamic properties of soils are obtained in laboratory by imposing a cyclic loading history to a material specimen. Few laboratory tests enable to measure the dynamic properties of soils at low strain levels. The most employed techniques are the cyclic triaxial test and the resonant column test, followed by the ultrasonic pulse test and the piezoelectric bender element test. The basic principle of the resonant column device (Figure 1.8) is to excite one end of a confined cylindrical soil specimen in a fundamental mode of vibration by means of (free or forced) torsional or longitudinal excitation. Then, the measured resonance frequency and the amplitude of vibration are used to compute the wave velocities and strain amplitudes in the specimen. The dissipation displayed by a cyclically loaded material can be characterized by two quantities, namely the energy dissipated during each loading cycle and the ratio of this energy to an elastic reference energy. The second is the *attenuation*  $Q^{-1}$ , a measure of the internal friction, defined as [9]:

$$Q^{-1}(\omega) = -\frac{\Delta E}{2\pi E} \quad (1.8)$$

where  $\omega$  is the angular frequency of excitation,  $\Delta E$  is the energy dissipated during each cycle and  $E$  is the peak strain energy stored in the volume. For a detailed introduction to anelasticity we address the reader to [70] (theory of viscoelasticity) and [9] (applied seismology).

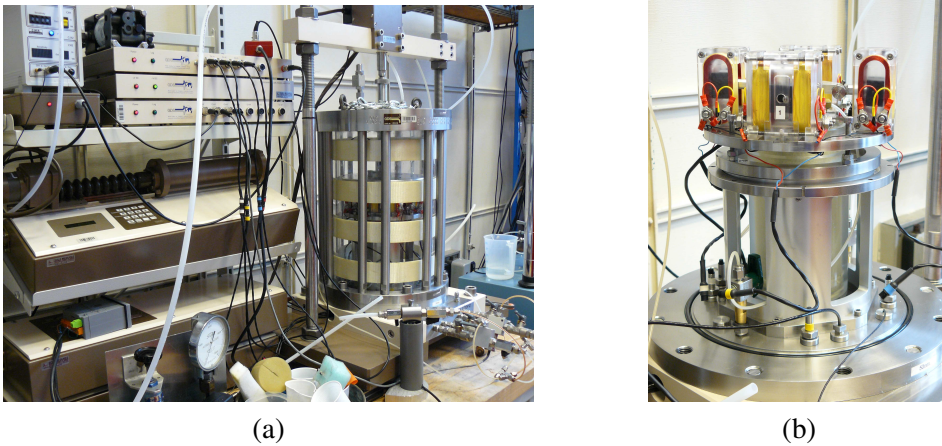


**Figure 1.8:** Pictures of a resonant column test device employed to measure the dynamic properties of soils up to medium strain levels of order  $\mathcal{O}(10^{-3})$  (courtesy of Luca Lenti, IFSTTAR). (a) Measuring system and (b) detail of the sample cell.

The attenuation plays an important role for vibrating systems close to their resonance frequency, because it allows the system to stay under a limited displacement amplitude. Another consequence of attenuation is the *phase velocity dispersion*, where the phase-velocity  $V_\Psi = \omega/k$  is defined as the velocity at which points of constant phase propagate ( $\omega$  being the circular frequency and  $k$  the real wavenumber) [174, 207]. The variations in phase velocity depend on viscoelastic properties of the medium, on the frequency content of the propagating wave and on the path followed by the latter. Due to this dispersion, wave data (body waves, surface waves, laboratory ultrasonic data, etc) can not be directly compared until a correction is made, e.g. by using the Futterman's theory for the body waves [57, 174].

### 1.3.4 Constitutive law for an isotropic linear viscoelastic medium

The constitutive relation for a linear viscoelastic medium is given by [70]

$$\sigma_{ij}(\mathbf{x}, t) = \int_{-\infty}^t \mathcal{C}_{ijkl}(t - \tau) \dot{\varepsilon}_{kl}(\mathbf{x}, \tau) d\tau, \quad (1.9)$$

where  $\sigma_{ij}(\mathbf{x}, t)$  and  $\varepsilon_{kl}(\mathbf{x}, \tau)$  are generic components of the stress and linearized strain tensors and  $\mathcal{C}_{ijkl}$  is the relaxation tensor, defined as the stress response for a Heaviside unit step function type strain variation. The constitutive law for a linear viscoelastic medium and the associated complex wavenumbers and mechanical parameters will be deepened in Chapter 2 to introduce the complex-wavenumber formulation of the fast-multipole boundary element method.

### 1.3.5 Rheological models

As the present work has been carried out in the frequency domain, the dependence of the material damping on the frequency does not play a significant role, thus no use has been made of any frequency-dependent dissipation model. However, time-domain analyses require the choice of an appropriate theoretical or empirical model for the lossy medium (soil) which takes into account the attenuation-frequency dependence [49, 285].

The rheological properties and behavior of soils can be well approximated by simple combinations of two elementary models: the Hooke body (reproducing a perfectly elastic behavior through a simple spring) and the Stokes or Newton body (also called Stokes or Newton dashpot, reproducing perfectly viscous behaviors). The most employed rheological models, the Maxwell body, the Kelvin-Voigt body and the Zener (or linear standard) body, are depicted in Fig.1.9. The expression of the complex modulus and of the relaxation and creep functions are different for each model, depending on the combination of elementary entities by which each model is constituted. The frequency-dependent attenuation relations of these three rheological models read:

$$Q_{Max}^{-1}(\omega) = \frac{E}{\omega\eta}$$

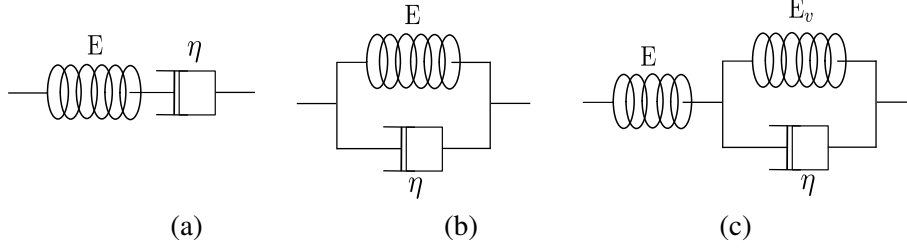


**Figure 1.9:** Various rheological models: (a) Maxwell, (b) Kelvin-Voigt and (c) Zener models.

$$Q_{K-V}^{-1}(\omega) = \frac{\omega\eta}{E}$$

$$Q_{Zen}^{-1}(\omega) = \frac{\omega\eta E}{E_v(E + E_v) + \omega^2\eta^2}$$

In Fig.1.10, the attenuation curves for the three rheological models are superposed. The Maxwell model does not allow instantaneous elasticity, as it involves an infinite attenuation in the zero-frequency limiting case (statics), the Kelvin-Voigt model attenuation is almost proportionate to the frequency and the Zener model presents a band-pass effect at low and high frequencies, and a band-cut effect in the middle-frequency range. For a detailed description of these simplest rheological models we refer the reader to the papers [226, 246] and monographs [49, 285]. Fig.1.11 shows the agreement of viscoelastic simulations compared with experimental results obtained by centrifuge testing [283]. In particular, the peaks of the signals due to the presence of high frequencies are strongly attenuated by the Kelvin-Voigt model, coherently with the observation made above around the frequency-dependent attenuation.

**Rheological models in seismic modelling.** A number of observations have shown that the quality factor  $Q^{-1}$  in the geological structures only slightly depends on frequency, remaining almost

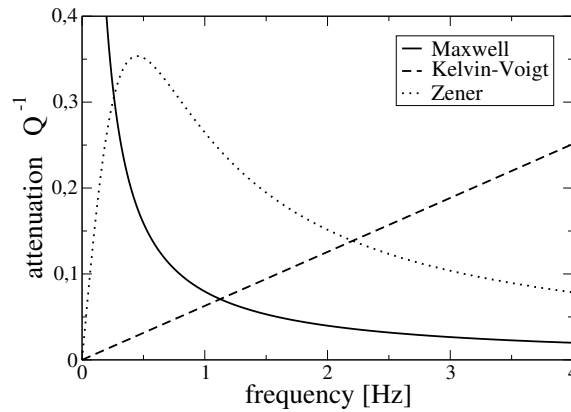


**Figure 1.10:** Attenuation versus frequency for different viscoelastic models.

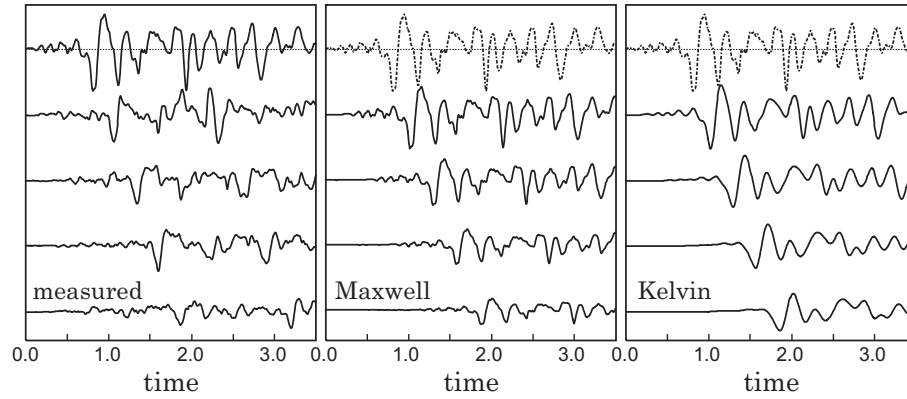


**Figure 1.11:** Signals of a longitudinal propagating wavefield registered at different points. Comparison of amplitude results obtained by experimental centrifuge testing (a) and by a numerical method that use different rheological models, namely (b) the Maxwell model and the (c) Kelvin-Voigt model (from [283]).

constant over a wide frequency range [188]. To fit with these experimental results, Liu et al. in 1976 proposed a complex viscoelastic model produced by the superposition of twelve Zener models, all having the same relaxed modulus but different central angular frequency [207]. This yields the *Nearly Constant Q* model (NCQ), whose frequency-dependence of attenuation and phase and group velocities as depicted in Fig.1.12. This model is quite flexible because its parameters can be set to obtain a nearly constant value of attenuation over the desired frequency range. However, the NCQ model holds only for  $Q > 30$ . Moreover, the width and cut-off frequency of the band over which  $Q^{-1}$  is constant is arbitrary, and the physical interpretation is weak, depending on the chosen model. A similar model was proposed in [106]. The NCQ model has been extended to non-linear behavior in [88]. In 1979, Kjartansson proposed the *Constant Q* model (CQ), which is a limit of the NCQ model for an infinite set of Zener models [185]. This model has the advantage of offering a frequency-independent  $Q$  and thus being easy to use in various situations. For a deeper insight in the rheological models (or relaxation mechanisms) we suggest [49, 285].

## 1.4 SIMULATING WAVE PROPAGATION

### 1.4.1 Analytical approaches

The first study of the vibration of an elastic half-space dates back to the classic work of Lamb in 1904 [196], who concentrated his attention on the vibrations generated by a point force normally applied to the free surface. With this work, carried out after the discovery of Rayleigh waves [253], Lamb endeavoured to make a step further in the theoretical understanding of earthquake phenomena, at that time analysed in the framework of the general laws of wave propagation in an infinite medium developed by Green and Stokes.

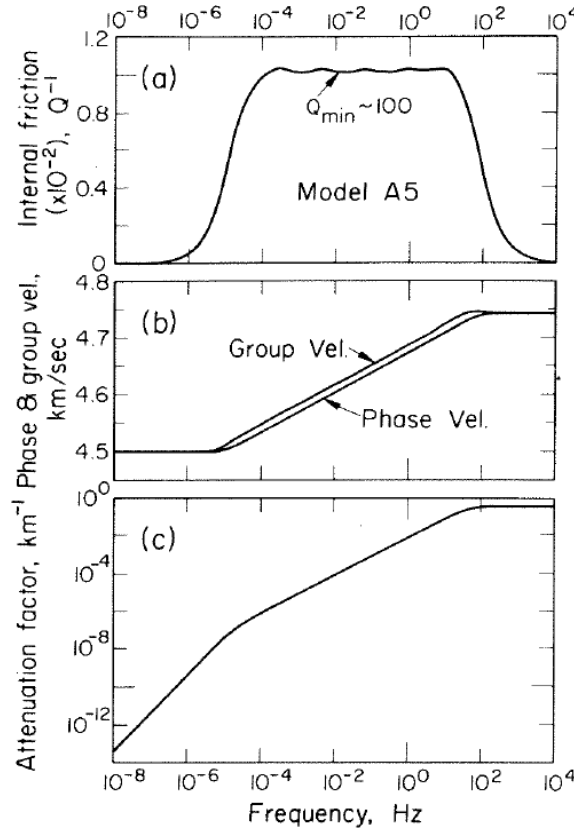


**Figure 1.12:** Frequency-dependence of (a) internal friction (or  $Q^{-1}$ ), (b) phase and group velocities and (c) attenuation factor for a Nearly Constant  $Q$  model having twelve relaxation mechanisms (from [207]).

**Seismic wave propagation** Nowadays, seismic problems involving simple geometries can be solved through modal approaches or analytical approaches. Modal approaches are based on the Rayleigh's method, an energy approach used in structural dynamics to find approximations to the lower natural frequency of a multi-degrees-of-freedom system; procedures based on such approach have been first devised for 1D soil profiles [92], then extended to two- and three-dimensional sedimentary valleys [239, 284]. Among the analytical approaches available in the literature to compute the scattering of a plane incident wave to an irregular interface we cite the *Aki-Larner technique* (AL), in which the scattered field is defined as the superposition of plane waves [9] and a *series expansion of wave functions* [268], which for simple geometries give a semi-analytical approximation of the scattered wave field.

**Railway-induced vibrations** In the last decades, considerable analytical efforts have been devoted to studying the response of a half-space to surface (static and harmonic) fixed or moving loads. After Lamb various researchers as [247], Bycroft [55], Lysmer and Richart [213] and Richart et al. [258] have studied the vibratory response of foundations. In 1994, Auersch studied the dynamic interaction of an infinite plate resting on a homogeneous half-space under a



vertical harmonic point load [19]. Results show that, at low frequencies, the behavior of the system was dominated by the half-space, at high frequencies by the plate, and in the intermediate range of frequencies by a dynamic interaction between the plate and the half-space, with a strong decreasing in waves amplitudes with distances. In 1998, Jones and Petyt employed a semi-analytical approach to study the ground vibrations caused by a rectangular harmonic load acting on a visco-elastic layer overlying a visco-elastic half-space [168]. Sheng et al. considered a harmonic unit point load acting on a railway track structure, defined as a beam resting on a layered ground [288]. A review of analytical models used to compute ground-borne vibrations can be found in [162, 200].

Barber has been one of the first who introduced the mobility of the source. In 1996, he proposed an exact expression for computing the normal surface displacements due to a normal point force moving at constant speed over the surface of an elastic half-space [24]. Later, various studies addressed the response of infinite periodic structure to moving loads [32, 289]. In 2006 and 2007, in various works Karlström and Boström proposed an analytical approach and a related numerical scheme to compute the ground vibrations from railways [175–177].

#### 1.4.2 Numerical modelling of wave propagation

##### Introduction

A variety of numerical methods exists for discretizing and solving the three-dimensional wave equation. Hereinafter, a brief survey of the most employed numerical methods for modelling wave propagation in unbounded domains is provided. These numerical methods differ in how they represent a continuous function and its time and space derivatives. In the next paragraphs, we review the most important *volume methods* (class of methods based on the three-dimensional discretization of the problem domain), namely the *finite and the spectral element methods*, the *finite difference method*, the *finite volume method*, the *discontinuous Galerkin method* and the *discrete element method*. The *boundary element method*, being of concern in the present work, is treated in details in the next Section.

The volume methods have in common some important computational issues. For example, the physical impossibility to discretize an infinite domain constrains them to consider a finite domain by introducing *artificial boundaries* through appropriate artificial boundary conditions to avoid the spurious reflections or wraparound from these fictitious boundaries. Another issue related to the volume methods concerns the discretization of large 3D regions. This leads to large systems of equations that easily involve millions of degrees of freedom and are prone to cumulative *numerical dispersion*.

Various other numerical methods allow to simulate the wave propagation in unbounded media but they are not discussed here. Among the others, the *Thin-Layer Method* (TLM) combines the FE method in the direction of layering together with analytical solutions for the remaining directions [180, 242]. The *ray theory* is based on the fact that propagating waves follow paths that respect the Snell's law and their amplitude at the wavefront is given by the geometrical

spreading of rays from the source to the receiver, and it is mainly used for wave propagation simulations on the earth crust and mantle scale [10]. The *reflectivity method* is based on a cylindrical coordinate system, through which wave equations are conveniently reduced into 1D [214, 232]. In [269], Sánchez-Sesma et al. proposed a choice of major contributions that triggered the development of powerful methods to compute ground motion. Among others, the Wong and Jennings' (1975) approach to topographical effects using boundary integrals [317], the Brebbia's book on the Boundary Element Method [51] and the Aki and Richards' book on Quantitative Seismology [10].

**Numerical models for attenuation and inelasticity.** At the origin, time-domain simulations were restricted to elasticity because the attenuation law for an isotropic viscoelastic medium expressed as a time convolution of a relaxation function and the strain rate (i.e. the Boltzmann principle) required too high storage capacities to be used and was therefore impractical to implement. To overcome this limitation, in 1984 Day and Minster proposed to approximate the viscoelastic modulus by a low-order rational function of frequency and to determine the coefficients of this function by the Padé approximant method [86]. This representation of the anelastic attenuation law was shown to be better suitable for time-stepping. Day and Minster observed that all approximants led to causal, stable and dissipative  $Q$  operators that form uniformly convergent sequences ( $\lim_{n \rightarrow \infty} Q^{-1} = Q^{-1}$ ). Some years later, Emmerich and Korn [106] and Carcione et al. [57] proposed the direct use of simple rheological models (a generalized Maxwell body like model and a generalized Zener model respectively) whose viscoelastic modulus was expressed as a rational function. They showed that more accurate and efficient results could be obtained with respect to the Day approach. In 2005, Moczo and Kristek have shown the equivalence of the Emmerich and Korn generalized Maxwell body and the generalized Zener body [226]. The limitation of the introduction of the additional memory variables as firstly proposed by [86] consists in the very large computational storage required. Recently, efforts have been made towards more memory-efficient implementations [84, 85]. In Sec. 1.3.5, the rheological models used in seismic wave propagation are briefly summarized. In the following, we will indicate how each method handles attenuation for wave propagation simulations in anelastic media.

### Overview of numerical methods in visco-elastodynamics

**Finite Difference Method.** The finite-difference (FD) method is based on a discretization of the domain by a space-time grid. This method is largely adopted because of its satisfactory accuracy, ease of implementation, and low memory needed per grid point. In 1968, a first paper by Alterman addressed wave propagation in a layered elastic medium triggered by a buried point source emitting a compressional pulse [14]. In this work, the propagation equation was solved in each homogeneous medium and boundary conditions between the different media were explicitly verified (*homogeneous approach*). Later, this approach was improved to implicitly satisfy the boundary conditions at the layer interfaces (*heterogeneous approach*) [182]. Some prob-

lems related to the numerical dispersion of the wave field were overcome with the introduction of *staggered grids*, that made the finite-difference method more efficient than the finite-element method in the high frequency range [309]. An overview of staggered-grid approaches can be found in [141]. In 2000, Saenger et al. proposed to use the *rotated staggered-grid* (RSG) to deal with high contrast discontinuities [267]. The RSG enables to model cracks, pores, free surfaces without using boundary conditions. Recently, the same authors apply the RSG to the wave equations for anisotropic and viscoelastic media [266]. A comparison of high-accuracy finite-difference schemes is addressed in [331].

As the classical FDM relies upon regular grids, it is limited in presence of strong contrast in the material stiffness because it is not easy to adapt to the local wavelengths of propagating waves. The discretization with respect to the shorter wavelength leads to an over-refinement of the stiffer regions, with a consequent growth of the required computational time and CPU memory. Moreover, the time step in an explicit time integrator is artificially small to accommodate the Courant-Friedrichs-Lewy (CFL) stability condition in the stiffer regions. To overcome these limitations, discontinuous grids can be employed [18, 194]. Alternatively, the FDM can be coupled with the finite-element method (FEM) in a *hybrid method*, where one or several regions are modelled by the FEM, and the propagation space by the FDM. In [228], the FEM is used to discretize a dynamically rupturing fault and the free-surface topography, and the FDM is used to discretize the heterogeneous medium of propagation.

Various studies addressed the stability, numerical dispersion, physical dispersion, and computational accuracy and efficiency of the viscoelastic finite-difference schemes [259]. Nowadays, large three-dimensional FD visco-elastic wave propagation modelling can be performed by using massive parallelization techniques [43].

**Finite Element Method and Spectral Element Method.** The *finite element method* (FEM) in dynamics is based on a discrete approximation of the equation of motion in its weak formulation [159, 330]. This method presents well known advantages, as the possibility to model complex geometries (e.g. arbitrary shapes, realistic topography profiles), complicated constitutive laws (e.g. non-linearities, inelasticity) and strong heterogeneities or inclusions. First applications of the FEM to seismology were carried out in the '70s in [212] (for surface waves) and [293] (for body waves). A recent review of the FEM in seismic wave modelling can be found in [216]. In the practice, the FEM is widely adopted to simulate ground-borne vibrations induced by dynamic sources located in the vicinity of the free-surface such as railway traffic [169, 170, 263, 287] or tunnels excavation [250, 322]. However, the classical FEM is based upon low-order approximations that are known to introduce numerical dispersion [221, 231]. Other purely numerical spurious effects may arise, e.g. numerical damping, polarization errors, numerical anisotropy introduced by the spatial discretization, errors in phase and group velocities, spurious diffraction and scattering or extraneous parasitic modes [285]. These numerical errors are non physical, and must be minimised. For this purpose, one possibility when using low order FE is to refine the discretization of the computational domain. However, this

choice involves a growth of the computational costs. Another possibility is to increase the degree of polynomials used in the basis functions. The efficiency of high-order FEM in ground motion simulations is discussed in [278]. High-order methods may also combine the accuracy of the global pseudo-spectral method with the flexibility of the finite-element method. They were originally introduced in computational fluid dynamics [244] and are called *spectral finite element method* (SEM or SFEM). Reviews of the SEM in seismology are addressed in [66, 192, 225]. Some applications of the SEM are the seismic inverse problems, that aim at improving source and Earth models [306], or the simulation of ground motion induced by surface moving loads [240].

With modern advances in parallel computing and supercomputing performances, the expensive time and memory requirements usually needed for problems involving a high number of degrees of freedom (DoF) have been broken down [22]. Parallelization techniques and multi-core computations can be easily exploited in the framework of the domain decomposition approaches [109, 305]. Domain decomposition methods (DDM) will be introduced in Section 3.2.2. An octree-based finite-element method has been proposed for ground motion simulation in realistic basins by Bielak et al. [40], and high-order FEM simulations have been recently performed on large clusters by Komatitsch et al. [190].

In FEM simulations in anelastic media, attenuation and dispersion are taken into account in the material constitutive law through a damping matrix. In structural dynamics, although the field of damping matrix identification is still widely open [249], usually the *proportional damping* is employed through the so called *Rayleigh matrix*, where damping is a linear combination of the mass and stiffness matrices [69]. In seismic wave propagation, nearly constant Q-models (NCQ) or constant-Q (CQ) models are usually employed (see Sec. 1.3.5). In 1997, Semblat gave a rheological interpretation of the Rayleigh matrix by showing the equivalence of the Rayleigh damping and the generalized Maxwell model for small to moderate values of damping ratio [277]. The finite-element frequency domain viscoelastic formulation will be recalled in Section 3.3.

**Discontinuous Galerkin Method.** The *discontinuous galerkin* (DG) method was introduced in the early seventies [254] for the numerical approximation of linear transport equations. The DGM can be thought as a hybrid of the finite-element and the finite-volume methods, the numerical solution being approximated by piecewise polynomials which allows discontinuities of the solution across the element interfaces. In fact, the finite-volume method (FVM) constitutes a particular case of the DGM, having zero-order approximations. The high-order accuracy of the DGM on unstructured and non-conforming meshes, the local hp-refinement, the weak boundary conditions allow accurate modelling of strong heterogeneities and discontinuities. Theoretical and computational developments of the DGM until 2000 are well described in [71]. Recent advances in seismic wave propagation modelling can be found in [98] (DGM) and in [99, 100] (FVM). In [227], Moczo et al. investigate and compare the accuracy of 3-D time-domain explicit numerical schemes based on the FD, FE, spectral-element (SE) and

discontinuous-Galerkin (DG) methods with respect to the  $V_P/V_S$  ratio in an unbounded homogeneous medium.

The incorporation of realistic attenuation properties in DGM consists in completing the linear hyperbolic system arising from the velocity-stress formulation with additional equations for the anelastic functions that result from the rheological model of the generalized Maxwell body [178].

**Discrete Element Method.** The discrete particle scheme was at the origin introduced for the physical modelling of microscopic crystals [157], then this approach was extended to rock mechanics problems and named the distinct-element method [78]. In the *discrete element method* (DEM) the medium is not considered as a continuum, but composed by discrete material particles. For equilibrium, these particles interact with each other at their contact points, are subjected to elastic forces proportional to their displacement and their movement is followed in the space by numerically solving their motion equations. Thus, the DEM does not solve the continuum wave equations directly, but try to replicate the underlying physics at a 'microscopic scale' discrete micro-mechanical interaction rules between the particles. An advantage of the discrete methods consists in the fact that discontinuities (e.g. fractures, pore fluids, non-welded interfaces) can be naturally handled. Moreover, a large range of heterogeneity in grain properties can be explored, such as size and bulk modulus, as well as a variety of spatial distributions of those properties. Application of the discrete-element method in ground motion simulations can be found in [237,304]. Recently, Munjiza proposed a new very promising method which merges finite element tools and techniques with discrete element algorithms, the *combined finite-discrete element method*. This method allows the transition from continua to discontinua (e.g. fracture and fragmentation processes, explosions) and to account for multi-phase materials [67], energy dissipation mechanisms (e.g. elastic hysteresis, plastic strain, friction) [233].

### 1.4.3 Artificial truncation of unbounded domains

A computational domain, i.e. the spatial domain over which an equation is solved numerically, must be of finite dimension. Therefore, when the problem at hand is defined over an infinite domain, an artificial boundary  $\mathcal{B}$  must be introduced to restrict the original problem over a bounded domain  $\Omega$ . To truncate infinite or large domains, three main classes of approaches are available: the boundary integral methods, the infinite elements techniques and the artificial boundary conditions (ABCs), see Figure 1.13. The objective is that the solution of the problem in  $\Omega$  together with the chosen approach on  $\mathcal{B}$  corresponds to the restriction to  $\Omega$  of the solution over the infinite domain. In the present work, attention is focused on the *boundary integral method*. Therefore, the use of coupled formulations finite/boundary element method to truncate the infinite domain is specifically addressed in Section 3.2.

*Infinite elements*, pioneered in early '90s by Bettess [37], are derived from standard finite elements and modified to represent a decay type behavior as one or more dimensions approach infinity [89, 330]. Coupling FEM/infinite elements formulations have been applied to vari-

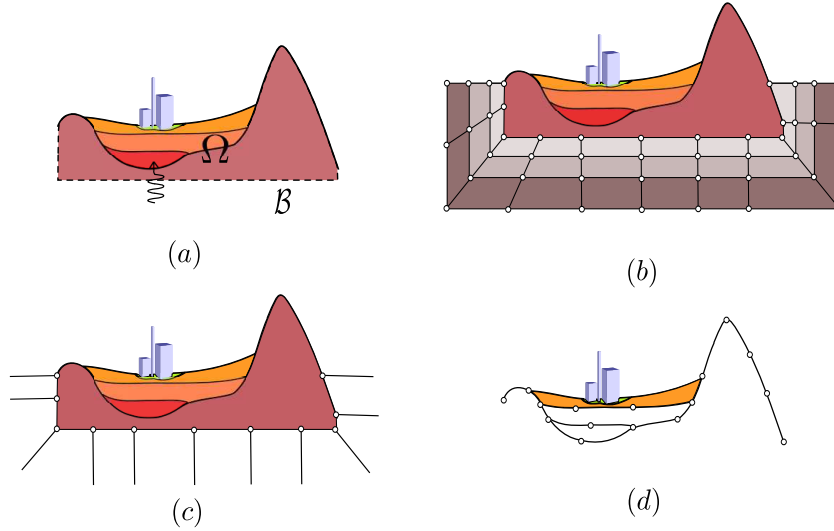


**Figure 1.13:** Various approaches to deal with the artificial truncation of unbounded domains. Example of wave propagation problem restricted to a finite domain  $\Omega$  with artificial boundary  $\mathcal{B}$ : (a) truncated domain and artificial boundary, (b) absorbing layers method (e.g. PML), (c) infinite elements technique, (d) boundary integral method. In (d), notice that piecewise homogeneous layers can be solved within the BEM, thus avoiding the discretization of large domains and consequent computational costs and numerical dispersion.

ous wave propagation problems in unbounded media, for example: seismic wave propagation in three dimensional continuum [327], in unbounded saturated porous media [183], to train-induced vibration studies [321, 322]. The third class of methods are the ABCs, which include non-reflecting boundary conditions (NRBCs) and absorbing layers (e.g. the perfectly matched layers, PML).

**Artificial boundary conditions.** Artificial boundary conditions (ABCs) are specific boundary conditions defined on the external artificial boundary  $\mathcal{B}$  of  $\Omega$  to reproduce the radiation conditions at infinity and to avoid spurious reflections. In the literature, depending on the field in which they are employed (e.g. acoustics, electromagnetics, meteorology, elastodynamics) ABCs are also called radiating, silent, open, free-space or transparent boundary conditions. The two main categories of available ABCs are the following:

- *Non-reflecting boundary conditions (NRBCs).* NRBCs divide into local (approximated) and non-local (exact). Low-order *local NRBCs*, introduced in the late 70's, approximate the NRBCs on  $\mathcal{B}$  [29, 107]. They are simple and easy to implement, numerically cheap and can be applied to any geometry. However, they lack accuracy. *Non-local NRBCs*, introduced in the late 80's [135, 181], have high accuracy and robustness at the price to be cumbersome and computationally expensive. Moreover, as the exact ABCs involve integral transforms along  $\mathcal{B}$  and pseudodifferential operators, such BCs can be easily applied only over simple geometries of  $\mathcal{B}$ . High-order local BCs were proposed more recently to improve accuracy performances of the local BCs [143, 151]. High-order local NRBCs

based on an optimally localized Dirichlet-to-Neumann BC (DtN) were derived by Givoli for a general class of wave problems, then applied to time-dependent waves in [136]. However, the better accuracy of high-order local NRBCs is obtained by somehow accounting for the non-local nature of ABCs. Thus, this procedure penalizes the typical advantages of the pure local NRBCs. A review of the NRBCs containing a comparative study of the local and non-local conditions can be found in [137, 307].

- *Absorbing layers.* This technique consists in adding one or more artificial absorbing layers on the external boundary  $\Gamma$  of the truncated domain. The mechanical characteristics of the layers are such that they are able to keep the energy of the wave and to soak it up, preventing any reflection. The simpler absorbing layers (called "sponge layers") only add some dissipative terms to damp the outgoing waves. However, this approach has two limitations, namely i) the properties of the layers depend on the frequency and direction of propagation of the incident wave and ii) the gradient within the absorbing layers may produce itself spurious reflections. The *perfectly matched layers (PML)* were first introduced for the Maxwell's equation in 1994 [34]. Besides the classical one [114], various types of PML formulations have been proposed recently as the filtering (or convolutional) PML [114] and the multidirectional PML [191, 281]. Stability of the PML model is addressed in [31].

## 1.5 FAST MULTIPOLE BOUNDARY ELEMENT METHOD

After the volume methods, we present the *boundary element method* and highlight the main features of the fast multipole algorithm and other techniques used to accelerate boundary element computations. The fast multipole boundary element method (FM-BEM) will be recovered in more detail in Section 1.5.

### 1.5.1 Boundary Element Method.

The *boundary element method* (BEM) is based on boundary integral equation (BIE) formulations [44, 51]. Two types of BIE formulations can be used for the description of boundary-value problems: *direct* BIE formulations relate the values taken on the boundary by the primary physical variables (i.e. the potential and its normal flux), whereas *indirect* BIE formulations use secondary variables, namely a real or fictitious source densities that usually do not have physical meaning. In the theory of elasticity, direct integral equations are formulated through the application of the Somigliana identity [297], whereas indirect integral equations stems from the potential theory. The present work is based on a direct BIE formulation. The BIEs can be discretized using a *collocation method*, that consists in enforcing the BIE in a certain number of discretization points or elements [44], or using a *Galerkin method*, a variational approach based on a weak formulation of the BIE [45]. The former leads to a non-symmetric system matrix, whereas the latter has the advantage that it may lead to a symmetric system of equations, although at the price of evaluating double surface integrals. In addition to the reduced

model size allowed by the boundary-only discretization, the boundary element method is very well suited to dealing with propagation in unbounded media because of the built-in, exact satisfaction of radiation conditions [48, 95]. Thanks to this property, the BEM does not need the introduction of artificial boundaries as in volume methods. For this reason, in various fields such as acoustics, electromagnetism or elastodynamics, the BEM is often coupled with the finite element method to solve wave propagation problems in infinite domains as an alternative to the use of non-reflecting boundary condition (NRBCs). As this aspect is of particular interest in the present work, it is addressed in more details in Section 3.2. The BE formulation relies upon the use of particular fundamental solutions in the reciprocity identity. As the Green tensors for configurations like the half-space or layered media are difficult and costly to implement, often the free-space Green tensor is used together with appropriate boundary conditions for dealing with piecewise homogeneous media and semi-infinite domains. The direct traditional BEM find numerous applications in two-dimensional and three-dimensional ground motion simulations [166, 230, 255]. Some interesting example of application of the BEMs to vibrations modelling can be found in [13, 21, 117, 179] simulations.

### 1.5.2 Viscoelasticity with BEMs.

Various approaches exist to adapt the elastodynamic BEM to viscoelasticity. In general, the time-domain boundary element method is characterized by a temporal convolution of the fundamental solutions with boundary data that are approximated by polynomial shape functions in time and in the finite elements. Three main approaches are available. The first consist in using directly the viscoelastic fundamental solutions in the time-domain and perform the convolution product analytically. However, viscoelastic fundamental solutions exist only for very simple problems (e.g. for quasi-static problems in visco- or poroelasticity time-dependent fundamental solutions), but they are complicated and yield to very sensitive algorithms. Moreover, time-stepping should be properly chosen to avoid instabilities and artificial damping [274]. The second possibility consists in performing a classical time-domain time-stepping by using the elastic-viscoelastic correspondence principle in the Laplace domain. The elastic-viscoelastic correspondence principle allows to obtain the viscoelastic fundamental solutions from the elastodynamic ones by substituting the elastic moduli in the Laplace transformed domain with the transformed impact response functions of the viscoelastic material model. This second approach has however the disadvantage of requiring an inverse transform back to the time-domain that depends strongly on the choice of the inverse formula parameters. The third approach is based on the convolution quadrature method (CQM) proposed by Lubich in 1988 [210]. In this approach, the convolution integral is approximated by a quadrature formula whose weights are determined by the Laplace transform of the fundamental solution and a linear multistep method, thus avoiding the back transformation from the Laplace domain [272, 274, 275].

In the frequency domain, usually the mechanical parameters are complex-valued, with the imaginary part expressing attenuation [94]. Recently, Chaillat and Bui proposed a simple method to formulate the viscoelastic BIEs by using the classical elastodynamics BEM formula-



tion and keeping the material parameters real-valued. To do this, they used a Zener rheological model and introduced new intermediate variables [64].

### 1.5.3 Inelasticity with BEMs.

Modelling material inelasticity is a modern challenge of numerical ground motion simulations [292]. In high seismic activity zones, experimental measurement by accelerometers have provided direct evidence of nonlinear soil behavior [314]. Various boundary-element formulations exist to handle dynamic inelastic problems under condition of small strains and displacements, involving for example elastoplastic or viscoplastic behaviors [35, 154, 296]. In [35], Beskos distinguished the formulations that employ elastodynamic fundamental solutions from those that use the elastostatic fundamental solution. The numerical method that use the elastostatic fundamental function is also called *domain-BEM* (D-BEM) [153]. However, both formulations involve inelastic domain integrals. A full domain discretization is required in the regions in which inelastic behavior is expected. As a consequence, the advantage of the elastic BE formulation of restricting the discretization to the only boundary is lost. To avoid the domain discretization, a new type of BEM has been proposed in which the inertial domain integral is transformed into a boundary integral by a suitable choice of interpolation functions, the *dual-reciprocity BEM* (DR-BEM) [243]. The discretized equations of motion are then solved by efficient time stepping algorithms. However, as in both the D-BEM and the DR-BEM the radiation condition is not fulfilled by the fundamental solution, non-reflecting boundary conditions should be provided. In 2005, Soares et al. proposed an iterative coupling between a D-BEM and a time domain BEM (TD-BEM) for non-linear dynamic analysis. The original problem domain was split into two subdomains. Then, the bounded subdomain containing non-linearities was modelled by D-BEM, whereas the complementary unbounded domain (that guarantee the wave radiation) was modelled by the TD-BEM [295].

As inelastic behavior are well handled by the finite-element method and the radiation in elastic infinite domains naturally fulfilled by the classical BE formulation, often hybrid methods which appropriately combine the advantages of both the FEM and the BEM are preferred. Several FEM/BEM coupling techniques have been presented in the literature. In this work, we are interested in coupling the FEM with the fast-multipole BEM in visco-elastodynamics, see Section 2.4.2 and Chapter 3. The algorithms presented here deserve further investigations in the near future, oriented in particular towards the account for inelastic behaviors in the FEM subdomain.

### 1.5.4 Fast BEMs.

Solving the potentially large fully-populated non-symmetric linear system arising in the classical BEM formulation entails unreasonably high CPU time and memory requirements (e.g. using direct solvers such as LU factorization  $\text{CPU} = \mathcal{O}(N^3)$ ). The use of iterative solvers (e.g. the generalized minimal residual method, GMRES) reduces to  $\text{CPU} = \mathcal{O}(N^2)$  per iteration,

but the size of the problems is limited to  $N = \mathcal{O}(10^4)$  on ordinary computers. To overcome this limitation and accelerate the solution of the BE linear system, various techniques have been developed during the last decades. Usually, they rely upon iterative solvers and aim at accelerating the matrix-vector product performed at each iteration, which is the most expensive task for an iterative solver. Some of these acceleration methods are based on approximations of the kernel function (e.g. the fast-multipole method), others are kernel-independent purely algebraic approaches based on fast representation of the coefficient matrix (e.g. the panel clustering method, the  $\mathcal{H}$ -matrix method, the adaptive-cross approximation). The *fast-multipole method* (FMM) was introduced for the rapid evaluation of the potential and force fields in systems involving large numbers of particles, and it is based on a multipole expansion of the fundamental solution [142, 260]. For a linear system of size  $N$ , the FMM combined with an iterative solver entails a solution time of order  $\mathcal{O}(N \log N)$ . The FMM applied to the BEM is used in the present work and will be detailed in Section 1.5. In 1989, the panel clustering discretization approach was applied to the fast solution of the boundary-element linear system in the so-called *panel clustering method* [150]. More recently, the  *$\mathcal{H}$ -matrix method* has been introduced. This approach uses the hierarchical  $\mathcal{H}$ -matrices to represent the collocation BEM matrix [149]. The *adaptive cross-approximation* (ACA) approach is based on the low-rank approximation technique, a block-wise approximation of the collocation matrix by low-rank matrices [30]. In the *wavelet-based methods*, the system matrix is approximated by a sparse matrix containing only nearby wavelet interactions [38].

### 1.5.5 Remark: BEM vs ABCs.

The main available techniques to deal with the numerical truncation of an infinite or large domain have been briefly summarized above. In the context of artificial BCs, Givoli divides wave problems in four categories of increasing difficulty [136]: (i) linear time-harmonic wave problems, (ii) linear time-dependent wave problems in non-dispersive homogeneous media, (iii) linear time-dependent wave problems in dispersive and/or stratified media and (iv) non-linear time-dependent wave problems. Problems (i) have been treated extensively with both local and exact NRBCs and various PML formulations. Problems of the type (ii) are more difficult to handle with the ABCs, but they have been addressed in some works, recalled in [136]. The treatment of dispersive or layered media is addressed only in very few works. Finally, problems having non-linearity extending to infinity have been very poorly discussed in the literature.

The present work addresses problems of type (i) in dispersive and/or stratified media, and the fast-multipole boundary element method (FMBEM) is used as an alternative to the ABCs. The main advantage of using the FMBEM with respect to the NRBCs is that the former combines the high accuracy of non-local NRBCs with the advantages of local NRBCs (geometrically more adaptable, numerically cheap). Compared to the PML, the FMBEM discretizes only the artificial boundary  $\mathcal{B}$  of the truncated domain  $\Omega$ . Moreover, eventual stratifications or piecewise homogeneous layers can be discretized within the same FMBEM, thus limiting the dimensions of  $\Omega$ , as shown in Figure 1.13.

## 1.6 OUTLINE

The objective of this thesis is to make a step forward in the numerical modelling of wave propagation in three-dimensional unbounded media. Intended applications vary from seismic wave propagation and amplification analysis to the modelling of railway-induced vibrations in the ground and propagation in adjacent structures. The starting point of the present work is the fast-multipole formulation of the boundary element method (FM-BEM) in frequency-domain elastodynamics proposed by Chaillat in [62, 63]. The FM-BEM and its variant multi-level (MLFM-BEM) strongly reduces the computational burden of the traditional BEM and enables the solution of problems involving up to  $\mathcal{O}(10^6)$  degrees of freedom (DoFs). Although the elastodynamic FM-BEM was limited to linear elastic behavior and piecewise homogeneous media, it has been successfully applied to the solution of seismic wave propagation problems. The present thesis aims at extending the potentialities of the existing FM-BEM in two directions. On the one hand, the ML-FMBEM formulation has been extended to viscoelasticity. Indeed, the ability to consider material attenuation enables more realistic wave propagation modelling, allowing to e.g. reproduce the amplitude decay of propagating waves or free vibrations or describe the finite amplitudes and phase shifts of systems excited near resonance. On the other hand, the possibility to couple the FM-BEM with the finite element method (FEM) has been investigated in order to increase the applicability of the method to deal with complex structures, strong heterogeneities or eventual non-linear behaviors.

Apart this introductory chapter, Chapter 2 is concerned with carrying over the existing single- and multi-domain elastodynamic multi-level FM-BEM formulations to the case of weakly dissipative viscoelastic media. In Chapter 3, two different strategies for coupling the FEM and the MLFM-BEM are proposed. The first approach consists in an *iterative Dirichlet-Neumann coupling* with interface relaxation of displacements. The main advantage of this approach is the easy implementation, because existing FEM and FMBEM software can be used in black-box fashion and be only driven by the external interface algorithm. However, the convergence of the overall algorithm depends strongly on the problem geometry, boundary data and on the choice of the relaxation parameter. The second strategy is a *simultaneous coupling* approach based on the solution of a global system of equations combined with the transmission conditions across the common interface. An implicit condensation for the FEM degrees of freedom is employed and the global system is solved by generalized minimal residual (GMRES). This second approach has the advantage to be robust and scalable. In this thesis, using available resources, we have integrated some needed FEM subroutines in the FMBEM software. Future applications of the FEM/FMBEM coupling are oriented towards the study of seismic waves propagation and soil-structure interaction, traffic-induced vibrations and their interaction with adjacent structures.

This thesis has four Appendices. Appendix A is devoted to the numerical evaluation of the spherical Hankel functions with complex-argument, an issues related to the evaluation of the Helmholtz Green's function expansion for the complex-wavenumber formulation.. Appendix B contains the analytical formula for the solution of the academic problems employed in Chapter

2. Appendix C is a brief review of the most used interface relaxation algorithms that can be possibly used in alternative to the Dirichlet-Neumann algorithm adopted in this work to study the iterative FEM/FMBEM coupling. Finally, Appendix D contains the User's guide to the three codes used in the present work, namely `COFFEE` (fast FMBEM solver for 3-D time-harmonic visco-elastodynamics), `CUSEQ` (iterative FEM/FMBEM coupling) and `CUSIM` (simultaneous FEM/FMBEM coupling).

## Chapter 2

# Application of the multi-level time-harmonic FM-BEM to 3-D visco-elastodynamics

### Contents

---

2.1	Introduction . . . . .	30
2.2	Elastodynamic Fast Multipole Boundary Element Method: survey . . . . .	31
2.3	Behavior of weakly dissipative media . . . . .	44
2.4	Multi-Level FMBEM formulation for viscoelastodynamics . . . . .	47
2.5	Truncation of the transfer function with complex-wavenumber . . . . .	50
2.6	Full ML-FMBEM examples in 3-D visco-elastodynamics . . . . .	55
2.7	Multi-domain ML-FMBEM in 3-D visco-elastodynamics . . . . .	60
2.8	Some remarks on preconditioning . . . . .	65
2.9	Conclusions . . . . .	66

---

## 2.1 INTRODUCTION

This work is concerned with carrying over the single- and multi-domain elastodynamic FMBEM formulations of [62, 63] to the case of weakly dissipative viscoelastic media. Indeed, the ability to consider material attenuation enables more realistic wave propagation modelling, allowing to e.g. reproduce the amplitude decay of propagating waves or free vibrations or describe the finite amplitudes and phase shifts of systems excited near resonance [128].

The overall FMBEM algorithm is identical to that for the corresponding lossless medium, but the setting of important algorithmic parameters such as the truncation parameter is affected by the damping factor, an issue which has not been studied in depth, in particular in terms of mathematical error analysis. A complex-wavenumber FMBEM formulation for electromagnetic scattering is proposed in [133, 134], where the truncation parameter is empirically shown to increase with  $\beta$  in order to maintain a given accuracy on the fundamental solution evaluation. Empirical studies on the low-frequency expansion [118] yield guidelines on the adjustment of the truncation parameter depending on  $\beta$ . The FMBEM analysis of sound fields in porous materials is addressed in [323], where contributions from cells located beyond a certain normalized distance from the evaluation point are simply ignored, resulting in a well-conditioned influence matrix and a reduced computational time. The latter approach is, however, not suitable for weakly dissipative media ( $\beta \ll 1$ ) because the cut-off distance is proportional to  $\beta^{-1}$ .

This Chapter is organized as follows. Section 2.2 recalls the classical elastodynamics BIE formulation and its solution using the multi-level fast-multipole boundary element method (FMBEM). Section 2.3 gathers necessary background about the time-harmonic behavior of weakly dissipative viscoelastic media. Section 2.4 details the key BIE formula affected by the introduction of the complex-wavenumber and complex mechanical parameters. Section 2.5 then concentrates on the crucial task of evaluating the multipole decomposition of the viscoelastodynamic fundamental solution. In the present work, a damping-dependent modification of the selection rule for the multipole truncation parameter, required by the presence of complex wavenumbers, is proposed, empirically adjusted so as to maintain a constant accuracy over the damping range of interest in the approximation of the fundamental solution, and validated on numerical tests focusing on the evaluation of the latter. The proposed modification is next assessed in Section 2.6 on full visco-elastodynamic examples for which an exact solution is known. In Section 2.7, the visco-elastodynamic settings are finally applied to the multi-domain version of the ML-FMBEM featuring a BE-BE coupling strategy, previously developed in [63] for the elastodynamic case, and validated on a simple spherically-symmetric configuration and on the problem of a wave propagating in a semi-infinite medium with a lossy semi-spherical inclusion (alluvial basin).

## 2.2 ELASTODYNAMIC FAST MULTIPOLE BOUNDARY ELEMENT METHOD: SURVEY

### 2.2.1 Boundary Element Method

Hereafter, we introduce the boundary integral equation formulation for frequency domain elastodynamics and the boundary-element method. First, we briefly recall the reciprocity identity and the fundamental solutions. Then, we define the integral representation formula, the boundary integral equation and their discretization in the framework of the frequency domain elastodynamic BEM.

**Reciprocity identity.** Let  $\Omega$  be a bounded elastic body with boundary  $\partial\Omega$  and density  $\rho$ . The reciprocity identity stems from the virtual work principle and expresses an integral relation between two general elastodynamic states  $(\mathbf{u}^{(1)}, \boldsymbol{\sigma}^{(1)}, \mathbf{F}^{(1)})$  and  $(\mathbf{u}^{(2)}, \boldsymbol{\sigma}^{(2)}, \mathbf{F}^{(2)})$  on  $\Omega$ :

$$\int_{\partial\Omega} [\mathbf{T}^n(\mathbf{u}^{(1)}) \cdot \mathbf{u}^{(2)} - \mathbf{T}^n(\mathbf{u}^{(2)}) \cdot \mathbf{u}^{(1)}] dS = \int_{\Omega} \rho [\mathbf{F}^{(2)} \cdot \mathbf{u}^{(1)} - \mathbf{F}^{(1)} \cdot \mathbf{u}^{(2)}] dV, \quad (2.1)$$

where  $\mathbf{u}$  denotes the displacement field,  $\boldsymbol{\sigma}$  the stress field,  $\mathbf{F}$  is a body force distribution and  $\mathbf{T}^n(\mathbf{u}) \equiv \boldsymbol{\sigma}(\mathbf{u}) \cdot \mathbf{n}$  is the traction vector operator. When  $\Omega$  is unbounded, eq. (2.1) holds provided that the two elastodynamic states satisfy the decay and radiation conditions at infinity, sufficient conditions to ensure the uniqueness of solution in exterior problems [108].

**Free-space fundamental solution.** Let  $\Omega'$  be an open subset of  $\mathbb{R}^3$  such that  $\Omega \subseteq \Omega'$ . The solutions to the local equation of motion in  $\Omega'$  for a point force source of unit amplitude applied at a point  $\mathbf{x} \in \mathbb{R}^3$  in the direction  $i$ , i.e.:

$$\rho F^i(\mathbf{y}) = \delta(\mathbf{y} - \mathbf{x}) \mathbf{e}_i, \quad \mathbf{y} \in \Omega'$$

are called *fundamental (or elementary) solutions*. For time-harmonic problems with circular frequency  $\omega$ , the fundamental solutions solve the Helmholtz equation:

$$\Delta \mathbf{U} + k^2 \mathbf{U} + \delta(\mathbf{y} - \mathbf{x}) = 0 \quad (2.2)$$

where  $k = \omega/c$  is the real wavenumber. In the particular case when  $\Omega' = \mathbb{R}^3$ , the fundamental solution which solves the Helmholtz equation is called the *Helmholtz fundamental solution* and reads [108]:

$$U_i^k(\mathbf{x}, \mathbf{y}; \omega) = \frac{1}{4\pi\mu r} [A\delta_{ik} + Br_{,i}r_{,k}], \quad (2.3a)$$

$$\Sigma_{ij}^k(\mathbf{x}, \mathbf{y}; \omega) = \frac{1}{4\pi\mu r^2} [2Cr_{,i}r_{,k}r_{,j} + (\delta_{ik}r_{,j} + \delta_{jk}r_{,i})D + \delta_{ij}r_{,k}E] \quad (2.3b)$$

where  $U_i^k(\mathbf{x}, \mathbf{y}; \omega)$  and  $\Sigma_{ij}^k(\mathbf{x}, \mathbf{y}; \omega)$  are respectively the  $i$ -th components of the displacement vector and traction tensor associated to the elastodynamic fundamental solution generated at a

point  $\mathbf{y} \in \mathbb{R}^3$  by a unit point force applied at  $\mathbf{x} \in \mathbb{R}^3$  along the direction  $k$ . Noting  $x_\alpha = k_\alpha r$  ( $\alpha = S, P$ ) (with  $k_\alpha$  real wavenumber) and  $\gamma = c_S/c_P$ , the coefficients in (2.3) are equal to:

$$\begin{aligned} A &= \left(1 + \frac{i}{x_S} - \frac{1}{x_S^2}\right) e^{ix_S} - \gamma^2 \left(\frac{i}{x_P} - \frac{1}{x_P^2}\right) e^{ix_P}, \\ B &= \left(\frac{3}{x_S^2} - \frac{3i}{x_S} - 1\right) e^{ix_S} - \gamma^2 \left(\frac{3}{x_P^2} - \frac{3i}{x_P} - 1\right) e^{ix_P}, \\ C &= \left(-\frac{15}{x_S^2} + \frac{15i}{x_S^2} - ix_S + 6\right) e^{ix_S} - \gamma^2 \left(-\frac{15}{x_P^2} + \frac{15i}{x_P^2} - ix_P + 6\right), \\ D &= (ix_S - 1)e^{ix_S} + 2B, \quad E = (1 - 2\gamma^2)(ix_P - 1)e^{ix_P} + 2B. \end{aligned}$$

The Helmholtz fundamental solutions are symmetric, i.e.  $\mathbf{U}(\mathbf{x}, \mathbf{y}) = \mathbf{U}(\mathbf{y}, \mathbf{x})$  and  $\Sigma(\mathbf{x}, \mathbf{y}) = \Sigma(\mathbf{y}, \mathbf{x})$ , and are singular at  $\mathbf{x} = \mathbf{y}$ :

$$\mathbf{U}(\mathbf{x}, \mathbf{y}; \omega) = \mathcal{O}(r^{-1}), \quad \Sigma(\mathbf{x}, \mathbf{y}; \omega) = \mathcal{O}(r^{-2}).$$

Between the time and the frequency domain fundamental solutions (respectively the Stokes and the Helmholtz fundamental solution), there exists a duality which can be expressed in the time domain by choosing the appropriate function of time as follows (the problem in the frequency domain can be seen as a time domain problem with the particular choice:  $f(t) = e^{-i\omega t}$ ):

$$\mathbf{U}(\mathbf{x}, \mathbf{y}; \omega) = \mathbf{U}[\mathbf{x}, t, \mathbf{y} \mid f(t)] = \mathbf{U}[\mathbf{x}, t, \mathbf{y} \mid e^{-i\omega t}].$$

In 2001, Yoshida proposed a reformulation of the fundamental solutions (2.3) in terms of derivatives of the scalar kernel  $G(r, k) = e^{ikr}/4\pi r$ , which is the free-space Green's function for the Helmholtz equation [325]. These read:

$$\begin{aligned} U_i^k(\mathbf{x}, \mathbf{y}; \omega) &= \frac{1}{k_S^2 \mu} \left[ (\delta_{qs} \delta_{ik} - \delta_{qk} \delta_{is}) \frac{\partial}{\partial x_q} \frac{\partial}{\partial y_s} G(\|\mathbf{y} - \mathbf{x}\|; k_S) + \frac{\partial}{\partial x_i} \frac{\partial}{\partial y_k} G(\|\mathbf{y} - \mathbf{x}\|; k_P) \right], \\ T_i^k(\mathbf{x}, \mathbf{y}; \omega) &= \mathcal{C}_{ijkl} \frac{\partial}{\partial y_\ell} U_h^k(\mathbf{x}, \mathbf{y}; \omega) n_j(\mathbf{y}), \end{aligned} \quad (2.4)$$

$\mathcal{C}_{ijkl}$  being the components of the fourth-order elasticity tensor and  $n_j(\mathbf{y})$  the outward unit normal. As the fast-multipole method relies upon a multipole expansion of the Green's function, the reformulation (2.4) is better suited to the application of the fast-multipole method to the boundary integral formulation than relations (2.3) and has indeed been used in [62] to extent the FMM to the BEM for frequency domain elastodynamics.

For wave propagation in semi-infinite media (e.g. ground motion or vibration problems), the use of the *half-space Green's function* would avoid the discretization of the free-surface, thus strongly enhancing the computational performances of the FM-BEM. However, as the half-space fundamental solutions are not derivatives of the Helmholtz fundamental solution nor of  $1/r$  their multipole expansion is difficult to define. Moreover, the half-space Green's function expansion can not be simply derived from the full-space one. Some works address the multipole



expansion of the half-space Green's function in the field of electromagnetism [132, 208, 271]. In elastodynamics, Chaillat has recently proposed a formulation for the half-space fundamental solutions in the form of a Fourier 2-D integral whose density is the product of a function of  $\mathbf{x}$  and a function of  $\mathbf{y}$ , [61]. However, there are no published results yet that use the half-space Green's function for fast-multipole accelerated boundary-element method.

**Integral representation.** The integral representation formula stems from the introduction in the reciprocity identity (2.1) of the Helmholtz fundamental solution (2.4) defined over the auxiliary domain  $\Omega'$  and the unknown field  $(u_i(\mathbf{y}), t_i(\mathbf{y}))$  defined over a domain  $\Omega \subseteq \Omega'$ . For any point  $\mathbf{x} \in \Omega$  but  $\mathbf{x} \notin \partial\Omega$ , the *integral representation formula* (IR) for the displacement field has the form:

$$\alpha u_k(\mathbf{x}) = \int_{\partial\Omega} [t_i(\mathbf{y})U_i^k(\mathbf{x}, \mathbf{y}; \omega) - u_i(\mathbf{y})T_i^k(\mathbf{x}, \mathbf{y}; \omega)]dS_y + \int_{\Omega} \rho F_i(\mathbf{y})U_i^k(\mathbf{x}, \mathbf{y}; \omega)dV_y \quad (2.5)$$

where  $\alpha u_k(\mathbf{x}) = \int_{\Omega} \delta(\mathbf{y} - \mathbf{x})u_k(\mathbf{y})dV_y$ , and  $\alpha = 1$  ( $\mathbf{x} \in \Omega$ ) or  $\alpha = 0$  ( $\mathbf{x} \notin \Omega$ ). Eq. (2.5) directly relates the displacement field in  $\Omega$  to the displacements and tractions on its boundary  $\partial\Omega$ . In a well-posed boundary-value problem, the value of either  $\mathbf{u}$  or  $\mathbf{t}$  is prescribed at any given point  $\mathbf{x} \in \partial\Omega$ , the remaining one being unknown. Assuming Neumann boundary conditions  $\mathbf{t}^D$  over the portion of boundary  $\partial_t\Omega$  for definiteness, in absence of body forces, eq. (2.5) becomes:

$$u_k(\mathbf{x}) = \int_{\partial\Omega} [t_i^D(\mathbf{y})U_i^k(\mathbf{x}, \mathbf{y}; \omega) - u_i(\mathbf{y})T_i^k(\mathbf{x}, \mathbf{y}; \omega)]dS_y, \quad (\mathbf{x} \in \Omega). \quad (2.6)$$

Notice that once the solutions on the boundary are known, the solution at any desired interior point of the domain can be recovered using eq. (2.6).

**Boundary integral equation.** The integral representation formula does not hold for  $\mathbf{x} \in \partial\Omega$ . When  $\mathbf{y} = \mathbf{x}$ , a strong singularity of the normal derivative of the fundamental solution occurs and the integral over  $\partial\Omega$  is not convergent. The limiting case  $\mathbf{x} \in \partial\Omega$  in the integral representation (2.6) yields the *singular boundary integral equation* (BIE) [44, 50, 146]:

$$c_{ik}(\mathbf{x})u_i(\mathbf{x}) = \int_{\partial\Omega} t_i(\mathbf{y})U_i^k(\mathbf{x}, \mathbf{y}; \omega)dS_y - (\text{P.V.}) \int_{\partial\Omega} u_i(\mathbf{y})T_i^k(\mathbf{x}, \mathbf{y}; \omega)dS_y \quad (\mathbf{x} \in \partial\Omega). \quad (2.7)$$

After introduction of the boundary conditions  $\mathbf{t}^D$  over  $\partial_t\Omega$ , it can be rewritten:

$$(\mathcal{K}u)(\mathbf{x}) = f(\mathbf{x}) \quad (\mathbf{x} \in \partial\Omega), \quad (2.8)$$

with the linear operator  $\mathcal{K}$  and the right-hand side  $f$  given by:

$$\begin{aligned} (\mathcal{K}u)(\mathbf{x}) &= c_{ik}(\mathbf{x})u_i(\mathbf{x}) + (\text{P.V.}) \int_{\partial\Omega} u_i(\mathbf{y})T_i^k(\mathbf{x}, \mathbf{y}; \omega)dS_y \\ f(\mathbf{x}) &= \int_{\partial\Omega} t_i^D(\mathbf{y})U_i^k(\mathbf{x}, \mathbf{y}; \omega)dS_y \quad (\mathbf{x} \in \partial\Omega), \end{aligned}$$

where (P.V.) indicates a Cauchy principal value (CPV) singular integral. The free-term  $c_{ik}(\mathbf{x})$  depends on the local boundary geometry and it is equal to  $\delta_{ik}/2$  at any smooth boundary point  $\mathbf{x} \in \partial\Omega$ . Regularized forms of the boundary integral free of the CPV equations can be found in [53, 80].

**Boundary element method** The boundary element method (BEM) is based on the numerical solution of the boundary integral equation (2.8) for those unknowns which are not specified by the boundary data (i.e. the boundary conditions). Once solved, both the displacement and traction fields are known, and the integral representation can be invoked for the evaluation of the solution at interior points. The numerical solution of BIE (2.8) is based on a discretization of the surface  $\partial\Omega$  into  $N_E$  non-intersecting boundary elements with  $N_{nE}$  nodes. If the boundary elements use the same set of shape functions to represent both the element geometry and displacement interpolations, they are termed *isoparametric elements*. Although low order isoparametric elements are poor, they are largely employed because they allow to easily map complex shapes and curved boundaries. In the present work, we use isoparametric boundary elements with piecewise-linear interpolation of displacements and constant interpolation of tractions. The *collocation method* is then employed, i.e. the solution is sought by enforcing the BIE at a finite number of collocation nodes (if the displacement is unknown at that node) or elements (if the traction is unknown at that element). Thus, the  $N_I$  displacement interpolation nodes ( $N_I \leq N_{nE}$ ) also serve as collocation points. A square complex-valued matrix equation of size  $N = 3N_I$  of the form:

$$\mathbb{K}\mathbb{U} = \mathbb{F}, \quad (2.9)$$

is obtained, where (i)  $\mathbb{U} \in \mathbb{C}^N$  collects the unknown nodal displacement components and (ii)  $\mathbb{K} \in \mathbb{C}^{N \times N}$  (influence matrix) and  $\mathbb{F} \in \mathbb{C}^N$  are discrete versions of  $\mathcal{K}$  and  $f$  in (2.8), respectively. Setting up  $\mathbb{K}$  classically entails computing all element integrals for each collocation point, at a  $\mathcal{O}(N^2)$  computational cost.  $\mathbb{K}$  is invertible, but fully-populated and non-symmetric, and its storage on ordinary computers is limited to models with  $N = \mathcal{O}(10^4)$ . Solving the linear system (2.8) by means of direct solvers (e.g. Gauss elimination, LU factorization) entails a cost of CPU =  $\mathcal{O}(10^3)$ , which becomes quickly impractical for models involving high values of  $N$  (e.g. large domains, high frequency problems). Usually, iterative solvers such as the GMRES are used, which requires a computing time of order  $\mathcal{O}(10^2)$ . However, to apply the BEM to problems involving up to  $N = \mathcal{O}(10^6)$  fast procedures are needed 1.4.2. In this work, we used the fast multipole method (FMM) to accelerate the boundary element method. More details concerning the implementation of the boundary element method can be found in [61].

### 2.2.2 Fast Multipole-Boundary Element Method

The Fast Multipole algorithm was introduced in 1985 by Vladimir Rokhlin [260] for the 2D Laplace equation in integral form, then in 1987 by Leslie Greengard [142] for multi particles simulations. The capabilities of the fast-multipole algorithm applied to the boundary element

method, i.e. the Fast Multipole-Boundary Element Method (FMBEM) and its recursive variant the Multi Level-FMBEM (ML-FMBEM) have rapidly progressed during the last two decades, allowing many engineering applications requiring large BEM models, in connection with e.g. acoustics [23], elastodynamics [63], Stokes flows [119] or electromagnetism [68]. FMBEMs for real values of the wavenumber  $k$ , which correspond to wave propagation problems in undamped media, have been extensively studied and implemented, see e.g. [81, 147, 236], while the collocation FMBEM for 3D-frequency domain elastodynamics in homogeneous or piecewise-homogeneous elastic media is addressed in [62, 63]. Importantly, these algorithms are backed by error analysis results for the multipole expansion of the fundamental solutions, which also provide guidelines about suitable settings of e.g. truncation parameters. In contrast, only scattered efforts have so far been devoted to FMMs for Helmholtz-type problems involving *complex wavenumbers* of the form  $k^* = k(1 + i\beta)$ , with  $\beta > 0$  quantifying material damping.

The present work is based on the FM-BEM formulation proposed in [62] for frequency domain elastodynamics. In particular, the fast multipole method uses a *diagonal form* of the Helmholtz Green's function [82, 251, 261], which is known to be well suited for mid-frequency regimes. In fact, this formulation breaks down at very low frequencies, where it has to be replaced by a low frequency formulation such as the classical multipole expansion of [83]. Hereafter, the multi-level FM-BEM formulation is recalled. For the sake of continuity and clarity, the same notations of Chaillat [61] will be used throughout this thesis.

**Diagonal multipole decomposition of the elastodynamic fundamental solutions** The main features of the fast multipole BEM (FMBEM) formulation considered herein are those previously developed in [62] for the elastodynamic (i.e. non-dissipative) case, based on the decomposition of the Helmholtz Green's function  $G(r; k)$  in diagonal form. The decomposition of  $G(r; k)$  rests upon choosing two poles  $\mathbf{x}_0, \mathbf{y}_0$  respectively close to  $\mathbf{x}, \mathbf{y}$ , recasting the position vector  $\mathbf{r} = \mathbf{y} - \mathbf{x}$  as  $\mathbf{r} = (\mathbf{y} - \mathbf{y}_0) + \mathbf{r}_0 + (\mathbf{x}_0 - \mathbf{x}) = \mathbf{r}_0 + \mathbf{r}'$  (Fig. 2.1) and invoking the Gegenbauer addition theorem (see [3, 81]) and reads:

$$G(r; k) = \lim_{L \rightarrow +\infty} G_L(r; k), \quad G_L(r; k) := \int_{\hat{\mathbf{s}} \in \mathcal{S}} e^{ik\hat{\mathbf{s}} \cdot (\mathbf{y} - \mathbf{y}_0)} \mathcal{G}_L(\hat{\mathbf{s}}; \mathbf{r}_0; k) e^{-ik\hat{\mathbf{s}} \cdot (\mathbf{x} - \mathbf{x}_0)} d\hat{\mathbf{s}} \quad (2.10)$$

where  $\mathcal{S} = \{\hat{\mathbf{s}} \in \mathbb{R}^3, \|\hat{\mathbf{s}}\| = 1\}$  is the unit sphere and the transfer function  $\mathcal{G}_L(\hat{\mathbf{s}}; \mathbf{r}_0; k)$  is given by

$$\mathcal{G}_L(\hat{\mathbf{s}}; \mathbf{r}_0; k) = \frac{ik}{16\pi^2} \sum_{\ell=1}^L (2\ell + 1) i^\ell h_\ell^{(1)}(kr_0) P_\ell(\hat{\mathbf{s}} \cdot \hat{\mathbf{r}}_0) \quad (2.11)$$

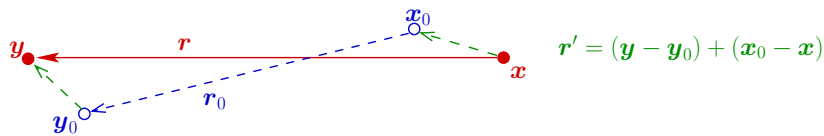


**Figure 2.1:** Plane wave expansion of the Helmholtz Green's function: decomposition of the position vector.

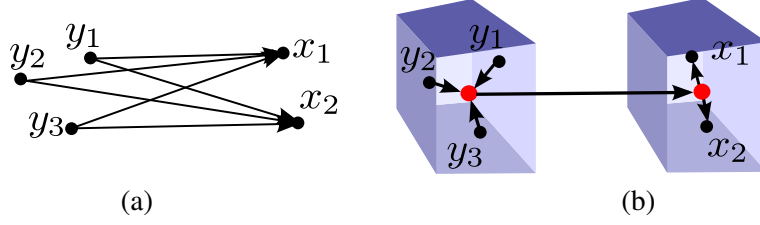


**Figure 2.2:** Schematic of the main idea beyond the application of the FMM to the BEM. (a) Standard BEM is non-local (unlike the finite element method) and requires the evaluation at each collocation point  $\mathbf{x}$  of the contributions (i.e. the fundamental solutions, which are everywhere non-zero) coming from all source points  $\mathbf{y}$ . For a problem of size  $N$ , this procedure needs  $\mathcal{O}(N^2)$  operations. (b) The FMM is based on a decomposition of the fundamental solutions in two local multipole expansions and a transfer function. This fast procedure needs only  $\mathcal{O}(N)$  operations.

in terms of the spherical Hankel functions of first kind  $h_\ell^{(1)}(kr_0)$  and Legendre polynomials  $P_\ell(\hat{\mathbf{s}} \cdot \hat{\mathbf{r}}_0)$ , and with  $\hat{\mathbf{r}}_0 = \mathbf{r}_0/r_0$ . This decomposition entails a reformulation of the fundamental solutions in terms of products of functions of  $\mathbf{x}$  and  $\mathbf{y}$ . This allows to re-use integrations with respect to  $\mathbf{y}$  when the collocation point  $\mathbf{x}$  is changed, and thus to lower the overall complexity (to  $\mathcal{O}(N \log N)$  using the multi-level form of the FMM), as shown in the schematic of Figure 2.2. Equation (2.10) essentially represents  $G$  as a superposition of plane waves [82]. The decomposition of the elastodynamic fundamental solutions follows by substituting eq. (2.10) in eq. (2.4):

$$U_i^k(\mathbf{x}, \mathbf{y}; \omega) = \lim_{L \rightarrow \infty} \int_{\hat{\mathbf{s}} \in S} e^{ik_P \hat{\mathbf{s}} \cdot (\mathbf{y} - \mathbf{y}_0)} \mathcal{U}_{i,L}^{k,P}(\hat{\mathbf{s}}; \mathbf{r}_0) e^{-ik_P \hat{\mathbf{s}} \cdot (\mathbf{x} - \mathbf{x}_0)} d\hat{\mathbf{s}} \\ + \lim_{L \rightarrow \infty} \int_{\hat{\mathbf{s}} \in S} e^{ik_S \hat{\mathbf{s}} \cdot (\mathbf{y} - \mathbf{y}_0)} \mathcal{U}_{i,L}^{k,S}(\hat{\mathbf{s}}; \mathbf{r}_0) e^{-ik_S \hat{\mathbf{s}} \cdot (\mathbf{x} - \mathbf{x}_0)} d\hat{\mathbf{s}}, \quad (2.12a)$$

$$T_i^k(\mathbf{x}, \mathbf{y}; \omega) = \lim_{L \rightarrow \infty} \int_{\hat{\mathbf{s}} \in S} e^{ik_P \hat{\mathbf{s}} \cdot (\mathbf{y} - \mathbf{y}_0)} \mathcal{T}_{i,L}^{k,P}(\hat{\mathbf{s}}; \mathbf{r}_0) e^{-ik_P \hat{\mathbf{s}} \cdot (\mathbf{x} - \mathbf{x}_0)} d\hat{\mathbf{s}} \\ + \lim_{L \rightarrow \infty} \int_{\hat{\mathbf{s}} \in S} e^{ik_S \hat{\mathbf{s}} \cdot (\mathbf{y} - \mathbf{y}_0)} \mathcal{T}_{i,L}^{k,S}(\hat{\mathbf{s}}; \mathbf{r}_0) e^{-ik_S \hat{\mathbf{s}} \cdot (\mathbf{x} - \mathbf{x}_0)} d\hat{\mathbf{s}}. \quad (2.12b)$$

where  $\mathcal{U}$  and  $\mathcal{T}$  are the elastodynamic transfer functions

$$\mathcal{U}_{i,L}^{k,P}(\hat{\mathbf{s}}; \mathbf{r}_0) = \frac{\gamma^2}{\mu} \hat{s}_i \hat{s}_k \mathcal{G}_L(\hat{\mathbf{s}}; \mathbf{r}_0; k_P), \quad (2.13a)$$

$$\mathcal{T}_{i,L}^{k,P}(\hat{\mathbf{s}}; \mathbf{r}_0) = \frac{ik_S \gamma^3}{\mu} \mathcal{C}_{ijhl} \hat{s}_\ell \hat{s}_h \hat{s}_k \mathcal{G}_L(\hat{\mathbf{s}}; \mathbf{r}_0; k_P) n_j(\mathbf{y}), \quad (2.13b)$$

$$\mathcal{U}_{i,L}^{k,S}(\hat{\mathbf{s}}; \mathbf{r}_0) = \frac{1}{\mu} (\delta_{ik} - \hat{s}_k \hat{s}_i) \mathcal{G}_L(\hat{\mathbf{s}}; \mathbf{r}_0; k_S), \quad (2.13c)$$

$$\mathcal{T}_{i,L}^{k,S}(\hat{\mathbf{s}}; \mathbf{r}_0) = \frac{ik_S}{\mu} (\delta_{hk} - \hat{s}_k \hat{s}_h) \mathcal{C}_{ijhl} \hat{s}_\ell \mathcal{G}_L(\hat{\mathbf{s}}; \mathbf{r}_0; k_S) n_j(\mathbf{y}). \quad (2.13d)$$

A key error analysis result for the real-wavenumber case [81] states that, if  $\mathbf{x}_0, \mathbf{y}_0$  are chosen so that

$$r'/r_0 \leq 2/\sqrt{5} \quad (r' := \|\mathbf{r}'\|, r_0 := \|\mathbf{r}_0\|) \quad (2.14)$$

there exist four constants  $C_1, C_2, C_3, C_4$  such that for given  $\epsilon < 1$ , one has  $|G_L(r; k) - G(r; k)| < \epsilon$  if [81]

$$L(r') = C_1 + C_2 kr' + C_3 \ln(kr') + C_4 \ln(\epsilon^{-1}). \quad (2.15)$$

The truncation parameter  $L(r')$  represents the expansion length and will be discussed in detail in section 2.2.4.

**Multi-level fast multipole formulation** The multi-level FM-BEM exploits a recursive subdivision of a cube enclosing the domain  $\Omega$  (level 0) into 8 cubic cells (levels 1, 2,  $\dots$ ), see Fig. 2.3. The subdivision process stops when the linear size of the smallest cells becomes smaller than the threshold

$$d_{\min} = \alpha \lambda_S, \quad (2.16)$$

corresponding to a certain preset fraction  $\alpha$  of the shear wavelength  $\lambda_S$ . The deepest level  $\bar{\ell}$  reached in the subdivision process, termed the *leaf level*, is such that  $d^{(\bar{\ell}+1)} \leq d_{\min} \leq d^{(\bar{\ell})}$ . The presence of a lower threshold  $d_{\min}$  is due to the divergent behavior of  $h_n^{(1)}(z)$  in the small-argument limit, entailing a loss of accuracy when using small cell sizes. The cell size threshold  $\alpha$  has to be estimated through numerical tests. The value  $\alpha = 0.3$  was found to be suitable in the elastodynamic case [62]. In this hierarchical structure,  $\mathbf{x}_0$  and  $\mathbf{y}_0$  in (2.10) are chosen as the centers of the two cubic cells  $\mathcal{C}_x$  (containing collocation points) and  $\mathcal{C}_y$  (containing source points). Cells  $\mathcal{C}_y$  that share at least a corner with  $\mathcal{C}_x$  are termed *adjacent cells*, i.e.  $\mathcal{C}_y \in \mathcal{A}(\mathcal{C}_x)$ . The set of cells  $\mathcal{C}_y$  that lie on the same level as  $\mathcal{C}_x$  and that are not directly adjacent but have a parent cell adjacent to that of  $\mathcal{C}_x$  constitute the *interaction list*, i.e.  $\mathcal{C}_y \in \mathcal{I}(\mathcal{C}_x)$ . These definitions are displayed in a 2D schematic example in Fig. 2.4. For two non-adjacent cells, one always has  $r'/r_0 \leq \sqrt{3}/2$ . Partitioning the space into cubic cells thus ensures verification of condition (2.14), and hence convergence of (2.10) for  $L \rightarrow +\infty$ , whenever the collocation

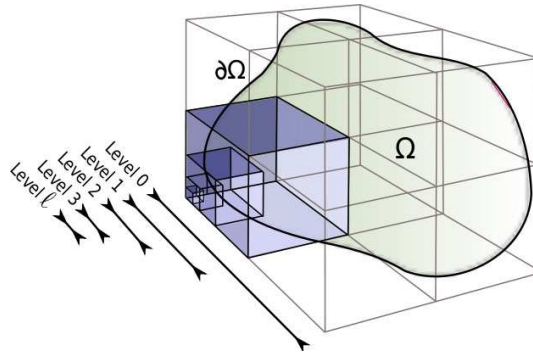


**Figure 2.3:** 3D recursive subdivision of a cube enclosing the domain boundary  $\partial\Omega$  up to the leaf level  $\ell$ .

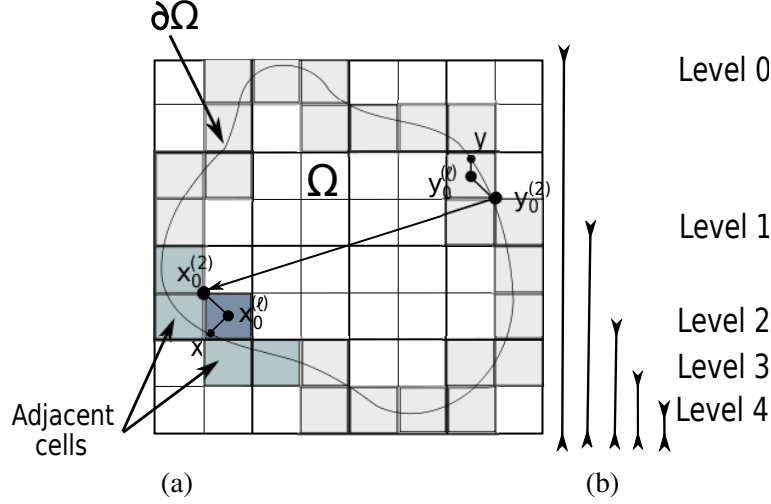


**Figure 2.4:** Simplified 2D sketch of the (a) single-level and (b) multi-level FMBEM. For a given collocation point  $\mathbf{x}$ , far field contributions from points  $\mathbf{y}$  belonging to non-adjacent cells are gathered at  $\mathbf{y}_0^{(\bar{\ell})}$ , accumulated upwards at all parent cell centers up to  $\mathbf{y}_0^{(2)}$ , transferred to same-level non-adjacent cell centers  $\mathbf{x}_0^{(2)}$  belonging to the interaction list of  $\mathbf{y}_0^{(2)}$ , accumulated downwards in all children cells down to  $\mathbf{x}_0^{(\bar{\ell})}$ , and finally locally expanded at  $\mathbf{x}$  about  $\mathbf{x}_0^{(\bar{\ell})}$ . In the single-level FMBEM is  $\ell^{(\bar{\ell})} = (2)$ .

points  $\mathbf{x}$  and the integration points  $\mathbf{y}$  lie in non-adjacent cells. The highest active level is  $\ell = 2$ , as pairs of non-adjacent cells cannot occur at levels 0 or 1. The multi-level FMBEM exploits the representation (2.10) to evaluate the influence of far integration points  $\mathbf{y}$  clustered around  $\mathbf{y}_0$  on the collocation points  $\mathbf{x}$  clustered around  $\mathbf{x}_0$ ,  $\mathbf{y}_0$  and  $\mathbf{x}_0$  being the center of non-adjacent clusters.

The influence matrix  $\mathbb{K}$  of the global BEM system (2.9) is then additively split into two parts:

$$\mathbb{K}\mathbf{U} = \mathbb{K}^{\text{near}}\mathbf{U} + \mathbb{K}^{\text{FMM}}\mathbf{U}, \quad (2.17a)$$

$$\mathbb{F} = \mathbb{F}^{\text{near}} + \mathbb{F}^{\text{FMM}}. \quad (2.17b)$$

The part  $\mathbb{K}^{\text{near}}$  containing the contributions from adjacent cells, which is sparse and to which the expansion (2.10) is not applicable, is set up using usual BEM integration and assembly techniques and stored. The contribution  $\mathbb{K}^{\text{FMM}}$  exploiting the expansion (2.10) is neither set up nor stored. Instead, the contribution  $\mathbb{K}^{\text{FMM}}\mathbf{U}$  to the matrix-vector product  $\mathbb{K}\mathbf{U}$  is computed for each GMRES iteration. Keeping the example of a Neumann problem with imposed traction distribution  $\mathbf{t}^D$ , the decomposition of the system has the form:

$$(\mathcal{K}u)^{\text{near}}(\mathbf{x}) = c_{ik}(\mathbf{x})u_i(\mathbf{x}) + \sum_{\mathcal{C}_y \in \mathcal{A}(\mathcal{C}_x)} (\text{P.V.}) \int_{\partial\Omega \cap \mathcal{C}_y} u_i(\mathbf{y})T_i^k(\mathbf{x}, \mathbf{y}; \omega) dS_y \quad (2.18a)$$

$$f(\mathbf{x})^{\text{near}} = \sum_{\mathcal{C}_y \in \mathcal{A}(\mathcal{C}_x)} \int_{\partial\Omega \cap \mathcal{C}_y} t_i^D(\mathbf{y})U_i^k(\mathbf{x}, \mathbf{y}; \omega) dS_y \quad (2.18b)$$

$$(\mathcal{K}u)^{\text{FMM}}(\mathbf{x}) = \sum_{\mathcal{C}_y \notin \mathcal{A}(\mathcal{C}_x)} \int_{\partial\Omega \cap \mathcal{C}_y} u_i T_i^k(\mathbf{x}, \mathbf{y}; \omega) dS_y, \quad (2.18c)$$

$$f(\mathbf{x})^{\text{FMM}} = \sum_{\mathcal{C}_y \notin \mathcal{A}(\mathcal{C}_x)} \int_{\partial\Omega \cap \mathcal{C}_y} t_i^D(\mathbf{y}) U_i^k(\mathbf{x}, \mathbf{y}; \omega) dS_y \quad (2.18d)$$

Summarizing, the acceleration introduced by the FM algorithm stems from (i) the reduction of the integrations on  $\partial\Omega$  coming from the separation of variables introduced in (2.10), and (ii) the optimal task partitioning allowed by the recursive subdivision. The *single-level fast multipole BEM* is the particular case in which the leaf level coincides with the first active level, i.e.  $\bar{\ell} = \ell^{(2)}$ .

The evaluation of far contributions by multi-level FMM at a general cell  $\mathcal{C}_x^{\bar{\ell}}$  passes through different steps. Starting from the leaf level  $\bar{\ell}$  to the maximum level  $\ell^{(2)}$  the so called *upward pass* consists in recursively computing the multipole moments for all cells  $\mathcal{C}_y$  at each level  $\ell^{(2)} \leq \ell^{(\ell)} \leq \ell^{(\bar{\ell})}$ , transfer their contribution close to  $\mathcal{C}_x$ , then extrapolate them to the upward level. Once reached the upper level  $\ell^{(2)}$ , the *downward pass* consists in descending the octree in the opposite sense (by means of inverse extrapolations) and aggregating the local expansion contributions at each level until the leaf level is reached, where final integration is performed. In formulae, the aforementioned steps read as follows [62].

1. *Initialization of the multipole moments.* The multipole moments, or radiation functions, are computed for each lowest cell  $\mathcal{C}_y = \mathcal{C}_y^{(\ell)}$  (with  $\ell = \bar{\ell}, \bar{\ell} - 1, \dots, 2$ ):

$$\mathcal{R}_k^{S,u}(\hat{\mathbf{s}}; \mathcal{C}_y) = -ik_S [\delta_{ik} \hat{s}_j + \delta_{jk} \hat{s}_i - 2\hat{s}_i \hat{s}_j \hat{s}_k] \int_{\partial\Omega \cap \mathcal{C}_y} u_i(\mathbf{y}) n_j(\mathbf{y}) e^{ik_S \hat{\mathbf{s}} \cdot (\mathbf{y} - \mathbf{y}_0)} dS_y, \quad (2.19a)$$

$$\mathcal{R}^{P,u}(\hat{\mathbf{s}}; \mathcal{C}_y) = -ik_S \gamma^3 \left[ \frac{2\nu}{1-2\nu} \delta_{ij} + 2\hat{s}_i \hat{s}_j \right] \int_{\partial\Omega \cap \mathcal{C}_y} u_i(\mathbf{y}) n_j(\mathbf{y}) e^{ik_P \hat{\mathbf{s}} \cdot (\mathbf{y} - \mathbf{y}_0)} dS_y, \quad (2.19b)$$

$$\mathcal{R}_k^{S,t}(\hat{\mathbf{s}}; \mathcal{C}_y) = \frac{1}{\mu} [\delta_{ka} - \hat{s}_k \hat{s}_a] \int_{\partial\Omega \cap \mathcal{C}_y} t_a(\mathbf{y}) e^{ik_S \hat{\mathbf{s}} \cdot (\mathbf{y} - \mathbf{y}_0)} dS_y, \quad (2.19c)$$

$$\mathcal{R}^{P,t}(\hat{\mathbf{s}}; \mathcal{C}_y) = \frac{\gamma^2}{\mu} \int_{\partial\Omega \cap \mathcal{C}_y} \hat{s}_a t_a(\mathbf{y}) e^{ik_P \hat{\mathbf{s}} \cdot (\mathbf{y} - \mathbf{y}_0)} dS_y. \quad (2.19d)$$

2. *Initialization of the transfer.* Local expansions are computed at each level for each collocation cell  $\mathcal{C}_x^{(\ell)}$ :

$$\mathcal{L}_k^{S,u}(\hat{\mathbf{s}}^{(\ell)}; \mathcal{C}_x^{(\ell)}) = \sum_{\mathcal{C}_y^{(\ell)} \in \mathcal{I}(\mathcal{C}_x^{(\ell)})} \mathcal{G}_L(\hat{\mathbf{s}}^{(\ell)}; \mathbf{r}_0; k_S) \mathcal{R}_k^{S,u}(\hat{\mathbf{s}}^{(\ell)}; \mathcal{C}_y^{(\ell)}), \quad (2.20a)$$

$$\mathcal{L}^{P,u}(\hat{\mathbf{s}}^{(\ell)}; \mathcal{C}_x^{(\ell)}) = \sum_{\mathcal{C}_y^{(\ell)} \in \mathcal{I}(\mathcal{C}_x^{(\ell)})} \mathcal{G}_L(\hat{\mathbf{s}}^{(\ell)}; \mathbf{r}_0; k_P) \mathcal{R}^{P,u}(\hat{\mathbf{s}}^{(\ell)}; \mathcal{C}_y^{(\ell)}). \quad (2.20b)$$

3. *Upward extrapolation.* The radiation functions are extrapolated to the upper level  $\ell^{(\ell-1)}$ :

$$\mathcal{R}_k^{S,u}(\hat{\mathbf{s}}; \mathcal{C}_y^{(\ell-1)}) = \sum_{\mathcal{C}_y^{(\ell)} \in \mathcal{S}(\mathcal{C}_y^{(\ell-1)})} \exp \left[ -ik_S \hat{\mathbf{s}} \cdot (\mathbf{y}_0^{(\ell)} - \mathbf{y}_0^{(\ell-1)}) \right] \mathcal{R}_k^{S,u}(\hat{\mathbf{s}}; \mathcal{C}_y^{(\ell)}), \quad (2.21a)$$

$$\mathcal{R}_k^{P,u}(\hat{\mathbf{s}}; \mathcal{C}_y^{(\ell-1)}) = \sum_{\mathcal{C}_y^{(\ell)} \in \mathcal{S}(\mathcal{C}_y^{(\ell-1)})} \exp \left[ -ik_P \hat{\mathbf{s}} \cdot (\mathbf{y}_0^{(\ell)} - \mathbf{y}_0^{(\ell-1)}) \right] \mathcal{R}_k^{P,u}(\hat{\mathbf{s}}; \mathcal{C}_y^{(\ell)}), \quad (2.21b)$$

where  $\hat{\mathbf{s}}$  indicates that the radiation functions are defined over the unit sphere of integration which is discretized differently at each level (because the quadrature rule depends on the truncation parameter  $L$ ) and  $\mathcal{S}(\mathcal{C})$  generally represents the set of children of a given cell  $\mathcal{C}$ .

4. *Downward inverse extrapolation.* At each level from  $\ell^{(3)}$  to  $\ell^{(\bar{\ell})}$ , the downward step consists in updating the local expansion at each level with contributions coming from the superior levels:

$$\mathcal{L}_k^{S,u}(\hat{\mathbf{s}}; \mathcal{C}_x^{(\ell)}) = \mathcal{L}_k^{S,u}(\hat{\mathbf{s}}; \mathcal{C}_x^{(\ell-1)}) + \exp \left[ -ik_S \hat{\mathbf{s}} \cdot (\mathbf{y}_0^{(\ell)} - \mathbf{y}_0^{(\ell-1)}) \right] \mathcal{L}_k^{S,u}(\hat{\mathbf{s}}; \mathcal{C}_x^{(\ell-1)}), \quad (2.22a)$$

$$\mathcal{L}_k^{P,u}(\hat{\mathbf{s}}; \mathcal{C}_x^{(\ell)}) = \mathcal{L}_k^{P,u}(\hat{\mathbf{s}}; \mathcal{C}_x^{(\ell-1)}) + \exp \left[ -ik_P \hat{\mathbf{s}} \cdot (\mathbf{y}_0^{(\ell)} - \mathbf{y}_0^{(\ell-1)}) \right] \mathcal{L}_k^{P,u}(\hat{\mathbf{s}}; \mathcal{C}_x^{(\ell-1)}). \quad (2.22b)$$

5. *Integration at the leaf level.* The final integration over the unit sphere use a quadrature method with quadrature points  $\hat{\mathbf{s}}_q$  and weights  $w_q$  and reads:

$$(\mathcal{K}u)_k^{\text{FMM}}(\mathbf{x}) \approx \sum_{q=1}^Q w_q \left[ e^{-ik_S \hat{\mathbf{s}}_q \cdot (\mathbf{x} - \mathbf{x}_0)} \mathcal{L}_k^{S,u}(\hat{\mathbf{s}}_q; \mathcal{C}_x) + e^{-ik_P \hat{\mathbf{s}}_q \cdot (\mathbf{x} - \mathbf{x}_0)} \mathcal{L}_k^{P,u}(\hat{\mathbf{s}}_q; \mathcal{C}_x) \right] \quad (2.23a)$$

$$f(\mathbf{x})_k^{\text{FMM}}(\mathbf{x}) \approx \sum_{q=1}^Q w_q \left[ e^{-ik_S \hat{\mathbf{s}}_q \cdot (\mathbf{x} - \mathbf{x}_0)} \mathcal{L}_k^{S,t}(\hat{\mathbf{s}}_q; \mathcal{C}_x) + e^{-ik_P \hat{\mathbf{s}}_q \cdot (\mathbf{x} - \mathbf{x}_0)} \mathcal{L}_k^{P,t}(\hat{\mathbf{s}}_q; \mathcal{C}_x) \right]. \quad (2.23b)$$

### 2.2.3 Multi-region FMBEM formulation for seismic wave propagation

Wave propagation analyses often involve heterogeneous media (e.g. seismic waves in geological structures). Following the single-domain elastodynamic ML-FMBEM formulation [62], a multi-region version of the elastodynamic ML-FMBEM was proposed in [63], allowing to study e.g. the amplification by topographical irregularities of seismic waves propagating in homogeneous media. Hereafter, we recall only the main steps of this ML-FM-based BE-BE coupling strategy. For a detailed explanation, we refer the reader to its exhaustive presentation addressed in [61, 63].

**Continuous BEM formulation for a mono-region seismic diffraction problem.** As often in seismic numerical modelling, the total displacement field  $\mathbf{u}$  is decomposed into the free-field motion



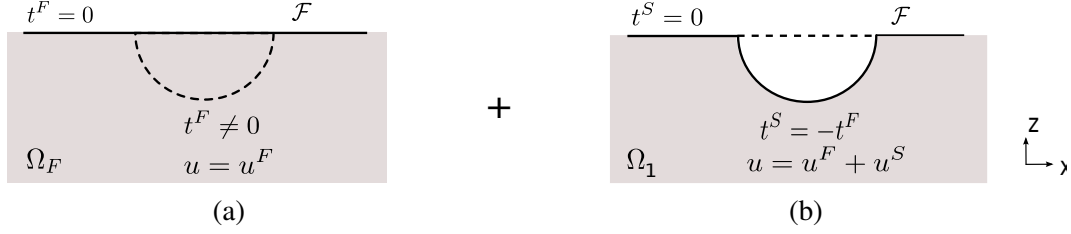


**Figure 2.5:** Decomposition of the traction field in case of incident wave. In the presence of topographical irregularities from the planar traction-free surface  $\mathcal{F}$ , e.g. a canyon,  $\mathbf{t}_F + \mathbf{t}_S = 0$  (where  $\mathbf{t}_F$  are the free-field tractions and  $\mathbf{t}_S$  is the scattered component of the incident wavefield) (from [63]).

$\mathbf{u}_F$  (i.e. the total motion induced by an incident wave travelling in the half-space  $\Omega_F$  superiorly limited by the planar free-surface  $\mathcal{F}$ , as in Fig.2.5a) and its scattered component  $\mathbf{u}_S$  that arises in presence of eventual topographical irregularities (see Fig.2.5b) such that  $\mathbf{u} = \mathbf{u}_F + \mathbf{u}_S$ .

Let first consider a homogeneous isotropic linear elastic domain  $\Omega_1$  of boundary  $\partial\Omega_1$  characterized by the presence of irregularities (e.g. canyons, hills) submitted to the incidence of a seismic wave, as in Fig. 2.6 where  $\Gamma = \partial\Omega_1 \cap \mathcal{F}$ ,  $\Gamma_1$  includes all topographical irregularities and  $\partial\Omega_1 = \Gamma \cup \Gamma_1$ . In this case, the Neumann boundary data on  $\partial\Omega_1$  are the known traction free-field  $\mathbf{t}_S = -\mathbf{t}^F$ , and the BIE can be solved for  $\mathbf{u}_S$  by applying the classical boundary integral equation (2.7). Alternately, the integral equation (2.7) can be reformulated in terms of the total field  $\mathbf{u}$  and of the free-field  $\mathbf{u}^F$  as:

$$c_{ik}(\mathbf{x})u_i(\mathbf{x}) + \int_{\Gamma_1 \cup \Gamma} u_i(\mathbf{y})T_i^k(\mathbf{x}, \mathbf{y}; \omega) dS_y - \int_{\Gamma_1} t_i(\mathbf{y})U_i^k(\mathbf{x}, \mathbf{y}; \omega) dS_y = c_{ik}^F(\mathbf{x})u_i^F(\mathbf{x}) + \int_{\mathcal{F}} u_i^F(\mathbf{y})T_i^k(\mathbf{x}, \mathbf{y}; \omega) dS_y, \quad (\forall \mathbf{x} \in \partial\Omega_1). \quad (2.24)$$

**Extension to multi-region problems.** We now apply the continuous BIE formulation (2.24) to the propagation of a seismic wave in a multi-region domain where the various subregions are

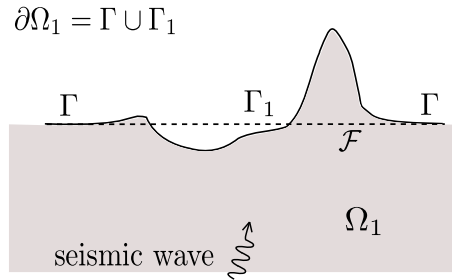


**Figure 2.6:** Seismic mono-domain scattering problem. The planar free surface  $\mathcal{F}$  is used to define the free-field. The boundary of the domain  $\Omega_1$  is  $\partial\Omega_1 = \Gamma \cup \Gamma_1$ , where  $\Gamma = \partial\Omega_1 \cap \mathcal{F}$  and  $\Gamma_1$  includes all topographical irregularities.

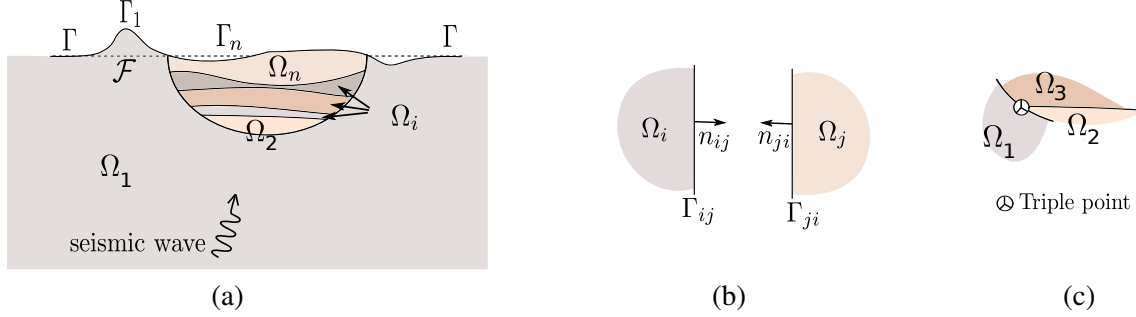


**Figure 2.7:** Seismic wave propagation problem in a multi-region domain:  $n$ -layered basin embedded in the homogeneous half-space  $\Omega_1$ . (a) Notation of the different domains and of the free-surface  $\Gamma \cup \Gamma_1 \cup \Gamma_n$ , (b) notations adopted for the definition of the interfaces and their (outwarding) normal and (c) definition of triple points arising at the intersection of three subregions.

characterized by different mechanical properties. For this class of problems, the continuous formulation in terms of the total field is convenient because transmission conditions are defined in terms of total field as well. Let the original domain  $\Omega$  be partitioned into  $n$  piecewise-homogeneous bounded subdomains  $\Omega_i$  ( $2 \leq i \leq n$ ), embedded in a complementary semi-infinite domain  $\Omega_1$ , such that  $\Omega = \Omega_1 \cup \Omega_2 \cup \dots \cup \Omega_n$ . The problem is depicted in Fig. 2.7a. Perfect bond is assumed between different subdomains, i.e.  $\Omega_k \cap \Omega_\ell = \emptyset$  (for  $1 \leq k, \ell \leq n$ ,  $k \neq \ell$ ). The notations adopted at the common interfaces are recalled in Fig. 2.7b, with the normals outwarding each region. The points in common between three subdomains are the *triple points* (Fig. 2.7c). The global free-surface is given by  $\Omega_n \cup \Gamma \cup \Gamma_1$ , where  $\Gamma$  and  $\Gamma_1$  respect the definition given in the previous paragraph for a mono-domain scattering. Hereafter, we use abbreviations  $U_i^k, T_i^k$  instead of  $U_i^k(\mathbf{x}, \mathbf{y}; \omega), T_i^k(\mathbf{x}, \mathbf{y}; \omega)$ . Moreover, the superscript  $\alpha$  in  $U_i^{k(\alpha)}, T_i^{k(\alpha)}$  will refer to the elastodynamic fundamental solutions defined in terms of the material parameters of the subdomain  $\Omega_\alpha$ . In the subdomain  $\Omega_1$ , the boundary integral equations corresponding to the collocation over the boundary  $\partial\Omega_1 = \Gamma \cup \Gamma_1 \cup \Gamma_{1m}$  (where  $2 \leq m \leq n$  refers to the subdomains that share a portion of boundary with  $\Omega_1$ , i.e. that are adjacent) reads:

$$\begin{aligned}
 c_{ik}(\mathbf{x})u_i^\alpha(\mathbf{x}) + \int_{\Gamma_1 \cup \Gamma} u_i^{1m}(\mathbf{y})T_i^{k(1)}dS_y + \sum_{m=2}^n \int_{\Gamma_{1m}} u_i^{1m}(\mathbf{y})T_i^{k(1)}dS_y - \int_{\Gamma_1} t_i^1(\mathbf{y})U_i^k(\mathbf{x}, \mathbf{y}; \omega)dS_y \\
 - \sum_{m=2}^n \int_{\Gamma_{1m}} t_i^{1m}(\mathbf{y})U_i^{k(1)}dS_y = c_{ik}^F(\mathbf{x})u_i^F(\mathbf{x}) + \int_{\mathcal{F}} u_i^F(\mathbf{y})T_i^k dS_y, \quad (\forall \mathbf{x} \in \partial\Omega_1),
 \end{aligned} \tag{2.25}$$

where  $\mathbf{x}$  is by convention the collocation point and  $\mathbf{y}$  is the source point. In the free-term  $c_{ik}(\mathbf{x})u_i^\alpha(\mathbf{x})$ ,  $\alpha = 1$  if the collocation point  $\mathbf{x}$  lies on the "irregular" surface  $\Gamma_1$  and  $\alpha = 1m$  if  $\mathbf{x}$  lies on a shared internal interface  $\Gamma_{1m}$ . The right-hand side term is defined over the planar free-surface  $\mathcal{F}$ , that does not necessarily coincides with the global domain boundary. In each

bounded subdomain  $\Omega_\ell$  ( $2 \leq \ell \leq n$ ) one has:

$$c_{ik}(\mathbf{x})u_i^\alpha(\mathbf{x}) + \int_{\Gamma_\ell} u_i^\ell(\mathbf{y})T_i^{k(\ell)} dS_y + \sum_{\substack{m \geq 1 \\ m \neq \ell}} \int_{\Gamma_{\ell m}} \left( u_i^{\ell m}(\mathbf{y})T_i^{k(\ell)} - t_i^{\ell m}(\mathbf{y})U_i^{k(\ell)} \right) dS_y, \quad (\forall \mathbf{x} \in \partial\Omega_\ell). \quad (2.26)$$

In the free-term, again  $\alpha$  varies with collocation, i.e.  $\alpha = \ell, \ell m$  depending on if  $\mathbf{x}$  lies on  $\Gamma_\ell$  or on  $\Gamma_{\ell m}$ . In the second term, the free-surface condition  $t_i^\ell(\mathbf{y})$  on the eventual  $\Gamma_\ell$  has been already taken into account. After invoking strong continuity  $\mathbf{u}^{\ell m} = \mathbf{u}^{m\ell}$  and equilibrium  $\mathbf{t}^{\ell m} + \mathbf{t}^{m\ell} = 0$  conditions, equation (2.26) can be rewritten in terms of interface unknowns  $\mathbf{u}^{\ell m}$  and  $\mathbf{t}^{\ell m}$  ( $\ell < m$ ) [63]:

$$c_{ik}(\mathbf{x})u_i^\alpha(\mathbf{x}) + \int_{\Gamma_\ell} u_i^\ell(\mathbf{y})T_i^{k(\ell)} dS_y + \sum_{m=2}^{\ell-1} \int_{\Gamma_{\ell m}} \left( u_i^{m\ell}(\mathbf{y})T_i^{k(\ell)} + t_i^{m\ell}(\mathbf{y}) \right) U_i^{k(\ell)} dS_y + \sum_{m=\ell+1}^n \int_{\Gamma_{\ell m}} \left( u_i^{\ell m}(\mathbf{y})T_i^{k(\ell)} - t_i^{\ell m}(\mathbf{y}) \right) U_i^{k(\ell)} dS_y = 0 \quad (\forall \mathbf{x} \in \partial\Omega_\ell). \quad (2.27)$$

**Fast-multipole BE-BE coupling strategy.** The BE-BE coupling strategy proposed in [63] for seismic scattering problems uses the continuous formulation of BIEs in terms of total field as proposed in the previous paragraphs. For each subdomain, a separate octree structure is defined, a boundary integral equation is formulated (eq. (2.26) for the semi-infinite  $\Omega_1$  and (2.27) for the bounded subdomains  $\Omega_i$ ,  $2 \leq i \leq n$ ) and the corresponding contributions to the global matrix-vector product are computed. To ensure a global square system of equations, linear combinations of the BE equations arising from collocation at nodes or interface element shared by more than one subregion are defined, and the global matrix-vector product is evaluated by combining accordingly the contributions coming from the various interfaces relative to each subregion.

#### 2.2.4 Computational aspects

**Truncation of the transfer function.** The multipole expansion (2.10) is convergent in the limit  $L \rightarrow +\infty$  allowing the convergence of the viscoelastodynamic kernels. However, for computational reasons, it is evaluated for a finite value of the truncation parameter  $L$ , and the FMBEM uses the truncated approximation  $G_L(r; k)$  of  $G(r; k)$ . Choosing a suitable truncation level  $L$  is delicate, as  $L$  has to be large enough to guarantee sufficient accuracy in the expansion (2.10), while not exceeding values significantly larger than  $kr$  so as to avoid blow-up of the Hankel functions  $h_n^{(1)}$  occurring for  $n \gg z$ .

Besides its influence on the convergence of (2.10), the parameter  $L$  affects both computational time and memory consumption. Indeed, the numerical integration over the unit sphere  $\mathcal{S}$

is based on a product rule in the angular spherical coordinates  $(\theta, \phi)$  which needs  $\mathcal{O}(L^2)$  points overall [82], since the polar coordinate  $\theta \in [0, \pi]$  and the azimuthal coordinate  $\phi \in [0, 2\pi]$  are treated using a  $(L+1)$ -point Gaussian rule and a  $2L$ -point uniform rule, respectively. This approach allows to integrate exactly the  $L^2(\mathcal{S})$ -orthonormal set of spherical harmonics  $(Y_{p,m}(\theta, \phi))_{0 \leq p \leq L, -p \leq m \leq p}$  of order  $\leq L$ .

The choice of the parameter  $L$  is thus critical for both the performance and the efficiency of the FMBEM algorithm. In real-wavenumber problems,  $L$  is set according to a rule involving  $kD$  (with  $D$  the length of the cell diagonal), and is thus level-dependent as a result. In particular, for an accurate evaluation of decomposition (2.10),  $L$  must be slightly greater than  $kD$  [74].

In practice, selecting the truncation parameter  $L$  using rules inspired by (2.15) requires adjusting the constants using numerical experiments [189, 299]. In elastodynamics, starting from a relation of the form

$$L_E(D; C) = kD + C \log_{10}(kD + \pi), \quad (2.28)$$

the constant  $C$  has been empirically set to  $C = 7.5$ , by seeking a trade-off between the RMS discrepancy between ML-FMBEM versus standard BEM and the CPU time per iteration [62]. Relation (2.28) depends on the cell linear size  $D$  through the dimensionless parameter  $k|\mathbf{r}'|$ , hence is level-dependent.

**Number of levels.** The minimum number of levels is three, i.e.  $\ell^{(0)}, \ell^{(1)}, \ell^{(2)}$ . This is the case of the *single-level* FMBEM. In the multi-level FMBEM, the maximum number of levels is established by the stopping criterion (2.16). In this range, choosing a low number of levels means having a large size  $kD$  of the leaf cells, thus increasing the near interactions evaluation through the standard BEM. As a consequence, the FMBEM would not be so convenient, involving a complexity close to the standard BEM  $\mathcal{O}(N^2)$ . On the other hand, if a large number of levels is chosen the number of transfers increases and the approximations introduced by the numerical truncation of the Green's function multipole expansion reduces the overall precision. These observations are explained in detail in [61].

## 2.3 BEHAVIOR OF WEAKLY DISSIPATIVE MEDIA

### 2.3.1 Constitutive law for a linear viscoelastic medium

The constitutive relation for a linear viscoelastic medium (1.9), recalled here for ease of readability, is [70]:

$$\sigma_{ij}(\mathbf{x}, t) = \int_{-\infty}^t C_{ijkl}(t - \tau) \dot{\varepsilon}_{kl}(\mathbf{x}, \tau) d\tau, \quad (2.29)$$

where  $\sigma_{ij}(\mathbf{x}, t)$  and  $\varepsilon_{kl}(\mathbf{x}, \tau)$  are generic components of the stress and linearized strain tensors and  $C_{ijkl}$  is the relaxation tensor. The integral (2.29) is also called hereditary integral and

represents a time convolution of the relaxation tensor and the strain rate:

$$\boldsymbol{\sigma}(\mathbf{x}, t) = \mathcal{C}(t) * \dot{\boldsymbol{\varepsilon}}(\mathbf{x}, t) . \quad (2.30)$$

Using the properties of convolution, (2.30) can be rewritten as:

$$\boldsymbol{\sigma}(\mathbf{x}, t) = \dot{\mathcal{C}}(t) * \boldsymbol{\varepsilon}(\mathbf{x}, t) = \mathbf{M}(t) * \boldsymbol{\varepsilon}(\mathbf{x}, t) , \quad (2.31)$$

where  $\mathbf{M}(t) = \dot{\mathcal{C}}(t)$ , time derivative of a Heaviside unit step function in strain, is the stress response to a Dirac  $\delta$ -function in strain. Applying the Fourier transform yields the complex, frequency-dependent viscoelastic modulus

$$\mathbf{M}^*(\omega) = \mathcal{F} \{ \mathbf{M}(t) \} = \mathcal{F} \{ \dot{\mathcal{C}}(t) \} . \quad (2.32)$$

The relation (2.29) shows that, unlike elastic materials, the stress in a viscoelastic medium at a given time  $t$  depends linearly on the strain history until that time  $t$  (i.e. the memory effect). This implies the validity of the *superposition principle*. Moreover, the upper integration limit ensures *causality* (i.e. that  $C_{ijkl}(t-\tau) = 0$  for  $\tau > t$ ). For a homogeneous isotropic viscoelastic medium, the relaxation tensor  $C_{ijkl}(t)$  in (2.29) is written in terms of two independent Lamé-type coefficients

$$C_{ijkl}(t) = [\lambda(t)\delta_{ij}\delta_{kl} + \mu(t)(\delta_{ik}\delta_{jl} + \delta_{il}\delta_{jk})]H(t), \quad (2.33)$$

where  $H(\cdot)$  is the Heaviside step function. In this work, time-harmonic motions with angular frequency  $\omega$  are considered, and the strain then takes the form  $\varepsilon_{ij}(\mathbf{x}, \tau) = \varepsilon_{ij}(\mathbf{x})e^{-i\omega\tau}$ ; a similar behavior is assumed for all other time-varying quantities. Eq. (2.29) then becomes [94]

$$\sigma_{ij}(\mathbf{x}, t) = \left[ i\omega \int_{-\infty}^{\infty} \lambda(\eta)H(\eta)e^{i\omega\eta}d\eta \right] \varepsilon_{kk}(\mathbf{x})\delta_{ij}e^{-i\omega t} + 2 \left[ i\omega \int_{-\infty}^{\infty} \mu(\eta)H(\eta)e^{i\omega\eta}d\eta \right] \varepsilon_{ij}(\mathbf{x})e^{-i\omega t},$$

having used the transformation  $\eta := t - \tau$  and with the zero lower bound of the integral replaced by  $-\infty$  by virtue of (2.33). The terms inside square brackets are the Fourier transforms  $\lambda^*(\omega)$  of  $\lambda(t)H(t)$  and  $\mu^*(\omega)$  of  $\mu(t)H(t)$ , respectively. With the time factor  $e^{-i\omega\tau}$  omitted hereon, the constitutive relation (1.9) is finally written in the form

$$\sigma_{ij}(\mathbf{x}, \omega) = C_{ijkl}^*(\omega)\varepsilon_{kl}(\mathbf{x}, \omega), \quad C_{ijkl}^*(\omega) = \lambda^*(\omega)\delta_{ij}\delta_{kl} + \mu^*(\omega)(\delta_{ik}\delta_{jl} + \delta_{il}\delta_{jk}), \quad (2.34)$$

which emphasizes the well-known formal analogy between linear viscoelastic and linear elastic time-harmonic problems, the main difference between the two situations being that the Lamé coefficients, wave velocities and wavenumbers are complex-valued and frequency-dependent in the viscoelastic case (in which case an asterisk is used, in (2.34) and hereafter, to distinguish them from their real-valued, elastic, counterparts). For the present work, carried out in the frequency domain, the dependence of the material damping on the frequency does not play a significant role, whereas time domain analyses would require an appropriate theoretical or

empirical model for the lossy medium (soil), e.g. a rheological model, which takes into account the attenuation-frequency dependence [49, 88].

### 2.3.2 Complex wavenumbers and mechanical parameters

Complex wavenumbers  $k^*$  have the form [49, 285]

$$(k^*(\omega))^2 = \rho\omega^2/M^*(\omega) \quad (2.35)$$

(where  $M^*(\omega) = M_r(\omega) - iM_i(\omega)$ , with  $M_r > 0$  and  $M_i \geq 0$ , is the complex modulus defined in (2.32) (e.g.  $M^* = \lambda^*$  or  $\mu^*$ ) and  $|M^*(\omega)| = \sqrt{M_r^2(\omega) + M_i^2(\omega)}$  its absolute value), and may be written as

$$k^*(\omega) = k(\omega) + i\alpha(\omega), \quad (2.36)$$

where  $k(\omega)$  (real wavenumber) and  $\alpha(\omega)$  (attenuation factor) are given by [195]:

$$k(\omega) = \omega \sqrt{\frac{\rho(|M^*| + M_r)}{2|M^*|^2}}, \quad \alpha(\omega) = \omega \sqrt{\frac{\rho(|M^*| - M_r)}{2|M^*|^2}}. \quad (2.37)$$

The ratio  $\chi(\omega)$  between the imaginary and the real part of the complex wavenumber is given by:

$$\chi(\omega) = \frac{\alpha(\omega)}{k(\omega)} = \sqrt{\frac{|M^*| - M_r}{|M^*| + M_r}} = \sqrt{Q^2 + 1} - Q, \quad (2.38)$$

where  $Q = M_r/M_i$  is called *quality factor* or loss tangent or loss angle, and its inverse  $Q^{-1}$  is the *attenuation*. Once the complex modulus  $M(\omega)$  is known, one can determine the phase velocity and the attenuation factor of harmonic waves propagating in linear viscoelastic media:

$$c(\omega) = \sqrt{\frac{M_r}{\rho}} \sqrt{\frac{2(1 + 1/Q^2)}{1 + \sqrt{1 + 1/Q^2}}},$$

$$\alpha(\omega) = k(\omega)\chi(\omega) = k(\omega) Q(\sqrt{1 + 1/Q^2} - 1).$$

Truncating the Maclaurin series expansion of  $\sqrt{1 + 1/Q^2}$  at the first order, i.e.  $\sqrt{1 + 1/Q^2} = 1 + 1/(2Q^2) + o((1/Q^2)^2)$  yields the approximations:

$$\tilde{c}(\omega) = c \frac{(1 + 2\beta^2(\omega))}{\sqrt{1 + \beta^2(\omega)}},$$

$$\tilde{\alpha}(\omega) = k(\omega)Q(1 + \frac{1}{2Q^2} - 1) = k(\omega)\frac{1}{2Q} = k(\omega)\beta(\omega), \quad (2.39)$$

$\beta(\omega)$  being the material damping ratio. The material damping parameter  $\beta$  is mostly used in geotechnical earthquake engineering. Damping is equivalently quantified using the loss fac-

tor  $\eta = 2\beta$  (in structural dynamics and vibration analysis), or the attenuation  $Q^{-1} = 2\beta$  (in seismology [193] or acoustics [49]); all these parameters are clearly dimensionless.

However, the approximation  $Q^{-1}(\omega) = 2\beta(\omega)$  is valid only under a certain threshold of attenuation, i.e. when the imaginary part of the complex modulus is much lower than the real part,  $\beta(\omega) \ll 1$ . Media belonging to this range are called weakly dissipative or low-loss media, and their low-strain properties are defined in (2.39) [195]. In Fig. 2.8, the approximations  $\tilde{\alpha}(\omega)$  and  $\tilde{c}(\omega)$  of the attenuation factor  $\alpha(\omega)$  and of the phase velocity  $c(\omega)$  are compared with their exact value as a function of attenuation. The error committed by doing these approximations is plotted in Figure 2.9. For considering weak dissipation, values of attenuation should be contained in the range  $0 \leq Q^{-1}(\omega) \leq 0.2$ , which implies  $0 \leq \beta(\omega) \leq 0.1$ . Damping in real soils follows the weak-dissipation assumption, with typical values in the range  $\beta = 0.03 - 0.06$ . In the present work, we adopt the weak dissipation assumption and thus limit our analysis to the corresponding range of  $\beta$  for which the assumption is valid. Finally, we can express the complex wavenumber for weakly dissipative soils as follows:

$$k^*(\omega) = k(\omega) + i\tilde{\alpha}(\omega) = k(\omega)[1 + i\beta(\omega)].$$

The complex-valued Lamé constants can then be written as [94]:

$$\mu^* = \mu(1 - 2i\beta_\mu) + o(\beta_\mu), \quad \lambda^* = \lambda(1 - 2i\beta_\lambda) + o(\beta_\lambda)$$

in terms of the distinct material damping ratios  $\beta_\mu, \beta_\lambda$  which allow to distinguish the contribution to the damping of shear and pressure waves. The complex shear wavenumber is hence given by  $k_S^* = k_S(1 + i\beta_\mu)$ , where  $k_S = \omega\sqrt{\rho/\mu}$  is the real shear wavenumber. The complex pressure wavenumber  $k_P^*$ , the complex Poisson's ratio  $\nu^*$  and the complex S- and P-wave velocities are then given by:

$$k_P^* = k_S^*\gamma^*, \quad \nu^* = \lambda^* / (2\lambda^* + 2\mu^*), \quad c_S^* = \sqrt{\mu^*/\rho} \quad \text{et} \quad c_P^* = c_S^*/\gamma^*, \quad (2.40)$$

with  $\gamma^{*2} = \mu^*/(\lambda^* + 2\mu^*) = (1 - 2\nu^*)/(2(1 - \nu^*))$ . For the sake of simplicity, the material damping ratios are assumed to be the same, i.e.  $\beta = \beta_\mu = \beta_\lambda$ . The complex Poisson's ratio then reduces to the real Poisson's ratio, i.e.  $\nu^* = \nu = \lambda/2(\lambda + \mu)$ .

## 2.4 MULTI-LEVEL FMBEM FORMULATION FOR VISCOELASTODYNAMICS

The FMBEM algorithm for viscoelastodynamics does not change from the corresponding real-wavenumber case recalled in section 2.2. However, some important algorithm parameters are affected by the presence of a damping factor  $\beta > 0$ . This Chapter is devoted to the study of the behavior of these numerical parameters (among which the truncation parameter) and to empirically establish their optimal setting in order to guarantee convergence and accuracy of the overall method. In this section, we explicit those relations of the FMBEM algorithm which are particularly concerned by the introduction of a positive  $\beta$ .

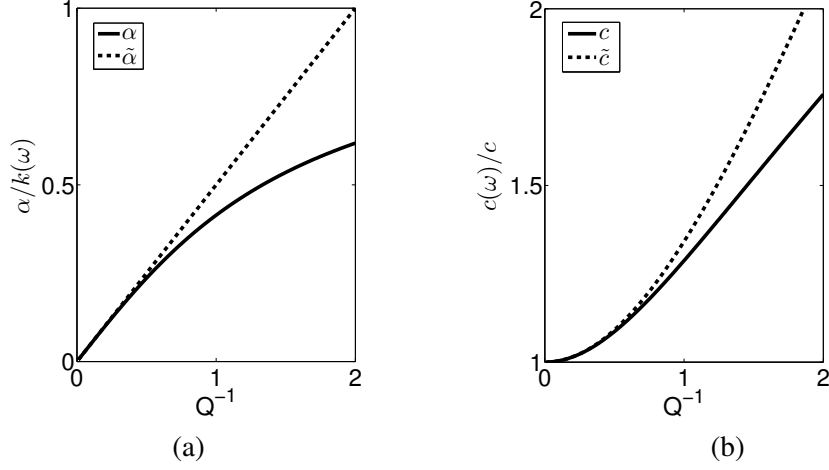


**Figure 2.8:** The approximations (a)  $\tilde{\alpha}(\omega)$  of the attenuation factor  $\alpha(\omega)$  and (b)  $\tilde{c}(\omega)$  of the phase velocity  $c(\omega)$  (in dotted line) are compared with the corresponding exact values (continuous line) ((2.39)). The weakly dissipation assumption means that approximations  $\tilde{\alpha}$  and  $\tilde{c}$  hold within limited values of  $Q^{-1}$  (quantified in Fig. 2.9).

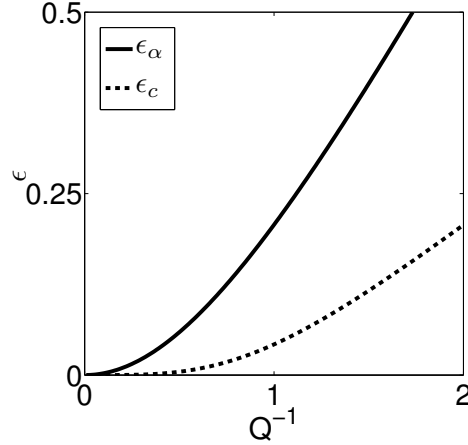


**Figure 2.9:** Quantification of the validity range for the weakly dissipation assumption. The relative error made using the approximations (2.39) of the attenuation factor  $\epsilon_\alpha$  and phase velocity  $\epsilon_c$  is plotted against the quality factor. Assuming that the approximations hold for a relative error  $\epsilon < 10^{-2}$ , their range of validity is  $0 \leq Q^{-1} \leq 0.2$ , which corresponds to a damping factor  $0 \leq \beta \leq 0.1$

### 2.4.1 Viscoelastodynamic boundary element formulation

Let  $\Omega \subset \mathbb{R}^3$  denote a region of space occupied by a three-dimensional isotropic homogeneous viscoelastic solid with boundary  $\partial\Omega$ , characterized by the complex shear modulus  $\mu^*$ , the complex Poisson's ratio  $\nu^*$  and density  $\rho$ . Assuming the absence of body forces, the displacement



$u$  is given at any interior point  $\mathbf{x} \in \Omega$  by the boundary integral representation formula

$$u_k(\mathbf{x}) = \int_{\partial\Omega} \left[ t_i(\mathbf{y}) U_i^k(\mathbf{y} - \mathbf{x}; \omega) - u_i(\mathbf{y}) T_i^k(\mathbf{x}, \mathbf{y}; \omega) \right] dS_y \quad (\mathbf{x} \in \Omega), \quad (2.41)$$

where  $\mathbf{t}$  is the traction vector. In the complex-wavenumber formulation,  $U_i^k(\mathbf{y} - \mathbf{x}; \omega)$  and  $T_i^k(\mathbf{x}, \mathbf{y}; \omega)$  denote the  $i$ -th components of the displacement and traction vector associated to the visco-elastodynamic fundamental solution generated at a point  $\mathbf{y} \in \mathbb{R}^3$  by a unit point force applied at  $\mathbf{x} \in \mathbb{R}^3$  along the direction  $k$ , given by

$$\begin{aligned} U_i^k(\mathbf{y} - \mathbf{x}; \omega) &= \frac{1}{k_S^{*2} \mu^*} \left( (\delta_{qs} \delta_{ik} - \delta_{qk} \delta_{is}) \frac{\partial}{\partial x_q} \frac{\partial}{\partial y_s} \bar{G}(\|\mathbf{y} - \mathbf{x}\|; k_S^*) + \frac{\partial}{\partial x_i} \frac{\partial}{\partial y_k} \bar{G}(\|\mathbf{y} - \mathbf{x}\|; k_P^*) \right) \\ T_i^k(\mathbf{x}, \mathbf{y}; \omega) &= C_{ijhl}^*(\omega) \frac{\partial}{\partial y_l} U_h^k(\mathbf{y} - \mathbf{x}; \omega) n_j(\mathbf{y}), \end{aligned} \quad (2.42)$$

in terms of the complex-wavenumber equivalent  $\bar{G}(r; k^*)$  of the free-space Green's function  $G(r; k)$  for the real- $k$  Helmholtz equation:

$$\bar{G}(r; k^*) = \frac{e^{ik^*r}}{4\pi r} = e^{-\beta kr} \frac{e^{ikr}}{4\pi r} = e^{-\beta kr} G(r; k), \quad (2.43)$$

and where  $\mathbf{n}(\mathbf{y})$  is the outward unit normal and the relaxation tensor components  $C_{ijhl}^*$  are given by (2.34). In (2.43), waves emitted by a source point  $\mathbf{x}$  are spatially oscillatory, which is reflected by the real wavenumber  $k$ , while also exponentially decaying away from  $\mathbf{x}$  when material damping is present, i.e.  $\beta > 0$ .

Assuming Neumann boundary conditions for definiteness, the limiting case  $\mathbf{x} \in \partial\Omega$  in the integral representation (2.41) yields the singular boundary integral equation (BIE) [44, 50]:

$$(\mathcal{K}u)(\mathbf{x}) = f(\mathbf{x}) \quad (\mathbf{x} \in \partial\Omega), \quad (2.44)$$

with the linear operator  $\mathcal{K}$  and the right-hand side  $f$  given by

$$\begin{aligned} (\mathcal{K}u)(\mathbf{x}) &= c_{ik}(\mathbf{x}) u_i(\mathbf{x}) + (\text{P.V.}) \int_{\partial\Omega} u_i(\mathbf{y}) T_i^k(\mathbf{x}, \mathbf{y}; \omega) dS_y \\ f(\mathbf{x}) &= \int_{\partial\Omega} t_i^D(\mathbf{y}) U_i^k(\mathbf{x}, \mathbf{y}; \omega) dS_y \quad (\mathbf{x} \in \partial\Omega). \end{aligned}$$

where (P.V.) indicates a Cauchy principal value (CPV) singular integral. The free-term  $c_{ik}(\mathbf{x})$  depends on the local boundary geometry and it is equal to  $\delta_{ik}/2$  at any smooth boundary point  $\mathbf{x} \in \partial\Omega$ .

As in the real-wavenumber case, the numerical solution of the BIE (2.44) is based on a discretization of the surface  $\partial\Omega$  into  $N_E$  isoparametric boundary elements, with piecewise-

linear interpolation of displacements, based on three-noded triangular boundary elements. The  $N_I$  displacement interpolation nodes thus defined also serve as collocation points. The square complex-valued matrix equation of size  $N = 3N_I$  has the same form of (2.9)

$$\mathbb{K}\mathbb{U} = \mathbb{F}.$$

We recall that (i)  $\mathbb{U} \in \mathbb{C}^N$  collects the unknown nodal displacement components and (ii)  $\mathbb{K} \in \mathbb{C}^{N \times N}$  (influence matrix) and  $\mathbb{F} \in \mathbb{C}^N$  are discrete versions of  $\mathcal{K}$  and  $f$ , respectively.

#### 2.4.2 Multi-Level Fast Multipole BEM (ML-FMBEM)

Setting up  $\mathbb{K}$  classically entails computing all element integrals for each collocation point, at a  $\mathcal{O}(N^2)$  computational cost. The fully-populated nature of  $\mathbb{K}$  makes both its storage and the application of direct solvers either impractical or impossible for BEM model sizes exceeding  $N = \mathcal{O}(10^4)$ . Instead, iterative solvers such as GMRES [265] must be used, but large BEM models require that integral operators (i.e., after discretization, matrix-vector products  $\mathbb{K}\mathbb{U}$ ) be evaluated using procedures which are faster than the standard method, whose  $\mathcal{O}(N^2)$  complexity is prohibitive. A widely used approach for that purpose is the fast multipole method (FMM), based on a reformulation of the fundamental solutions in terms of products of functions of  $\mathbf{x}$  and  $\mathbf{y}$ . This allows to re-use integrations with respect to  $\mathbf{y}$  when the collocation point  $\mathbf{x}$  is changed, and thus to lower the overall complexity (to  $\mathcal{O}(N \log N)$ ) using the multi-level form of the FMM).

In visco-elastodynamics, the decomposition of  $\overset{\star}{G}(r; k^\star)$  in diagonal form reads

$$\begin{aligned} \overset{\star}{G}(r; k^\star) &= \lim_{L \rightarrow +\infty} \overset{\star}{G}_L(r; k^\star), \\ \overset{\star}{G}_L(r; k^\star) &:= \int_{\hat{\mathbf{s}} \in \mathcal{S}} e^{ik^\star \hat{\mathbf{s}} \cdot (\mathbf{y} - \mathbf{y}_0)} \overset{\star}{\mathcal{G}}_L(\hat{\mathbf{s}}; \mathbf{r}_0; k^\star) e^{-ik^\star \hat{\mathbf{s}} \cdot (\mathbf{x} - \mathbf{x}_0)} d\hat{\mathbf{s}}, \end{aligned} \quad (2.45)$$

where  $\mathcal{S} = \{\hat{\mathbf{s}} \in \mathbb{R}^3, \|\hat{\mathbf{s}}\| = 1\}$  is the unit sphere and the transfer function  $\overset{\star}{\mathcal{G}}_L(\hat{\mathbf{s}}; \mathbf{r}_0; k^\star)$  is given by

$$\overset{\star}{\mathcal{G}}_L(\hat{\mathbf{s}}; \mathbf{r}_0; k^\star) = \frac{ik^\star}{16\pi^2} \sum_{\ell=1}^L (2\ell + 1) i^\ell h_\ell^{(1)}(k^\star \mathbf{r}_0) P_\ell(\hat{\mathbf{s}} \cdot \hat{\mathbf{r}}_0), \quad (2.46)$$

in terms of the spherical Hankel functions of first kind  $h_\ell^{(1)}(k^\star \mathbf{r}_0)$  and Legendre polynomials  $P_\ell(\hat{\mathbf{s}} \cdot \hat{\mathbf{r}}_0)$ , and with  $\hat{\mathbf{r}}_0 = \mathbf{r}_0/r_0$ .

### 2.5 TRUNCATION OF THE TRANSFER FUNCTION WITH COMPLEX-WAVENUMBER

This section is concerned with the numerical evaluation of the plane-wave decomposition (2.45) when using complex wavenumbers, so as to determine practical settings for the visco-elastodynamic ML-FMBEM exploiting that representation of the fundamental solution.

### 2.5.1 Evaluation on the transfer function

**Empirical observations in the real-wavenumber case.** The viscoelastic constitutive parameters of the medium, e.g. the wave velocities and wavenumbers, are complex-valued and frequency-dependent (Sec. 2.3). This is expected to affect the ML-FMBEM mainly through the setting of  $L$  for the evaluation of the kernel approximation (2.10). The latter, after replacing the integral over the unit sphere  $\mathcal{S}$  by a discrete quadrature with points  $\hat{\mathbf{s}}_q \in \mathcal{S}$  and weights  $w_q$ , reads:

$$G(r; k^*) \sim \sum_{q=1}^Q w_q e^{ik^* (\hat{\mathbf{s}}_q \cdot \mathbf{r}')} \mathcal{G}_L(\hat{\mathbf{s}}_q; \mathbf{r}_0; k^*). \quad (2.47)$$

In general, the error induced by using decomposition (2.10) for a finite value of  $L$  and substituting the integration over  $\mathcal{S}$  by the discrete numerical quadrature (featuring  $Q = \mathcal{O}(L^2)$  points) depends on  $\mathbf{r}'$  (position of points  $\mathbf{x}, \mathbf{y}$  with respect to local poles  $\mathbf{x}_0, \mathbf{y}_0$ ),  $|k^* D|$  (dimensionless cell size),  $r_0$  (distance between cells) and on the choice of the quadrature over  $\mathcal{S}$ . At any given level, the most unfavorable configuration, leading to the least accurate evaluation of  $G(r; k^*)$ , corresponds to non-adjacent cells that are closest (Fig. 2.10). This particular configuration has been considered as a reference configuration in the following. When  $r_0$  increases, the approximation  $G_L(r; k^*)$  of  $G(r; k^*)$  becomes more accurate, as shown in Fig. 2.11(a-c), where the relative error  $\varepsilon = |G_L - G|/|G|$  is depicted as a function of  $|k^* d|$  and  $L$  for three different relative distances between cells  $r_0 = 2d, 2D$  and  $3D$  (Fig. 2.11, top left),  $d$  being the linear cell size and  $D = \sqrt{3}d$  the cell diagonal. When  $r'$  increases, i.e. the points  $\mathbf{x}, \mathbf{y}$  move farther from poles  $\mathbf{x}_0, \mathbf{y}_0$ , the exponential in (2.47) oscillates, reducing the accuracy of  $G_L$ , see Fig. 2.12.

**Loss of accuracy of the multipole expansion in the damped case.** For a given configuration of cells and points, increasing values of the damping ratio  $\beta$  lead to a loss of accuracy in the evaluation of  $G(r; k^*)$ . This is shown in Fig. 2.13 for two points  $\mathbf{x}, \mathbf{y}$  lying in a pair of closest non-adjacent cells and such that  $r' = 0.8D$ . The behavior of the spherical Hankel functions with complex arguments influences the computation of the transfer operator (2.46), as it is addressed in [97, 155]. The classical ascending three-term recurrence (TTR) formula [3] is stable and can be employed for the evaluation of  $h_\ell^{(1)}(k^* r_0)$  with ascending  $\ell$ . The value of  $L$  defined by equation (2.28) becomes suboptimal for  $\beta > 0$  and needs to be adjusted as a function of  $\beta$ . To study the error due to the choice of  $L$  on the approximation  $G_L(k^*, |\mathbf{r}_0 + \mathbf{r}'|)$  of  $G(k^*, r)$ , a relative error  $\xi$  has been defined for the most unfavorable cell configuration ( $r_0 = 2d$ ) in the

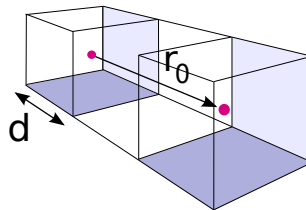


**Figure 2.10:** Closest non-adjacent cells ( $r_0 = 2d$ ), for which  $G_L$  yields a least accurate approximation of  $G$ .

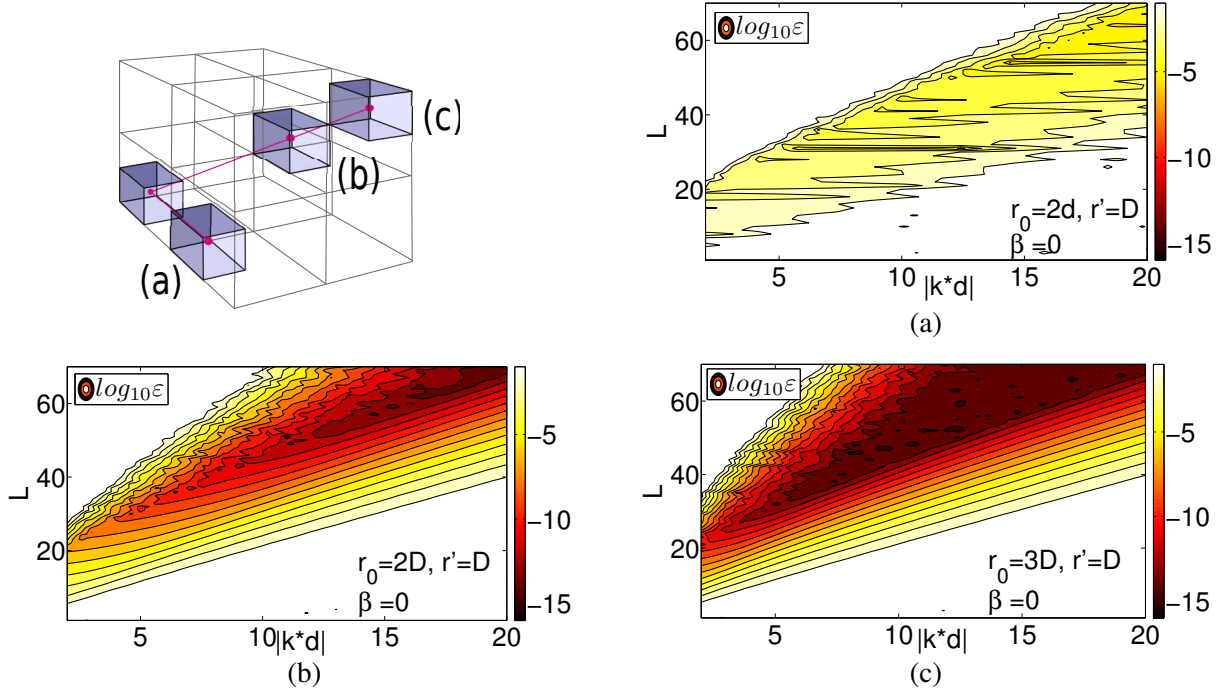


**Figure 2.11:** Influence of the distance  $r_0$  between cells on the accuracy of the multipole expansion: contour lines of  $\log_{10}(\epsilon)$ .  $\mathbf{x}$  and  $\mathbf{y}$  are located at a fixed distance  $r' = D$ .

form:

$$\xi^2(\beta) = \left( \sum_{|k^*d|} \sum_{r'} |G - G_L|^2 \right) / \left( \sum_{|k^*d|} \sum_{r'} |G|^2 \right). \quad (2.48)$$

Mesh nodes or quadrature points may lie anywhere in a cell. Thus, to obtain a realistic set of points inside a cell, uniform and Gaussian distributions have been considered for  $\mathbf{r}'$ . The error  $\xi(\beta)$  is depicted in Fig. 2.14 (solid lines) for one distribution of  $\mathbf{r}'$  of each type. Although  $\xi(\beta)$  is lower for the Gaussian distribution, the accuracy in the evaluation of  $G(k^*, r)$  for both distributions progressively deteriorates as  $\beta$  increases. In the following, we propose to modify the selection rule (2.28) by making it dependent on  $\beta$  so as to achieve a constant average accuracy  $\xi$  over the damping range  $0 \leq \beta \leq 0.1$  representative of weakly dissipative materials.

### 2.5.2 New damping-dependent selection rule for truncation parameter $L$

Having shown in section 2.5.1 that selecting  $L$  according to (2.28) does not guarantee that  $G_L$  given by (2.10) approximates  $G$  sufficiently well in the complex-wavenumber case, a modified selection rule that depends on the damping level  $\beta$ , where  $L_E(D; C)$  defined by (2.28) is replaced by  $L_V(D; \beta, C_1, C_2)$  defined by

$$L_V(D; \beta, C_1, C_2) = k^*D + (7.5 + C_1\beta) \log_{10}(k^*D + \pi) + C_2\beta, \quad (2.49)$$

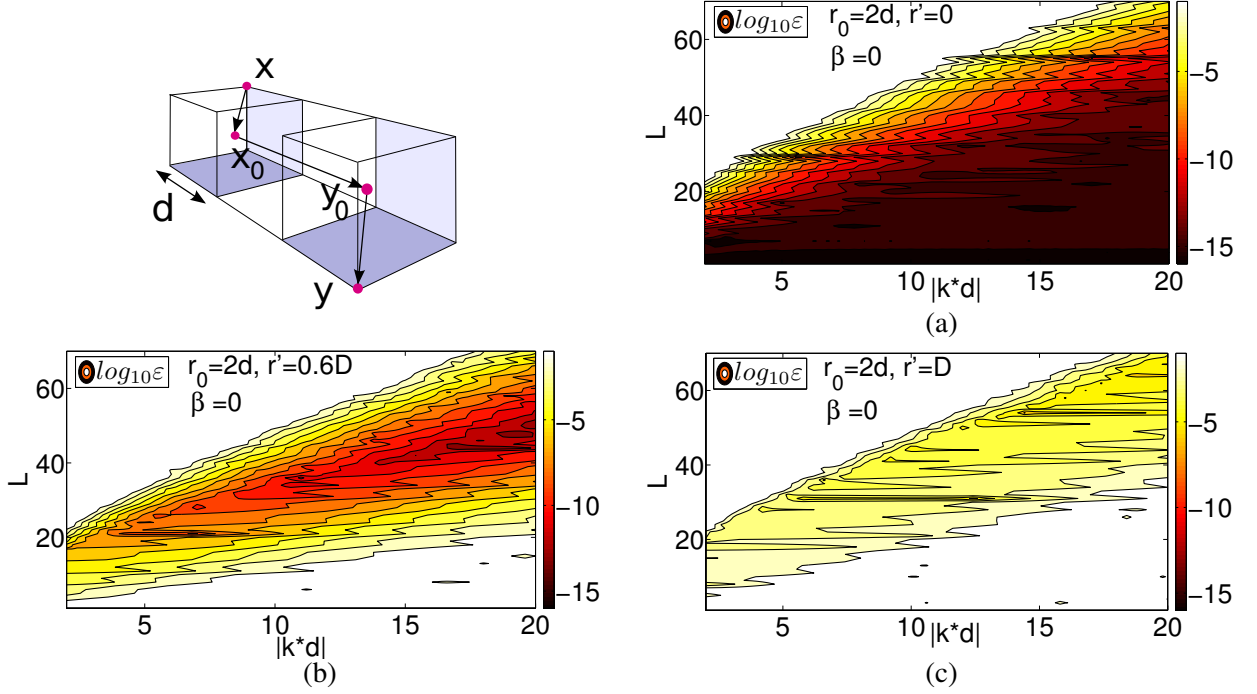


**Figure 2.12:** Influence of  $r'$  on the accuracy of expansion (2.10): contour lines of  $\log_{10}\varepsilon$  (a)  $r' = 0$ , i.e.  $\mathbf{x} = \mathbf{x}_0$ ,  $\mathbf{y} = \mathbf{y}_0$ ; (b)  $r' = 0.6D$ ; (c)  $r' = D$ , i.e.  $\mathbf{x}, \mathbf{y}$  lie on opposite vertices.

is now considered. Note that (2.28) is a special case of (2.49), since  $L_V(D; 0, 0, 0) = L_E(D)$ , and that the influence of  $\beta$  on the selection rule is controlled by the adjustable constants  $C_1, C_2$ . The relative error indicator (2.48) has accordingly be redefined so as to perform an averaging over the damping range  $0 \leq \beta \leq 0.1$ :

$$\zeta^2(C_1, C_2) = \left( \sum_{\beta} \sum_{|k^*d|} \sum_{r'} |G - G_L|^2 \right) / \left( \sum_{\beta} \sum_{|k^*d|} \sum_{r'} |G|^2 \right). \quad (2.50)$$

Suitable settings of  $C_1, C_2$  are now sought from empirical tests. Figure 2.15 shows the contour lines of  $\zeta(C_1, C_2)$  for  $0 \leq C_1, C_2 \leq 50$  (dotted lines) and the value of  $L_V(D; \beta, C_1, C_2)$ . As  $C_1, C_2 > 0$  increase, the value of  $L$  increases while decomposition (2.10) approximates  $G$  better. Many combinations of  $C_1, C_2$  thus achieve a given error level  $\zeta$ . Among these, setting  $C_2 = 0$  and using a nonzero value for  $C_1$  only is seen to correspond to the lowest value of  $L$ , i.e. is cheapest in terms CPU time. This led to reformulate the adjustment rule for  $L$  in terms of a new function  $L'_V$ , with

$$L'_V(D; \beta, C) = k^*D + (7.5 + C\beta) \log_{10}(k^*D + \pi) = L_V(D; \beta, C, 0). \quad (2.51)$$

instead of  $L_V$  defined by (2.49). To further illustrate this choice, which is retained thereafter, Fig 2.14, shows  $\xi(\beta)$  defined by (2.48) as a function of  $\beta$  for the uniform and Gaussian distributions of points and  $(C_1, C_2) = (0, 0), (50, 50)$  or  $(60, 0)$ . In particular, the combination

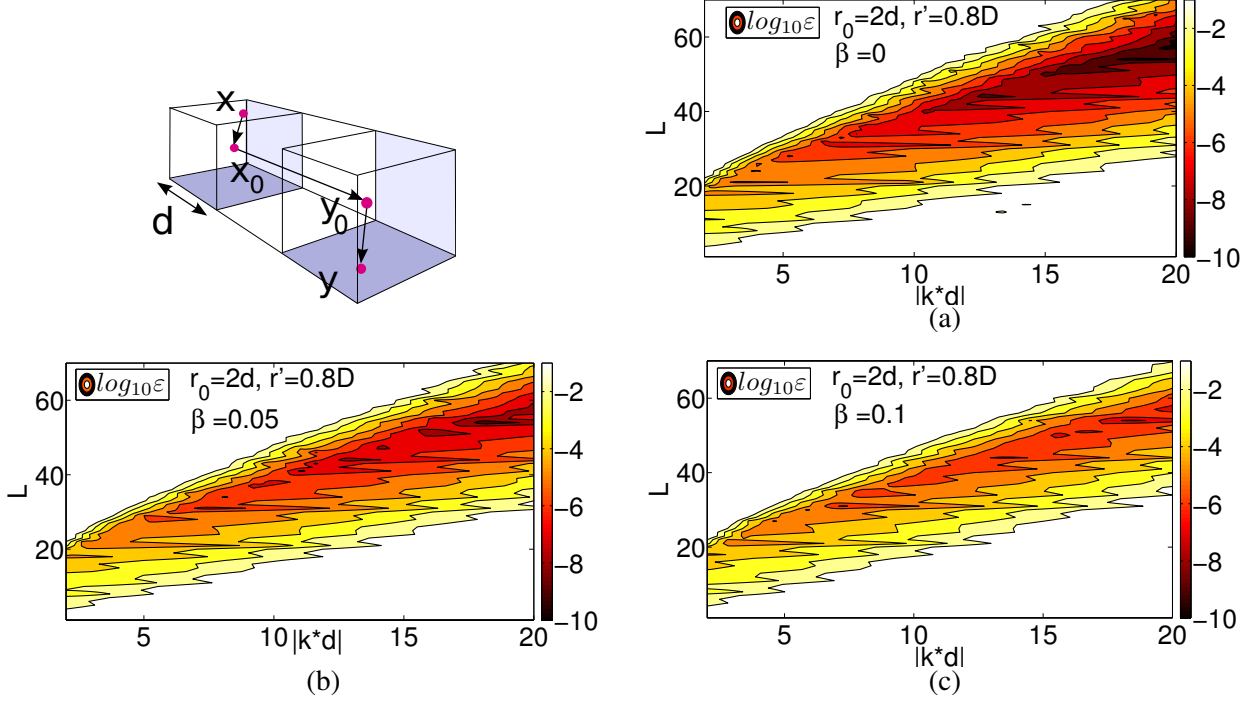


**Figure 2.13:** Influence of  $\beta$  on the accuracy of expansion (2.10): contour lines of  $\log_{10}\varepsilon$  for two given points belonging to the closest non-adjacent cells ( $r_0 = 2d$ ) at a fixed distance from poles ( $r' = 0.8D$ ).

$(C_1, C_2) = (60, 0)$  is seen to return an almost constant accuracy over the damping range of interest, while  $(C_1, C_2) = (0, 0)$  leads to a deteriorating accuracy as  $\beta$  increases.

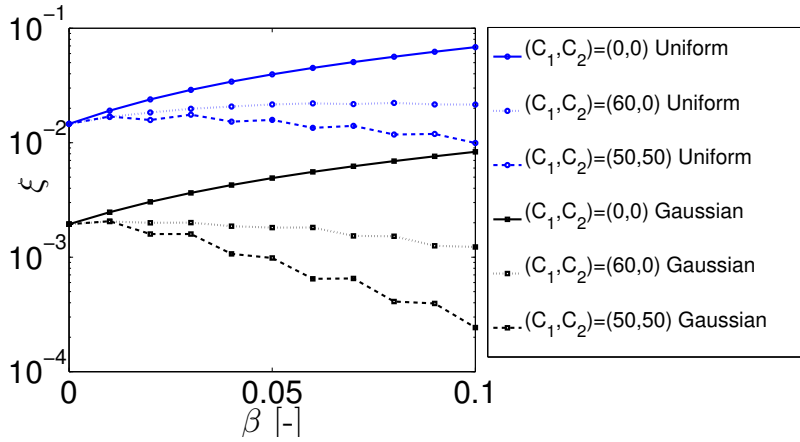


**Figure 2.14:** Relative error  $\xi$  in the numerical evaluation of expansion (2.10): influence of  $\beta$  and constants  $C_1, C_2$ , for two assumed distributions of  $\mathbf{r}'$ , with  $r_0 = 2d$  fixed.

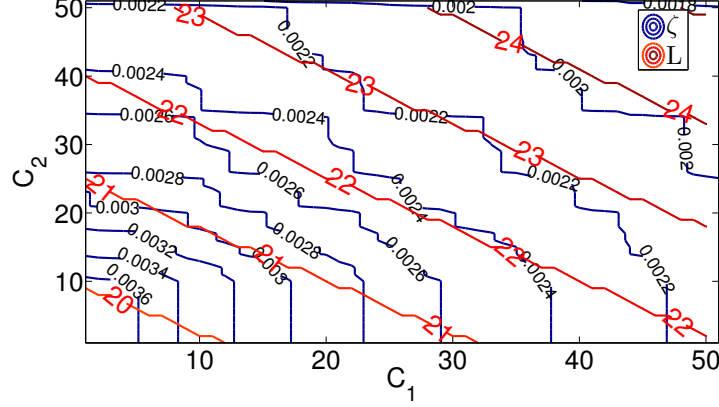


**Figure 2.15:** Contour lines of relative error (blue) and of averaged  $L$  (red) in  $(C_1, C_2)$ -space.

## 2.6 FULL ML-FMBEM EXAMPLES IN 3-D VISCO-ELASTODYNAMICS

In this section, the effect of introducing the complex wavenumbers  $k_{P,S}^*$  into the complete ML-FMBEM formulation, and in particular the importance of evaluating the kernels  $G(r; k_{P,S}^*)$  using the damping-dependent selection rule (2.51) for  $L$ , are studied on two 3D visco-elastodynamic examples for which analytical solutions are known. Both examples involve a spherical cavity of radius  $R$  embedded in a viscoelastic isotropic infinite medium. In the first example the cavity surface is subjected to a time-harmonic uniform pressure  $P$  (Fig. 2.16.a), while the second example considers the scattering by the cavity, now assumed traction-free, of an incident plane P-wave (Fig. 2.16.b) defined by  $\mathbf{u}_{\text{inc}} = \nabla \exp(ik_P^* z - \beta k_P R)$ . The corresponding analytic solutions are given for convenience in the Appendix. Only the surface of the spherical cavity is meshed. The Poisson ratio is set to  $\nu = 0.25$ , and the dimensionless frequency defined as  $\eta_P = k_P R / \pi$ . Three values of  $\eta_P$  have been considered, with the size of the models adjusted so as to maintain a mesh density of about 10 points per S-wavelength, see Table 2.1.

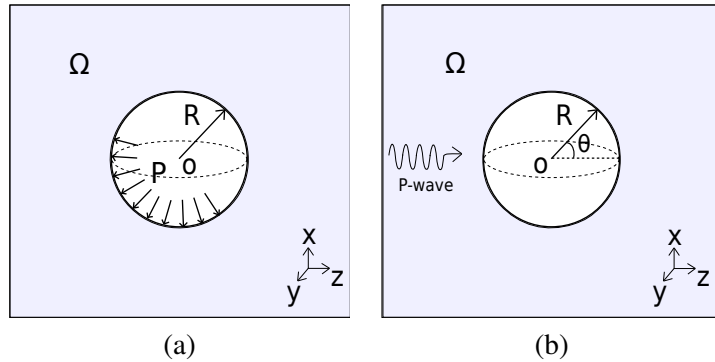


**Figure 2.16:** Geometry and notation: (a) pressurized spherical cavity, and (b) diffraction of a P-wave by a spherical cavity.

Mesh	sphere3	sphere4	sphere5
$N$	7 686	30 726	122 886
$\eta_P$	1.5	3	6
Nb. levels	4	5	6

**Table 2.1:** Reference tests for the cavity problems.  $\eta_P = k_P R / 2\pi$  is the normalized frequency.

The results obtained by selecting  $L$  according to either the existing real-wavenumber rule  $L_E$  (2.28) or the proposed complex-wavenumber rule  $L'(\cdot, \beta, C)$  (2.51) are compared, in terms of relative RMS error, CPU time per GMRES iteration and number of GMRES iterations and for the two examples considered.

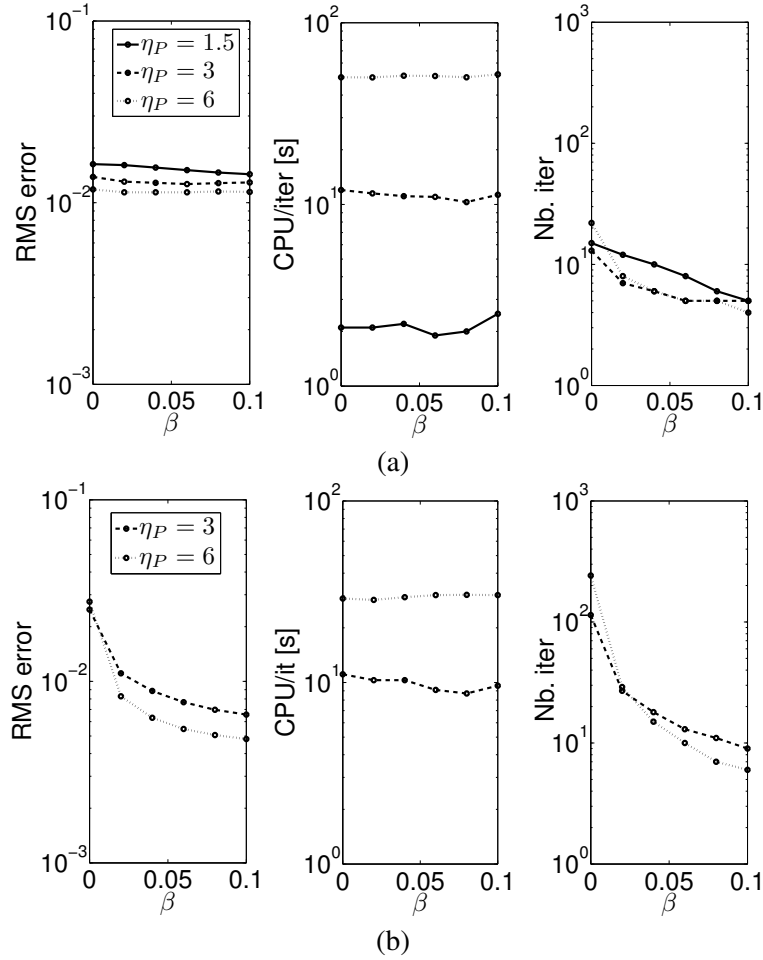


**Figure 2.17:** Results obtained by selecting  $L$  using the real-wavenumber rule  $L_E$ , for (a) the pressurized spherical cavity, and (b) the scattering of a P-wave by a spherical cavity.



**Performance of the previous rule  $L_E$ .** When  $L_E$  is used (Fig. 2.17), i.e. for  $L$  independent on  $\beta$ , the relative RMS error remains almost constant (or slightly decreases) as  $\beta$  increases, with the CPU time per iteration also relatively insensitive to  $\beta$ , and GMRES converges within fewer iterations. The reduction in the iteration count is ascribed to the exponential spatial decay of  $G(r; k^*)$  with  $r$  for  $\beta > 0$ , which balances the loss of accuracy in the kernel approximation.

**Performance of the new  $\beta$ -dependent rule  $L'_V$ .** To evaluate the influence of the constant  $C$ , the two examples have been solved using several values of  $C$  in  $L'_V(\cdot, \beta, C)$ , with results depicted in Fig. 2.18. In addition to the improved accuracy in the evaluation of  $G$  permitted by rule (2.51) (see Sec. 2.5.2), this choice yields increasing solution accuracy (i.e. decreasing relative RMS solution error), at the cost of a growing CPU time (due to the  $\mathcal{O}(L^2)$  quadrature points) as  $\beta$  increases. The case  $C = 0$  corresponds to  $L'_V = L_E$  (real-wavenumber rule) and is reported for comparison. When too-large  $L$  are generated ( $C = 150$ ), the divergence threshold of the

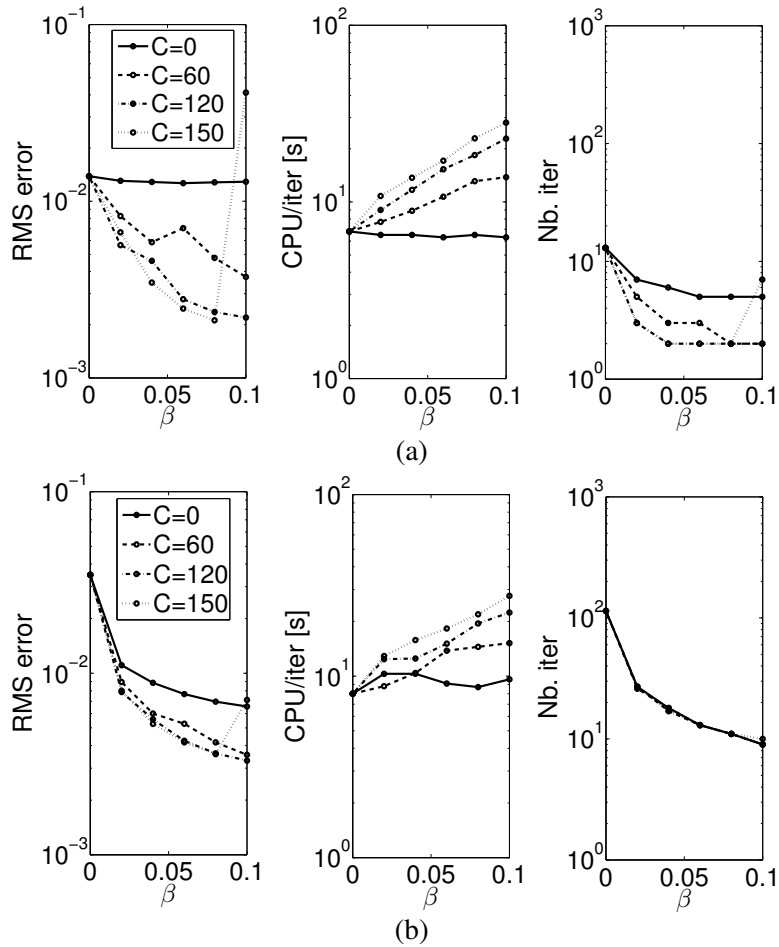


**Figure 2.18:** Influence of different values of the constant  $C$  in relation (2.51) : pressurized cavity (a) and scattering by a spherical cavity (b) for  $\eta_P = 3$ .

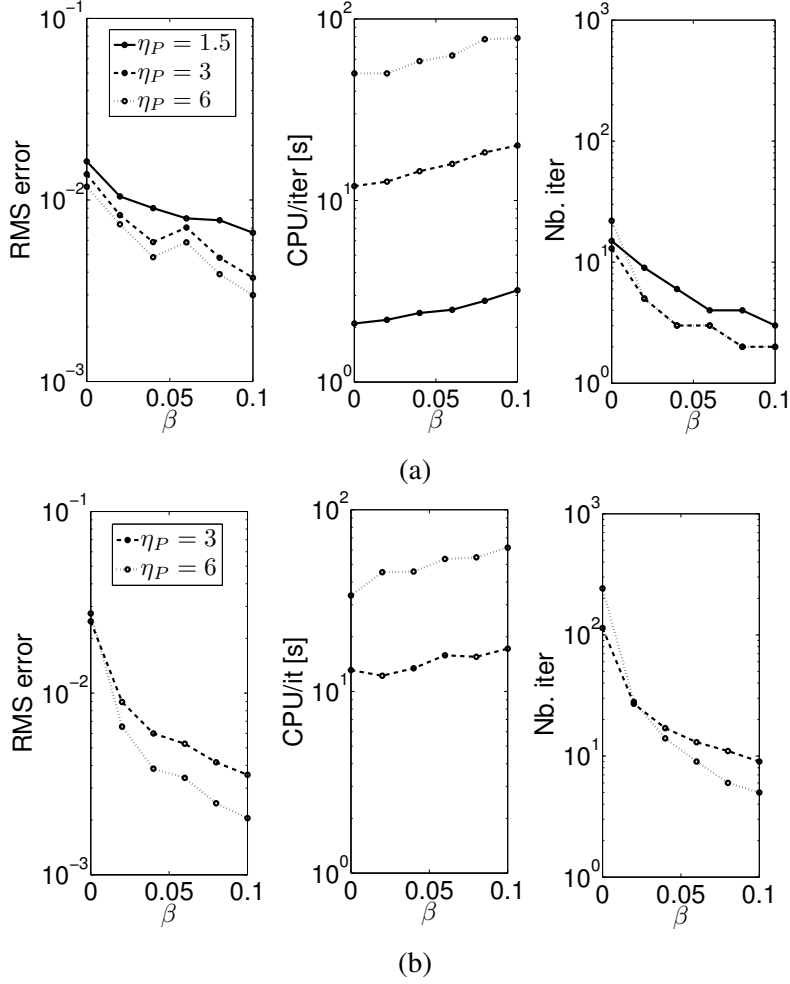


**Figure 2.19:** Results using  $L = L''_V$ : (a) pressurized cavity and (b) scattering by a spherical cavity, for different values of  $\eta_P$ .

Hankel functions is reached for  $\beta = 0.1$ , with a sharp drop in solution accuracy. The choice  $C = 60$ , which yields an approximately constant accuracy in the evaluation of  $G$ , offers a good compromise in terms of computational efficiency. Hence, the finally proposed damping-dependent selection rule is:

$$L''_V(D; \beta) = k^* D + (7.5 + 60\beta) \log_{10}(k^* D + \pi) = L'_V(D; \beta, 60) \quad (2.52)$$

Results obtained on the two example configurations using (2.52) are reported in Fig. 2.19. The good agreement between the ML-FMBEM and analytical solutions is further stressed on Fig. 2.20 for the scattering problem, with comparisons for the total radial displacement along radial lines emanating from the sphere shown for several azimuths ( $\theta = 0, \pi/4, \pi/2, 3\pi/4, \pi$ ) and damping factors ( $\beta = 0, 0.04, 0.08$ ). For  $0 \leq \theta \leq \pi/2$ , the amplitude reduction occurring with increasing damping is clearly seen. For  $\theta > \pi/2$ , the amplitude growth with  $\beta$  is due to

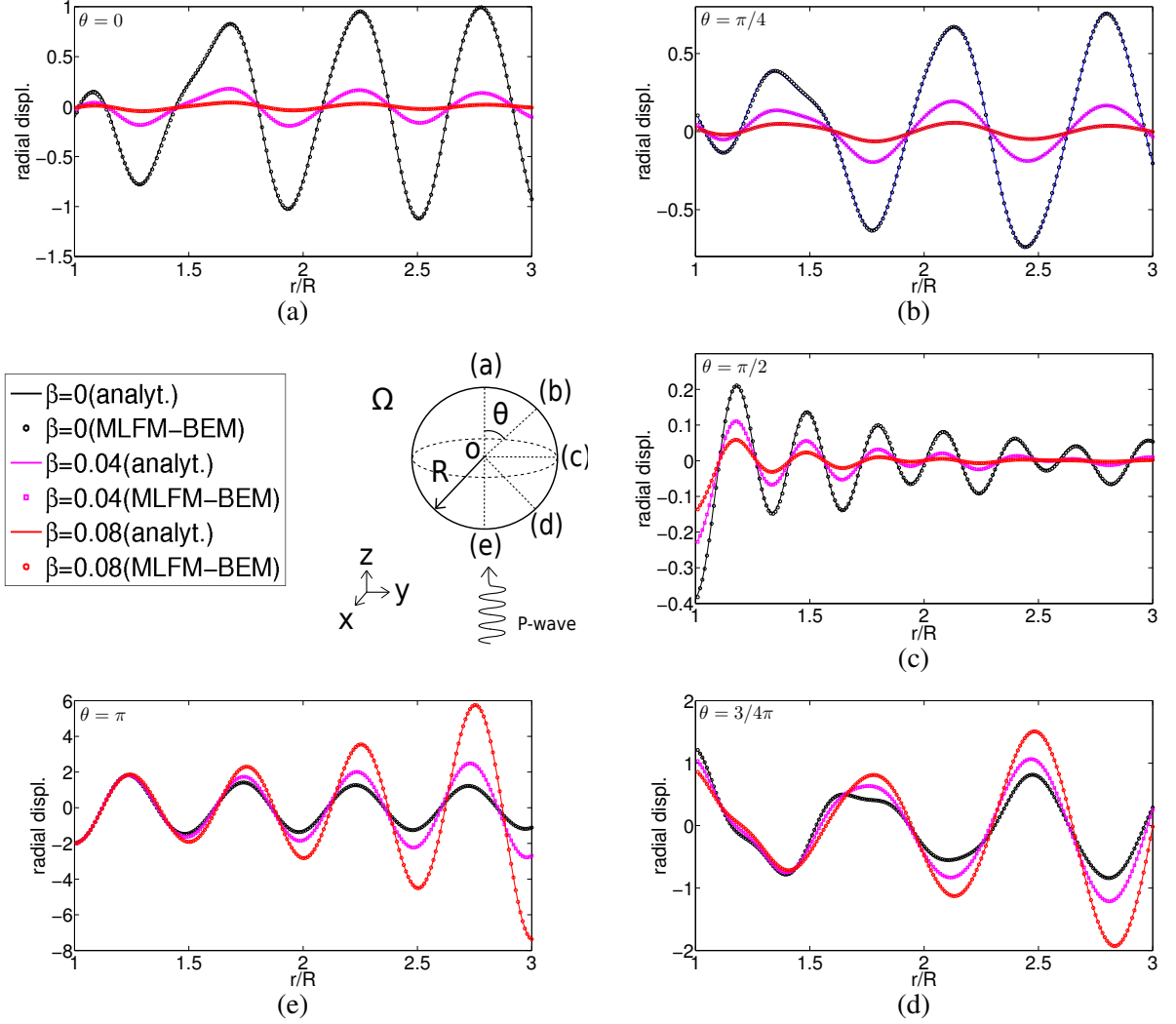


**Figure 2.20:** Scattering of an incident plane P-wave by a spherical cavity (with  $\eta_P = 4$ ): comparison between the ML-FMBEM and analytical solutions (radial displacement along radial lines emanating from the sphere) for several azimuths ( $\theta = 0, \pi/4, \pi/2, 3\pi/4, \pi$ ) and damping factors ( $\beta = 0, 0.04, 0.08$ ).

the apparent backward propagation on the  $r/R$  axis (forward amplitude decay appearing as a backward exponential growth).

**Remarks on the cell size threshold.** The possibility to adjust the cell size threshold  $d_{min} = \alpha \lambda_S$  (Sec. 2.2.2) as a function of  $\beta$  is now investigated. Recall that  $\alpha = 0.3$  was found to be suitable in the elastodynamic case [62]. Setting  $\alpha = 0.15$  instead adds one level to the octree. This extra level results in loss of solution accuracy (of about one order of magnitude in terms of RMS), which for viscoelastic cases is only partially compensated by the accuracy gains observed for increasing  $\beta$ , see Fig. 2.21 where the effect of an extra level is tested for the two examples, with

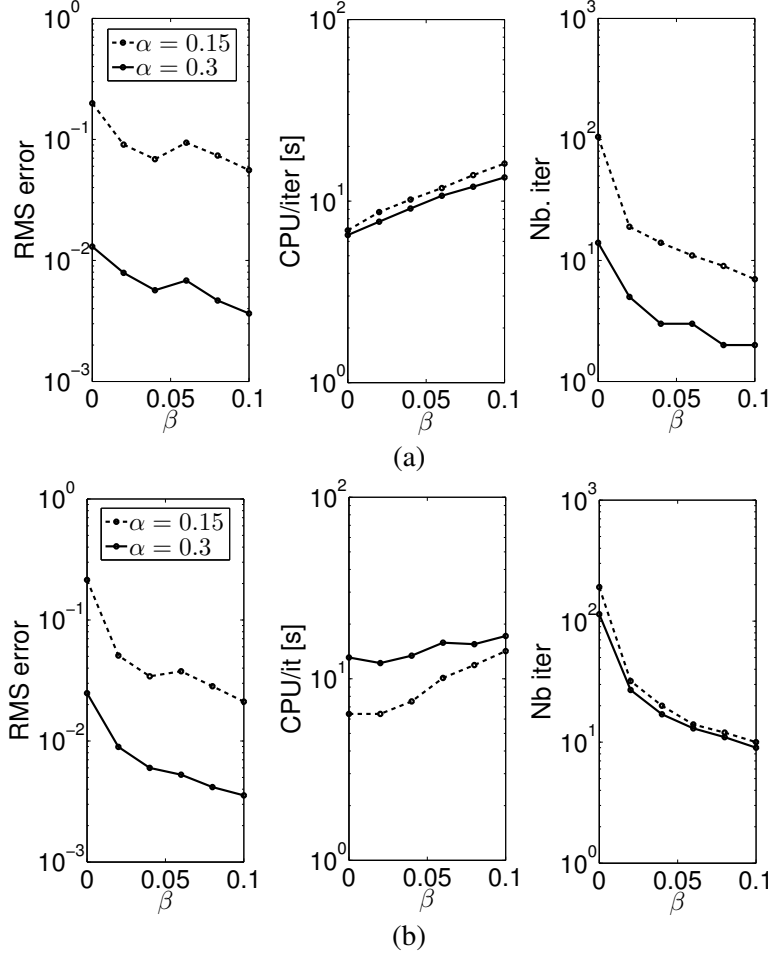


**Figure 2.21:** Influence of the cell size threshold  $\alpha = 0.3, 0.15$  using the proposed  $L$ -relation: (a) pressurized cavity and (b) scattering by a spherical cavity.

$L$  set using (2.52). In Fig. 2.21b, the relative RMS error for  $\alpha = 0.15$  and  $\beta > 0.08$  has a value comparable to the elastodynamic combination  $\alpha = 0.3$  and  $\beta = 0$  (in which case adding the new level led to acceptable results). However, this is not the case for the other example. Thus, the presence of viscoelastic damping does not appear to allow a modification of the  $\alpha = 0.3$ , e.g. by making it dependent upon  $\beta$ , that is guaranteed to yield uniform acceptable solution accuracy. In fact, a simple  $\beta$ -dependent rule for determining  $\alpha = 0.3$  was tried, leading to similar conclusions.

## 2.7 MULTI-DOMAIN ML-FMBEM IN 3-D VISCO-ELASTODYNAMICS

The possibility to account for material damping allows a more realistic modelling of seismic wave propagation in alluvial soil deposits, which are lossy materials. Here, the previously discussed alterations to the elastodynamic ML-FMBEM allowing its extension to visco-elastodynamics have been introduced into the multi-domain ML-FM BE-BE coupling of [63],

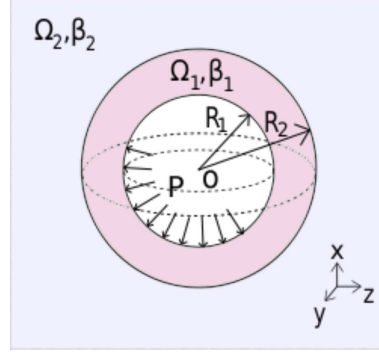


**Figure 2.22:** Multi-domain validation problem.

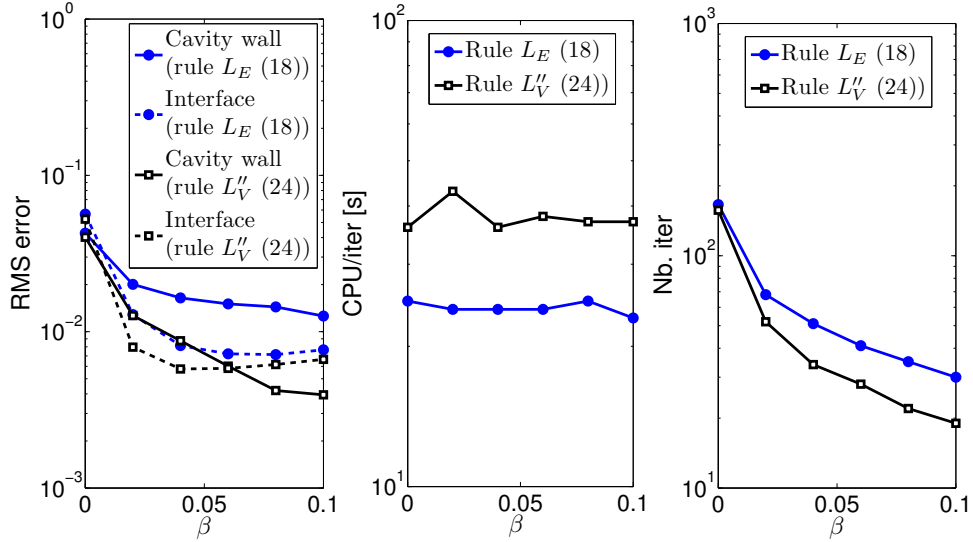


**Figure 2.23:** Two-region example, comparison of results obtained with  $L$  set using either  $L_E$  (2.28) or  $L_V''$  (2.52).

recalled in the subsection 2.2.3. The visco-elastodynamic multi-domain ML-FM BE-BE thus obtained is now studied on numerical examples derived from those of [63], with the objective to study the effect of damping.

### 2.7.1 Verification on a two-region example

Consider a spherical cavity of radius  $R_1$ , surrounded by a spherical layer  $\Omega_1$  of outer radius  $R_2$  and embedded in a 3-D visco-elastic isotropic infinite medium  $\Omega_2$ , submitted to an internal uniform time-harmonic pressure  $P$ , see Fig. 2.22. The materials in  $\Omega_1$  and  $\Omega_2$  are homogeneous and their mechanical properties are detailed in Table 2.2. This problem has an analytical solution, given in the Appendix B .

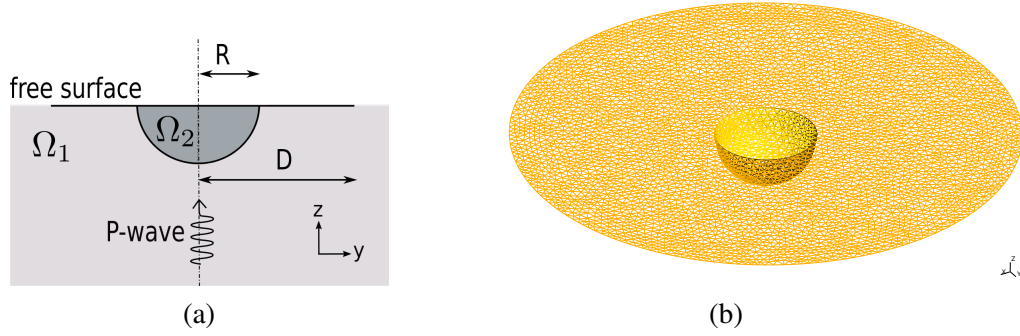
The damping in  $\Omega_2$  is  $\beta_2 = 0.05$ , while various values in the range  $0 \leq \beta_1 \leq 0.1$  are considered for  $\Omega_1$ . The size of the problem is  $N = 307, 224$ , and the octree for each region

	$\mu$	$\nu$	$\rho$
$\Omega_1$	4	0.25	3
$\Omega_2$	2	1/3	1

$\ell$	$L_1^{(\ell)} = L_E(\cdot)$	$L_1^{(\ell)} = L_V''(\cdot; \beta_1)$ ( $\beta_1 = 0.04$ )    ( $\beta_1 = 0.1$ )	
2	25	28	32
3	16	18	22
4	10	13	15

**Table 2.2:** Two-region example: material properties (left), value of  $L_1$  for active levels 2, 3, 4 using rules (2.28) or (2.52), for  $\beta_1 = 0.04$  or 0.1 (right).



**Figure 2.24:** Vertically incident P-wave in a viscoelastic half-space containing a semi-spherical soft basin: geometry and finite boundary element discretization.

has a leaf level  $\bar{\ell}_1 = \bar{\ell}_2 = 5$ . This problem has been solved with  $L$  set using either the elastic rule (2.28) or the damping-dependent rule (2.52). Results on the relative error between the numerical and analytical solutions for the displacement on the cavity wall and the interface between  $\Omega_1$  and  $\Omega_2$  are shown in Fig. 2.23, while the values of  $L_1$  at the active levels  $\ell_1 = 2, 3, 4$  given by rules (2.28) and (2.52) are reported in Table 2.2. Compared to the elastic rule  $L_E$ , the proposed damping-dependent rule  $L_V''$  brings improvement on solution accuracy while requiring fewer GMRES iterations, each iteration being however somewhat more expensive due to the fact that  $L''(D; \beta)$  increases with  $\beta$ .

### 2.7.2 Seismic wave propagation in a damped basin

In this section, an example previously used in [268] and [63] for elastic waves is considered, where a vertically-incident plane P-wave propagates in a viscoelastic half-space containing a semi-spherical soft basin  $\Omega_2$  (Fig. 2.24). As the present FM-BEM is based on the full-space fundamental solution, the BE mesh must include the free surface (Fig. 2.24, here truncated within a radius  $D = 5R$  from the basin center). The basin  $\Omega_2$  and the complementary semi-infinite medium  $\Omega_1$  are constituted of homogeneous, isotropic and visco-elastic materials, with equal damping ratios ( $\beta^{(1)} = \beta^{(2)} = \beta$ ) and other mechanical parameters such that  $\nu^{(1)} = 0.25$ ,  $\nu^{(2)} = 1/3$ ,  $\mu^{(2)} = 0.3\mu^{(1)}$  and  $\rho^{(2)} = 1.2\rho^{(1)}$ . Four different normalized frequencies  $\eta_P = k_P^{(1)} R/\pi$  are considered. Computational data and results are summarized, for each frequency

$k_P^{(1)} R/\pi = 0.5$	Pb size	$d_{min}/\lambda_S$	$\bar{\ell}_1; \bar{\ell}_2$	CPU/Iter;Nb Iter ( $\beta = 0$ )	CPU/Iter ;Nb Iter ( $\beta = 0.05$ )	CPU/Iter;Nb Iter ( $\beta = 0.1$ )
0.5	17,502	0.15	5; 4	7.6; 26	7.7; 23	9.2; 22
0.7	17,502	0.15	6; 4	5.7; 34	5.9; 27	7.1; 24
1	90,057	0.3	5; 4	62.6; 51	72.7; 34	95.5; 29
2	190,299	0.3	6; 5	120.3; 95	153.7; 49	189.9; 35

**Table 2.3:** Vertically incident P-wave in a viscoelastic half-space containing a semi-spherical soft basin: computational data and results.

and damping values  $\beta = 0.0, 0.05, 0.1$ , in Table 2.3, in terms of BEM model size  $N$ , cell division threshold  $\alpha = d_{min}/\lambda_S$ , number of levels of the octree for each subregion, CPU time per GMRES iteration, and GMRES iteration count. The results obtained are consistent with observations made in the previous sections. In particular, for increasing  $\beta$ , the iteration count drops while the CPU time per iteration increases. Moreover, the necessary coincidence of the results for  $\beta = 0$  with the corresponding ones of [63] has been successfully checked.

Contour maps for the vertical and horizontal displacements,  $u_z$  and  $u_y$ , on the free surface are shown in Fig. 2.25 for three levels of damping  $\beta$ , illustrating the effect of damping on the

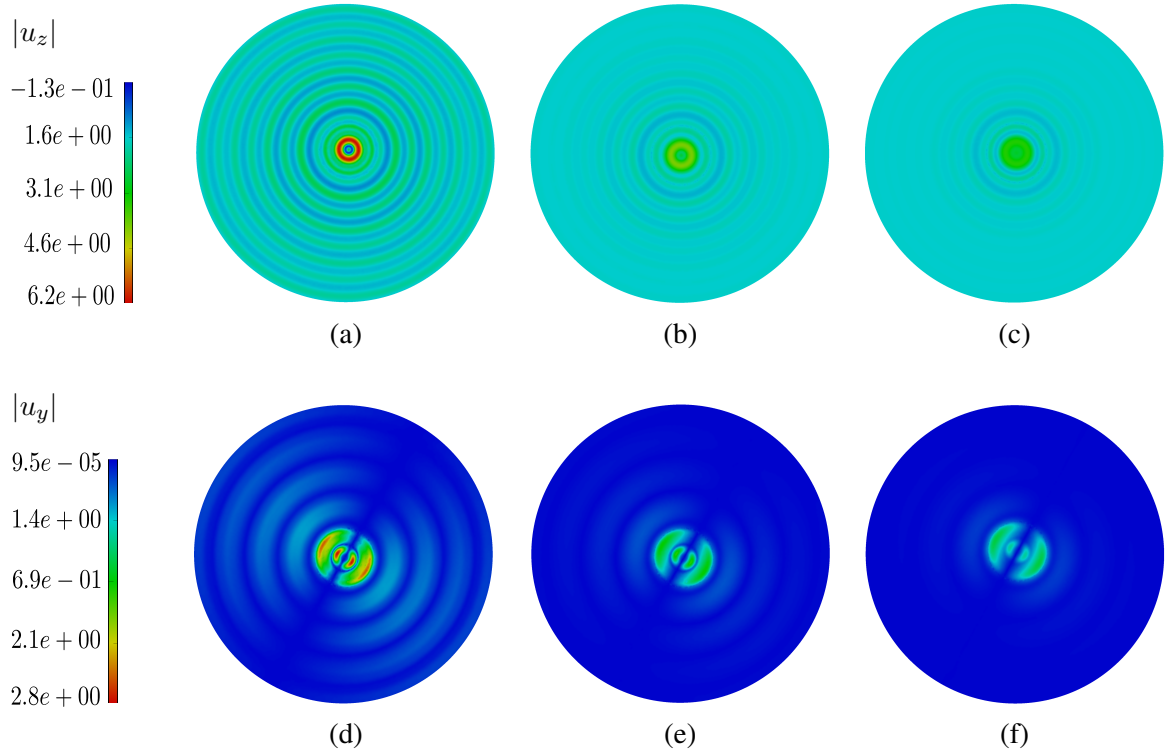


**Figure 2.25:** Vertically incident P-wave in a viscoelastic half-space containing a semi-spherical soft basin: contour maps of (a,b,c)  $|u_z|$  and (d,e,f)  $|u_y|$  at  $k_P^{(1)} R/\pi = 2$  for three levels of damping in both media ( $\beta_1 = \beta_2 = \beta$ ): (a,d)  $\beta = 0$  (purely elastic case), (b,e)  $\beta = 0.05$  and (c,f)  $\beta = 0.1$ .

basin response. The surface displacements are then compared on Fig. 2.26 with corresponding (elastic) results of [63] for the four frequencies  $\eta_P = 0.5, 0.7, 1.0, 2.0$ . Results are reported in Figs. 2.26. The amplitude decrease at the basin center in the  $\beta = 0.1$  case reaches 30% for the  $z$ -component.

**Influence of the truncation radius  $D$ .** An interesting issue concerns the choice of the truncation radius  $D$  of the discretized free surface, i.e. the smallest value  $D_{\min}$  of  $D$  for which the solution is insensitive to the free-surface truncation. Such parametric studies were conducted for the elastic case in [63], and the results compared with those obtained using a semi-analytical approach in [268]. Here, it is important to determine how  $D_{\min}$  depends on damping. Figure 2.27a shows  $|u_z|$  on the soft basin surface computed using meshes corresponding to different values  $D$ . The oscillations reflecting the sensitivity of the solution to the choice of  $D$  in the elastic case ( $\beta = 0$ ) are apparent. Convergence was found to be achieved for  $D \geq 13R$  in the elastic case [63], with oscillations of up to  $\pm 4\%$  about the reference solutions when using  $D < 13R$ . Here, with  $\beta = 0.05$ , such oscillations are strongly reduced, as shown in Fig. 2.27b. Figure 2.28 emphasizes these observations by plotting the ratio  $|u_z|(D)/|u_z|_{\text{ref}}$  at the basin center,

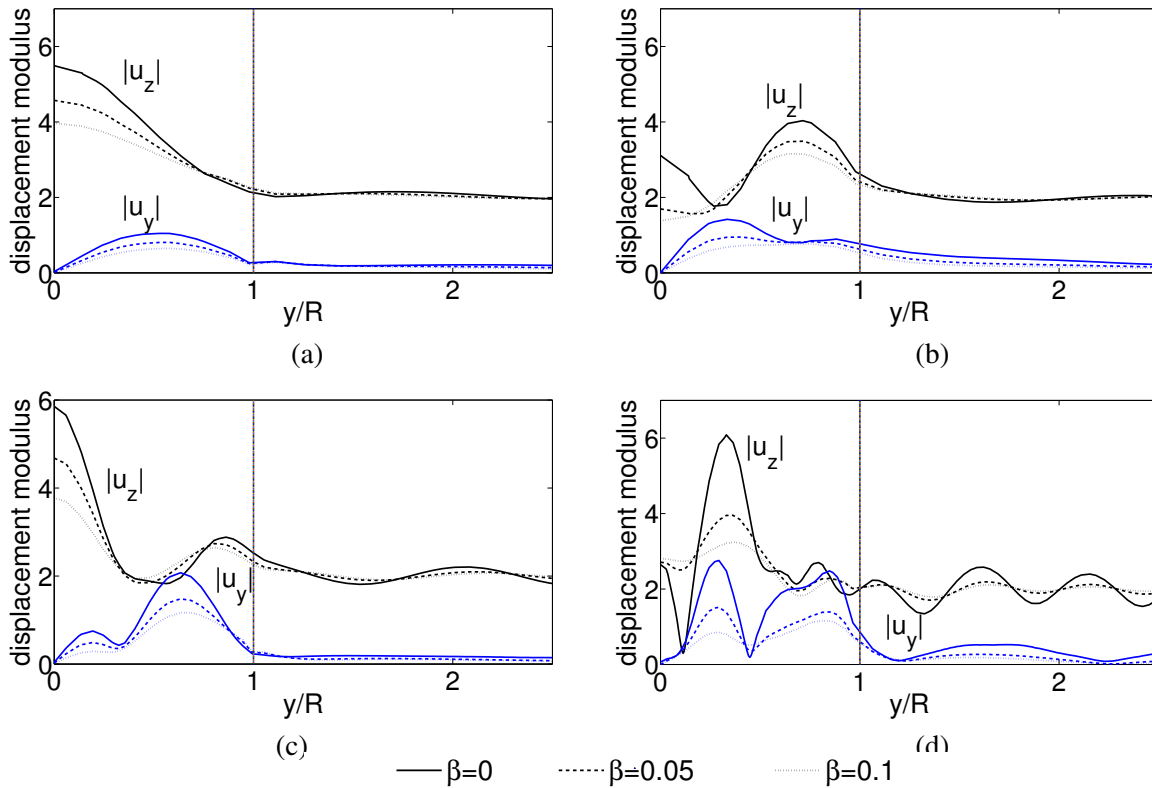


**Figure 2.26:** Vertically incident  $P$ -wave in a viscoelastic half-space containing a semi-spherical soft basin: influence of the damping ( $\beta = 0, 0.05, 0.1$ ) on the surface displacements  $|u_y|$  and  $|u_z|$  at  $k_P^{(1)} R/\pi = 0.5$  (a), 0.7 (b), 1 (c) and 2 (d).



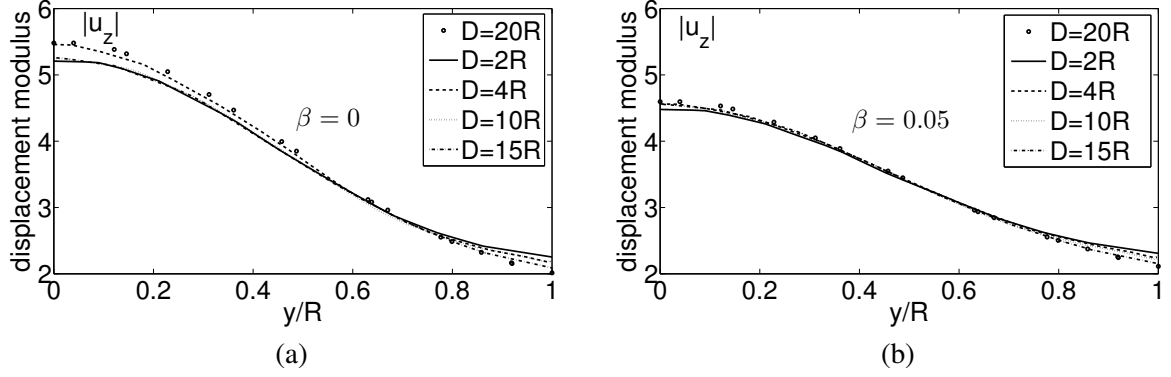


**Figure 2.27:** Vertically incident P-wave in a viscoelastic half-space containing a semi-spherical soft basin: influence of damping on the basin surface displacements at  $k_P^{(1)} R/\pi = 0.5$  for different free surface truncation radii  $D/R = 2, 4, 10, 15, 20$ : (a)  $\beta = 0$ , i.e. elastic case; (b)  $\beta = 0.05$ .

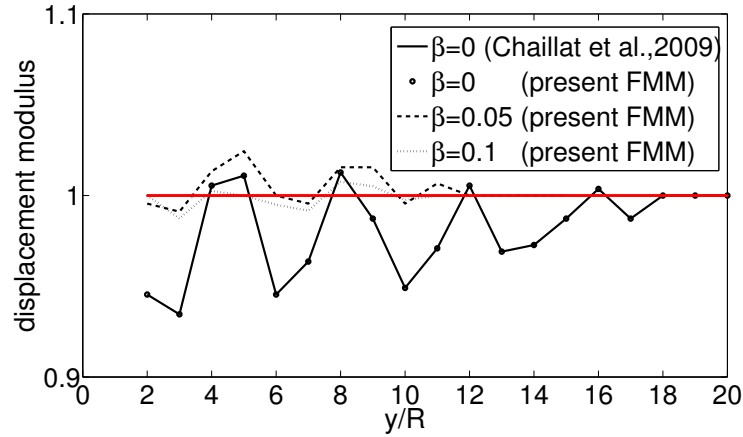


**Figure 2.28:** Vertically incident P-wave in a viscoelastic half-space containing a semi-spherical soft basin: ratio  $|u_z|(D)/|u_z|_{\text{ref}}$  for the vertical displacement at the basin center, with  $|u_z|_{\text{ref}} := |u_z|(D = 20R)$ .

with  $|u_z|(D)$  computed using given truncation radius  $D$  and  $|u_z|_{\text{ref}} := |u_z|(D = 20R)$  a reference solution obtained using  $D = 20R$ , the normalized frequency being set to  $\eta_P = 0.5$ . The fact that damping reduces the solution errors caused by the free surface truncation allows to use lower values of  $D$  when dealing with viscoelastic media, with truncation values  $D_{\min} = 6R$  (resp.  $D_{\min} = 3R$ ) found to be suitable for  $\beta = 0.05$  (resp.  $\beta = 0.1$ ).

## 2.8 SOME REMARKS ON PRECONDITIONING

This work does not address the very important, and still largely open, issue of preconditioning the FMBEM. Frequently-used techniques include block-diagonal preconditioners [124, 298], the incomplete LU factorization with threshold [286], the flexible generalized minimal residual method (fGMRES) proposed in [264] and used e.g. in [148] for the 3-D Helmholtz equation, the sparse approximate inverse (SPAI [58]). More recently, a preconditioning based on the

Calderon identities for periodic transmission problems for the 3-D Helmholtz equation has been proposed [235] for accelerating the convergence in the presence of sharp solution variations caused by high velocity contrasts.

For multi-domain problems, the system matrix is populated with various blocks whose magnitude depend on material properties, with magnitude disparities leading to significant increases in GMRES iteration count. In a previous work [63], an equation scaling approach was implemented and shown on various examples to reduce this problem. The iteration count is nevertheless known to increase with  $N$  or  $k$ . A simple preconditioning strategy is proposed in [65], where the matrix of near interactions (i.e. gathering the contributions from adjacent cells to the influence matrix  $\mathbb{K}$ ) is used in a preconditioning matrix equation, which is solved using GMRES set with a low accuracy threshold (hence the iterative solution algorithm features two nested GMRES solvers).

No preconditioner was used in this work, in order to compare “raw” versions of the FMBEM with or without attenuation. The latter, moreover, does not appear to harm the GMRES convergence, since the iteration count was usually found to reduce as  $\beta$  increases (see Figs. 2.17-2.19). The inner-outer preconditioned GMRES solver previously used for the elastodynamic FMBEM can easily, and in due course will, be incorporated into the present visco-elastodynamic FMBEM, with expected computational savings similar to those observed in [65].

## 2.9 CONCLUSIONS

In this Chapter, the application of a previously-published ML-FMBEM for 3-D time-harmonic elastodynamics (involving real wavenumbers) to linear visco-elastodynamics (involving complex wavenumbers, with a small imaginary part accounting for weakly dissipative materials) has been investigated. While the underlying BIE and FM formulations are formally identical to that of elastodynamics, the presence of complex wavenumbers called for a reassessment of the main settings of the ML-FMBEM, and especially of the level-dependent rule for choosing the truncation parameter  $L$ . An empirical study has been conducted, showing that a modified, damping-dependent selection rule for  $L$  improves the average accuracy for the evaluation of the visco-elastodynamic fundamental solution over a range of material damping ratio values  $\beta$  consistent with intended applications in civil engineering or geophysics. The resulting visco-elastodynamic ML-FMBEM has been tested on several 3D example problems involving either single-domain or multi-domain configurations, with comparisons to known analytical solutions made in both cases. These examples involved BE models of size up to  $N \approx 3 \cdot 10^5$  boundary unknowns. Finally, the multi-region formulation was applied to the problem of a (seismic) wave propagating in a semi-infinite medium with a lossy semi-spherical inclusion (alluvial basin). The influence of the truncation radius on the free surface was tested on this problem, using BE models of size up to  $N \approx 2 \cdot 10^5$ . As expected, accounting for material damping was found to permit lower values of the truncation spatial radius than in the purely elastic case, implying substantial savings on the BE model size.

## Chapter 3

# FEM / FMBEM coupling in 3D visco-elastodynamics

### Contents

---

3.1	Introduction . . . . .	68
3.2	FEM / BEM coupling approaches for wave propagation problems: survey . . . . .	70
3.3	Finite element method for time-harmonic visco-elastodynamics . . . . .	77
3.4	Domain decomposition and interface problem . . . . .	81
3.5	Iterative FEM/FMBEM coupling . . . . .	85
3.6	Simultaneous FEM/FMBEM coupling . . . . .	96
3.7	Perspectives . . . . .	111

---

### 3.1 INTRODUCTION

The coupling of the finite element method (FEM) with the boundary element method (BEM) takes advantage of the versatility of the FEM to model complex geometries and non-linearities and the exact account for infinite domains, mobile boundaries or unknown boundaries offered by the boundary integral approach. Usually, this coupling is realized through conventional approaches or in the framework of the domain decomposition methods, both introduced in Section 3.2. The main idea is to separate one or more bounded regions containing the vibrating complex structure, any steady source or complex-shaped receiver from the complementary semi-infinite space of propagation. The bounded subdomains are modelled by the FEM, whereas the half-space where they are embedded is solved within the BEM, which formulation allows the exact physical radiation of the waves in the surrounding soil. In the present work, interest is focused on wave propagation problems in semi-infinite domains. The media are supposed to have linear visco-elastic behavior. Non-linearities are not considered here, although their treatment may be considered as a natural extension of this work. Figure 3.1 shows various possible applications of the FEM/BEM coupling in the field of seismic wave propagation, vibrations in urban environment and soil-structure interaction (SSI).

#### 3.1.1 Contribution of this thesis

To the author's knowledge, no approaches have been proposed to date for coupling the FEM and the fast multipole BEM for solving 3-D seismic wave propagation problems. With this purpose in mind, the objective of this part of thesis is to compare two FEM/FMBEM coupling approaches.

The first strategy consists of an *iterative coupling*, which makes use of a modified version of the algorithm proposed by [205]. The algorithm alternates between Dirichlet solutions on

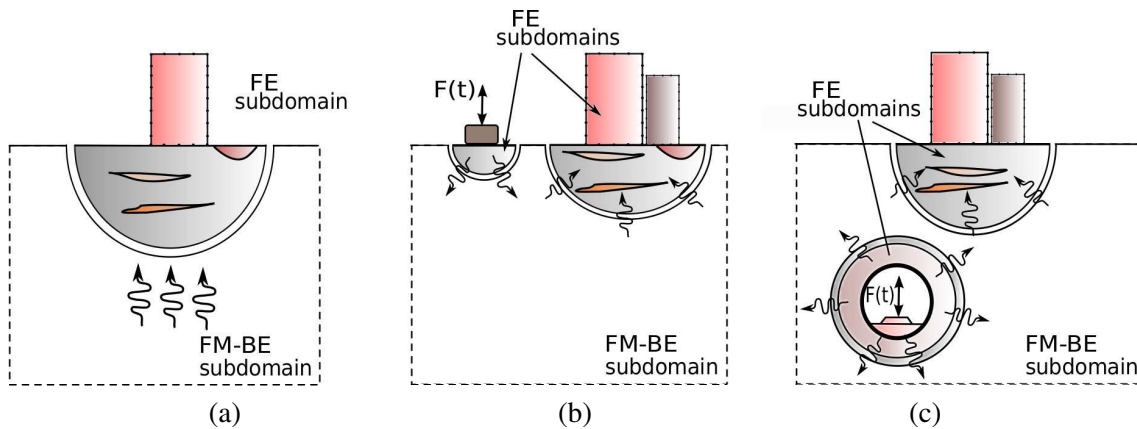


**Figure 3.1:** Various possible applications of the FE/FM-BE coupling in three-dimensional wave propagation and soil-structure interaction (SSI): (a) incident seismic wave, (b,c) induced vibration in urban environment. Complex geometrical details, anisotropies, non-linearities are confined in a bounded subdomain modelled by FEM ( $\Omega_F$ ), whereas the complementary semi-infinite space of propagation is modelled by BEM ( $\Omega_B$ ).

$\Omega_F$  and Neumann solutions on  $\Omega_B$ . A relaxation of the displacement field on the FEM/BEM interface is performed at each iteration. Existing FEM and BEM software are used in black-box fashion, driven by an external interface algorithm, a strategy often adopted in previous formulations of BEM-FEM coupling because of its easy implementation [103]. However, it has two main drawbacks: (i) the convergence depends on the value chosen for the relaxation parameter, and (ii) each global iteration in general would require  $N_{\text{FMBEM}}$  internal GMRES iterations for the fast solution of the BE global system, i.e. it would need  $N_{\text{glob}} \times N_{\text{FMBEM}}$  iterations for a single computation. This latter disadvantage can be partially smoothed by setting at each new global iterate the GMRES initial guess to the solution of the previous iterate.

The second strategy is a *simultaneous coupling* approach based on solving a global system of equations combined with the transmission conditions across  $\Phi$ . An implicit condensation for the FEM degrees of freedom is employed, and the global system is solved by generalized minimal residual (GMRES). The blocks corresponding to the BEM equations are never explicitly built. At each iteration, the matrix-vector product is computed by the FMBEM (with a complexity of order  $\mathcal{O}(N \log N)$  instead of  $\mathcal{O}(N^2)$  using traditional BEM). The FEM damped dynamic stiffness matrix is set up once and for all, stored in the compressed sparse row (CSR) format then invoked at each iteration to solve the FE system.

This Chapter is organized as follows. After an introduction to the domain decomposition methods and a bibliographic survey of the available FEM/BEM coupling approaches, the *iterative* and the *simultaneous* FEM/FMBEM couplings are presented. A distinctive feature of the FEM/FMBEM coupling is the possibility to solve geometrically complex problems. However, in this work the validation of the proposed algorithms has been carried out on deliberately simple examples to allow the comparison with FMBEM results. Before the concluding remarks, the perspectives of applicability of the presented coupling approaches are discussed. Details of the implementation of both coupling approaches are addressed in Appendix D.

### 3.1.2 Work choices and constraints

The purpose of this part of work is to compare different FEM/FMBEM coupling strategies and to identify the most effective one in sight of the intended application, i.e. seismic wave propagation in large domains potentially containing localized non-linearities, anisotropies or complex geometries. During the work, some choices have been driven by external constraints, that we introduce in the following.

As this thesis has been conducted within the IFSTTAR<sup>1</sup> (ex Laboratoire Central des Ponts et Chaussées, LCPC), we took the natural choice of using the IFSTTAR own code *CESAR-LCPC*<sup>2</sup> for the FEM part. *CESAR-LCPC* is a civil engineering computation software with modular architecture, mainly based on the finite element method, having its own pre-processing and post-processing program (called *Cleo* and *Peggy* respectively) [160, 161]. The computational core of *CESAR-LCPC* is called *CESAR*. In particular, the *CESAR* module required to solve 3-

<sup>1</sup>French institute of science and technology for transport, development and networks ([www.ifsttar.fr](http://www.ifsttar.fr))

<sup>2</sup>[www.itech-soft.com/fr/cesar/cesar.htm](http://www.itech-soft.com/fr/cesar/cesar.htm)

D time-harmonic linear visco-elastodynamic problems within the FEM and used in the present work is called *LINC*.

The initial idea was to use CESAR in a black-box fashion for the *iterative coupling* and in an interactive manner for the *simultaneous coupling* without modifying the original module *LINC*. Indeed, *LINC* includes some features as for example to store the FEM dynamic stiffness matrix. However, this module it is not yet able to freely interact with an external code. Therefore, whereas the *iterative coupling* algorithm partially exploits the capabilities of the module *LINC* (code CUSEQ, see Appendix D), for the *simultaneous coupling* we have preferred to implement directly the needed FEM subroutines in the existing FMBEM code COFFEE. This latter choice was dictated by time constraints, and has some drawbacks. In particular, as a consequence of the conforming coupling (i.e. matching grids at the FE/BE subdomains interface) the type of finite elements that can be used in the FEM subdomains is limited to linear four-node tetrahedra, which are known to be particularly dispersive in FEM dynamics computations.

We are aware of the limitation caused by these choices, taken for lack of time. Therefore, forthcoming improvements include (i) the implementation of a non-conforming coupling allowing non-matching grids at the FE/BE interface (see Sec. 3.7) and (ii) the possibility to couple the code CUSIM with an external FEM code (including modification to the module *LINC* and an opening to free FEM codes). These measures will ensure a total freedom in the definition of the FEM subdomain in terms of material behavior, type of finite element (beam elements for a better modelling of structures, contact elements to account for the soil-structure dynamic interaction, etc), etc. We refer to Section 3.7 for a more detailed explanation of the expected further improvements.

### 3.2 FEM / BEM COUPLING APPROACHES FOR WAVE PROPAGATION PROBLEMS: SURVEY

In Section 1.4.2, we have introduced some of the main existing methods for the numerical modelling of wave propagation in 3-D unbounded media. Depending on the formulation and on the type of discretization, each method has its own advantages and drawbacks in dynamics. Among the other methods, the finite element method (FEM) and the boundary element method (BEM) are of interest in the present work because of their complementarity, which has been largely exploited in the last decades through coupled formulations. The FEM is usually employed to discretize one or more bounded regions containing complex structures or portion of material where non-linearities are expected to occur, whereas the BEM is adopted as an alternative to the non-reflecting boundary conditions (NRBCs) to assure continuity at the artificial boundary and simulate the radiation to infinity of the wave field. The FEM/BEM coupling can be performed either through *conventional approaches* or *domain decomposition approaches*.

#### 3.2.1 Conventional approaches

The conventional approaches use an entire unified system of equations for the whole domain by altering the formulation of one of the two methods to make it compatible with the other. Con-

ventional approaches divides into *BEM-hosted* (or 'equivalent' or 'local' BE) and *FEM-hosted* (or 'equivalent' or 'local' FE). In BEM-hosted approaches, the FEM system is modified by introducing a matrix that transforms the tractions applied on the domain in the equivalent vector of nodal forces. This transformation matrix only depends on the spatial interpolation functions, i.e. the shape functions, for the elements along the interaction boundary. Then, the FEM and BEM systems are assembled as shown in the diagram of Figure 3.2. Similarly, in FEM-hosted approaches the boundary element domain is transformed into a macro finite element defined by the equivalent dynamic stiffness matrix, as shown in Figure 3.3. In general, conventional approaches are rarely used because the advantages of FEM system properties, namely symmetry, sparsity and bandedness, are lost. Moreover, implementation of conventional approaches needs an integrated finite element-boundary element computational environment, a highly undesirable requirement because of high intrusivity with respect to existing FEM and BEM codes. A forced symmetrization of the indirect BEM was proposed for FEM-hosted approaches in [328]. However, some authors criticized this artifice to be mechanically inconsistent, and to lead to a non-accurate numerical solution [219]. A review of classical BEM/FEM coupling methods can be found in [158]. In particular, for elliptic problems we refer to [302] and for symmetric hybrid methods to [45, 77].

$$\begin{array}{ccc}
 \text{BEM} & & \text{FEM} \\
 [H] \{u_B\} = [G] \{t_B\} & & [K] \{u_F\} = \{f_F\} \\
 \downarrow & \Longleftrightarrow & \downarrow \\
 \begin{bmatrix} H_B^I & H_B^\Phi \end{bmatrix} \begin{Bmatrix} u_B^I \\ u_B^\Phi \end{Bmatrix} = \begin{bmatrix} G_B^I & G_B^\Phi \end{bmatrix} \begin{Bmatrix} t_B^I \\ t_B^\Phi \end{Bmatrix} & & \begin{bmatrix} K_F^I & K_F^\Phi \end{bmatrix} \begin{Bmatrix} u_F^I \\ u_F^\Phi \end{Bmatrix} = \begin{bmatrix} M_F^I & M_F^\Phi \end{bmatrix} \begin{Bmatrix} t_F^I \\ t_F^\Phi \end{Bmatrix}
 \end{array}$$

**Figure 3.2:** BEM-hosted approach: the FEM right-hand side is slightly modified to be hosted by the BEM system. The transformation matrix  $[M]$  is defined as  $\{f\} = [M] \{t\}$ , where  $\{f\}$  is the vector of nodal forces equivalent to the tractions  $\{t\}$  applied on the domain. Superscripts  $\Phi$  and  $I$  separate the DoFs belonging to the FE/BE interface  $\Phi$  from the internal DoFs  $I$ .

$$\begin{array}{ccc}
 \text{BEM} & & \text{FEM} \\
 [H] \{u_B\} = [G] \{t_B\} & & \\
 \downarrow & & \\
 [M] [G]^{-1} [H] \{u_B\} = [M] \{t_B\} & & \\
 \downarrow & & \\
 [\tilde{K}] \{u_B\} = \{f_B\} & \Longleftrightarrow & [K] \{u_F\} = \{f_F\}
 \end{array}$$

**Figure 3.3:** In FEM-hosted approach, an equivalent dynamic stiffness matrix  $[\tilde{K}]$  is defined for the BE domain and the BEM system is slightly modified to be hosted by the FEM system.

Despite their computational burden, conventional approaches are often used in the engineering practice for problems of limited size. For example, a BEM-hosted FEM/BEM coupling method has been used for the 3D analysis of a half-space stiffened by piles [72, 73]. FEM-hosted methods have been successfully applied since the late 1980s [125, 312]. Recently, they have been used for example in time-domain soil-structure interaction (SSI) [300], in the study of railway-induced vibrations [17, 290] or surface vibrations induced by underground traffic [5, 15]. Andersen et al. [16] define a moving load source in a convected coordinate system to describe the ground vibrations due to the passage of a train. Problems involving non-linearities in the FEM subregions have been addressed for example in [245, 324].

### 3.2.2 Domain decomposition methods: introduction

**Main idea.** In general, a *coupled system* consists either of two or more physical systems interacting with each other and which solution can not be sought independently, or of one single problem which solution is split in subdomains for computational reasons. According to the spatial decomposition of the global domain, domain decomposition methods (DDMs) divide in two categories: overlapping and non-overlapping [330]. In the *non-overlapping approach* (called Class I), the subdomains share a portion of boundary and the coupling has the form of specific boundary conditions defined on the common interface. The need for the splitting of a domain into two or more subdomains may be motivated by the interaction of different physical problems, e.g. fluid-structure interaction, or because different procedures are computationally desirable on the subdomains, e.g. different meshes, different time-stepping procedures or combination of different numerical methods. In the *overlapping approach* (called Class II), the subdomains overlap (partially or totally) and the coupling occurs in the differential equations describing the different phenomena involved.

Continuity of displacements and equilibrium of the tractions across the common interfaces must be assured through appropriate *transmission conditions* (TC) to recover the original problem. Depending on the type of connection between two subdomains, transmission conditions can be enforced in a weak or in a strong sense. *Strong coupling conditions* require *conforming connection* of the interface meshes, i.e. that (i) there is a one-to-one correspondence between

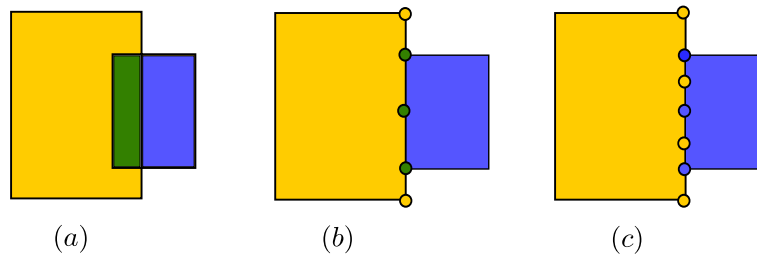


**Figure 3.4:** Diagram of the possible domain decompositions: (a) overlapping subdomains, (b) non-overlapping subdomains with matching grids at the common interface and (c) non-overlapping subdomains with non-matching grids.



degrees of freedom on the interface (i.e. meshes coincide) and that (ii) the traces of interpolation functions on the shared faces are the same. In this case, continuity and equilibrium conditions are directly imposed on the interface nodes. Otherwise, if the above conditions are not respected the subdomains connection is said to be *non-conforming* and *weak coupling conditions* are imposed.

**Origin and development.** The first Domain Decomposition Method was proposed in a pioneering paper in 1870 by the German mathematician Hermann Schwarz. It consisted in an alternating method to solve a PDE defined over two overlapping subdomains. Despite this old origin however, the interest of the numerical community towards Domain Decomposition Methods arose only in the 1980's (the first international congress on DDM took place in Paris in 1987). Two are the main reasons for this resumption. On the one hand, the enormous progresses made in the numerical modelling field during last decades has enabled the solution of more complex and larger problems, i.e. problems with increasing memory and time consumption requirements. On the other hand, concurrent advances in parallel computing have provided powerful computational tools to support this demand. Nowadays, Domain Decomposition Methods constitute a class of numerical methods and the framework in which efficient solvers for the iterative solution of substructured problems are derived. Fundamental theory of DDMs can be found in [305]. The web page of Domain Decomposition Methods, [www.ddm.org](http://www.ddm.org), offers all the proceedings of the almost annual International Conference on Domain Decomposition Methods, links to people working in the field and information about books and other material related to Domain Decomposition.

### 3.2.3 Classical non-overlapping domain decomposition methods

In non-overlapping DDMs (or iterative substructuring methods), the original problem defined over a domain  $\Omega$  is partitioned into a set of subdomains as [305]:

$$\Omega = \bigcup_{i=1}^n \Omega_i, \quad \text{with } \Omega_i \cap \Omega_\ell = \Phi_{i\ell}, \quad i \neq \ell,$$

where  $\Phi_{i\ell}$  is the portion of surface shared by adjacent subdomains  $i$  and  $\ell$ . The subdomains are linked through the definition of relevant transmission conditions (TC) on the common interfaces  $\Phi$ . Then, the global solution is either found by solving a global system of equations incorporating the TC or constructed iteratively from the repeated solution of local problems (by means of direct or iterative local solvers). An iterative domain decomposition method for the solution of a linear system is said to be *optimal* if its rate of convergence to the exact solution is independent of the size of the system, and *scalable* if its rate of convergence does not deteriorate when the number of subdomains grows [305]. The iterative substructuring algorithms should assure optimality and scalability. Usually, for two-structures problems these two properties are satisfied. For multi-structures systems, suitable preconditioners ensure optimality and the incorporation

of a coarse global problem ensures scalability. In particular, in parallel computing there exist two definitions of scaling that represent how the execution time varies with the number of processors: the *strong scaling* refers to a problem of fixed size, whereas the *weak scaling* refers to a fixed-size problem per processor.

The literature concerning DDMs is huge. However, the classical strategies developed for potential or linear elasticity problems can be divided into several categories depending on how each method deals with the boundary conditions at the interface  $\Gamma$  [139]. In *primal approaches*, the interface primal variable (the displacement field in elasticity) is chosen as the main unknown. The balancing domain decomposition (BDD) [217] and the balancing domain decomposition by constraints (BDDC) [93] are examples of primal approaches applied within the finite element method. The first step consists of solving a Dirichlet problem on each subdomain  $\Omega^{(i)}$  considering an initial guess  $u_0^\Gamma = 0$ . Then, the difference of the normal derivatives of the solutions of the two Dirichlet problems ( $\underline{u}_{1/2}^\Gamma$ ) is imposed as Neumann data on  $\Gamma$  and a Neumann problem is solved on each subdomain as an intermediate  $n + 1/2$  iteration. Finally, the values obtained ( $\lambda_{n+1}^{(i)}$ ) are used to correct the initial guess  $u_0^\Gamma$  and find the new iterate  $u_1^\Gamma$ , see Fig. 3.5.

In *dual approaches*, the interface dual variable (force density in elasticity) is chosen as the main unknown, see Fig. 3.6. The finite element tearing and interconnecting method

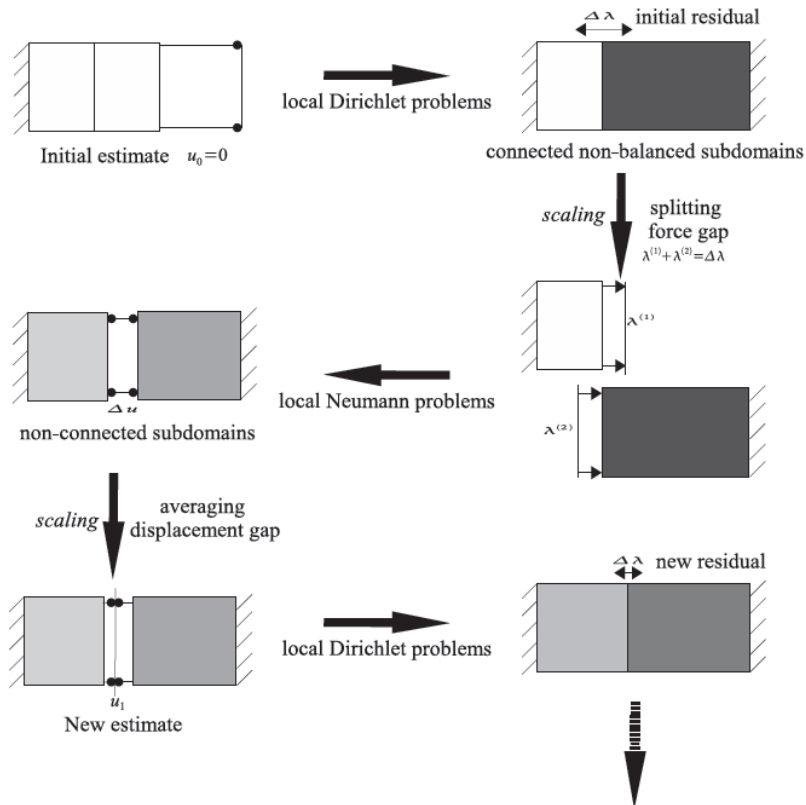
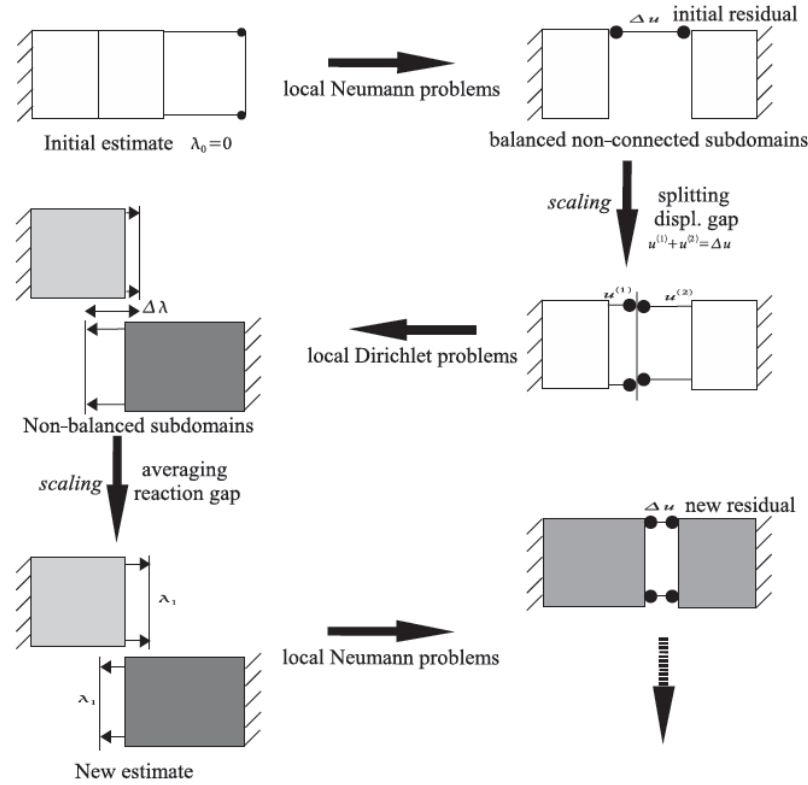


Figure 3.5: Step of a primal approach [139].



**Figure 3.6:** Step of a dual approach [139].

(FETI) [112] is an example. In FETI methods the continuity of primal unknowns is enforced using discrete Lagrange multipliers, and the corresponding saddle-point problem is solved iteratively via a preconditioned conjugate gradient (PCG) subspace iteration. The inexact FETI considers both primal and dual variables as unknowns and uses inexact subdomain solvers instead of the direct ones [186]. *Mixed approaches* consider a linear combination of primal and dual variables as principal unknown on the interface, then solve the global system iteratively and post-compute the primal and dual solution field [138]. In *hybrid approaches*, different boundary conditions (primal, dual or mixed) are assigned to different parts of the interface [110]. For a comprehensive introduction to non-overlapping DDM in computational mechanics we refer the reader to [116, 139, 203, 305].

In 2003, Langer and Steinbach introduce the boundary element counterpart of FETI, i.e. the boundary element tearing and interconnecting method (BETI) [197], later extended to an inexact fast multipole BETI [199]. They also propose a coupled FETI/BETI method based on symmetric coupled boundary and finite element equations that preserves the optimality, scalability and robustness of FETI [198].

Among the available non-overlapping DDM, the *interface relaxation* (IR) approaches involve separated computations on each subdomain (possibly by means of different codes) with successive updating of the boundary conditions on the common interface until final convergence

is reached [102, 103, 257]. Relaxation algorithms are distinguished by the type of interface smoothing procedure applied at each iteration, called *relaxation*. The main existing interface relaxation FEM/BEM coupling algorithms are summarized in Appendix C. The main advantage of IR methods consists of the fact that they allow the use of existing codes as black boxes. However, the interface relaxation depends on empirical coefficients that vary with the problem at hand and that strongly influence the convergence. In [172], N. Kamiya et al. implemented a BE-BE coupling analysis using different IR algorithms on a cluster computing system and compared three alternative schemes for the solution of internal virtual boundaries: the Uzawa method (equivalent to a parallel Dirichlet-Dirichlet algorithm) with a non-overlapping Schwarz Neumann-Neumann and a Schwarz Dirichlet-Neumann algorithm. In this study, the coefficients appearing in the definition of the new iterate have been derived through numerical tests. Performances of individual schemes have also been investigated, and as a result the Schwarz D-N seems to be the fastest and the most stable. In successive studies, the same authors have implemented a CBEM-FEM coupling using first the non-overlapping Schwarz Dirichlet-Neumann combined method resulting from the previous work [173], then a conjugate gradient method (CGM) for the renewal of unknowns on the combination boundary [171]. Recently, a symmetric BEM has been coupled with the FEM in electroencephalography, to simulate on the scalp the potential of an electromagnetic field generated by a simulated source. This coupling uses a Dirichlet-Neumann algorithm with interface relaxation [238].

**Coarse space.** In the case of many subdomains, to avoid data transmission through intermediate subdomains and to propagate information through the whole problem, the possibility to define a second coarse level has been introduced (historically at the DD1, 1987, Paris). The main purpose of the coarse space is to provide a minimal amount of global transfer of information, at each step, across the entire domain (i.e. minimize data exchange between local problems) in order to obtain optimal bounds [218, 315].

**Domain decomposition methods for the Helmholtz problem.** Application of the classical non-overlapping domain decomposition methods to Helmholtz-like problems is not straightforward. Local eigensolutions may appear when solving the local boundary value problems causing possible non-uniqueness of the solution. Various approaches have been proposed to extend the application of DDM to Helmholtz problems. In 1990, Despres extended the Schwarz non-overlapping domain decomposition method of [206] to time-harmonic wave propagation problems and showed that using Sommerfeld-type boundary conditions between adjacent subdomains leads to a unique solution of the Helmholtz equation in a given finite domain [91]. Later, La Bourdonnaye et al. [87] abandoned the iterative relaxation-like algorithm of Despres to formulate the interface problem in terms of Lagrange multipliers, and for its solution they develop a scalable preconditioned Krylov method. To date, some of the existing approaches consist in: (i) the definition of a coarse mesh finite element problem [56, 111], (ii) the use of Robin boundary conditions at the interface  $\Phi$  [301] and (iii) the extent of the Robin conditions to a first- or a second-order optimal transmission conditions [126]. A survey of non-overlapping DDM for harmonic wave propagation models is presented in [75].

### 3.2.4 Coupling of FEM with BEM and FMBEM for wave propagation problems

In 1996, Lin proposed an interface relaxation algorithm for linear elastostatics [113, 205]. This algorithm was then applied in transient elastodynamics [311]. Recently, Soares [294] applied an iterative interface relaxation algorithm for 2D structural analyses in the time domain. Here, distinct time-step discretizations were considered in different subdomains. Moreover, to match the 'time-disconnected' results in the different subdomains, adapted time interpolation/extrapolation procedures were used. Non-linear behavior confined in the FEM subregions have been addressed in several works [79, 104, 296, 310].

To take advantage of the acceleration induced by the fast multipole method (FMM) to the BEM, the finite element has been sometimes combined with the fast-multipole boundary Element method (FMBEM) to solve engineering problems. The electromagnetic scattering of inhomogeneous objects, with the interior problem modelled by the FEM and the exterior problem modelled by the fast multipole BEM was used in [291]. In 2005, Fisher used a FMBEM/FEM mortar coupling to study fluid-structure interaction [115]. He used finite plate elements to model the vibrating structure and a Galerkin formulation for the acoustic BEM domain. The interface pressure was modelled as a Lagrange multiplier, and non-matching grids were assumed at the interface. A unique coupled system was solved within a Uzawa-type scheme, where the matrix-vector product of the BEM submatrices was carried out by multi-level diagonal FMM. Margonari and Bonnet coupled the FEM with a collocation FMBEM in elastostatics, using a global iterative GMRES (generalized minimal residual) solver improved by a preconditioner based on the sparse approximate inverse (SPAI) of the BEM block [222]. Frangi employed an implicit condensation to solve a magnetostatic problem [120]. Schneider [276] applied in fluid-structure interaction field the approach proposed by Burton and Miller in 1971 [54] that suggested the use of a linear combination of the boundary integral equation and its normal derivative to obtain a unique solution of the exterior problem at all wave numbers. In his work, he solved the global system of equations by using the diagonal fast multipole method. The Burton-Miller formulation was used also in a coupling of the FEM with the symmetric Galerkin BEM accelerated by a diagonal multi-level FMM applied to frequency-domain acoustic scattering [129, 220] and to fluid-structure interaction [52].

## 3.3 FINITE ELEMENT METHOD FOR TIME-HARMONIC VISCO-ELASTODYNAMICS

In this Section, the weak formulation of a time-harmonic wave propagation problem and its discretization by the finite element method are briefly recalled.

### 3.3.1 Time-harmonic formulation

Let the subdomain  $\Omega \in \mathbb{R}^3$  be a homogeneous viscoelastic body with boundary  $\partial\Omega$ , submitted to external boundary conditions harmonic in time with circular frequency  $\omega$ . Assume that Dirichlet boundary conditions are imposed on a portion  $\partial_U\Omega$  and that Neumann conditions on a portion  $\partial_T\Omega$  such that  $\partial\Omega = \partial_U\Omega \cup \partial_T\Omega$ , as depicted in Fig. 3.7. In the following, the factor  $e^{-i\omega t}$  is

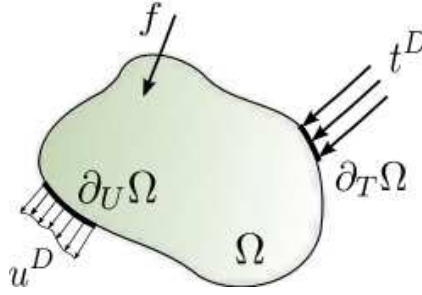


**Figure 3.7:** Equilibrium of a viscoelastic solid  $\Omega$  under time-harmonic boundary data  $\mathbf{u}^D, \mathbf{t}^D$ .

systematically omitted. The problem is governed by the local equations

$$\nabla \cdot \boldsymbol{\sigma}(\mathbf{x}, \omega) + \rho \omega^2 \mathbf{u}(\mathbf{x}, \omega) = 0, \quad (\mathbf{x} \in \Omega) \quad (3.1a)$$

$$\boldsymbol{\varepsilon}(\mathbf{x}, \omega) = \frac{1}{2}(\nabla \mathbf{u} + \nabla \mathbf{u}^T)(\mathbf{x}, \omega), \quad (\mathbf{x} \in \Omega) \quad (3.1b)$$

$$\boldsymbol{\sigma}(\mathbf{x}, \omega) = \mathcal{C}^*(\omega) : \boldsymbol{\varepsilon}(\mathbf{x}, \omega), \quad (\mathbf{x} \in \Omega) \quad (3.1c)$$

with the boundary conditions

$$\mathbf{u}(\mathbf{x}, \omega) = \mathbf{u}^D(\mathbf{x}, \omega), \quad (\mathbf{x} \in \partial_U \Omega) \quad (3.1d)$$

$$\boldsymbol{\sigma}(\mathbf{x}, \omega) \cdot \mathbf{n}(\mathbf{x}) = \mathbf{t}^D(\mathbf{x}, \omega), \quad (\mathbf{x} \in \partial_T \Omega), \quad (3.1e)$$

where  $\mathcal{C}^*$  is the complex relaxation tensor. Multiplying the equation (3.1a) by the kinematically admissible virtual field  $\mathbf{w}$ , integrating by parts and introducing the constitutive law (3.1c) leads to the weak formulation:

$$\begin{aligned} & \int_{\Omega_F} \boldsymbol{\varepsilon}[\mathbf{u}(\mathbf{x}, \omega)] : \mathcal{C}^* : \boldsymbol{\varepsilon}[\mathbf{w}(\mathbf{x}, \omega)] \, dV \\ &= \int_{\Omega_F} \rho \omega^2 \mathbf{u}(\mathbf{x}, \omega) \cdot \mathbf{w}(\mathbf{x}, \omega) \, dV + \int_{\partial \Omega_F} [\boldsymbol{\sigma}(\mathbf{x}, \omega) \cdot \mathbf{n}(\mathbf{x})] \cdot \mathbf{w}(\mathbf{x}, \omega) \, dS. \end{aligned} \quad (3.2)$$

Hereinafter, we omit the dependence  $(\mathbf{x}, \omega)$  for convenience. Let  $\tilde{\Omega}$  denote the approximation of the domain  $\Omega$  after the three-dimensional finite element discretization, and  $\partial \tilde{\Omega}$  the discretization of  $\partial \Omega$ . Separating the unknown displacement degrees of freedom  $\mathbf{u}^0$  from those imposed by the boundary data  $\mathbf{u}^D$  (such that  $\mathbf{u} = \mathbf{u}^0 + \mathbf{u}^D$ ) yields

$$\begin{aligned} & \int_{\tilde{\Omega}} \boldsymbol{\varepsilon}[\mathbf{u}^0] : \mathcal{C}^* : \boldsymbol{\varepsilon}[\mathbf{w}] \, dV - \int_{\tilde{\Omega}} \rho \omega^2 \mathbf{u}^0 \cdot \mathbf{w} \, dV \\ &= - \int_{\tilde{\Omega}} \boldsymbol{\varepsilon}[\mathbf{u}^D] : \mathcal{C}^* : \boldsymbol{\varepsilon}[\mathbf{w}] \, dV + \int_{\tilde{\Omega}} \rho \omega^2 \mathbf{u}^D \cdot \mathbf{w} \, dV + \int_{\partial_T \tilde{\Omega}} \mathbf{t}^D \cdot \mathbf{w} \, dS, \end{aligned} \quad (3.3)$$

where  $\mathbf{u}^D$  is an extension in  $\Omega$  of the  $\mathbf{u}^D$  appearing in the definition (3.1d). Moreover,  $\mathbf{u}^0 = 0$  and  $\mathbf{w} = 0$  on  $\partial_U \Omega$ . The weak formulation (3.3) can be rewritten in the form:

$$\mathbb{W}^T \mathcal{K} \mathbb{U} = \mathbb{W}^T \mathbb{F},$$

which is equivalent to the linear system:

$$\mathcal{K} \mathbb{U} = \mathbb{F}, \quad (3.4)$$

where  $\mathcal{K}$  is the damped dynamic stiffness matrix,  $\mathbb{U}$  collects all unknown displacement degrees of freedom in the subdomain  $\tilde{\Omega}$ ,  $\mathbb{F} = \mathbb{F}^U + \mathbb{F}^T$  is the vector of generalized nodal forces associated respectively with prescribed displacements on  $\partial_U \tilde{\Omega}$  and tractions on  $\partial_T \tilde{\Omega}$ . The matrix  $\mathcal{K}$  is given by:

$$\mathcal{K} = \mathbb{K} - i\omega \mathbb{C} - \omega^2 \mathbb{M} \quad (3.5)$$

$\mathbb{K}$  being the elastic stiffness matrix,  $\mathbb{C}$  the damping matrix and  $\mathbb{M}$  the mass matrix. The “ $-i\omega \mathbb{C}$ ” in (3.5) stems from the assumption of harmonic time-dependence factor  $e^{-i\omega t}$ . There exist different methods to define the damping matrix (e.g. viscoelastic models, Rayleigh, Caughey, etc). In this work, since the problem is solved in the frequency domain, we consider a simple model, the proportional Rayleigh damping.

### 3.3.2 The Rayleigh damping matrix

The Rayleigh formulation defines the damping as proportional to the mass and stiffness matrices:

$$\mathbb{C}_F = a\mathbb{K}_F + b\mathbb{M}_F.$$

Coefficients  $a, b$  are related to the damping factor  $\beta$  by [277]

$$2\beta = a\omega + b/\omega, \quad (3.6)$$

where  $\omega$  is the circular frequency. This relation is important because it allows to establish a consistency between the definition of damping in the BE and the FE subdomains. Infinite damping of low and infinite frequencies is expected from (3.6). The coefficients  $a, b$  should be chosen such that the damping is almost constant over the seismic frequency range [207]. For small to moderate values of the damping ratio, an interpretation of the Rayleigh damping as a particular Generalized Maxwell rheological model is discussed in [277]. For time-domain analyses, the proposed equivalence allows to easily derive  $a, b$  from the constitutive parameters of the rheological model. However, when working in the frequency domain, this step is not necessary and one should only respect the relation (3.6). Therefore,  $a, b$  are not a priori unique. In this work, to define  $a, b$  we refer to the structural dynamics theory, where the damping factor  $\beta$  is defined as a modal damping ratio  $\xi_n$  (for  $n$  structural modes), related to the natural frequency  $\omega_n$  by the relation (3.6) (with  $\beta := \xi_n$  and  $\omega = \omega_n$ ). Here, the  $(a, b)$  coefficients are derived by solving two algebraic equations of type (3.6) for the two modes  $\omega_i$  and  $\omega_j$  and imposing  $\xi =$

$\xi_i = \xi_j$  [69], in order to obtain almost the same values of damping for all the desired  $n$  modes. In the present work, we have chosen  $(a, b)$  as the couple of coefficients which correspond to the minimum of the Rayleigh curve (3.6), i.e.  $a = \beta/\omega$  and  $b = \beta \omega$ . This choice allows to recover the pure elastic behavior in case of lossless materials.

### 3.3.3 FEM numerical dissipation and dispersion for wave propagation problems

Accurate modelling of wave propagation with FEM depends strongly on the wavenumber  $k$ . Usually, for low wavenumber problems the 'rule of thumb'  $kh = \text{const}$  is used ( $h$  being the finite element mesh size) [152]. However, for medium to high wavenumber, this rule deteriorates the numerical results [28]. An analysis of stability and error estimation for a one-dimensional model problem subjected to a constraint of the  $kh$  magnitude for  $h$ -FEM is addressed in [164]. In particular, the influence of the topology of triangles or tetrahedra elements for the discretization of 2D, respectively 3D domains on the solution of Helmholtz problems is addressed in [313, 320]. For 3D problems, it was observed that the numerical dispersion using non-uniform unstructured meshes of linear tetrahedra is smaller if compared to uniform structured meshes. A possible explanation is that each finite element introduces a numerical dispersion that results in a positive or negative phase error depending on the shape and orientation of the element w.r.t. the propagating wave. For a uniform mesh this leads to a cumulative error, whereas for a non-uniform mesh (made of random-oriented and shaped elements) is likely to facilitate the cancellation of the phase error [320]. A direct effect of the numerical dispersion is the *pollution*, defined as the difference between the discretization  $u_I$  of the exact solution  $u$  and the discrete FE solution  $u_h$ , as shown in Fig. 3.8 [90].

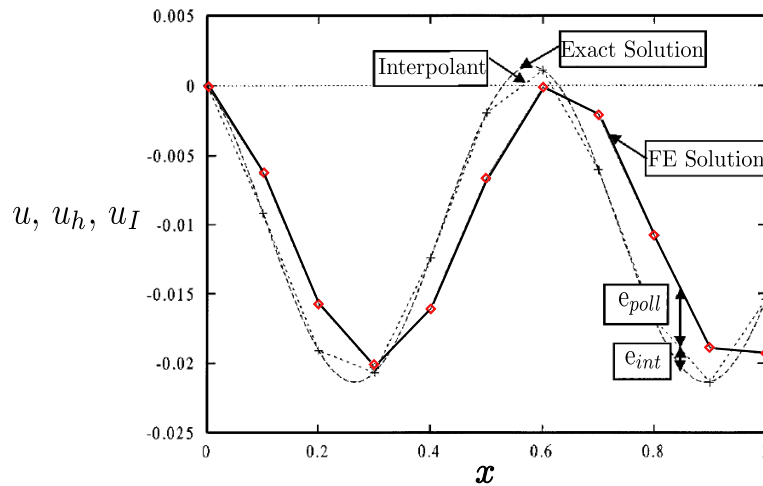


**Figure 3.8:** Numerical dispersion in the FEM solution of a 1D wave propagation problem ( $0 \leq x \leq 1$ ) on a uniform mesh with element size  $h = 0.1$  [90]. The superposition of the exact and numerical solution shows the error on the wavenumber produced by the discretization. The pollution error, directly related to the dispersion, is defined as the difference between the discretization  $u_I$  of the exact solution  $u$  and the discrete FE solution  $u_h$ .



### 3.3.4 Influence of the mass matrix formulation on numerical dispersion

The approximation of the mass through the mass matrix  $\mathbb{M}$  in (3.5) influences the numerical dispersion. The two main methods to construct the mass matrix of an individual element are the consistent and the lumped mass [159, 252, 285]. To build the *consistent mass matrix*, the same shape functions  $[N]$  used for deriving the element stiffness matrix are used. Therefore, the consistent mass matrix is fully populated. For the finite element of density  $\rho$  the elementary mass matrix  $M^{(e)}$  reads:

$$[M_{\text{consist}}^{(e)}] = \int_{V^{(e)}} \rho [N]^T [N] dV. \quad (3.7)$$

The *lumped mass matrix* is apportioned through concentrated masses  $m_i$  at the  $i$  node points. This excludes the dynamic coupling between the element displacements given by the shape functions, resulting in a purely diagonal element mass matrix:

$$[M_{\text{lump}}^{(e)}] = \frac{\rho V^{(e)}}{4} [I_{12}], \quad (3.8)$$

where  $[I_{12}]$  is the  $(12 \times 12)$  identity matrix. On the one hand, the lumped mass matrix is preferred when the physical problem approaches the assumption of concentrated masses, e.g. in structural dynamics (modal analysis), when multi-storey buildings are considered as multiple-DoF systems. Moreover, the diagonal lumped mass matrix offers computational and storage advantages, for example in explicit time integration. However, (i) it overlooks the inertial effects due to bending and (ii) it overestimates the rotational inertia in rigid-body beams rotations. On the other hand, the consistent mass matrices are more accurate, at the price of being computationally more expensive for large problems.

The consistent and the lumped mass matrix formulations introduce a numerical dispersion with opposite effects. For example, the consistent mass overestimates, while the lumped mass underestimates, the natural frequency of oscillating systems [159]. Therefore, a *mixed mass matrix* formulation was proposed as a linear combination of the previous two methods [211]:

$$[M_{\text{mix}}^{(e)}] = \alpha [M_{\text{consist}}^{(e)}] + (1 - \alpha) [M_{\text{lump}}^{(e)}], \quad (3.9)$$

with the coefficient  $\alpha$  varying between  $0 < \alpha < 1$ . The mixed formulation often leads to better numerical results, minimizing the numerical error introduced by the mass approximation. Hereinafter, sometimes we will compare performances of these different formulations.

## 3.4 DOMAIN DECOMPOSITION AND INTERFACE PROBLEM

### 3.4.1 Surface loading and far field excitation

In any homogeneous isotropic viscoelastic domain  $\Omega \in \mathbb{R}^3$ , the wave field generated by time-harmonic boundary conditions applied on any portion of the boundary  $\partial\Omega$  of  $\Omega$  radiates from the source towards infinity. Throughout this chapter, we will refer to this particular case of loading

with the general term *surface loading*. Some examples of this kind of excitation are illustrated in Fig. 3.1b-c. On the other side, the propagation in the computational domain of an incident wave coming from infinity will be denoted as *far field excitation*, like in the example depicted in Fig. 3.1a. The two denominations are inspired by the most common applications related to the two phenomena, namely the ground vibration generated by a surface loading and the propagation of seismic waves generated by a remote source. The formulation of each numerical method is defined in terms of total or of scattered field, depending on the problem at hand. The FEM formulation presented in Sec. 3.2 is expressed in terms of the total field. The boundary integral equation (2.7) can be used for seismic scattering single-domain problems. For multi-domain problems, one should use the continuous formulation of the BIE in terms of total wavefield recalled in Sec. 2.2.3. When defining a coupled problem, it is thus necessary to establish a consistent definition of the adopted formulations and/or of the transmission conditions.

For a pure surface loading, the classical FEM formulation in terms of total field as introduced in Section 3.3 and the boundary integral equation as written in (2.7) holds. If a far field excitation is analysed, one should choose between solving the equation of motion in terms of total field or of scattered field. The former case would need to employ the continuous formulation of the BIE in terms of total field, the latter to use a FEM formulation in terms of scattered field. During the Chapter we will specify in each case which formulation has been used.

### 3.4.2 Interface problem statement

Let  $\Omega \subset \mathbb{R}^3$  denote a region of space occupied by a three-dimensional isotropic homogeneous (visco)elastic solid with boundary  $\partial\Omega$ , as depicted in Fig. 3.9a. Body forces and boundary conditions are assumed time-harmonic with circular frequency  $\omega$ , the implicit factor  $e^{-i\omega t}$  being systematically omitted in the following. As the domain  $\Omega$  may feature complex geometrical

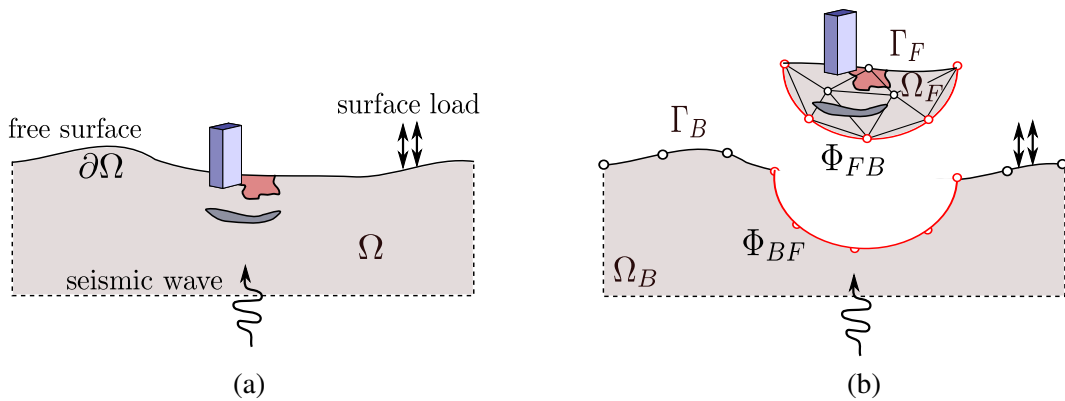


**Figure 3.9:** Spatial domain decomposition for FEM/BEM coupling: (a) original time-harmonic problem defined in the semi-infinite domain  $\Omega$  and (b) decomposition in the two non-overlapping subdomains  $\Omega_B$  (discretized by BEM) and  $\Omega_F$  (discretized by FEM). The portion of surface shared by the two subdomains is the interface  $\Phi_{ij}$ , where by convention  $ij$  subscript indicates the subdomain to which the interface belongs ( $i$ ) and the adjacent one ( $j$ ). Normals are oriented outwards each subdomain.

details, heterogeneous or anisotropic materials (all of these features being here assumed to be confined in a bounded region) a solution of the wave propagation problem by FMBEM is not feasible for many applications. Therefore, a spatial decomposition of  $\Omega$  into a bounded subdomain  $\Omega_F$  (which embraces the above mentioned "irregularities") and into its unbounded complement  $\Omega_B$  (which allows the wave radiation and dispersion at infinity) is introduced. Allowing more flexibility, the finite element method is used to discretize the problem in  $\Omega_F$ , while the boundary element method is used for the subdomain  $\Omega_B$ . Possible piecewise homogeneous regions in  $\Omega_B$  are treated with the BE-BE coupling presented in Sec. 2.2.3. The two subdomains  $\Omega_B, \Omega_F$  are supposed to be non-overlapping. The portion of boundary shared by the subdomains is the interface  $\Phi = \partial\Omega_B \cap \partial\Omega_F$ . Hereinafter, the notation  $\Phi_{ij}$  will indicate the portion of surface of the subdomain  $\Omega_i$  adjacent to  $\Omega_j$  and having the normal  $\mathbf{n}$  oriented from  $\Omega_i$  to  $\Omega_j$ . Summarizing (with reference to Fig. 3.9):

$$\begin{cases} \Omega = \Omega_B \cup \Omega_F, & \text{(domain decomposition)} \\ \Omega_B \cap \Omega_F = \emptyset, & \text{(non-overlap)} \\ \Phi = \partial\Omega_B \cap \partial\Omega_F, & \text{(interface)} \end{cases}$$

where

$$\begin{cases} \partial\Omega_F = \Gamma_F \cup \Phi_{FB}, \\ \Gamma_F = \partial\Omega \cap \partial\Omega_F, \end{cases} \quad \begin{cases} \partial\Omega_B = \Gamma_B \cup \Phi_{BF}, \\ \Gamma_B = \partial\Omega \cap \partial\Omega_B. \end{cases}$$

Continuity of the displacement field and equilibrium of the traction field across the common interface  $\Phi$  must be enforced through appropriate transmission conditions. Depending on the type of connection between the subdomains, transmission conditions can be enforced in a weak or in a strong sense. As recalled in the introductory Chapter 1, strong coupling conditions require conforming connection of the interface meshes, i.e. that (i) there is a one-to-one correspondence between degrees of freedom on the interface (i.e. meshes coincide) and that (ii) the traces of interpolation functions on the shared faces are the same. In this case, continuity and equilibrium conditions are directly imposed on interface nodes. In the present work, matching grids and conforming connections are considered along the interfaces, where a strong coupling is imposed. Displacements  $\mathbf{u}^D(t)$  and tractions  $\mathbf{t}^D(t)$  can be imposed on the portions  $\partial_u\Omega$  and  $\partial_t\Omega$  of the boundary. The system of local equations governing the elastodynamic problem restricted to each subdomain  $\Omega_s$  ( $s = B, F_i$ ) reads (neglecting body forces):

$$\nabla \cdot \boldsymbol{\sigma}_s(\mathbf{x}) + \rho_s \omega^2 \mathbf{u}_s(\mathbf{x}) = 0, \quad (\mathbf{x} \in \Omega_s), \quad (3.10a)$$

$$\boldsymbol{\epsilon}_s(\mathbf{x}) = \frac{1}{2}(\nabla \mathbf{u}_s + \nabla \mathbf{u}_s^T)(\mathbf{x}), \quad (\mathbf{x} \in \Omega_s), \quad (3.10b)$$

$$\boldsymbol{\sigma}_s(\mathbf{x}) = \mathcal{D}_s : \boldsymbol{\epsilon}_s(\mathbf{x}), \quad (\mathbf{x} \in \Omega_s). \quad (3.10c)$$

where  $\rho_s$  is the mass density of the domain  $\Omega_s$  and  $\mathcal{D}_s$  is the fourth-order tensor expressing the constitutive behavior. The boundary conditions of Dirichlet or Neumann type read

$$\mathbf{u}_s(\mathbf{x}) = \mathbf{u}_s^D(\mathbf{x}), \quad (\mathbf{x} \in \partial_U \Omega_s), \quad (3.10d)$$

$$\boldsymbol{\sigma}_s(\mathbf{x}) \cdot \mathbf{n}_s(\mathbf{x}) = \mathbf{t}_s^D(\mathbf{x}), \quad (\mathbf{x} \in \partial_T \Omega_s). \quad (3.10e)$$

In elasticity,  $\mathcal{D}_s$  would be the fourth-order elasticity tensor, whereas in visco-elasticity it would be the relaxation tensor  $\mathcal{C}^*$ . Considering the unit normal  $\mathbf{n}$  as pointing outward from each  $\Omega_s$ , the transmission conditions on each general  $\Phi_{i\ell}$  read:

$$\mathbf{u}^i(\mathbf{x}) = \mathbf{u}^\ell(\mathbf{x}), \quad (\mathbf{x} \in \Phi_{i\ell}), \quad (3.10f)$$

$$\boldsymbol{\sigma}^i(\mathbf{x}) \cdot \mathbf{n}^i(\mathbf{x}) + \boldsymbol{\sigma}^\ell(\mathbf{x}) \cdot \mathbf{n}^\ell(\mathbf{x}) = 0, \quad (\mathbf{x} \in \Phi_{i\ell}). \quad (3.10g)$$

### 3.4.3 Assumptions common to the coupling algorithms

The presence of surface piecewise homogeneous layers (see Fig. 3.10) can be taken into account by using the multi-region BE-BE coupling presented in Section 2.2.3. To distinguish the BE/BE interfaces from the FE/BE ones, we will denote the former with  $\Gamma$  and the latter with  $\Phi$  throughout the Chapter.

**Convention for normal vectors.** As already mentioned, the normals are considered outwarding each subdomain, as shows Fig. 3.11. Subscript  $ij$  (where  $i, j$  can be alphanumerical depending on the domain to which one is referring) always indicates that the degree of freedom (DoF) belongs to domain  $i$ , whereas  $j$  specifies the subdomain with which the DoF is shared.

**Discretization of the subdomains.** The surface of  $\Omega_B$  is discretized with three-node triangular boundary elements, and the FE volumes  $\Omega_F$  are discretized with four-node isoparametric lin-

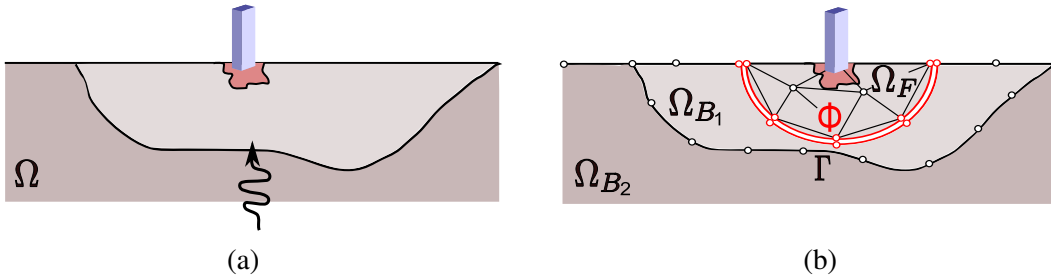


**Figure 3.10:** Coupling FE and multi-region FM-BE: (a) the original domain of the wave propagation problem and (b) the spatial decomposition in subdomains and their discretization. The thin structure and the closer complex material heterogeneities are enclosed in a bounded 3-D subdomain, which is modelled by FEM. The geological layers are modelled by a multi-region FMBEM.

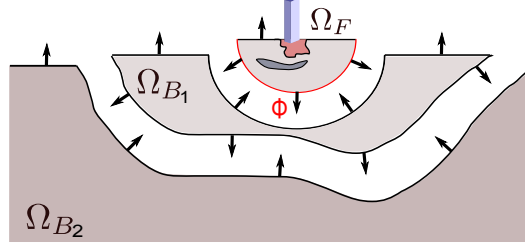


**Figure 3.11:** Outwarding normal convention for the subdomains FE and BE.

ear tetrahedral elements. The set of three-node triangular faces of the tetrahedra lying on the interface  $\Phi$  constitutes the discretization of the corresponding BEM surface, as shown in Fig. 3.12. Consequently, each part of the BEM mesh intersecting the interface  $\Phi$  and the trace of the FEM three-dimensional mesh on  $\Phi$  are the same by construction. Moreover, they are associated with the same interpolation functions, namely piecewise linear interpolation of displacements. As the interpolation on the interface is conforming, perfect bonding conditions are expressed in strong form on the nodal values. The two subdomains cannot be solved independently, and the original problem is recovered by the transmission conditions on the interfaces.

### 3.5 ITERATIVE FEM/FMBEM COUPLING

#### 3.5.1 Introduction

To solve the coupled problem we use a single relaxation sequential Dirichlet-Neumann algorithm. This algorithm was first proposed in 1996 by Lin in the form of an interface relaxation algorithm for linear elastostatic [205]. Convergence studies [101, 103] proved that the convergence depends on many factors such as the material properties of the subdomains, the boundary conditions, the mesh density and the coefficients governing the interface relaxation. The algorithm of Lin was then adapted to transient elastodynamics by Soares et al. [296] and by Von Erstoff and Hagen [311]. In the following, we distinguish between the surface loading case and the far field excitation case, the latter being an extension of the former to the case of an incident wave field.

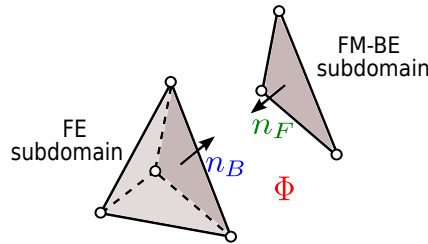


**Figure 3.12:** Assumptions on the discretization of the subdomains. (a) Finite tetrahedral elements and boundary triangular elements match at the interface  $\Phi$ , (b)

### 3.5.2 Interface relaxation algorithm for a surface loading

Let the domain  $\Omega \in \mathbb{R}^3$  be a homogeneous viscoelastic body with boundary  $\partial\Omega$ , submitted to external time-harmonic tractions  $\mathbf{t}^D$  with circular frequency  $\omega$  applied to a portion  $\partial_T\Omega$  of the free surface  $\partial\Omega$ , see Fig. 3.13. Let us split the domain in two non-overlapping complementary subdomains such that:

$$\Omega = \Omega_B \cup \Omega_F, \quad \text{with} \quad \Omega_B \cap \Omega_F = \emptyset, \quad \text{and} \quad \partial\Omega_B \cup \partial\Omega_F = \partial\Omega. \quad (3.11)$$

The surface of the subdomain  $\Omega_B$ , defined as  $\Gamma_B \cup \Phi_{BF}$  (where  $\Gamma_B = \Omega_B \cap \partial\Omega$ ), is discretized by BEM. The volume  $\Omega_F$  is discretized by FEM. Continuity and equilibrium at the interface  $\Phi$  are imposed through transmission conditions  $u_F^\Phi = u_B^\Phi$  (where  $u_B^\Phi$  indicates the trace of the displacement field  $u_B$  on the interface  $\Phi_{BF}$ ) and  $t_F^\Phi + t_B^\Phi = 0$  (where  $t_F^\Phi$  is derived in a post-processing step from the FEM displacement solution). Starting from an initial guess on the interface, the solution of the global problem is sought by alternating the local solution of the two subproblems until convergence of the displacement field on the interface  $\Phi$ . At each iteration  $n$ , the (squared) relative error between the displacement field on the interface  $\Phi$  at successive iterates is defined as:

$$\zeta_r^2 = |u_{F,n}^\Phi - u_{B,n}^\Phi|^2 / |u_{B,n}^\Phi|^2.$$

Convergence is reached when  $\zeta_r < \epsilon$ , for a given accuracy  $\epsilon$ . The adopted interface relaxation algorithm is summarized in Alg. 1. At the iteration  $n = 0$ , an estimate is made of the Dirichlet boundary conditions on the interface  $\Phi_{FB}$ . For simplicity, we set to zero the displacement field  $u_{F,0}^\Phi$ . Then, the local FE problem is solved and the corresponding post-computed tractions on  $\Phi_{FB}$  are imposed in turn as Neumann boundary condition on the BE subdomain to solve for displacements. At each iteration, the interface smoothing procedure (relaxation) is applied in

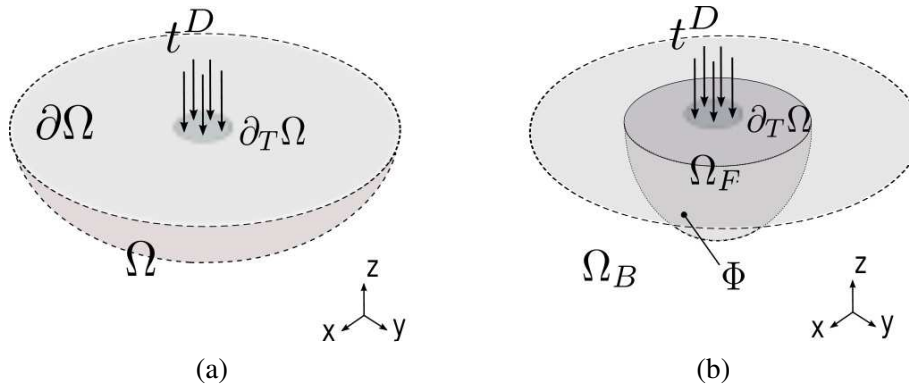


**Figure 3.13:** Time-harmonic load on a semi-infinite space. (a) Initial problem defined in the infinite domain  $\Omega$  and (b) corresponding decomposition in a bounded subdomain modelled by the FEM and the infinite space of propagation modelled by the BEM.  $\Phi$  defines the portion of surface shared by the FE- and the BE-subdomain, i.e.  $\Phi = \partial\Omega_B \cap \partial\Omega_F$ .

the form:

$$u_{F_i,n+1}^\Phi := (1 - \theta)u_{F_i,n}^\Phi + \theta u_{B,n}^\Phi \quad (3.12)$$

The empirical relaxation parameter  $\theta$ , handles the relaxation and it ensures or accelerates the convergence [103]. The relaxer  $\theta$  can either be chosen as constant throughout a computation, or dynamically be determined at each iteration by minimizing the square error functional of interfacial displacements. In this work  $\theta$  has been considered as a constant. The convergence of the interface relaxation (IR) algorithm depends on various factors, namely the mesh density, the geometry, the material properties and of the initial guess of the boundary conditions on the interface. Elleithy et al. [102] studied the convergence conditions for the Lin algorithm in elastostatics, and provided a parametric study allowing the choice of empirical parameters depending on the type of problem.

---

**Algorithm 1** Sequential Dirichlet-Neumann for a surface loading

---

```

1: Initial guess:  $\mathbf{u}_{F,0}^\Phi$  on  $\Omega_F$ 
2: for  $n = 0, k$  do
3:   solve Dirichlet problem on  $\Omega_F$  for  $\mathbf{u}_{F,n}^\Phi$ 
4:   compute corresponding interface tractions  $\mathbf{t}_{B,n}^\Phi$ 
5:   solve Neumann problem on  $\Omega_B$  for  $\mathbf{u}_{B,n}^\Phi$ 
6:   compute relative error  $\zeta_r = |\mathbf{u}_{F,n}^\Phi - \mathbf{u}_{B,n}^\Phi|/|\mathbf{u}_{B,n}^\Phi|$ 
7:   if  $\zeta_r < \epsilon$  then
8:     stop
9:   else
10:    relaxation
11:   end if
12: end for

```

---

### 3.5.3 Interface relaxation algorithm for a far field excitation

Let the domain  $\Omega \in \mathbb{R}^3$  be a heterogeneous viscoelastic body with boundary  $\partial\Omega$ , with the heterogeneities concentrated close to a generic superficial structure. The domain is submitted to an incident time-harmonic plane wave with circular frequency  $\omega$ , see Fig. 3.14.

The algorithm employed to solve the global problem is illustrated in Alg. 2. First, the FMBEM is used to pre-compute the scattered displacement field  $\mathbf{u}_{B_S}$  induced on the boundary  $\Gamma_B \cup \Phi_{BF}$  of  $\Omega_B$  (where  $\Gamma_B = \Omega_B \cap \partial\Omega$ ) by the incident wave. The corresponding solution in terms of total field is obtained by adding the incident wave field to the scattered solution, i.e.  $\mathbf{u}_B = \mathbf{u}_{B_S} + \mathbf{u}_{B_I}$ . Then, after invoking continuity conditions, the restriction  $\mathbf{u}_B^\Phi$  of  $\mathbf{u}_B$  to the interface  $\Phi_{BF}$  is relaxed (by applying the relation (3.12)) and employed as initial guess for the iterative algorithm. At this point, the solution of the problem involves the alternating solution of a local Dirichlet problem in the FE subdomain and of a local Neumann problem in the BE subdomain until convergence of the displacement field on  $\Phi$  is reached. At a given iteration  $n$ , the former implies the solution of the FEM system (3.4) for  $\mathbf{u}_F$ , followed by the computation

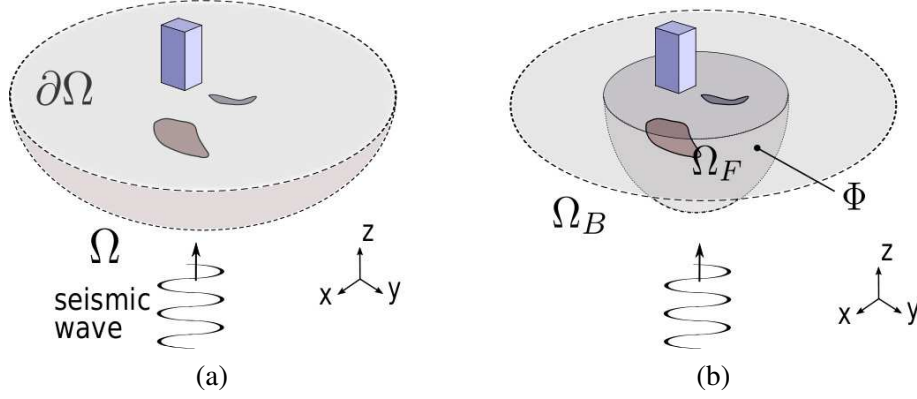


**Figure 3.14:** Incident plane wave coming from a far field excitation source. (a) Initial problem defined in the infinite domain  $\Omega$  with boundary  $\partial\Omega$  and (b) corresponding decomposition in a bounded subdomain modelled by the FEM (containing anisotropies and structures) and the infinite space modelled by the BEM.

of total interface tractions  $\mathbf{t}_{F,n}^\Phi$ . The scattered traction field, given by

$$\mathbf{t}_{FS,n}^\Phi = \mathbf{t}_{F,n}^\Phi - \mathbf{t}_{FI,n}^\Phi, \quad (3.13)$$

is then applied to the BE-interface  $\Phi_{BF}$  after invoking continuity  $\mathbf{t}_{B,n}^\Phi = -\mathbf{t}_{FS,n}^\Phi$ . Alternatively, the total field formulation for the BEM can be used. However, in this work this possibility has not been exploited.

---

**Algorithm 2** Sequential Dirichlet-Neumann for incident wavefield

---

- 1: **Pre-step** define incident wave  $\mathbf{t}_{BS}$  on  $\partial\Omega_B$
  - 2: solve Neumann problem on  $\Omega_B$  for scattered  $\mathbf{u}_{BS}^\Phi$
  - 3: compute total field  $\mathbf{u}_B^\Phi = \mathbf{u}_{BS}^\Phi + \mathbf{u}_{BF}^\Phi$
  - 4: relaxation of  $\mathbf{u}_B^\Phi$
  - 5: **Initial guess:**  $\mathbf{u}_{F,0}^\Phi := \mathbf{u}_B^\Phi$
  - 6: **for**  $n = 0, k$  **do**
  - 7: solve Dirichlet problem on  $\Omega_F$  for  $\mathbf{u}_{F,n}^\Phi$
  - 8: compute corresponding interface tractions  $\mathbf{t}_{F,n}^\Phi$
  - 9: compute the tractions diffracted by the FE subdomain  $\mathbf{t}_{FS,n}^\Phi$ , Eq. (3.13)
  - 10:  $\mathbf{t}_{B,n}^\Phi := -\mathbf{t}_{FS,n}^\Phi$
  - 11: solve Neumann problem on  $\Omega_B$  for  $\mathbf{u}_{B,n}^\Phi$
  - 12: compute relative error  $\zeta_r = |\mathbf{u}_{F,n}^\Phi - \mathbf{u}_{B,n}^\Phi| / |\mathbf{u}_{B,n}^\Phi|$
  - 13: **if**  $\zeta_r < \epsilon$  **then**
  - 14: stop
  - 15: **else**
  - 16: relaxation
  - 17: **end if**
  - 18: **end for**
-



### 3.5.4 Implementation

The iterative nature of the algorithm involves separate computations of the BEM and FEM local problems defined respectively on  $\Omega_B$  and  $\Omega_F$ . A Matlab program called CUSEQ has been written to drive the iterative solution of domain decomposition problems involving either surface loading or far field excitation. Details concerning the program can be found in Appendix D.

In the FE subdomain, the time consumption for the assembly and the factorization of the global damped stiffness matrix  $\mathcal{K}$  of (3.4) increases with the size of the problem. However, as at each iteration only the displacement boundary conditions on  $\Phi$  vary on the  $\Omega_F$  domain, the matrix  $\mathcal{K}$  needs to be evaluated and factorized only once, at the iteration corresponding to the initial guess, then stored in sparse format to squeeze out any zero elements and save memory. Also the vector of generalized forces associated to eventual Neumann BC  $\mathbb{F}_F^T$  (e.g. surface loading) is computed only at the first iteration, then stored. At each iteration and until convergence, only the vector of nodal forces associated to Dirichlet BC  $\mathbb{F}_F^U$  on  $\Phi$  is recomputed in order to update the RHS of (3.4) and solve the linear system for global displacements. In this work, the precision of the algorithm has been set to  $\epsilon = 10^{-3}$ , see Fig. 3.15a.

**Refinement of the iterative algorithms.** The iterative interface relaxation algorithms proposed above have two main drawbacks. The first is that the convergence depends on the chosen value of the relaxation parameter  $\theta$ . This aspect will be investigated in Section 3.5.5. The second consists of the fact that each global iteration a priori requires  $N_{\text{FMBEM}}$  internal GMRES iterations for the fast solution of the BE global system, i.e.  $N_{\text{glob}} \times N_{\text{FMBEM}}$  iterations are needed for a complete computation. This disadvantage can be reduced by setting at each new global iterate the GMRES initial guess to the solution of the previous iterate. This modification is simple to implement and has a strong influence on the acceleration of the convergence process. This is shown for a simple example test in Fig. 3.15b, where the dotted line indicates the convergence acceleration induced by this refinement of the algorithm.

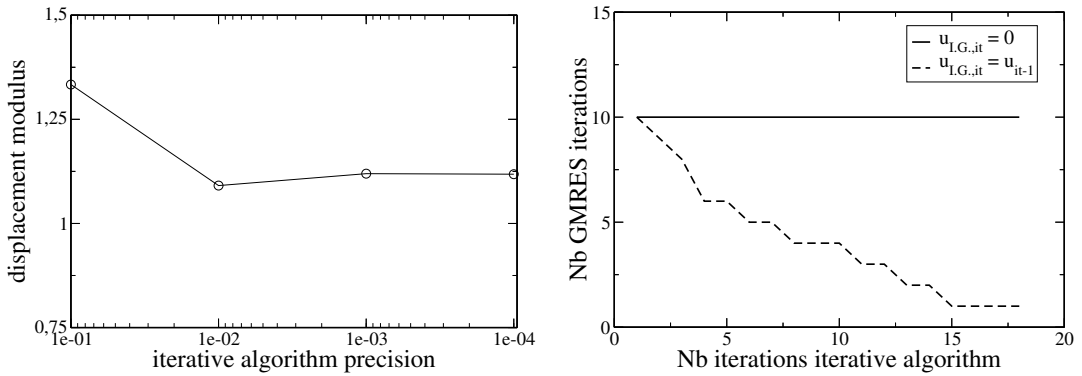


**Figure 3.15:** (a) Study of the precision of the algorithm: ratio  $|u|(\epsilon)/|u|_{ref}$  for the displacement resultant at the canyon edge  $x/R = 1$ . The precision of  $\epsilon = 10^{-3}$  has been imposed as required precision in the iterative algorithm. (b) Number of iterations of GMRES solver when setting the Initial Guess (I.G.) to zero  $u_{I.G.,it} = 0$  or to the solution at the previous iteration  $u_{I.G.,it} = u_{it-1}$ . Results in (a) and (b) refer to the scattering of a vertically incident P-wave by a semi-spherical canyon test.

### 3.5.5 Verification

We now present some verification examples on simple test problems representing the two loading possibilities described above, namely a surface loading and a far field excitation. In each example, the results obtained using CUSEQ have been compared with the solution of the same problem solved by using the pure fast multipole BEM. In fact, the geometries of the chosen examples are deliberately simple to allow the modelling of the same problem by using the FMBEM. The first example consists of a simple time-harmonic load applied on the free-surface of a homogeneous half-space  $\Omega$ . The second is an example of screening of the ground vibrations generated by a superficial load by semi-circular trenches excavated in the ground. The third example consists of the study of the scattering of a vertically-incident seismic wave field by a semi-spherical canyon.

#### Example of surface loading: time-harmonic load on a half-space

Let us consider the case of a time-harmonic load applied on a portion  $\partial_T\Omega$  of the free-surface  $\partial\Omega$  of a homogeneous isotropic linear (visco-)elastic half-space  $\Omega$ , as illustrated in Fig. 3.13. Let the medium be characterized by normalized shear modulus  $\mu = 2$ , Poisson's ration  $\nu = 0.25$  and density  $\rho = 1$ . For a normalized frequency  $\eta_P = k_P/\omega = 0.75$ , results are displayed in the form of contour maps in Figs. 3.16, 3.17 and 3.18. In particular, Fig. 3.17 is an example of the post-processing visualizations that can be performed with existing external codes. CUSEQ is able to read and write data sheets readable by CESAR-LCPC and its post-processing part PEG3D. For a lower frequency example, Fig. 3.18 shows the contour map of FMBEM results side by side with the BE-subdomain coupling results for two different values of damping factor  $\beta = 0$  and  $\beta = 0.1$ .

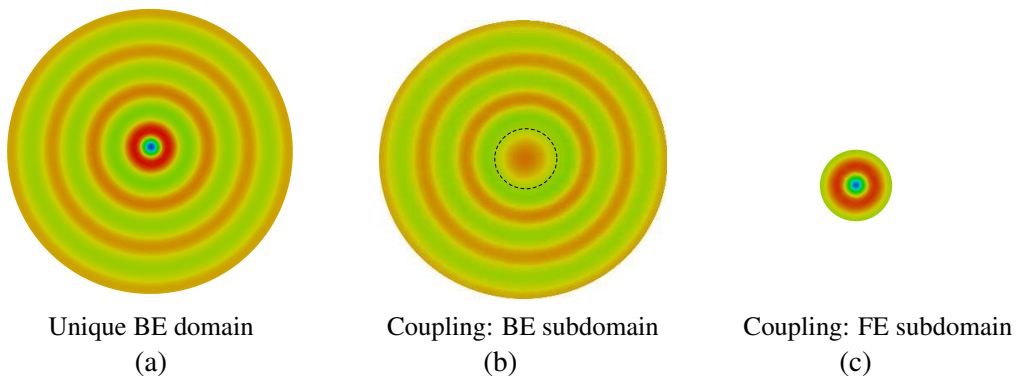


**Figure 3.16:** Time-harmonic load on a half-space. Contour maps of the vertical displacement on the free surface in the plane  $(x,y)$  by using the FMBEM and the proposed iterative FEM/FMBEM coupling. (a) FMBEM results, (b) coupling BEM subdomain results (the semi-spherical cavity due to the absence of the FE subdomain in the middle of the surface is recalled by a dotted line) and (c) coupling FEM subdomain results after convergence.

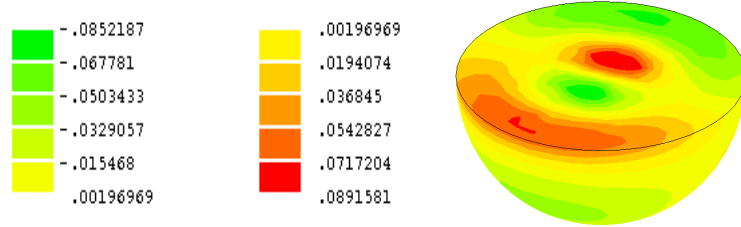


**Figure 3.17:** Time-harmonic load on a half-space. Contour map of the horizontal displacement  $u_x$  in the FE subdomain (post-processing with CESAR-LCPC).

#### Example of surface loading: vibration isolation through semi-circular trenches

A simple problem has been considered to analyse the behaviour of the algorithm and evaluate the effect of the relaxation parameter  $\theta$ . Let  $\Omega$  be a homogeneous isotropic semi infinite medium submitted to a uniform time-harmonic load on the portion of surface  $\partial_T \Omega$ , as depicted in Fig. 3.19a. To test the domain decomposition coupling, the original problem domain is decomposed into two subdomains, as shown in Fig. 3.19b. The semispherical volume  $\Omega_F$  contains the loaded surface and is modelled by FEM. The complementary semi infinite domain  $\Omega_B$  allows the wave

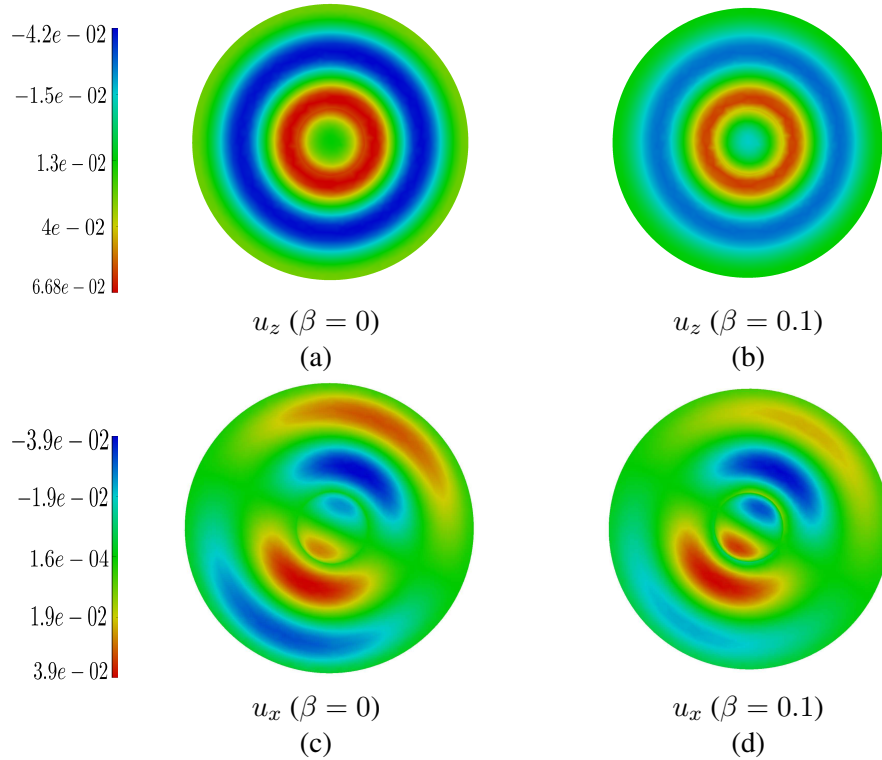


**Figure 3.18:** Time-harmonic load on a half-space. Contour map of the vertical and horizontal displacements  $u_z$  and  $u_x$  on the free surface in the plane  $(x,y)$  for different damping factor  $\beta = 0$  and  $\beta = 0.1$ .

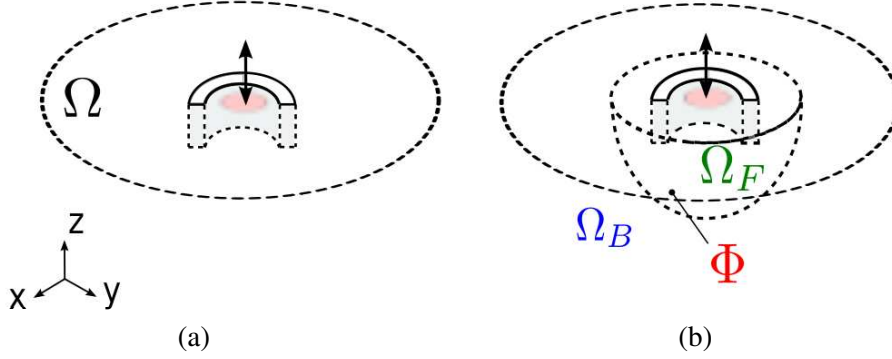


**Figure 3.19:** Vibration isolation through semi-circular trenches: geometry of the problem with notations.

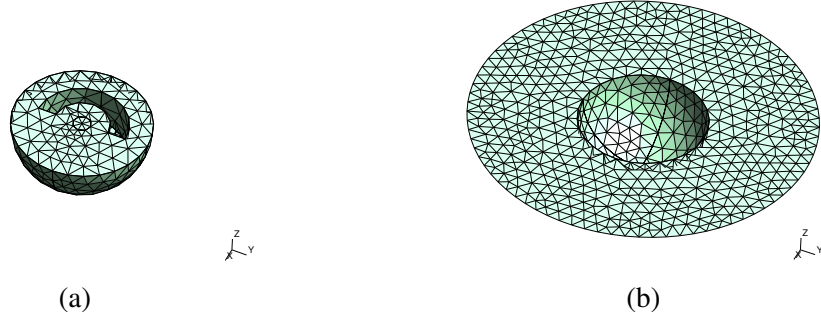


**Figure 3.20:** Vibration isolation through semi-circular trenches: coarse mesh (a) of the FEM subdomain and (b) of the BEM subdomain.

radiation and it is modelled by fast BEM. Again,  $\Omega$  is supposed to involve a single material, characterized by normalized values of the shear modulus  $\mu = 2$ , Poisson's ratio  $\nu = 0.25$  and density  $\rho = 2$ . To assess the accuracy of the solution, the surface displacement field computed on the coupled problem with the sequential iterative algorithm has been compared to the corresponding solution computed by using only the FMBEM method.

Results presented in the following refer to a harmonic load at normalized frequency  $\eta_P = k_P/\pi = 0.5$ . The BE subdomain is discretized with 2,774 three-node triangular elements, and the FE semispherical volume is discretized with 2,560 tetrahedra. The interface  $\Phi = \partial\Omega_B \cap \partial\Omega_F$  is a semi-spherical surface, here discretized with 312 triangular three-node elements. As expected, the relaxation parameter  $\theta$  strongly affects the convergence, as shown in Fig. 3.22 for three values of  $\theta$ . At each  $n+1$  iteration, the interfacial displacement field  $u_{F,n+1}^\Phi$  is updated with a fraction  $\theta$  of the BE subdomain displacement field contribution  $u_{B,n}^\Phi$ . Therefore, when  $\theta$  increases the convergence accelerates. However, there is an upper threshold beyond which convergence is lost. A more detailed parametric study is needed in order to account for the influence of the mesh density or of eventual material heterogeneities.

The increase of intrinsic attenuation in the material accelerates the convergence. Although

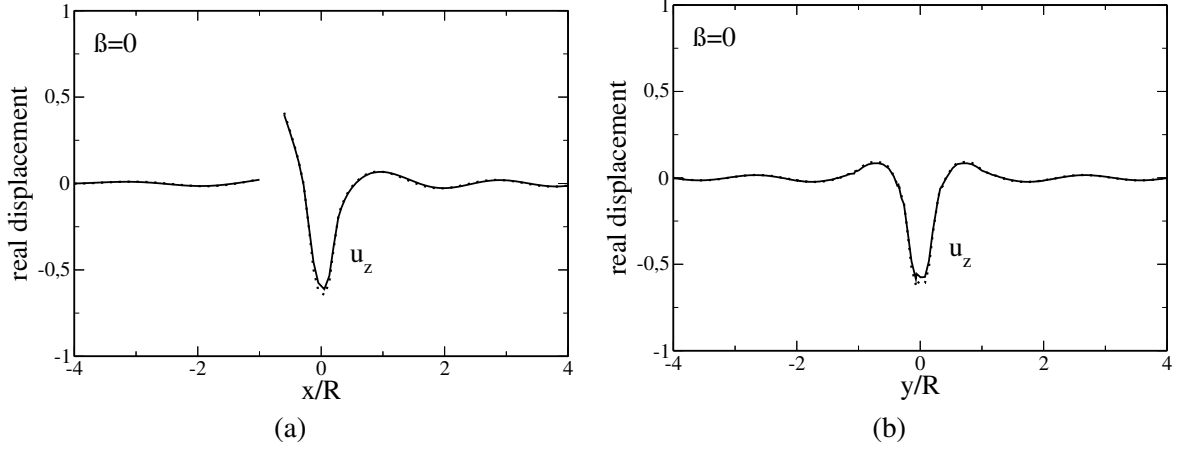


**Figure 3.21:** Vibration isolation through semi-circular trenches. Real part of the surface vertical displacements  $u_z$  along the (a)  $x$  and the (b)  $y$  axis: comparison of results obtained using the interface relaxation FEM/FMBEM coupling (continuous line) and the FMBEM as reference (dotted line).

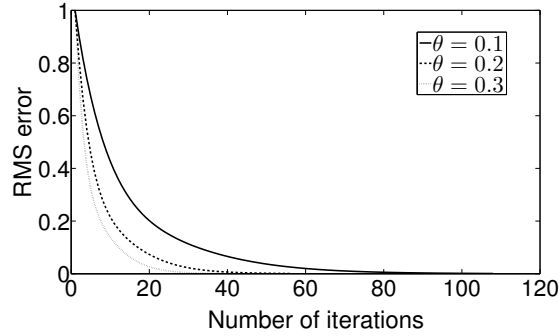


**Figure 3.22:** Time-harmonic load on a semi-infinite space: influence of the relaxation parameter  $\theta$  on the convergence history.

the number of iterations on the interface does not change in the coupling algorithm, the iterative solution of the BE subdomain by fast multipole method is accelerated when  $0 < \beta \leq 0.1$  [140]. In Fig. 3.16, the contour maps of the vertical and horizontal displacements  $u_z$  and  $u_x$  on the BE subdomain surface (with the semi-spherical interface in the middle of the domain)  $\partial\Omega_B$  are depicted for the purely elastic material ( $\beta = 0$ , Fig. 3.16a,c) and the damped material, ( $\beta = 0.1$ , Fig. 3.16b,d). Fig. 3.17 displays the contour map of the horizontal displacements  $u_x$  in the FE volume.

#### Example of far field excitation: scattering by a semi-spherical canyon

To assess the iterative algorithm for far field excitations sources, the canonical problem of the scattering of a vertically incident P-wave on unit amplitude has been considered. A mesh of the model (coarse for the sake of clarity) is displayed in Fig. 3.23. As in the previous examples,

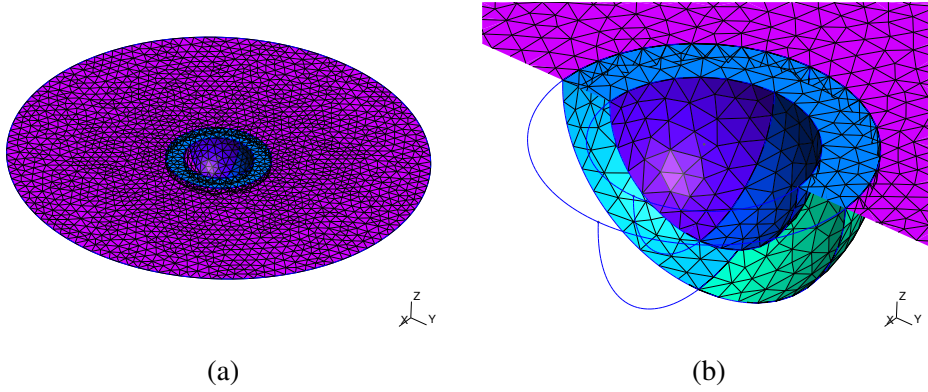


**Figure 3.23:** Scattering of a vertically incident P-wave by a semi-spherical canyon: (a) global mesh and (b) cross section detail of the FE subdomain boundary mesh.

the medium is assumed to be constituted by a single material, which has the same properties of previous verification tests. Two normalized frequencies have been considered, namely  $\eta_P = 0.25$  and  $\eta_P = 0.5$ . The absolute vertical displacement on the positive x-axis are reported in Fig. 3.24 for three values of the damping ratio  $\beta = 0$  (top),  $0.05$  (middle),  $0.1$  (bottom) at normalized frequencies  $\eta_P = 0.25$  (a,c,e) and  $\eta_P = 0.5$  (b,d,f).

### 3.5.6 Conclusions

In this section, a sequential interface relaxation method (IRM) is used to couple the finite element method and the fast-multipole boundary element method (FMBEM) to solve 3D time-harmonic linear elastic problems over unbounded domains. The method is based on a domain decomposition in several disjoint, non-overlapping subdomains. In particular, a bounded region is extracted from the complementary semi-infinite space of propagation. The bounded subdomain is modelled by the finite element method, whereas the half-space where it is embedded is solved by the boundary element method, which formulation allows the exact radiation of the waves in the surrounding soil. At each iteration of the algorithm, a smoothing procedure is applied on the boundary conditions transmitted between the subdomains in order to guarantee and speed up the convergence. The range of the relaxation parameter to obtain convergence has been established for each problem considered, and no empirical parametric studies have been conducted to extrapolate global range of validity. Although in this section only one material has been considered, the algorithm can be easily extended to consider the presence of heterogeneities located inside each subdomain. The presented algorithm deserves further investigations in the near future, oriented in particular towards the modelling of soil-structure interaction problems.

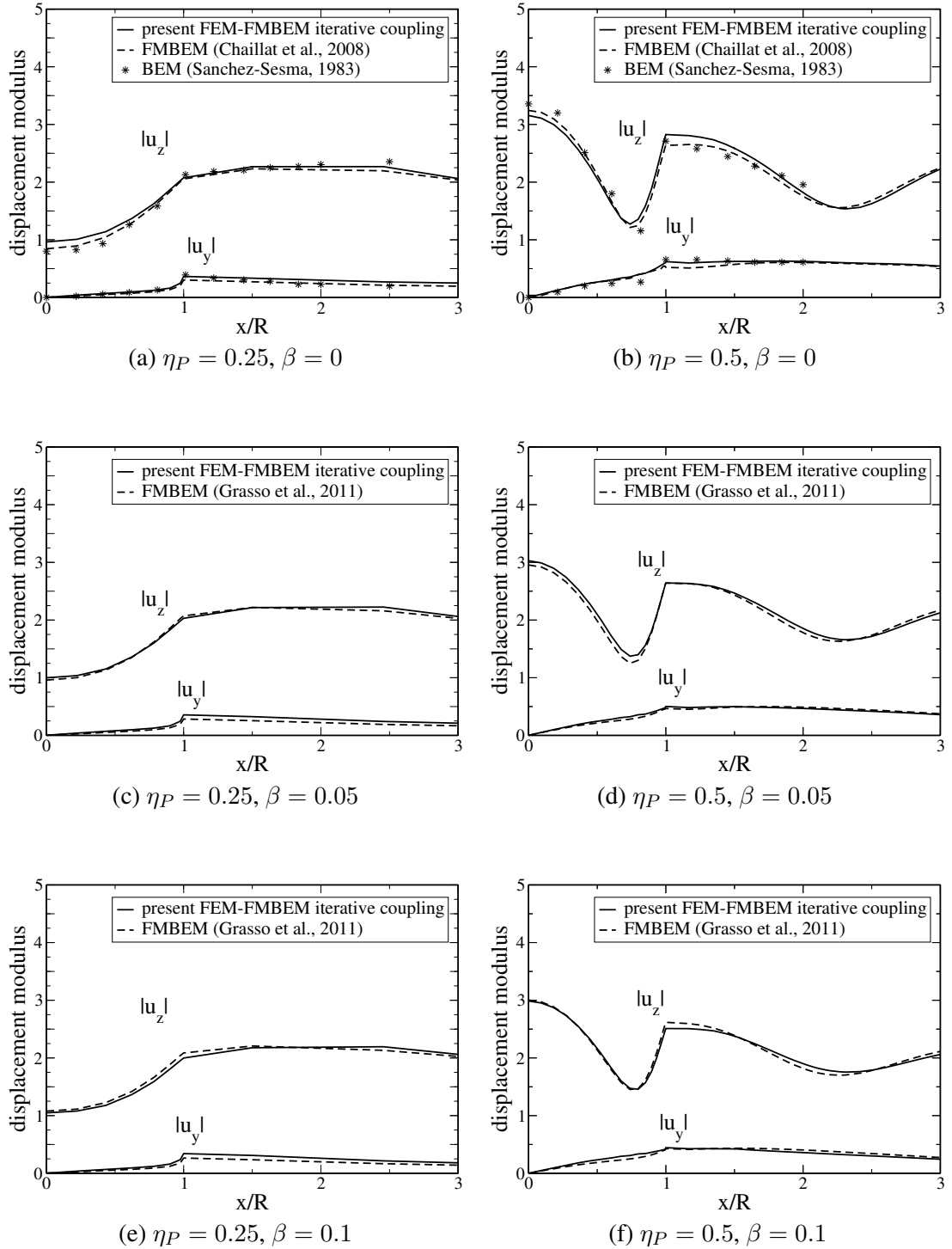


**Figure 3.24:** Scattering of a vertically incident P-wave by a semi-spherical canyon at normalized frequency: surface displacements  $|u_y|$  and  $|u_z|$  for three values of damping ratio  $\beta = 0$  (top), 0.05 (middle), 0.1 (bottom) at normalized frequencies  $\eta_P = 0.25$  (a,c,e) and  $\eta_P = 0.5$  (b,d,f).

### 3.6 SIMULTANEOUS FEM/FMBEM COUPLING

#### 3.6.1 Introduction

The second strategy that has been applied in this thesis for coupling the FEM and the FMBEM is a simultaneous approach based on solving a global system of equations combined with the transmission conditions across the common interface. In particular, we apply a modified version of the approach proposed by Frangi in [120], based on an implicit condensation for the FEM degrees of freedom. The global system is then solved by generalized minimal residual (GMRES). The simultaneous coupling algorithm has been implemented in a Fortran 90 based code called CUPSIM. The capabilities offered by this code and instruction for use are addressed in Appendix D.

For the moment, the study of this approach has been *limited to problems where the load consist in time-harmonic boundary data imposed on a part of the BE-subdomain boundary* (free surface or internal BE boundaries, e.g. cavities embedded in the BE-subdomain). Adaptation of the algorithm to far field excitations requires only minor modifications but it has not been implemented in the present work. Adaptation of the algorithm to problems having a time-harmonic source in the FE-subdomain are slightly more complicated to implement, because the global algorithm needs to be modified.

#### 3.6.2 Domain decomposition for the simultaneous coupling: notation

We now consider the wave propagation problem depicted in Fig. 3.25a, defined in the unbounded domain  $\Omega \in \mathbb{R}^3$  and generated by a time-harmonic distributed load. For simplicity of exposition let  $\Omega$  be a homogeneous domain characterized by a complex shear modulus  $\mu^*$ , density  $\rho$  and Poisson's ratio  $\nu$ . Let us split the original domain into two non-overlapping subdomains, as depicted in Fig. 3.25b. The corresponding interface problem has been described in Sec. 3.4.2. Decomposition can include more than one bounded FE-subdomains. However,

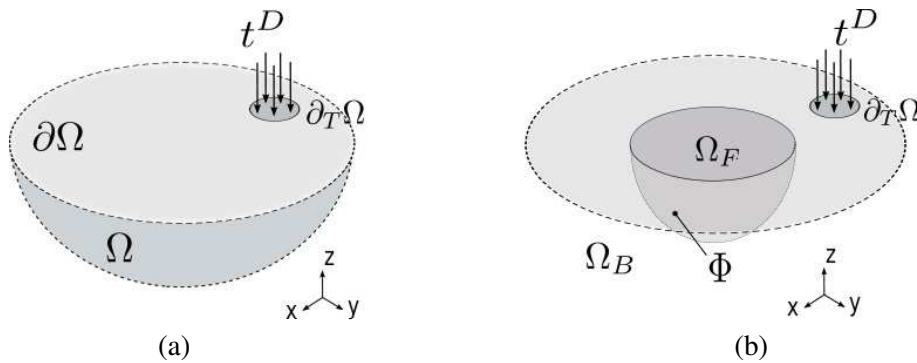


**Figure 3.25:** Time-harmonic load on a semi-infinite space. (a) Initial problem defined in the infinite domain  $\Omega$  and (b) corresponding decomposition in a bounded subdomain modelled by the FEM and the infinite space of propagation modelled by the BEM, separated by the interface  $\Phi$ . The source is assumed to be applied on the boundary of  $\Omega_B$ .



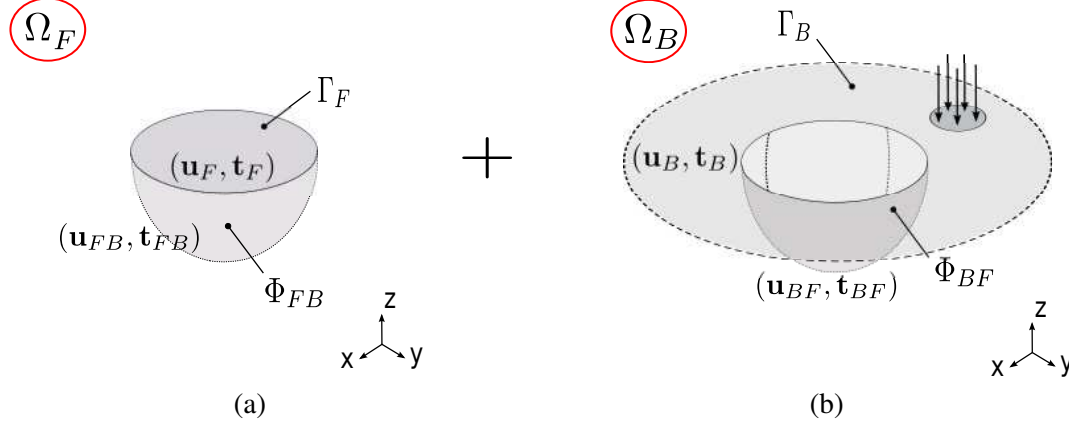


**Figure 3.26:** Subdomains of the domain decomposition shown in Fig. 3.25b: notations of the separation between internal and interface degrees of freedom. (a) FEM subdomain  $\Omega_F$  and (b) BEM subdomain  $\Omega_B$ .

this possibility has been treated later in order to evaluate its influence on the algorithm scalability. The bounded subdomain  $\Omega_F \in \mathbb{R}^3$  has the boundary  $\partial\Omega_F = \Gamma_F \cup \Phi_{FB}$  whereas the BEM-subdomain  $\Omega_B \in \mathbb{R}^3$  has the boundary  $\partial\Omega_B = \Gamma_B \cup \Phi_{BF}$ .

The interfaces  $\Phi_{BF}$  and  $\Phi_{FB}$  refer to the same surface, but to different numerical discretizations of it.  $\Phi_{BF}$  is discretized by three-node BE linear triangles, whereas the three-node linear triangles that discretize  $\Phi_{FB}$  are the trace on  $\Phi$  of the four-node linear tetrahedra coming from the 3-D FEM discretization. Finally, as matching grids are considered on  $\Phi$ ,  $\Phi_{BF}$  and  $\Phi_{FB}$  differ only for the normal orientation (outwarding each subdomain), which is defined by the local elements numbering and cross product.

In the following two subsections, we detail the formulation of the FEM and of the FMBEM for the reference case of Fig. 3.25. Notations in both formulations refer to the separation of the total degrees of freedom (DoFs) between internal and interface degrees of freedom as displayed in Fig. 3.26. On the one hand, vectors  $(\mathbf{u}_F, \mathbf{t}_F)$  collect all DoFs that belong to the volume  $\Omega_F$  except those lying on the interface  $\Phi_{FB}$  (i.e.  $\Omega_F \setminus \Phi_{FB}$ ), these latter being specifically denoted by  $(\mathbf{u}_{FB}, \mathbf{t}_{FB})$ , see Fig. 3.26a. On the other hand, vectors  $(\mathbf{u}_B, \mathbf{t}_B)$  refer to the DoFs belonging to the surface  $\Gamma_B$  and  $(\mathbf{u}_{BF}, \mathbf{t}_{BF})$  to those lying on the interface  $\Phi_{BF}$ , see Fig. 3.26b. DoFs lying on surfaces edge, i.e.  $\Gamma_F \cap \Phi_{FB}$  or  $\Gamma_B \cap \Phi_{BF}$ , are considered as interface DoF, i.e. belonging to  $\Phi_{FB}$  and  $\Phi_{BF}$  respectively.

### 3.6.3 The finite element subdomain

The three-dimensional subdomain  $\Omega_F$  is discretized by four-node linear tetrahedra, each node having three translational DoFs. In the weak formulation (3.3), the vector of all displacement DoFs  $\mathbf{u}$  was split in  $\mathbf{u} = \mathbf{u}^0 + \mathbf{u}^D$  to distinguish unknown displacement DoFs  $\mathbf{u}^0$  from those DoFs imposed by the boundary data  $\mathbf{u}^D$ . In the simultaneous FEM/FMBEM coupling, the load is applied on the BEM surface  $\Gamma_B$ . Thus, there are no imposed displacements nor tractions inside the volume  $\Omega_F \setminus \Phi_{FB}$ , and the internal DoFs  $\mathbf{u}_F$  are therefore always unknown. As

we will see later, the coupling algorithm provides that continuity across  $\Phi_{FB}$  is guaranteed by imposing the displacement field on the interface coming from the adjacent BE-subdomain, i.e.  $\mathbf{u}_{FB} := \mathbf{u}_{BF}$ . After substituting  $\mathbf{u}^0 := \mathbf{u}_F$ ,  $\mathbf{u}^D := \mathbf{u}_{FB}$ ,  $\mathbf{t}^D = 0$  in the weak formulation (3.3), the final linear system reads:

$$\mathcal{K}_F \mathbb{U}_F = \mathbb{F}_F, \quad (3.14)$$

where  $\mathcal{K}_F$  is the dynamic damped stiffness matrix as defined in 3.5,  $\mathbb{U}_F$  is the vector collecting all unknown (internal) degrees of freedom and  $\mathbb{F}_F$  is the vector of generalized forces associated with displacements  $\mathbf{u}_{FB}$  imposed on  $\Phi_{FB}$ . Separation of internal and interface degrees of freedom leads to

$$\begin{bmatrix} \mathcal{K}_F^F & \mathcal{K}_{FB}^F \\ \mathcal{K}_F^{FB} & \mathcal{K}_{FB}^{FB} \end{bmatrix} \begin{Bmatrix} \mathbf{u}_F \\ \mathbf{u}_{FB} \end{Bmatrix} = \begin{Bmatrix} 0 \\ \mathbf{f}_{FB} \end{Bmatrix}. \quad (3.15)$$

### 3.6.4 The boundary element subdomain

The subdomain  $\Omega_B$  has boundary  $\partial\Omega_B = \Gamma_B \cup \Phi_{BF}$ . For a Neumann problem, the traction DoFs are known on  $\Gamma_B$  and unknown on the interface  $\Phi_{BF}$ , whereas displacement DoFs are unknown on the whole  $\partial\Omega_B$ . The boundary integral equation (BIE) (2.7) reads:

$$c_{ik}(\mathbf{x})u_i(\mathbf{x}) + (\text{P.V.}) \int_{\partial\Omega_B} u_i(\mathbf{y})T_i^k(\mathbf{x}, \mathbf{y}; \omega) dS_y - \int_{\partial\Omega_B} t_i(\mathbf{y})U_i^k(\mathbf{x}, \mathbf{y}; \omega) dS_y = 0, \quad (\mathbf{x} \in \partial\Omega_B).$$

where  $U_i^k(\mathbf{x}, \mathbf{y}; \omega)$  and  $T_i^k(\mathbf{x}, \mathbf{y}; \omega)$  are the visco-elastodynamic fundamental solution as defined in (2.42). After the boundary element discretization of  $\partial\Omega_B$ , the following linear system of equations rises:

$$\mathbb{H}_B \mathbb{U}_B - \mathbb{G}_B \mathbb{T}_B = 0,$$

where  $\mathbb{H}_B$  and  $\mathbb{G}_B$  are fully populated, non-symmetric integral operators, and  $\mathbb{U}_B$ ,  $\mathbb{T}_B$  gather all the displacement and traction degrees of freedom. Separating internal and interface degrees of freedom as shown in Fig. 3.26 yields to the collocation BIE:

$$\begin{aligned} c_{ik}(\mathbf{x})u_i(\mathbf{x}) + (\text{P.V.}) \int_{\Gamma_B} u_i^B(\mathbf{y})T_i^k(\mathbf{x}, \mathbf{y}; \omega) dS_y + (\text{P.V.}) \int_{\Phi_{BF}} u_i^{BF}(\mathbf{y})T_i^k(\mathbf{x}, \mathbf{y}; \omega) dS_y \\ - \int_{\Gamma_B} t_i^B(\mathbf{y})U_i^k(\mathbf{x}, \mathbf{y}; \omega) dS_y - \int_{\Phi_{BF}} t_i^{BF}(\mathbf{y})U_i^k(\mathbf{x}, \mathbf{y}; \omega) dS_y = 0, \quad (\mathbf{x} \in \partial\Omega_B). \end{aligned}$$

This, using matrix-notation corresponds to:

$$\begin{bmatrix} H_B^B & H_{BF}^B \\ H_B^{BF} & H_{BF}^{BF} \\ \bar{H}_B^B & \bar{H}_{BF}^B \\ \bar{H}_B^{BF} & \bar{H}_{BF}^{BF} \end{bmatrix} \begin{Bmatrix} \mathbf{u}_B \\ \mathbf{u}_{BF} \end{Bmatrix} - \begin{bmatrix} G_B^B & G_{BF}^B \\ G_B^{BF} & G_{BF}^{BF} \\ \bar{G}_B^B & \bar{G}_{BF}^B \\ \bar{G}_B^{BF} & \bar{G}_{BF}^{BF} \end{bmatrix} \begin{Bmatrix} \mathbf{t}_B \\ \mathbf{t}_{BF} \end{Bmatrix} = \begin{Bmatrix} \mathbf{0} \\ \mathbf{0} \\ \mathbf{0} \\ \mathbf{0} \end{Bmatrix}$$

where the superscript of the integral operators indicates the portion of surface where collocation is performed, and the subscripts indicates the portion of surface where the source lie. Overbars on integral operators (e.g.  $\bar{G}_B^B$ ) indicate that element collocation is performed. Separation of unknowns leads to

$$\begin{bmatrix} H_B^B & H_{BF}^B & -G_{BF}^B \\ H_B^{BF} & H_{BF}^{BF} & -G_{BF}^{BF} \\ \bar{H}_B^B & \bar{H}_{BF}^B & -\bar{G}_{BF}^B \\ \bar{H}_B^{BF} & \bar{H}_{BF}^{BF} & -\bar{G}_{BF}^{BF} \end{bmatrix} \begin{Bmatrix} \mathbf{u}_B \\ \mathbf{u}_{BF} \\ \mathbf{t}_B \\ \mathbf{t}_{BF} \end{Bmatrix} = \begin{bmatrix} \mathbf{b}_B^B \\ \mathbf{b}_B^{BF} \\ \bar{\mathbf{b}}_B^B \\ \bar{\mathbf{b}}_B^{BF} \end{bmatrix}, \quad (3.16)$$

where  $\mathbf{b}_i^j = G_i^j \mathbf{t}_i$  and  $\bar{\mathbf{b}}_i^j = \bar{G}_i^j \mathbf{t}_i$ . The system (3.16) can be written as:

$$\mathbb{K}_B \mathbb{X}_B = \mathbb{B}_B \quad (3.17)$$

### 3.6.5 Simultaneous algorithm for a BE surface loading

To solve the FEM/FMBEM coupled problem we use a modified version of the approach proposed by Frangi et al. for magnetostatics [120], where the problem of a ferromagnetic interior domain surrounded by an unbounded domain containing a current source was studied. In the present work, we use the main idea beyond that approach to couple the FEM and the FMBEM for time-harmonic visco-elastodynamics.

No global FEM/FMBEM system of equations is built. Instead, the FEM system is solved implicitly in the FMBEM system. The displacements on the FE-BE interface  $\Phi$  are chosen as primary unknowns, and continuity across the interface  $\Phi$  is guaranteed by the strong conditions

$$\mathbf{u}_{FB} = \mathbf{u}_{BF}, \quad (3.18a)$$

$$\mathbf{t}_{FB} = -\mathbf{t}_{BF}. \quad (3.18b)$$

The simultaneous algorithm is based on the following steps, see Alg. 3. The system (3.16) is solved iteratively by GMRES. At each iteration  $n$ , the approximation built by GMRES of the interface displacement field  $\tilde{\mathbf{u}}_{BF}^n$  in  $\tilde{\mathbb{X}}_B^n$  is used as boundary condition  $\tilde{\mathbf{u}}_{FB}^n$  for the subdomain  $\Omega_F$  by invoking continuity (3.18a) across the interface. The vector  $\tilde{\mathbb{F}}_F^n$  of nodal forces associated with the imposed displacements  $\tilde{\mathbf{u}}_{FB}^n$  on  $\Phi_{FB}$  is computed. Then, the following FEM system is solved directly:

$$\mathcal{K}_F \tilde{\mathbf{U}}_F^n = \tilde{\mathbb{F}}_F^n, \quad (3.19)$$

where the sparse dynamic damped stiffness matrix  $\mathcal{K}_F$  has been set up and stored in a pre-processing step. The tractions  $\tilde{\mathbf{t}}_{FB}^n$  on the interface elements  $\Phi_{FB}$  are computed from element stresses and substituted back in the GMRES approximated vector  $\tilde{\mathbb{X}}_B^n$  using the condition (3.18b) for the evaluation the fast-multipole matrix-vector product and the computation of the residual. The simultaneous coupling algorithm have been implemented by integrating the FEM and the coupling steps into an existing FMBEM code. Implementation details are addressed in App. D.

**Algorithm 3** Simultaneous coupling algorithm

- 
- 1: **Pre-step** Domain decomposition of  $\Omega$  in non-overlapping  $\Omega_F$  and  $\Omega_B$  (Sec. 3.6.2)
  - 2:       Discretization of  $\Omega_F$  (3-D) and  $\partial\Omega_B$  (2-D), definition of  $\Phi_{FB}$  and  $\Phi_{BF}$
  - 3:       Define and store vector of corresponding interface nodes
  - 4:       Define FEM problem in  $\Omega_F$ , store coordinates and connectivity tables
  - 5:       Set up and store sparse  $\mathcal{K}_F$  and  $\mathbb{F}_F$  (eq.(3.14))
  - 6:       Define FMBEM problem in  $\Omega_B$  and prepare data and geometry input file

**Main algorithm**

- 7: Definition of the FMM-octree for  $\partial\Omega_B$
  - 8: Compute and store BEM near contributions  $\mathbb{K}^{\text{near}}$  and  $\mathbb{F}^{\text{near}}$  (eq.(2.17b))
  - 9: Read stored FEM- $\mathcal{K}_F$ ,  $-\mathbb{F}_F$ , -coordinates and -connectivity tables
  - 10: Initialize GMRES (solution vector and restart parameter)
  - 11: **for**  $n = 0, k$  **do**
  - 12:    Compute  $\tilde{\mathbb{F}}_F^n$  associated with the approximated displacements  $\tilde{\mathbf{u}}_{FB}$
  - 13:    Solve FEM system (3.19)
  - 14:    Compute  $\tilde{\mathbf{t}}_{FB}^n$  and substitute back in  $\tilde{\mathbb{X}}_B^n$
  - 15:    FMM matrix-vector product and compute residual
  - 16:    **if** convergence **then**
  - 17:      stop
  - 18:    **end if**
  - 19: **end for**
- 

**3.6.6 Remark on GMRES accuracy**

The simultaneous FEM/FMBEM coupling algorithm has been implemented in the code CUSIM, which capabilities are detailed in Appendix D.2. We recall that in FMBEM visco-elastodynamics (in the code COFFEE), the tolerance used to stop the iterative solver GMRES was recommended to  $10^{-3}$  [61]. In CUSIM, after numerous computations at different normalized frequencies and for different configurations, this tolerance of GMRES has been set to  $10^{-2}$ . Indeed, with the simultaneous algorithm described above we could not reach better accuracy results. Despite this limitation, the simultaneous coupling algorithm leads to results that are acceptable for the intended applications (i.e. seismic wave propagation, traffic vibrations).

**3.6.7 Verification**

The simultaneous FEM/FMBEM algorithm has been tested on various three-dimensional examples, which have been chosen deliberately simple to allow a direct comparison with FMBEM results. Three general types of material have been defined to simulate various impedance ratios between adjacent media. The corresponding material properties are listed in Tab.3.1. The first example consists of a propagation problem in a homogeneous isotropic linear (visco-)elastic domain. We use this basic test to study the influence of the 3-D FEM inclusion in the homogeneous medium and consequently the influence of the mass matrix definition in the finite element formulation. The following examples introduce heterogeneities inside the FEM subdomain and

Material type	$\mu$	$\nu$	$\rho$	$c_S$
A	2	0.25	2	1
B	$0.5 \mu(A)$	0.2	$0.75 \rho(A)$	0.8
C	$0.16 \mu(A)$	0.3	$0.6 \rho(A)$	0.5

**Table 3.1:** Dimensionless mechanical properties of three types of material used for the validation tests and corresponding shear wave velocity.

at the FE/BE interface  $\Phi$  in order to verify the continuity across the interface in case of strong wave velocity ratio between the subdomains. For each test, the effects of material attenuation on the algorithm accuracy has been examined and compared to the purely elastic cases. Coherently with the weakly dissipation assumption of Chapter 2, values for the damping factor of  $0 \leq \beta \leq 0.1$  have been considered. Three damping factor values  $\beta = 0$ ,  $\beta = 0.05$  and  $\beta = 0.1$  have been used as reference values for the comparison. This study shows a strong improvement on global accuracy and decrease of the FEM numerical dispersion with growing  $\beta$ .

### Wave propagation in a homogeneous half-space

Let  $\Omega \in \mathbb{R}^3$  be a semi-infinite homogeneous isotropic visco-elastic medium with boundary  $\partial\Omega$ , as depicted in Fig. 3.27a. A spatial domain decomposition is applied as shown in Fig. 3.27b, following the decomposition rules and notations introduced in Sec. 3.6.2. As indicator of accuracy we adopt the relative error  $\xi$  between the vertical displacement field computed by the FEM/FMBEM simultaneous coupling ( $u_{\text{CUP}}$ ) and that computed using the FMBEM of reference ( $u_{\text{REF}}$ ) along the x-axis (see Fig. 3.27c):

$$\xi^2 = \sum (|u_{\text{REF}} - u_{\text{CUP}}|^2) / \left( \sum |u_{\text{REF}}|^2 \right). \quad (3.20)$$

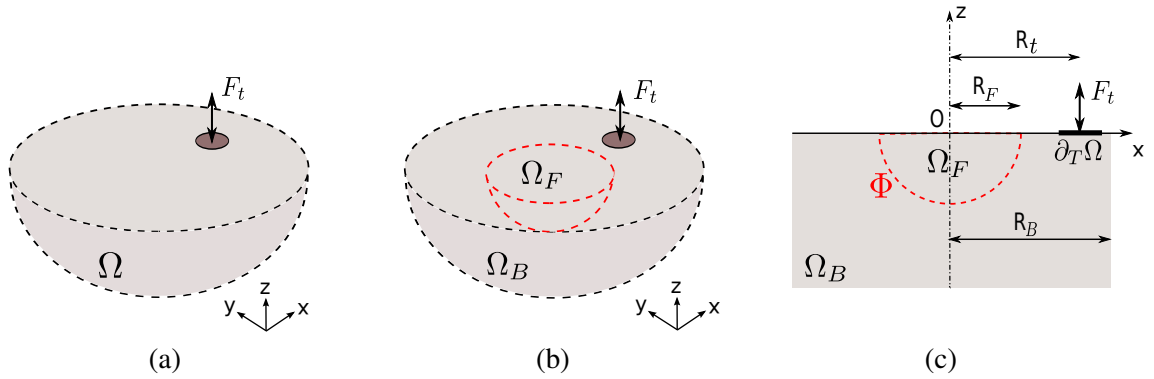


**Figure 3.27:** Time-harmonic load on homogeneous half-space (A-type material), geometry and notation. (a) Initial problem defined in the semi-infinite domain  $\Omega$ , and (b,c) corresponding decomposition in a bounded subdomain modelled by the FEM ( $\Omega_F$ ) and the infinite space of propagation modelled by the BEM ( $\Omega_B$ ).

$\eta_P$	1		
Pts/ $\lambda_S$	10	15	20
$N_{BEM}$	26 766	60 444	115 068
$N_{FEM}$	15 834	46 470	127 818
$N_{T4}$	28 317	87 454	250 306

**Table 3.2:** Time-harmonic load on homogeneous half-space made of A-type material (Fig. 3.27). Reference tests here at normalized frequency  $\eta_P = 1$ . The wavelength is  $\lambda_S = 1.15$  ( $\beta = 0$ ).

Results presented in the following refer to a time-harmonic surface loading at normalized frequency  $\eta_P = k_P R_F / 2\pi = 1$ , where  $R_F$  is the radius of the FEM subdomain. The plane BE-free surface  $\Gamma_B = \Omega_B \cap \partial\Omega$  has been truncated at a distance  $R_B = 4R_F$ . For simplicity, radius  $R_F$  has been chosen of unit length, thus resulting in  $R_B = 4$ . The circular portion of surface  $\partial_T\Omega$  on which time-harmonic tractions are imposed has radius 0.2 and it is located at a distance  $R_t = 2$  from the axis origin. Results presented hereinafter refer to three numerical models which sizes are reported in Tab.3.2 for different choices of mesh density.

**Influence of the mass matrix on attenuation.** Results obtained using the mesh densities of Tab.3.2 are reported in Fig. 3.28. These results have been obtained adopting the consistent mass matrix definition in the FEM formulation. The graphs on the left column display the vertical component of real displacements, whereas those on the right the horizontal components. Graphs (a,b) correspond to the purely elastic case, (c,d) to a viscoelastic medium characterized by damping factor  $\beta = 0.05$  and (e,f) to a viscoelastic medium with  $\beta = 0.1$ . In (a,b), the numerical dispersion introduced by the FEM-subdomain is clearly visible. Using the classical "rule of thumb", i.e. ten points per wavelength, leads to a relative error  $\xi = 0.01$ , as shown in the first column of Tab.3.3. Figure 3.29a,b are a zoom of Fig. 3.28a,b on the abscissae interval that corresponds to the FEM subdomain (i.e.  $-1 \leq x \leq 1$ ). Here, results obtained using three different mesh densities are compared with the reference FMBEM solution. Using 10 points per S-wavelength (p/WL) the numerical dispersion appears in the form of numerical damping (spurious amplitude reduction) and wavelength modification, exactly as defined in Fig. 3.8. Using 15 p/WL improves results and reduces dispersion. The best performance is obviously reached with 20 p/WL, although this choice implies a larger size for the FEM problem and (as a consequence of the matching grid assumption on the interface  $\Phi$ ) for the BEM problem and it therefore slows down computations, as proved in Tab.3.3. The imaginary part of displacements follows the same global trend, as shown in Fig. 3.30.

The numerical dispersion, so apparent in the purely elastic case, tends to reduce with the introduction and growth of the attenuation level. This is shown in Fig. 3.28c-f and quantified in Tab. 3.3 through the relative error  $\xi$ . The number of GMRES iterations reduces with growing  $\beta$ , whereas the CPU time per iteration increases, coherently with the visco-elastodynamics FMBEM results presented in Chapter 2.

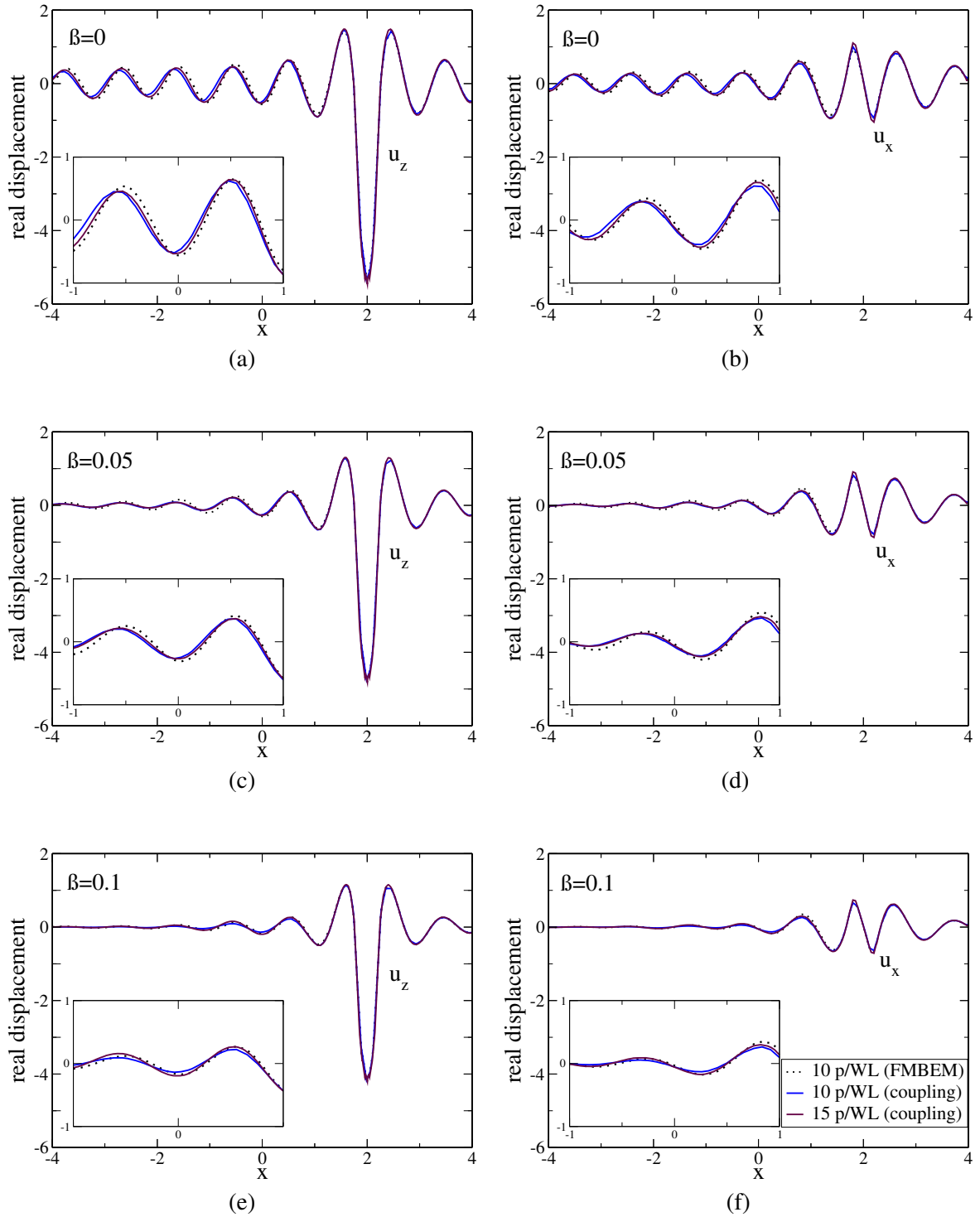


**Figure 3.28:** Time-harmonic load on homogeneous half-space (A-type material), mesh density study. Comparison of the real vertical  $u_z$  (left) and horizontal  $u_x$  (right) displacements along the  $x$ -axis computed by the FMBEM and by the simultaneous FEM/FMBEM coupling using different number of points per wavelength, 10, 15 p/WL and the consistent mass matrix formulation. The subplots are closer views on the portion of surface modelled by FEM ( $-1 \leq x \leq 1$ ). The damping factor worth  $\beta = 0$  in (a,b),  $\beta = 0.05$  in (c,d) and  $\beta = 0.1$  in (e,f).

FEM Mass matrix Pts/ $\lambda_S$	$M_{consist}$			$M_{lump}$		
	10	15	20	10	15	20
$\beta = 0$						
Nb. Iter	18	18	18	19	18	18
CPU/Iter. [sec]	14	58	170	16	59	100
$\xi$	0.01	0.05	0.046	0.06	0.044	0.042
$\beta = 0.05$						
Nb. Iter	13	13	14	13	13	13
CPU/Iter. [sec]	20	51	256	23	74	240
$\xi$	0.051	0.047	0.045	0.039	0.037	0.034
$\beta = 0.1$						
Nb. Iter	10	11	12	10	10	11
CPU/Iter. [sec]	19	71	310	29	58	247
$\xi$	0.027	0.025	0.024	0.024	0.023	0.021

**Table 3.3:** Time-harmonic load on homogeneous half-space made of A-type material (problem of Fig. 3.27; model properties are detailed in Tab.3.2) at normalized frequency  $\eta_P = 1$ : comparison of results obtained using two different formulations for the FEM mass matrix. The GMRES accuracy is  $\epsilon = 10^{-2}$  (coupling) and  $\epsilon = 10^{-3}$  (FMBEM).

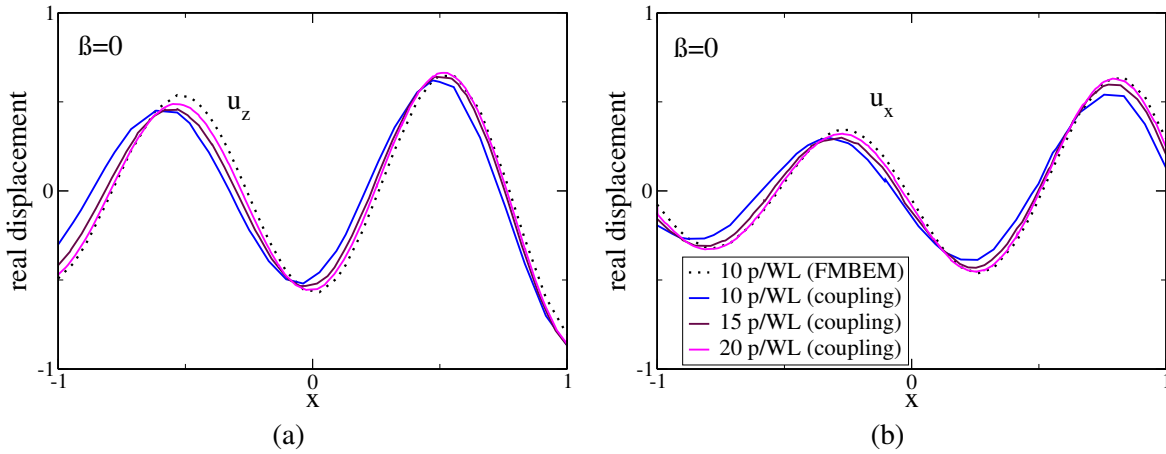


**Figure 3.29:** Time-harmonic load on homogeneous half-space (A-type material), mesh density study. Zoom of the previous Fig. 3.28a,b on the case  $\beta = 0$  on the FEM subdomain surface  $(-1 \leq x \leq 1)$ .

**FEM dispersion and influence of the mass matrix.** Using different formulations of the FEM mass matrix is observed to influence the FEM numerical dispersion described in the previous paragraph. In Fig. 3.31, the results obtained considering the consistent and the lumped mass matrices are compared, the mixed mass matrix oscillating between the two curves as a function of the coefficient  $\alpha$ , see Sec. 3.9. For this specific example, this picture shows that the lumped matrix displays a lower numerical dispersion than the consistent formulation. Indeed, although the amplitude reduction is similar, the lumped matrix fits slightly better the FMBEM wavelength of reference.



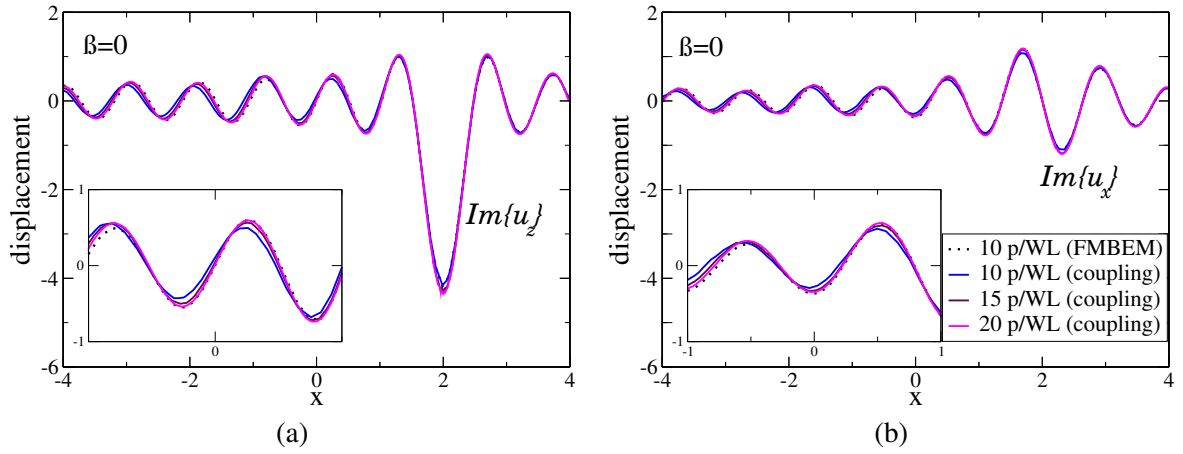


**Figure 3.30:** Time-harmonic load on homogeneous half-space (A-type material), mesh density study. Plot of imaginary part of displacements for  $\beta = 0$  with a zoom on the FEM subdomain surface ( $-1 \leq x \leq 1$ ).

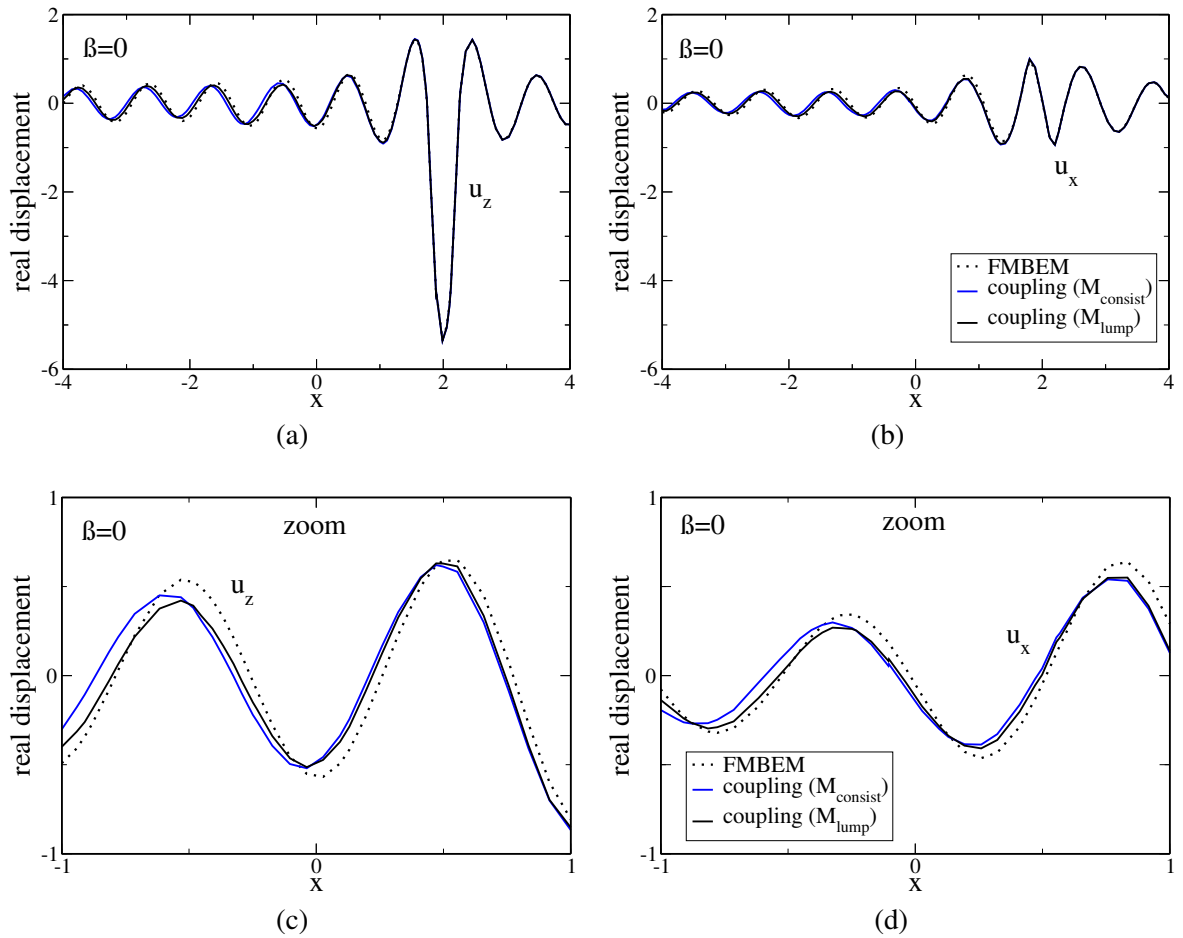


**Figure 3.31:** Time-harmonic load on homogeneous half-space (A-type material). Comparison of the real (a) vertical  $u_z$  and (b) horizontal  $u_x$  displacements along the x-axis computed by the FMBEM (dotted line) and by the simultaneous FEM/FMBEM coupling using different formulations for the mass matrix (consistent in solid blue line and lumped in solid black line). A zoom on the portion of surface modelled by FEM (i.e.  $-1 \leq x \leq 1$ ) is reported in (c,d).

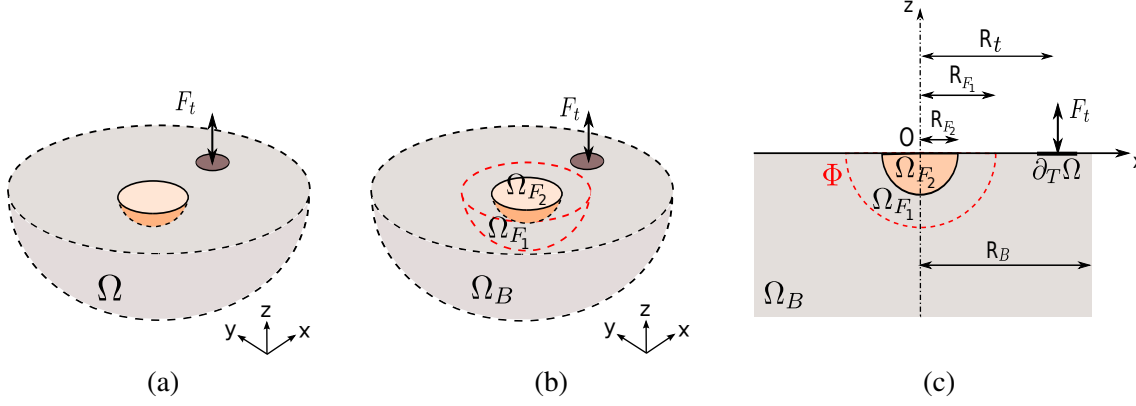


**Figure 3.32:** Time-harmonic load on a homogeneous half-space containing a soft superficial basin. The basin has C-type material properties, the surrounding soil has A-type properties.

### Wave propagation in a homogeneous half-space containing a soft inclusion

Let now  $\Omega \in \mathbb{R}^3$  be a semi-infinite homogeneous isotropic visco-elastic medium with A-type mechanical properties containing a soft inclusion (e.g. a basin) of C-type properties, as depicted in Fig. 3.32a. The geometry of the load surface is the same of the previous example, i.e.  $R_{F_1} = 1$ ,  $R_B = 4$  and  $R_t = 2$ . The soft inclusion has semi-spherical shape with radius  $R_{F_2} = 0.5$ . The spatial domain decomposition is shown in Fig. 3.32b. The relative error  $\xi$  is again employed as indicator of accuracy between the vertical displacement field computed by the FEM/FMBEM simultaneous coupling and the reference FMBEM displacement field along the x-axis (as defined in (3.20)). Results presented hereinafter refer to a time-harmonic surface loading at normalized frequency  $\eta_P = k_P R_{F_1} / 2\pi = 1$  in the homogeneous unbounded domain  $\Omega_B$ .

The mesh sizes of the employed numerical models are listed in Tab.3.4. As in the previous example, the case of purely elastic media displays higher numerical dispersion than the case of lossy media. This is shown in Fig. 3.33 and quantified in Tab.3.5 where the consistent mass matrix has been adopted. Fig. 3.34 shows the contour plot of the vertical and horizontal displacements in the x-y plane. The little circular solid line centered in the origin is the soft basin, whereas the dotted line is the trace of the interface  $\Phi$  on the plane free surface.

$\eta_P$	1
Pts/ $\lambda_S$ (basin)	10
$N_{BEM}$	165 816
$N_{FEM}$	161 832
$N_{T4}$	352 200

**Table 3.4:** Reference tests for the vibration problem of a homogeneous half-space containing a soft superficial basin. The degrees of freedom in each domain are reported for the case at normalized frequency  $\eta_P = 1$  and 10 points per  $\lambda_S$  in the basin region.

$(\beta_{soil}, \beta_{basin})$	(0,0)	(0.05,0.1)
Nb. Iter	14	11
CPU/Iter. [sec]	25	30
$\xi$	0.056	0.027

**Table 3.5:** Results in term of CPU time per iteration and number of iterations for a purely elastic and a pure viscoelastic problem ( $\beta_{soil} = 0.05$  and  $\beta_{basin} = 0.1$ ).

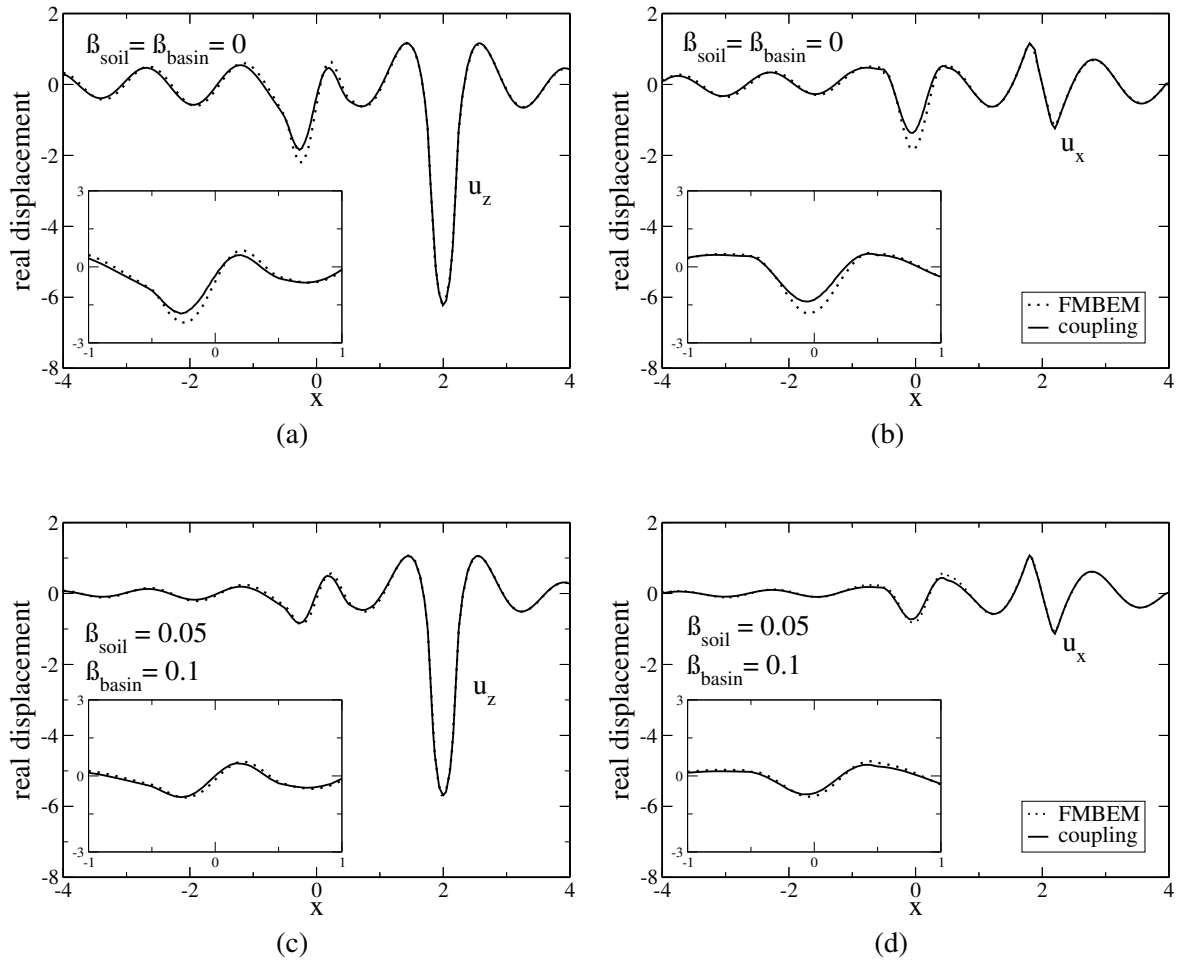


**Figure 3.33:** Time-harmonic load on a homogeneous half-space containing a soft superficial basin. The wave velocity in the soil worth  $c_S(soil) = 2 c_S(basin)$ . The plot displays real vertical  $u_z$  and horizontal  $u_y$  displacements along the  $x$ -axis at normalized frequency  $\eta_P = 0.75$ . In (a),(b) ( $\beta_{soil} = \beta_{basin} = 0$ , in (c) and (d)  $\beta_{soil} = 0.05$  and  $\beta_{basin} = 0.1$ .

#### Wave propagation in a homogeneous half-space containing a soft inclusion: contrast at the interface $\Phi$

Let now consider again the problem of a C-type soft inclusion embedded in a homogeneous half space having A-type material properties. Let increase the radius of the basin to  $R_{F1} = R_{F1} = R_F$ ,

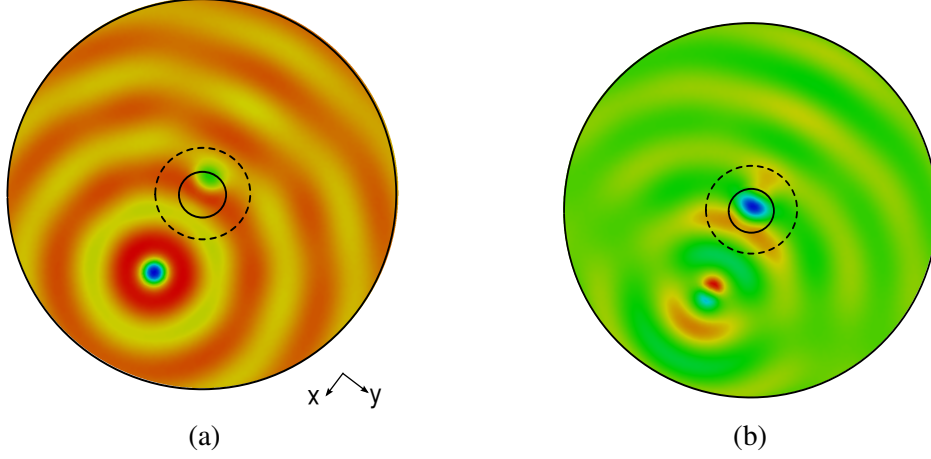


**Figure 3.34:** Time-harmonic load on a homogeneous half-space containing a soft superficial basin. Contour of the real vertical (a) and horizontal (b) displacements ( $\beta = 0$ ,  $\eta_P = 0.75$ ).

as shown in Fig. 3.35a. In this case, the interface between different media coincides completely with the FE/BE interface  $\Phi$ . The results in terms of real displacement field obtained by using the consistent and the lumped matrices are plotted and displayed in Fig. 3.36. In the purely elastic case, the best approximation is clearly given by the lumped mass matrix, that reaches a largely better accuracy w.r.t. the consistent mass matrix. In the case of lossy media, this disparities in accuracy caused by the choice of the mass matrix formulation attenuate. In Fig. 3.37, we report only results obtained with a consistent mass definition. The following Fig. 3.38 is a zoom on the interval  $-1 \leq x \leq 1$  and the real displacement amplitudes using the consistent, mixed and lumped mass matrix are compared.

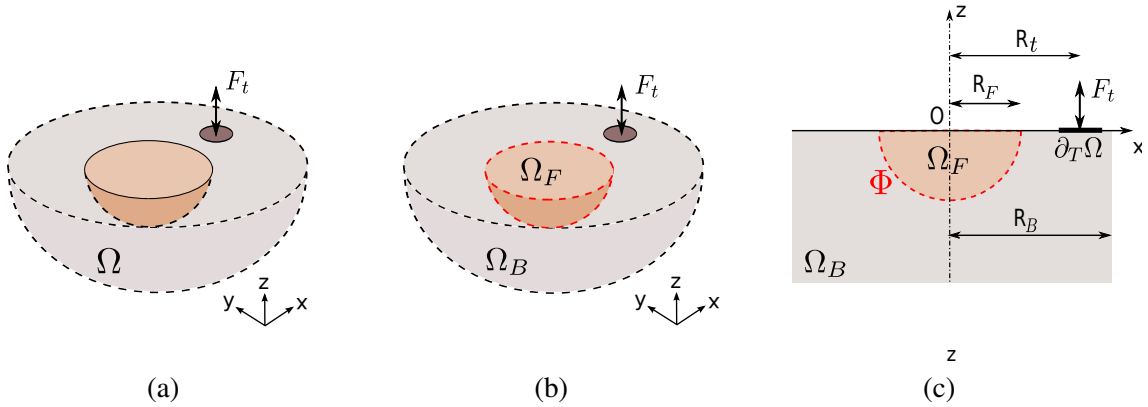


**Figure 3.35:** Time-harmonic load on a homogeneous half-space (of A-type material) containing a soft superficial basin (of C-type material). Here, the heterogeneity boundary coincides with the interface  $\Phi$ .

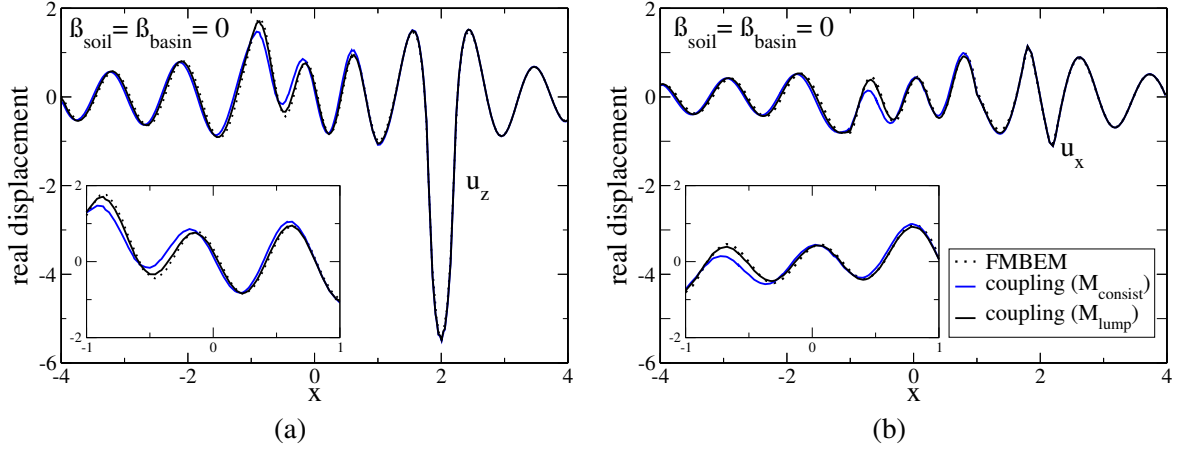


**Figure 3.36:** Time-harmonic load on a homogeneous linear elastic half-space containing a soft superficial elastic basin. Real vertical  $u_z$  and horizontal  $u_x$  displacements are depicted along the  $x$ -axis for  $\beta = 0$  and  $\eta_{PB} = 1$  in the unbounded BEM domain. The soft basin is discretized with ten points per wavelength. Results obtained by using the consistent mass matrix (solid blue line) and the lumped mass matrix (solid dark line).

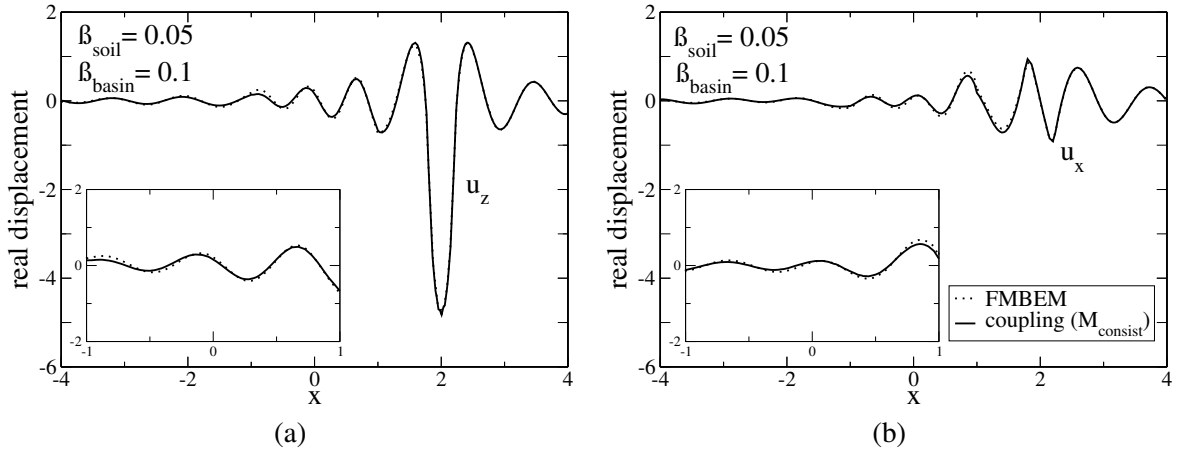


**Figure 3.37:** Time-harmonic load on a homogeneous viscoelastic half-space containing a soft superficial lossy basin. Real vertical  $u_z$  and horizontal  $u_x$  displacements along the  $x$ -axis at normalized frequency  $\eta_{PB} = 1$  in the unbounded BEM domain and  $\eta_{PF} = 1.3$  in the FEM basin. Damping factors is worth  $\beta_{soil} = 0.05$  and  $\beta_{basin} = 0.1$ .

### 3.6.8 Straightforward improvements

The simultaneous coupling is a very promising approach. Due to time constraints, the code that we implemented is for the moment limited to surface loading sources applied on the BEM subdomain boundary. However, only minor modifications are needed to extend CUSIM to the following features.

1. *Multi-BE region problem.* As CUSIM is an hybrid code based on the FMBEM code COFFEE, the BE-BE coupling strategy that enables multi-region BEM problems is al-

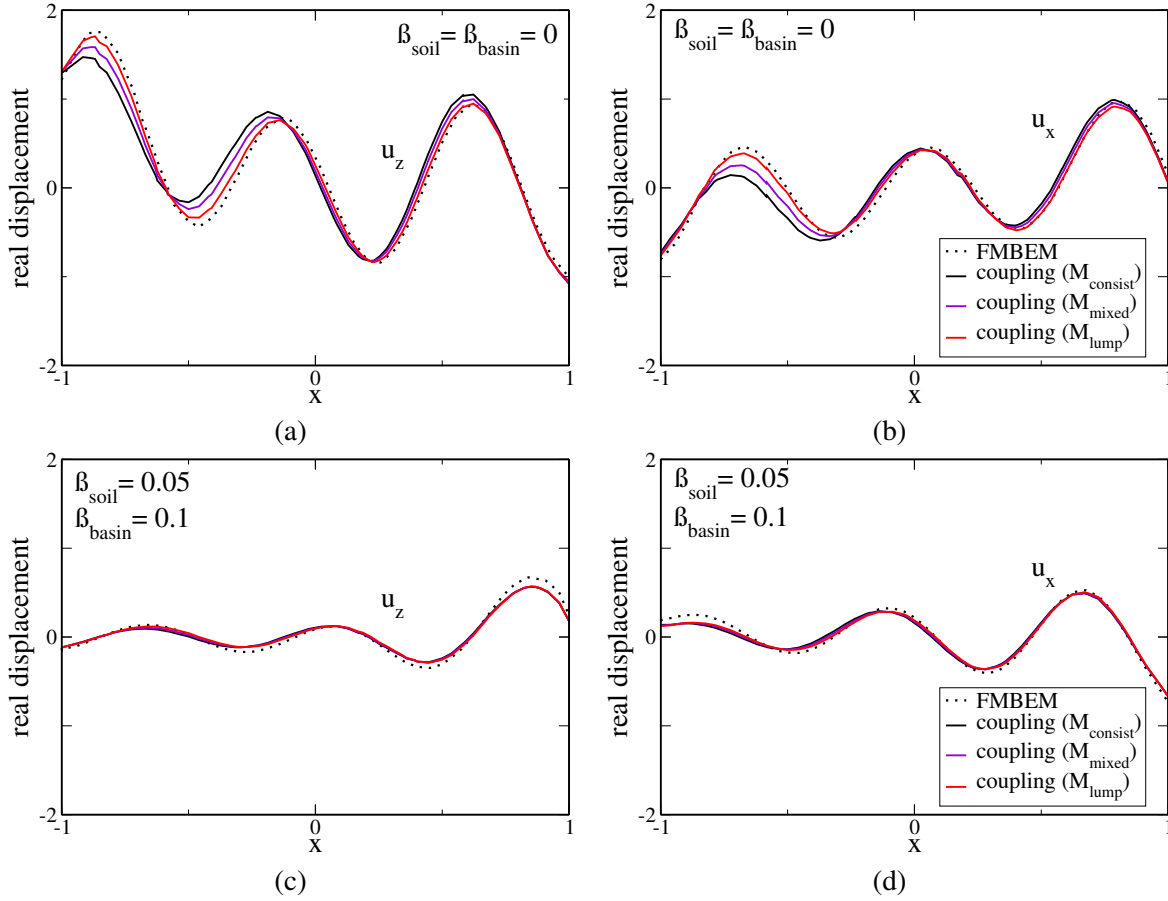


**Figure 3.38:** Zoom on the vertical  $u_z$  and horizontal  $u_x$  displacements along the  $x$ -axis (the segment that intersect the FEM subdomain, i.e.  $-1 \leq x \leq 1$ ) for the example of Fig. 3.35. The soft basin is discretized with ten points per wavelength. The dotted line traces the reference solution obtained using the pure multi-region FMBEM, the solid lines represents the solution of the FEM/FMBEM coupling obtained by using three different definitions of the mass matrix: the consistent mass matrix (black), the mixed matrix (purple) and the lumped mass matrix (red).

ready implemented. The corresponding subroutines should only be updated with minor modifications in order to be validated.

2. *Far field excitation problems.* As for the multi-BE region problem, the extension of incident wave-field (i.e. to the total field formulation) is straightforward, needing only little modifications in order to be validated.
3. *Sources located in the FEM subdomain.* If non-zero tractions BC are prescribed in the FEM subdomain, the coupling algorithm should be slightly modified.
4. *Dialogue with an external FEM code.* The use of an external, dedicated FEM code has the important advantage to give total freedom in the modelling of the FEM subdomain (e.g. account for different types of finite elements, complex geometry details, etc). The

main capability required to the FEM code is to be able to execute the following duties *separately* on demand: (i) set up and return the dynamic stiffness matrix, (ii) compute and return the vectors of nodal forces associated to prescribed traction and displacements, (iii) solve the FEM linear system and return the solution, (iv) compute the stress tensor from the nodal displacement solution and return the corresponding tractions on the surface shared with the BEM subdomain (i.e. the interface  $\Phi$ ). This step is not difficult to put into practice and will strongly enhance the potentiality of the simultaneous coupling.

### 3.6.9 Conclusions

In this Section, a simultaneous approach to couple the finite element method and the fast-multipole boundary element method has been proposed to model three-dimensional visco-elastodynamics problems in unbounded domains. The algorithm is based on the fast solution of the BEM global system of equations and by an implicit condensation of the FEM internal degrees of freedom performed at each global GMRES iteration. This approach has been applied on examples having very simple shapes in order to allow an easy comparison with the reference results obtained with the FMBEM method. This algorithm has proved to be stable after the introduction of various forms of heterogeneities, including strong material contrast at the FE/BE interface. Introduction of complex structures of heterogeneities in the subdomain  $\Omega_F$  is straightforward and do not need modifications of the implemented code (CUSIM, detailed in App. D.2).

## 3.7 PERSPECTIVES

The present work has extended the capabilities of the FMBEM fast solver for 3-D frequency-domain elastodynamics originally developed by Chaillat (COFFEE) [61] in two directions. Firstly, to account for a more realistic material behavior, the FMBEM has been adapted to visco-elastodynamics through a complex-wavenumber formulation. This first step has enabled to model wave propagation problems in unbounded, isotropic linear visco-elastic media. Secondly, the FMBEM has been coupled with the FEM through a simultaneous algorithm, opening to the modelling of more complex media. The promising results obtained are encouraging. Further efforts will be devoted on the one hand to the introduction of a non-conforming FEM/FMBEM coupling, on the other hand to introduce more complex formulations for the soil material, e.g. possibly non-linearities or anisotropies confined in the FEM subdomain and poro-elastodynamics.

**Non-conforming coupling.** In the engineering practice it is often desirable that the meshes of two adjacent regions do not match, because this relaxes significantly the constraints imposed on the mesh generation. Non-matching grids are preferable for time-dependent problems, jumps of mechanical properties (that involves the over-refinement of stiffer regions), corner singularities, local anisotropies, etc. The combination of different discretization schemes on non-overlapping

subdomains or the coupling between non-matching grids typical of overlapping subdomains lead to non-conforming grids which can be analysed in the framework of mortar methods. In the case of non-overlapping subdomains, a mortar finite element space is defined on the non-matching interface and continuity of the trace of the solution is enforced by Lagrange multipliers [316]. The mortar element method was originally introduced by Maday [215], whereas the formulation with Lagrange multipliers was proposed later by Ben Belgacem [33].

Recently, Fisher and Gaul have employed a mortar-type approach for coupling the FEM with the fast multipole BEM using Lagrange multipliers on the coupling interface for studying acoustic-structure interaction [115]. In linear elastodynamics, Lagrange multipliers have been used to couple the FEM and the BEM for example in [262]. In fact, the use of these approaches offers the important advantage that non-conforming discretizations can be coupled. In the present work we used conforming coupling with interface matching grids. As a consequence, problems presenting high contrast in material properties at the FEM/BEM interface may be characterized by over-refinements.

Let us consider the problem of wave propagation in a soft basin of C-type material embedded in a "stiffer" half-space of A-type material (stiff soil). The shear-velocity ratio between the two regions is  $c_S^{soil}/c_S^{basin} = 2$ . The interface  $\Phi$  separating the FEM and the BEM subdomains can be defined (i) inside the homogeneous semi-infinite space (as in Fig. 3.32) or (ii) coincident with the heterogeneity interface as in Fig. 3.35. In the latter case, to respect the "rule of thumb" in the FEM subdomain one would have 20 pt/WL in the BEM subdomain, resulting in a useless computational burden. In fact, using conforming coupling leads to a total size of  $N_{conf} = N_B + N_F = 2 N_F$  ( $N_F$  and  $N_B$  denoting the size of the FEM and of the BEM discretized local problems respectively). Non-conforming coupling would lead to  $N_{non-conf} = N_F + N'_B$  (with  $N'_B \ll N_B$ ).

This drawback can be partially overcome by avoiding that the coupling interface  $\Phi$  coincide with the boundary of a strong heterogeneity (the above case (i)). In this case, variable densities can be used for the FEM subdomain mesh (finer in the inclusion, coarser at the FEM interface  $\Phi_{BF}$ ), as shown in Fig. 3.39. As explained in Sec. 3.6.8, further improvements of the present work include enabling the simultaneous coupling algorithm to completely dialogue with an external FEM code. This will allow more flexibility in the choice of the finite elements (possible coupling of different finite elements, e.g. beam elements, within the FEM subdomain), and will further smooth the limitation of interface matching grids.

**Material non-linear behavior.** Depending on the level of attained strain, materials can display non-linearities. The more simple approach to account for non-linearities is to employ a linear equivalent approach. A brief survey of how to deal inelasticity within the boundary element method is addressed in Sec. 1.5.3.

**Material anisotropy.** Anisotropy of soil materials, i.e. the directivity of the mechanical properties, reflects the history of the medium (deposition, deformation, consolidation, etc). The



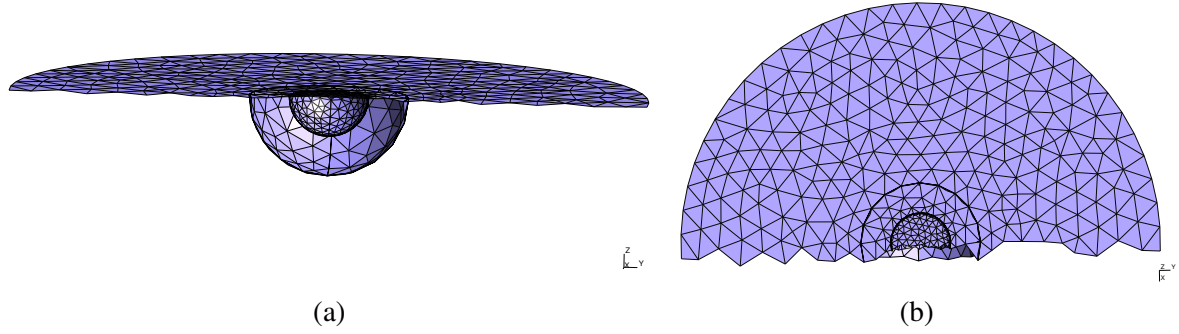


**Figure 3.39:** Conforming coupling: clipping of the FEM mesh refinement of a soft inclusion embedded in a stiffer half-space (see the problem of Fig. 3.32). View of the clipping in the  $Y, Z$  (a) and in the  $X, Y$  (b) planes (for clarity, only a 2-D mesh of the FEM mesh is drawn).

description of an anisotropic elastic material requires the specification of 21 elastic constants (whereas purely isotropic materials need only 2 of them). These are difficult to be empirically determined. However, the possible presence of symmetry planes may considerably reduce their number (e.g. the transverse anisotropy requires only 5 constants) [318]. Simple anisotropic behavior could be easily introduced in the simultaneous FEM/FMBEM coupling presented in this work.

**Poro-elastodynamics.** In the practice, the soil is often assimilate to a viscoelastic continuum. However, its multi-phase nature (viscoelastic soil particles interacting with the surrounding fluid phase) can be taken into account through poroelastic formulations. The first consistent theory of wave propagation in fluid-saturated solids was provided by Biot [41]. Poro-elastodynamics FEM formulations can be used for bounded domains [329]. To solve wave propagation problems in unbounded domains, the finite element method can be coupled with the infinite elements [183, 234] or with the boundary element method [204, 224, 273].



## Appendix A

# Numerical evaluation of the spherical Hankel functions with complex-argument

### Contents

---

A.1 Spherical Hankel functions . . . . .	116
A.2 Numerical evaluation of spherical $h_n^{(1)}(z^*)$ with complex argument . . . . .	117
A.3 The Helmholtz Green's function expansion . . . . .	119

---

Chapter 2 addresses the application of the time-harmonic fast multipole boundary element method (FMBEM) to 3-D visco-elastodynamics under the assumption of weakly dissipative media, i.e. damping factor  $0 \leq \beta \leq 0.1$  (see sec.2.3). A key aspect in this work is the numerical evaluation of the complex-wavenumber  $k^*$  Helmholtz Green's function truncated expansion as defined in (2.45) and (2.46) and recalled here for simplicity:

$$\begin{aligned} \bar{G}(r; k^*) &= \lim_{L \rightarrow +\infty} \bar{G}_L(r; k^*), \\ \bar{G}_L(r; k^*) &:= \int_{\hat{\mathbf{s}} \in \mathcal{S}} e^{ik^* \hat{\mathbf{s}} \cdot (\mathbf{y} - \mathbf{y}_0)} \bar{\mathcal{G}}_L(\hat{\mathbf{s}}; \mathbf{r}_0; k^*) e^{-ik^* \hat{\mathbf{s}} \cdot (\mathbf{x} - \mathbf{x}_0)} d\hat{\mathbf{s}}, \end{aligned} \tag{A.1}$$

where  $\mathcal{S} = \{\hat{\mathbf{s}} \in \mathbb{R}^3, \|\hat{\mathbf{s}}\| = 1\}$  is the unit sphere and the transfer function  $\bar{\mathcal{G}}_L(\hat{\mathbf{s}}; \mathbf{r}_0; k^*)$  is given by

$$\bar{\mathcal{G}}_L(\hat{\mathbf{s}}; \mathbf{r}_0; k^*) = \frac{ik^*}{16\pi^2} \sum_{\ell=1}^L (2\ell + 1) i^\ell h_\ell^{(1)}(k^* \mathbf{r}_0) P_\ell(\hat{\mathbf{s}} \cdot \hat{\mathbf{r}}_0). \tag{A.2}$$

Main observations and results concerning the FMBEM are discussed in Chapter 2. In this Appendix, we give some details about the free space Helmholtz Green's function expansion (A.1) and its numerical evaluation in the presence of real- and complex-valued wavenumber.

### A.1 SPHERICAL HANKEL FUNCTIONS

In visco-elastodynamics, the numerical evaluation of the truncated expansion (A.1) of the Helmholtz Green's function requires the evaluation of the spherical Hankel function  $h_\ell^{(1)}(k^*r_0)$  having possibly complex-valued argument. We now introduce the Bessel and Hankel functions. The Bessel's spherical differential equation reads [3]

$$z^2 w'' + 2zw' + [z^2 - n(n+1)]w = 0 \quad n = (0, \pm 1, \pm 2, \dots)$$

Linearly independent solutions are the spherical Bessel functions (of fractional order) of the first kind  $j_n(z)$  and of the second kind  $y_n(z)$ :

$$j_n(z) = \sqrt{\frac{\pi}{2z}} J_{n+1/2}(z) \quad y_n(z) = \sqrt{\frac{\pi}{2z}} Y_{n+1/2}(z), \quad (\text{A.3})$$

where the index  $n$  takes integer values and  $J_{n+1/2}(z)$  and  $Y_{n+1/2}(z)$  are the Bessel functions of fractional order of first and second kind respectively. The spherical Hankel functions of first and second kind  $h_n^{(\alpha)}(z)$  ( $\alpha = 1, 2$ ) are a linear combination of the first two spherical Bessel functions (and therefore also called spherical Bessel functions of third kind):

$$h_n^{(1)}(z) = j_n(z) + iy_n(z) = \sqrt{\frac{\pi}{2z}} H_{n+1/2}^{(1)}(z), \quad (\text{A.4})$$

$$h_n^{(2)}(z) = j_n(z) - iy_n(z) = \sqrt{\frac{\pi}{2z}} H_{n+1/2}^{(2)}(z), \quad (\text{A.5})$$

where  $H_{n+1/2}^{(1)}$  and  $H_{n+1/2}^{(2)}$  are the Hankel function of fractional order and of first and second kind. Explicitly, the first  $n=0, 1, 2$  functions  $j_n(z)$ ,  $y_n(z)$  are:

$$\begin{aligned} j_0 &= \frac{\sin z}{z}, & y_0 &= -j_{-1}(z) = -\frac{\cos z}{z}, \\ j_1 &= \frac{\sin z}{z^2} - \frac{\cos z}{z}, & y_1 &= j_{-2}(z) = -\frac{\cos z}{z^2} - \frac{\sin z}{z}, \\ j_2 &= \left(\frac{3}{z^3} - \frac{1}{z}\right) \sin z - \frac{3}{z^2} \cos z, & y_2 &= -j_{-3}(z) = \left(-\frac{3}{z^3} + \frac{1}{z}\right) \cos z - \frac{3}{z^2} \sin z. \end{aligned}$$

In particular, we are interested in the spherical Hankel function of first kind  $h_n^{(1)}(z)$  appearing in (A.2). This can be written [3]:

$$h_n^{(1)}(z) = (-i)^{n+1} \frac{e^{iz}}{z} \sum_{m=0}^n \binom{n}{m} (-2iz)^{-m} = (-i)^{n+1} \frac{e^{iz}}{z} \sum_{m=0}^n \frac{(n+m)!}{m!(n-m)!(2z)^m},$$

and the first two read:

$$h_0^{(1)}(z) = -i \frac{e^{iz}}{z}, \quad h_1^{(1)}(z) = -e^{iz} \frac{z+i}{z^2}.$$

## A.2 NUMERICAL EVALUATION OF SPHERICAL $H_N^{(1)}(Z^*)$ WITH COMPLEX ARGUMENT

The spherical Hankel function of first kind with complex argument  $h_n^{(1)}(z^*)$  can be computed either via superposition (A.4) or directly with the ascending three terms recurrence relation (TTRR) for Bessel functions [3]:

$$f_{n+1}(z^*) = (2n+1)z^{*-1}f_n(z^*) - f_{n-1}(z^*), \quad (f_n = j_n, y_n, h_n) \quad (\text{A.6})$$

where  $z^*$  is the complex argument  $z^* = z(1 + i\alpha)$ . Notice that in our application of the fast multipole method, the argument of the Bessel and Hankel functions is  $z^* := k^*r_0$ , where  $k^*$  is the complex wavenumber and  $r_0$  is the distance between the center of two cubic cells in the FMM-octree. Thus,  $\alpha$  corresponds to the damping factor  $\beta$  defined in Chapter 2. Relation (A.6) enables to calculate the values of the function at any order  $n+1$  starting from function values of two known consecutive orders  $n-1$  and  $n$ . However, the stability of the recurrence has to be analysed before use in order to avoid the accumulation of round-off errors while repetitively applying the recurrence formula [130, 248]. In the following, we compare the values of the spherical Hankel function of first kind  $h_n^{(1)}(z^*)$  computed (i) by superimposing the first and second kind Bessel functions as in (A.4) and (ii) by using the direct ascending recurrence formula (A.6). The numerical evaluation of complex-argument Bessel and Hankel functions by superposition is addressed in [97] and [155] respectively. The former proposed an algorithm to overcome the numerical instabilities related to the numerical computation of the Bessel functions of integer order and complex argument. The latter suggested a technique for the evaluation of the integer order Hankel functions with complex-valued argument having a large imaginary part by combining the Bessel functions of first and second kind without running into round-off errors.

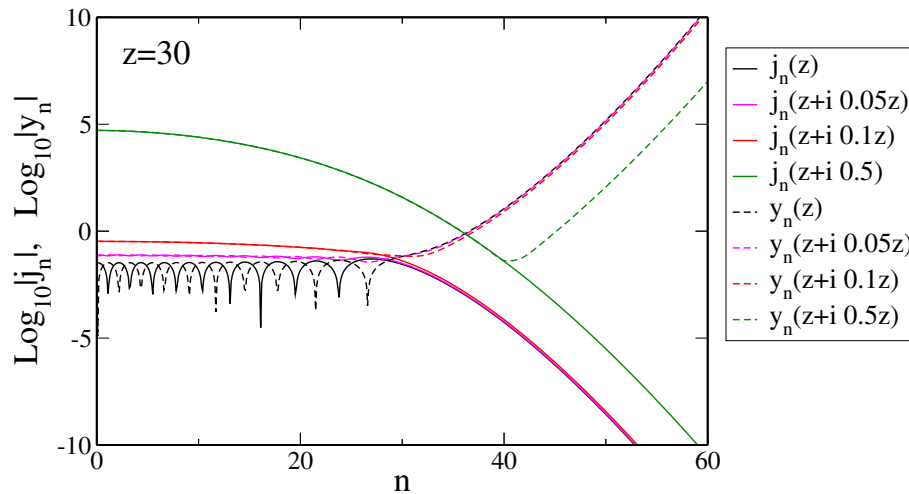


**Figure A.1:** Spherical Bessel functions for fixed argument  $z$  versus increasing order  $n$  [97].

**Algorithm 4** Backward algorithm for the numerical computation of  $j_n(z^*)$ 


---

```

1: Initialization:  $\{j\}(0:n) = \{0\}$ 
2:  $j_0 := 0$ 
3:  $j_1 := 1$ 
4:  $m = \text{int}(n + 2|z^*|)$ 
5: for  $k = m : -1 : 0$  do
6:    $j_k = (2k + 3)j_1/z^* - j_0$ 
7:   if  $k \leq n$  then
8:      $\{j\}(k) := j_k$ 
9:   end if
10:   $j_0 := j_1$ 
11:   $j_1 := j_k$ 
12: end for
13:  $j_0 := \sin z^*/z^*$ 
14:  $\{j\} := j_0 \cdot \{j\} / \{j\}(0)$ 

```

---

**Evaluation of the spherical Hankel function by superposition of Bessel functions.** Results from old studies indicate that the relation (A.6) can be applied safely provided that  $|f_n(z)|$  is monotonically increasing in the direction  $n$  of the recurrence and that backward recurrence relations should be used when  $|f_n(z)|$  decreases with growing  $n$  [130]. In Fig. A.1, the spherical Bessel functions of first and second kind are depicted for four values of coefficient  $\alpha$ , namely  $\alpha = 0, 0.05, 0.1, 0.5$ . This figure let two important aspects emerge. First, for both real- and complex-valued argument the spherical Bessel functions behave differently before and after the threshold  $n = |z|$  (in the figure,  $n = 30$ ). Second, the growth of the imaginary part of the argument affects the global trend in magnitude and in movement. The following considerations are drawn on previous works about the integer order-Bessel function of first and second kind with complex argument [97, 155], but still apply for the spherical Bessel functions:

1. *Real argument  $z$ .* This is the case of  $|\Im[z^*]| = 0$  or  $|\Re[z^*]| \gg |\Im[z^*]|$ , and correspond to the black continuous and dotted lines in Fig. A.1. The magnitude of the functions  $|f_n(z^*)|$  holds steady for  $n < |z^*|$ . In this range either the forward or the backward TTRR (recurrence applied toward decreasing  $n$ ) apply. At  $n > |z|$  the global trend change. Function  $y_n(z)$  increases against  $n$  and can be calculated with a forward TTRR starting from generic  $y_0(z)$  and  $y_1(z)$ , whereas  $j_n(z)$  drops and thus the lower orders have to be computed through a backward TTRR, starting from arbitrary orders  $j_q(z)$  and  $j_{q+1}(z)$ . The employed backward algorithm is detailed in Alg.4. Therefore, usually the computation of real-argument Bessel functions is computed using the forward TTRR (A.6) for  $j_n(z^*)$  and the backward Alg.4 for  $j_n(z^*)$ .
2. *Complex argument  $z^*$ .* For a fixed real part  $z$  of the argument, the growth of the imaginary part through the coefficient  $\alpha$  influences the function  $|f_n(z)|$  as shown in Fig. A.1. In this case, the backward TTRR still applies for  $j_n(z)$ , whereas for  $y_n(z)$  one should use the backward TTRR for  $n < n^*$ , and the forward TTRR for  $n > n^*$ , where  $n^*$  is the order

at which the minimum of the function is located. After some experimentations, Du Toit evaluated  $n^* \approx |z| + |\Im(z)|/2$ .

Due to the weak-dissipation assumption described in Chapter 2, in the present work the range of damping factor  $\beta$  is limited to  $0 \leq \beta \leq 0.1$ . In this range, we find that Alg.4 for the  $y_n(z^*)$  holds and that there is no need to find the minimum in the function nor to split the algorithm for its numerical computation as suggested in [97, 155] (and valid for larger values of  $\beta$ ).

**Direct evaluation of the spherical Hankel function.** The spherical Hankel function  $h_n^{(1)}(z^*)$  can be computed directly by using the recurrence formula A.6. The corresponding algorithm, summarized in Alg.5, gives accurate results and can be used safely provided that the imaginary part of the argument respect the assumption of  $\alpha \leq 0.1$ .

---

**Algorithm 5** Forward recurrence relation for the numerical computation of  $h_n^{(1)}(z^*)$

---

- 1: **Initialization:**  $\{h\}(1 : n + 1) := \{0\}$
  - 2:  $\{h\}(1) := e^{iz^*}/(iz^*)$
  - 3:  $\{h\}(2) := -e^{iz^*}(z^* + 1)/z^{*2}$
  - 4: **for**  $k = 2 : n$  **do**
  - 5:    $\{h\}(k + 1) = (2k + 1)\{h\}(k)/z^* - \{h\}(k - 1)$
  - 6: **end for**
- 

### A.3 THE HELMHOLTZ GREEN'S FUNCTION EXPANSION

#### A.3.1 The Gegenbauer series

For arguments  $z \gg 1$ , the following asymptotic approximation holds [82]:

$$h_n^{(1)}(z) \sim (-i)^n \frac{e^{iz}}{iz} \quad (z \rightarrow +\infty), \quad (\text{A.7})$$

which means that  $h_n^{(1)}(z)$  behaves at infinity as the elementary solution. Given  $r, \rho, \theta, \lambda$  arbitrary complex and denoting  $R = \sqrt{r^2 + \rho^2 - 2r\rho\cos\theta}$  the addition theorem reads [3]:

$$\begin{aligned} \frac{\sin \lambda R}{\lambda R} &= \sum_{n=0}^{+\infty} (2n + 1) j_n(\lambda r) j_n(\lambda \rho) P_n(\cos \theta) \\ -\frac{\cos \lambda R}{\lambda R} &= \sum_{n=0}^{+\infty} (2n + 1) j_n(\lambda r) y_n(\lambda \rho) P_n(\cos \theta) \end{aligned} \quad (\text{A.8})$$

The expansion of  $h_0^{(1)}(\lambda|R|)$  (i.e. the Gegenbauer series) can be written:

$$\begin{aligned} h_0^{(1)}(\lambda R) &= j_0(\lambda R) + iy_0(\lambda R) = \frac{\sin \lambda R}{\lambda R} - i \frac{\cos \lambda R}{\lambda R} \\ &= \sum_{l=0}^{+\infty} (2l + 1) j_l(\lambda r) P_l(\cos \theta) [j_l(\lambda \rho) + iy_l(\lambda \rho)] \end{aligned}$$

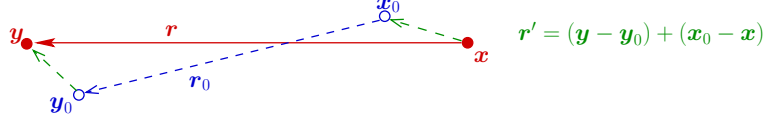


**Figure A.2:** Recast of the position vector  $\mathbf{R}$ .

$$= \sum_{l=0}^{+\infty} (2l+1) j_l(\lambda r) h_0^{(1)}(\lambda \rho) P_l(\cos \theta) \quad (\text{A.9})$$

Recasting the general distance vector in the form  $\mathbf{R} = \mathbf{y} - \mathbf{x} = \mathbf{r}_0 + \mathbf{r}'$ , where

$$\mathbf{r}_0 = \mathbf{y}_0 - \mathbf{x}_0, \quad \mathbf{r}' = (\mathbf{y} - \mathbf{y}_0) + (\mathbf{x}_0 - \mathbf{x})$$

and using (A.7) with  $z = k|\mathbf{R}|$  and (A.9), the Gegenbauer series can be written:

$$\frac{e^{ik|\mathbf{R}|}}{ik|\mathbf{R}|} = \sum_{l=0}^{+\infty} (2l+1) j_l(k|\mathbf{r}'|) h_0^{(1)}(k|\mathbf{r}_0|) P_l(\mathbf{r}_0 \cdot \mathbf{r}') \quad (\text{A.10})$$

### A.3.2 The spherical harmonics

The spherical harmonics satisfy the spherical harmonic differential equation given by the angular part of Laplace's equation. In spherical coordinates, the Laplace's spherical harmonics form an orthogonal system:

$$\int_S Y_l^m(\boldsymbol{\zeta}) \overline{Y_{\ell'}^{m'}(\boldsymbol{\zeta})} d\boldsymbol{\zeta} = \delta_{\ell\ell'} \delta_{mm'} \quad (\forall (\ell, \ell') \in \mathbb{N}, \forall (m, m') \in \{-\ell, \dots, +\ell\} \times \{-\ell', \dots, +\ell'\}), \quad (\text{A.11})$$

where  $S = \{\boldsymbol{\zeta} \in \mathbb{R}^3 / |\boldsymbol{\zeta}| = 1\}$  is the unit sphere,  $\delta$  is the Kronecker delta. The spherical harmonics verify the addition theorem:

$$P_\ell(\boldsymbol{\xi} \cdot \boldsymbol{\zeta}) = \frac{4\pi}{2\ell+1} \sum_{m=-\ell}^{\ell} Y_\ell^m(\boldsymbol{\xi}) \overline{Y_\ell^m(\boldsymbol{\zeta})} \quad (\text{A.12})$$

where  $P_\ell(z)$  denote the  $\ell$ -order Legendre polynomial.

### A.3.3 Plane wave expansion

Using the addition theorem (A.12), the definition (A.11) and the Jacobi-Anger expansion (expansion of exponentials of trigonometric functions in the basis of their harmonics) for plane wave in the direction  $\hat{\mathbf{s}}$

$$e^{iK(\hat{\mathbf{s}} \cdot \mathbf{r}')} = \sum_{\ell=0}^{+\infty} (2\ell+1) i^\ell j_\ell(K|\mathbf{r}'|) P_\ell(\hat{\mathbf{s}} \cdot \mathbf{r}') \quad (\forall \mathbf{r}' \in \mathbb{R}^3) \quad (\text{A.13})$$



we can finally write the *plane wave expansion*:

$$\begin{aligned}
\frac{e^{ik|\mathbf{R}|}}{|\mathbf{R}|} &= ik \sum_{\ell=0}^{+\infty} (2\ell+1) j_{\ell}(k|\mathbf{r}'|) h_0^{(1)}(k|\mathbf{r}_0|) \frac{4\pi}{(2\ell+1)} \sum_{m=-\ell}^{\ell} Y_{\ell}^m(\mathbf{r}_0) Y_{\ell}^m(\mathbf{r}') \int_{\hat{\mathbf{s}} \in S} Y_{\ell}^m(\hat{\mathbf{s}}) \overline{Y_{\ell}^m(\hat{\mathbf{s}})} d\hat{\mathbf{s}} \\
&= ik \sum_{\ell=0}^{+\infty} (2\ell+1) j_{\ell}(k|\mathbf{r}'|) h_0^{(1)}(k|\mathbf{r}_0|) \frac{(2\ell+1)}{4\pi} \int_{\hat{\mathbf{s}} \in S} P_{\ell}(\hat{\mathbf{s}} \cdot \mathbf{r}') P_{\ell}(\hat{\mathbf{s}} \cdot \mathbf{r}_0) d\hat{\mathbf{s}} \\
&= \frac{ik}{4\pi} \int_{\hat{\mathbf{s}} \in S} e^{ik(\hat{\mathbf{s}} \cdot \mathbf{r}')} \sum_{\ell=0}^{+\infty} (2\ell+1) i^{-\ell} h_0^{(1)}(k|\mathbf{r}_0|) P_{\ell}(\hat{\mathbf{s}} \cdot \mathbf{r}_0) d\hat{\mathbf{s}} \\
&= \int_{\hat{\mathbf{s}} \in S} e^{ik(\hat{\mathbf{s}} \cdot \mathbf{r}')} \mathcal{G}_L(\hat{\mathbf{s}}; \mathbf{r}_0; k) d\hat{\mathbf{s}}
\end{aligned} \tag{A.14}$$

where the transfer function  $\mathcal{G}_L$ :

$$\mathcal{G}_L(\hat{\mathbf{s}}; \mathbf{r}_0; k) = \frac{ik}{4\pi} \sum_{\ell=0}^{+\infty} (2\ell+1) i^{-\ell} h_{\ell}^{(1)}(k|\mathbf{r}_0|) P_{\ell}(\hat{\mathbf{s}} \cdot \mathbf{r}_0).$$

After replacing the integral over the unit sphere  $S$  by a discrete quadrature with points  $\hat{\mathbf{s}}_q \in S$  and weights  $w_q$ , reads:

$$G(r; k^*) \sim \sum_{q=1}^Q w_q e^{ik^*(\hat{\mathbf{s}}_q \cdot \mathbf{r}')} \mathcal{G}_L(\hat{\mathbf{s}}_q; \mathbf{r}_0; k^*). \tag{A.15}$$

The plane wave approximation has a physical interpretation. The field  $e^{ikr}/r$  radiating from a point source can be approximated by superimposing plane waves, as depicted in Fig. A.3 [82]. For  $r \rightarrow \infty$ , the field can be locally considered as a plane wave propagating in one direction. Approaching the source, i.e.  $r \rightarrow \mathcal{O}(1)$ , the approximation should account for different directions through superposition of several plane waves. Finally, closed to the source the radiating field is approximated by a number of radially propagating plane waves. The discrete directions of propagations are the discrete quadrature points of the unit sphere in (A.15).

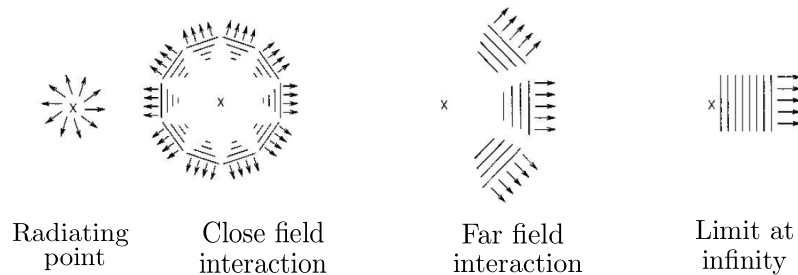


**Figure A.3:** Plane wave approximation [82].



## Appendix B

# Analytical solutions for test problems

### Contents

---

<b>B.1 Spherical cavity under uniform pressure . . . . .</b>	<b>123</b>
<b>B.2 Spherical cavity under uniform pressure surrounded by a spherical shell . . . . .</b>	<b>123</b>
<b>B.3 Scattering of a P-wave by a spherical cavity . . . . .</b>	<b>124</b>

---

### B.1 SPHERICAL CAVITY UNDER UNIFORM PRESSURE

Let  $R$  be the radius of a spherical cavity embedded in a viscoelastic isotropic infinite medium and subjected to an internal time-harmonic uniform pressure  $P$ . This spherically-symmetric problem has a closed-form solution, with the radial displacement and stress given (with  $\alpha = ik_P^* R$ ,  $\theta = 4(1 - \alpha) + \alpha^2/\gamma^{*2}$  and  $\gamma^*$  defined as in (2.40)), by

$$u_r(r) = \frac{PR^2}{\mu^* \theta r^2} (R - \alpha r) \exp\left[\alpha\left(\frac{r}{R} - 1\right)\right], \quad (\text{B.1a})$$

$$\sigma_{rr}(r) = \frac{PR}{\theta r^3} \left(-\frac{\alpha r}{\gamma^{*2}} + 4\alpha Rr - 4R^2\right) \exp\left[\alpha\left(\frac{r}{R} - 1\right)\right] \quad (\text{B.1b})$$

### B.2 SPHERICAL CAVITY UNDER UNIFORM PRESSURE SURROUNDED BY A SPHERICAL SHELL

This spherically-symmetric problem also has a closed-form solution. Referring to Fig. 2.22, the radial displacement  $u_r^{(i)}$  in domains  $\Omega_i$  ( $i = 1, 2$ ) is such that  $u_r^{(i)} = \partial\phi_i/\partial r$ , with potentials  $\phi_i$  given by

$$\phi_1 = \frac{A_1}{r} \exp(ik_P^{*(1)} r) + \frac{B_1}{r} \exp(-ik_P^{*(1)} r), \quad \phi_2 = \frac{A_2}{r} \exp(ik_P^{*(2)} r) \quad (\text{B.2})$$

where the coefficients  $A_1$ ,  $A_2$ ,  $B_1$  are found by solving

$$\begin{bmatrix} e^{\alpha_1}(\alpha_1 - 1) & -e^{-\alpha_1}(\alpha_1 + 1) & e^{\alpha_2}(1 - \alpha_2) \\ e^{\alpha_1}\mu_1\theta_1 & e^{-\alpha_1}\mu_1(\theta_1 + 8\alpha_1) & -e^{\alpha_2}\mu_2\theta_2 \\ e^{\alpha_3}\mu_1\theta_3 & e^{-\alpha_3}\mu_1(\theta_3 + 8\alpha_3) & 0 \end{bmatrix} \begin{Bmatrix} A_1 \\ B_1 \\ A_2 \end{Bmatrix} = \begin{Bmatrix} 0 \\ 0 \\ -PR_1^3\gamma_1^{*2} \end{Bmatrix}$$

with  $\alpha_1 = ik_P^{*(1)}R_2$ ,  $\alpha_2 = ik_P^{*(2)}R_2$ ,  $\alpha_3 = ik_P^{*(1)}R_1$  and  $\theta_i = 4(1 - \alpha_i) + \alpha_i^2/\gamma_i^{*2}$  ( $i = 1, 2$ ) where  $\gamma_i^*$  is defined in each domain as in (B.1b).

### B.3 SCATTERING OF A P-WAVE BY A SPHERICAL CAVITY

$$u_r = \frac{1}{r} \sum_{n=0}^{+\infty} [\Phi_0 i^n (2n+1) U_1^{(1)}(k_P^* r) + A_n U_1^{(3)}(k_P^* r) + C_n U_3^{(3)}(k_S^* r)] P_n(\cos \theta) \quad (\text{B.3})$$

$$u_\theta = \frac{1}{r} \sum_{n=0}^{+\infty} [\Phi_0 i^n (2n+1) V_1^{(1)}(k_P^* r) + A_n V_1^{(3)}(k_P^* r) + C_n V_3^{(3)}(k_S^* r)] \frac{d}{d\theta} P_n(\cos \theta) \quad (\text{B.4})$$

with

$$\begin{aligned} U_1^{(1)}(z) &= nj_n(z) - zj_{n+1}(z) & V_1^{(1)}(z) &= j_n(z) \\ U_1^{(3)}(z) &= nh_n^{(1)}(z) - zh_{n+1}^{(1)}(z) & V_1^{(3)}(z) &= h_n^{(1)}(z) \\ U_3^{(3)}(z) &= n(n+1)h_n^{(1)}(z) & V_3^{(3)}(z) &= (n+1)h_n^{(1)}(z) - zh_{n+1}^{(1)}(z) \end{aligned}$$

and where the constants  $A_n$ ,  $C_n$ , obtained from enforcing the traction-free boundary condition on the surface of the spherical cavity, are given by

$$\begin{aligned} A_n &= \phi_0 i^n (2n+1) [T_{11}^{(1)}(k_P^* R) T_{43}^{(3)}(k_S^* R) - T_{41}^{(1)}(k_P^* R) T_{13}^{(3)}(k_S^* R)] / \Delta_n \\ C_n &= \phi_0 i^n (2n+1) [T_{11}^{(1)}(k_P^* R) T_{41}^{(3)}(k_S^* R) - T_{41}^{(1)}(k_P^* R) T_{11}^{(3)}(k_S^* R)] / \Delta_n \end{aligned}$$

with

$$\begin{aligned} T_{11}^{(1)}(z) &= (n^2 - n - \frac{1}{2}k_S^{*2}r^2)j_n(z) + 2zj_{n+1}(z) \\ T_{41}^{(1)}(z) &= (n-1)j_n(z) - zj_{n+1}(z) \\ T_{11}^{(3)}(z) &= (n^2 - n - \frac{1}{2}k_S^{*2}r^2)h_n^{(1)}(z) + 2zh_{n+1}^{(1)}(z) \\ T_{13}^{(3)}(z) &= n(n+1)[(n-1)h_n^{(1)}(z) - zh_{n+1}^{(1)}(z)] \\ T_{41}^{(3)}(z) &= (n-1)h_n^{(1)}(z) - zh_{n+1}^{(1)}(z) \\ T_{43}^{(3)}(z) &= (n^2 - 1 - \frac{1}{2}k_S^{*2}r^2)h_n^{(1)}(z) + zh_{n+1}^{(1)}(z) \end{aligned}$$

and

$$\Delta_n = T_{11}^{(3)}(k_P^* R) T_{43}^{(3)}(k_S^* R) - T_{41}^{(3)}(k_P^* R) T_{13}^{(3)}(k_S^* R)$$

The series appearing in the displacement fields formula (B.3) and (B.4) converges after a certain number of terms, as shown in Fig.B.1 for the example of diffraction by a spherical cavity.

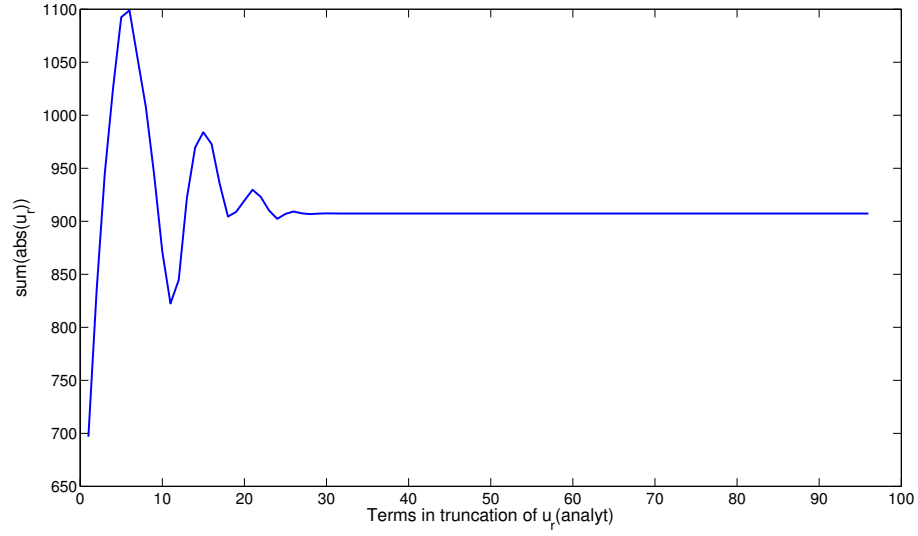


**Figure B.1:** Scattering of a plane P-wave from a spherical cavity : convergence of the analytical  $u_r$  field as a function of the truncation parameter.



## Appendix C

# Interface relaxation algorithms for non-overlapping domain decomposition

### Contents

---

C.1 Interface problem statement in elasticity. . . . .	127
C.2 Algorithms. . . . .	128

---

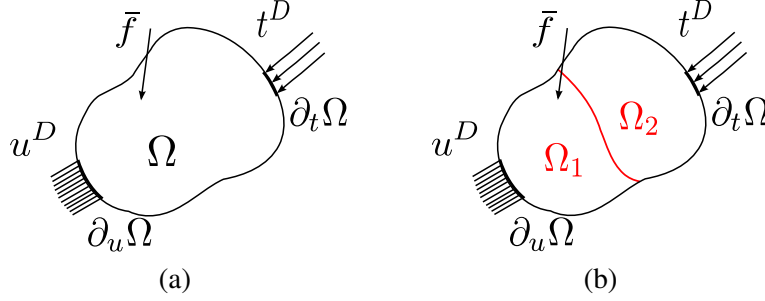
In this Appendix, the main interface relaxation FEM-BEM coupling algorithms used in the literature are summarized. Although the algorithms are here presented for the elasticity problem, they can be applied in frequency-domain elastodynamics provided that the natural frequency of boundary conditions do not coincide with a resonant frequency of the interior problem. In the present work, we applied a modified sequential Dirichlet-Neumann interface relaxation algorithm to a fast multipole BEM/FEM coupling for wave propagation problems in three-dimensional unbounded domains. A review of the interface relaxation algorithms for elliptic problems can be found in [103,257].

### C.1 INTERFACE PROBLEM STATEMENT IN ELASTICITY.

Let consider a domain  $\Omega \in \mathbb{R}^3$  submitted to a classical linear elasticity problem, Figure C.1. Denoting  $\mathcal{A}$  the elasticity tensor and  $\underline{f}$  the the volumic efforts imposed on  $\Omega$ , the system is governed by the following equations:

$$\left\{ \begin{array}{ll} \operatorname{div}(\underline{\sigma}) + \rho \underline{f} = 0 & \text{in } \Omega \\ \underline{\epsilon}(\underline{u}) = \frac{1}{2}(\nabla \underline{u} + \nabla \underline{u}^T) & \text{in } \Omega \\ \underline{\sigma} = \mathcal{A} : \underline{\epsilon}(\underline{u}) & \text{in } \Omega \\ \underline{u} = \underline{u}_D & \text{on } \partial_u \Omega \\ \underline{\sigma} \cdot \underline{n} = \underline{t}_D & \text{on } \partial_t \Omega \end{array} \right. \quad (\text{C.1})$$

The boundary conditions are such that  $\partial_u \Omega \cup \partial_t \Omega = \partial \Omega$  and  $\partial_u \Omega \cap \partial_t \Omega = \emptyset$ . Assuming that  $\mathcal{A}$  define s a symmetric positive definite bilinear form on 2nd-order symmetric tensors and that

**Figure C.1:** Reference problem.

$mes(\partial_u \Omega) > 0$  (no floating structures), problem (C.1) has a unique solution. Supposing  $\Omega$  partitioned into two non-overlapping subdomains  $\{\Omega^{(s)}, s = 1, 2\}$ :

$$\begin{cases} \Omega = \Omega^{(1)} \cup \Omega^{(2)} \\ \Omega^{(1)} \cap \Omega^{(2)} = \emptyset \\ \Gamma = \partial\Omega^{(1)} \cap \partial\Omega^{(2)} \end{cases} \quad (C.2)$$

with  $(\partial\Omega^{(s)} \cap \partial\Omega) > 0$ . System (C.1) can be rewritten in a form restricted to subdomains  $\Omega^{(s)}$ :

$$\begin{cases} \text{div}(\underline{\underline{\sigma}}^{(s)}) + \rho \underline{f}^{(s)} = 0 & \text{in } \Omega^{(s)} \\ \underline{\underline{\epsilon}}(\underline{u}^{(s)}) = \frac{1}{2}(\nabla \underline{u}^{(s)} + \nabla \underline{u}^{(s)T}) & \text{in } \Omega^{(s)} \\ \underline{\underline{\sigma}}^{(s)} = \mathcal{A} : \underline{\underline{\epsilon}}(\underline{u}^{(s)}) & \text{in } \Omega^{(s)} \\ \underline{u}^{(s)} = \underline{u}_D^{(s)} & \text{on } \partial_u \Omega \cap \partial_u \Omega^{(s)} \\ \underline{\underline{\sigma}}^{(s)} \cdot \underline{n}^{(s)} = \underline{t}_D^{(s)} & \text{on } \partial_t \Omega \cap \partial_u \Omega^{(s)} \end{cases} \quad (C.3)$$

Considering the normal as pointing away from  $\Omega^{(s)}$ , the transmission conditions on  $\Gamma$  read:

$$\begin{cases} \underline{u}^{(1)} = \underline{u}^{(2)} & \text{on } \Gamma \\ \underline{\underline{\sigma}}^{(1)} \cdot \underline{n}^{(1)} + \underline{\underline{\sigma}}^{(2)} \cdot \underline{n}^{(2)} = 0 & \text{on } \Gamma \end{cases} \quad (C.4)$$

The displacement-based finite element approximation of the problem gives rise to a linear system in the form :

$$[K^{(s)}] \{u^{(s)}\} = \{f^{(s)}\} + \{\lambda^{(s)}\} \quad (C.5)$$

where  $\{\lambda^{(s)}\}$  is the vector of nodal generalized forces associated with tractions along  $\Gamma$ .

## C.2 ALGORITHMS.

In the following, five algorithms are collected: a sequential Dirichlet-Neumann, three parallel algorithms (Neumann-Neumann, Dirichlet-Neumann and Dirichlet-Dirichlet) and an averaging Dirichlet-Neumann.



**Algorithm 6** Sequential Dirichlet-Neumann

---

```

1: Initial guess:  $u_{B,0}^\Gamma$ 
2: for  $n = 0, k$  do
3:   solve Dirichlet-pb on BE subdomain  $\rightarrow t_{B,n}^\Gamma$ 
4:    $f_{F,n}^\Gamma = Mt_{B,n}^\Gamma$ 
5:   solve Neumann-pb on FE subdomain  $\rightarrow u_{F,n}^\Gamma$ 
6:   if  $u_{F,n}^\Gamma = u_{B,n}^\Gamma$  then
7:     stop {convergence}
8:   else
9:      $u_{B,n+1}^\Gamma := (1 - \theta)u_{B,n}^\Gamma + \theta u_{F,n}^\Gamma$  {relaxation}
10:  end if
11: end for

```

---

**Algorithm 7** Parallel Neumann-Neumann

---

```

1: Initial guess:  $t_{B,0}^\Gamma, t_{F,0}^\Gamma$ 
2: for  $n = 0, k$  do
3:   solve Neumann-pb on BE subdomain  $(t_{B,n}^\Gamma) \rightarrow u_{B,n}^\Gamma$ 
   solve Neumann-pb on FE subdomain  $(f_{F,n}^\Gamma = Mt_{B,n}^\Gamma) \rightarrow u_{F,n}^\Gamma$ 
4:   relaxation
    $t_{B,n+1}^\Gamma := t_{B,n}^\Gamma + \beta(u_{F,n}^\Gamma - u_{B,n}^\Gamma)$ 
    $t_{F,n+1}^\Gamma := -t_{B,n+1}^\Gamma$ 
5:   if  $(t_{B,n+1}^\Gamma = t_{B,n}^\Gamma) \ \& \ (t_{F,n+1}^\Gamma = t_{F,n}^\Gamma)$  then
6:     stop {convergence}
7:   end if
8: end for

```

---

**Algorithm 8** Parallel Dirichlet-Neumann

---

```

1: Initial guess:  $u_{B,0}^\Gamma, t_{F,0}^\Gamma$ 
2: for  $n = 0, k$  do
3:   solve Dirichlet-pb on BE subdomain  $(u_{B,n}^\Gamma) \rightarrow t_{B,n}^\Gamma$ 
   solve Neumann-pb on FE subdomain  $(f_{F,n}^\Gamma = Mt_{B,n}^\Gamma) \rightarrow u_{F,n}^\Gamma$ 
4:   relaxation
    $u_{B,n+1}^\Gamma := (1 - \gamma)u_{B,n}^\Gamma + \gamma u_{F,n}^\Gamma$ 
    $t_{F,n+1}^\Gamma := -t_{B,n}^\Gamma$ 
5:   if  $(u_{B,n+1}^\Gamma = u_{B,n}^\Gamma) \ \& \ (t_{F,n+1}^\Gamma = t_{F,n}^\Gamma)$  then
6:     stop {convergence}
7:   end if
8: end for

```

---

**Algorithm 9** Geometric contraction: parallel Dirichlet-Dirichlet

---

```

1: Initial guess:  $u_{B,0}^\Gamma, u_{F,0}^\Gamma$ 
2: for  $n = 0, k$  do
3:   solve Dirichlet-pb on BE subdomain  $(u_{B,n}^\Gamma) \rightarrow t_{B,n}^\Gamma$ 
   solve Dirichlet-pb on FE subdomain  $(u_{F,n}^\Gamma) \rightarrow f_{F,n}^\Gamma$ 
4:    $t_{F,n}^\Gamma = M^{-1} f_{F,n}^\Gamma$ 
5:   scaling  $u_{B,n}^\Gamma$  with  $t_{B,n}^\Gamma, t_{F,n}^\Gamma$ 
6:   relaxation {geometric contraction}
    $u_{B,n+1}^\Gamma := u_{B,n}^\Gamma - \alpha(t_{B,n}^\Gamma + t_{F,n}^\Gamma)$ 
    $u_{F,n+1}^\Gamma := u_{B,n+1}^\Gamma$ 
7:   if  $(u_{B,n+1}^\Gamma = u_{B,n}^\Gamma) \ \& \ (u_{F,n+1}^\Gamma = u_{F,n}^\Gamma)$  then
8:     stop {convergence}
9:   end if
10: end for

```

---

**Algorithm 10** Averaging Dirichlet-Neumann

---

```

1: Initial guess:  $u_{B,0}^\Gamma, u_{F,0}^\Gamma$ 
2: for  $n = 0, k$  do
3:   solve Dirichlet-pb on BE subdomain  $(u_{B,n}^\Gamma) \rightarrow t_{B,n}^\Gamma$ 
   solve Dirichlet-pb on FE subdomain  $(u_{F,n}^\Gamma) \rightarrow f_{F,n}^\Gamma$ 
4:    $t_{F,n}^\Gamma = M^{-1} f_{F,n}^\Gamma$ 
5:   averaging
    $t_{B,n+1/2}^\Gamma := (1 - \phi_1)t_{B,n}^\Gamma - \phi_1 t_{F,n}^\Gamma$ 
    $t_{F,n+1/2}^\Gamma := (1 - \phi_1)t_{F,n}^\Gamma - \phi_1 t_{B,n}^\Gamma$ 
6:   solve Neumann-pb on BE subdomain  $(t_{B,n+1/2}^\Gamma) \rightarrow u_{B,n+1/2}^\Gamma$ 
   solve Neumann-pb on FE subdomain  $(f_{F,n+1/2}^\Gamma = M t_{F,n+1/2}^\Gamma) \rightarrow u_{F,n+1/2}^\Gamma$ 
7:   averaging
    $u_{B,n+1}^\Gamma := (1 - \phi_2)u_{B,n+1/2}^\Gamma + \phi_2 u_{F,n+1/2}^\Gamma$ 
    $u_{F,n+1}^\Gamma := (1 - \phi_2)u_{F,n+1/2}^\Gamma + \phi_2 u_{B,n+1/2}^\Gamma$ 
8:   if  $(u_{B,n+1}^\Gamma = u_{B,n}^\Gamma) \ \& \ (u_{F,n+1}^\Gamma = u_{F,n}^\Gamma)$  then
9:     stop {convergence}
10:  end if
11: end for

```

---

## Appendix D

# User's guides

### Contents

---

D.1	COFFEE program . . . . .	131
D.2	CUSIM program . . . . .	137
D.3	CUSEQ program . . . . .	144

---

The present thesis aims at extending the capabilities of the existing time-harmonic elastodynamic FMBEM in two directions. On the one hand, the FMBEM formulation have been extended to the case of weakly dissipative viscoelastic media. The existing ML-FMBEM code for 3-D time-harmonic elastodynamic, called COFFEE [61], has been modified to account for weakly dissipative media through the complex wavenumber formulation detailed in Chapter 2. On the other hand, two strategies have been applied to couple the FMBEM and the FEM to solve three-dimensional wave propagation problems in unbounded domains. For this purpose, two codes have been conceived for the FEM/FMBEM coupling corresponding to the two approaches proposed in Chapter 3. CUPSEQ is a Matlab-based code that drives the iterative coupling between two external software, treated as black-boxes. CUPSIM is a Fortran 90-based code that integrates COFFEE and FEM subroutines in order to solve a unique system of equations by GMRES. This Appendix is devoted to an introduction to the use of the three codes including their capabilities, the instructions needed for the preparation of input data files and the post-processing of results.

### D.1 COFFEE PROGRAM

#### D.1.1 Introduction

The code COFFEE is a Fortran-based program that solves 3-D linear (visco-)elastodynamics problems in the frequency domain by the boundary element method accelerated by fast multipole method (FMBEM). Our contribution consist in the extent of the capabilities of the program written by Chaillat [61], originally limited to linear elastic problems, to deal with weakly dissi-

pative media. The code is capable to solve mono-region problems involving a single isotropic homogeneous domain (Fig.D.1a) and multi-region problems involving piecewise isotropic homogeneous media (Fig.D.1b). For single-region problems, the code uses the formulation detailed in Section 2.2.2. For multi-region problems, the BE-BE coupling approach described in Section 2.2.3 is used. The type of problem to be solved is dictated by the time-harmonic boundary conditions defined on the whole domain boundary. For seismic problems, the incident wave field should be analytically computed in a pre-processing step by the user, then imposed as boundary data through the input files.

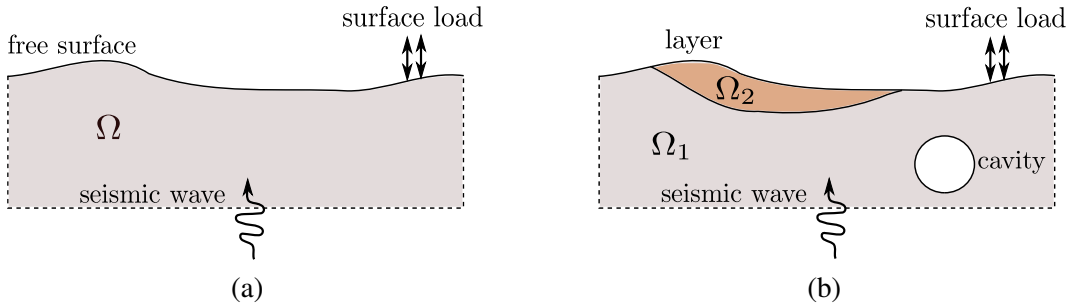


**Figure D.1:** Main intended applications of the FMBEM solver *COFFEE* are seismic problems or local boundary excitations problems in (a) homogeneous media or (b) piecewise heterogeneous media. Cavities or inclusions of simple shape can be also modelled by the BEM (b).

### D.1.2 Installation requirements.

The program *COFFEE* is written in Fortran 90 language and should be compiled within an Intel Fortran compiler provided with Math Kernel Library (MKL), a library of optimized mathematical routines including the Basic Linear Algebra Subprograms (BLAS) and the Linear Algebra PACKage (LAPACK) [1]. The GMRES and Flexible-GMRES invoked in *COFFEE* are public domain routines provided by CERFACS [121, 122]. A Makefile example for compiling *COFFEE* on a Linux platform is shown in Fig.D.2.

### D.1.3 Input files

The program *COFFEE* needs three input files, namely (i) a geometry file (*problem.GEO*), (ii) a problem data file (*problem.DAT*) and (iii) a computation parameters file (*Parameter.txt*). Only the problem data file has been slightly modified w.r.t. the original version to account for the damping factor in the definition of the mechanical properties of each "zone" (i.e. each subregion).

If the problem at hand requires the use of the continuous formulation in terms of total field (see Sec.2.2.3), e.g. for a basin problem, two additional input file are needed, providing the geometry of the planar free surface (*problem.GEO2*) and the known displacement field (*problem.DAT2*) that appears in the right hand side term of the boundary equation (2.24). In both cases (classical or total field formulation), the displacement field can be computed in any do-

---

```

EXE = coffee.exe                                # Name of the executable program
FC90 = ifort                                    # Invoke Intel Fortran Compiler
MKL_PATH = /opt/intel/Compiler/11.1/072/lib/
MKL_INCLUDE = /opt/intel/Compiler/11.1/072/include

# Debug options
# OPT= -g -CB -W1 -check format -check uninit -ftrapuv -warn unused -cpp -check nopower -warn all -check all
# Standard options
OPT = -I $MKL_INCLUDE

# List of object files, i.e. all source files with extension ".o".
# (NOTE: use the tabular key (Tab) at the beginning of each row)
OBJECTS = all_contributions.o read_parameters.o read_input_file_size.o read_input_file.o \
          read_input_file2.o build_cell.o pre-octree.o pre_build_octree.o \
          (...)
          zPackgmres.o zPackfgmres.o interface_main.o main.o

MKL_OBJECT= mkl_dfti.o

all: coffee

#Compilation
coffee: $(MKL_OBJECT) $(OBJECTS)
        $(FC90) $(OPT) $(MKL_OBJECT) $(OBJECTS) -L$(MKL_PATH) -lmkl_intel_lp64
        -lmkl_intel_thread -lmkl_core -liomp5 -lpthread -o $(EXE)

%.o : %.f90
$(FC90) $(OPT) -c $i
%.o : %.f
$(FC90) $(OPT) -c $i
clean :
rm -f *.o ; rm -f *~; rm -f *.obj ; rm -f *.mod

```

---

**Figure D.2:** Makefile for compiling *COFFEE* on a Linux platform (use terminal command *make* to compile). In the Makefile, comment lines are preceded by symbol *#*.

main point by applying the integral representation (IR) (2.5). For this purpose, an additional input file called *problem.POSTGEO* should be provided, containing the coordinate table of the points where the IR is applied.

We stress that the extension of input files must respect the capital letters format, where indicated. For a detailed description of the input files we refer the reader to the *COFFEE* User's Guide in [61]. Here, we limit our exposition to the main characteristics of each input file in order to highlight the modifications related to the presence of lossy media.

1. *Geometry file (problem.GEO)*. This text file contains all information about the problem geometry and is divided in three sections, separated by the symbol *#*. This three sections

are identified by the keywords *Zones*, *Vertices* and *Triangles* and contain respectively the number of BEM regions (piecewise homogeneous layers having different mechanical parameters), the coordinate table and the connectivity table, see Fig.D.3. Noting with  $NN$  the total number of nodes and  $NZ$  the number of zones, the coordinate table has size  $NN \times (3+NZ)$  because for each boundary node it contains its three Cartesian coordinates and the list of the zones to which the node belongs. For example, if a node lies on the interface between the Zone 1 and the Zone 2 in a problem counting three regions, the interface node references are given by  $\text{ind}_Z(\text{node}) = [1, 2, 0]$ . In the section *Triangles*, after a single-row list of the number of boundary elements per zone ( $NE_{NZ}$ ), the connectivity tables are listed per zone, after the keyword *Zone* and the corresponding label. Notation  $E_\ell^{NZ}(i)$  corresponds to the label of the  $i$ -th node of the  $\ell$ -th boundary element belonging to the zone  $NZ$ .

2. *Problem data file (problem.DAT).* This text file contains the definition of (i) the angular

---

```

Zones
NZ
#
Vertices
NN
x1    y1    z1    indZ(1)
⋮
xNN    yNN    zNN    indZ(NN)
#
Triangles
NE1    ...    NENZ
Zone
1
E11(1)  E11(2)  E11(3)
⋮
ENE11(1)  ENE11(2)  ENE11(3)
(...)
Zone
NZ
ENENZNZ(1)  ENENZNZ(2)  ENENZNZ(3)
⋮
ENENZNZ(1)  ENENZNZ(2)  ENENZNZ(3)
#

```

---

**Figure D.3:** Format of the geometry input file *problem.GEO*. Sections are separated by the symbol  $\#$ .  $NZ$  is the number of zones or subregions in the domain,  $NN$  the number of mesh nodes and  $NE_{NZ}$  is the number of boundary elements in the zone  $NZ$ .

frequency  $\omega$  to which the system is harmonically submitted, (ii) the material properties of each zone and (iii) the boundary data and unknown degrees of freedom. For each zone  $NZ$ , the material properties needed for the definition of the mechanical parameters are the shear modulus  $\mu_{NZ}$ , the Poisson's ratio  $\nu_{NZ}$ , the mass density  $\rho_{NZ}$  and the shear and compression damping factors  $\beta_{NZ}^S$  and  $\beta_{NZ}^P$  for characterizing the attenuation in shear and compression waves respectively. Often, the same value is considered for the two factors, i.e.  $\beta_{NZ}^S = \beta_{NZ}^P$  [94]. The format of the data file is shown in Fig.D.4. Sections are always separated by the symbol  $\#$ . After the definition of the angular frequency and the material properties, six sections define the boundary data and unknown degrees of freedom (DoFs). In sections *DISP\_UNK* and *TRAC\_UNK* the unknown displacement and traction DoFs are defined. By convention,  $i$  ( $i = 1, 3$ ) defines the Cartesian direction of the  $j$ -th collocation node or element. The keyword *DIR* must be specified for each DoF. Sections *DISP\_B* and *TRAC\_B* contain the displacement and tractions time-harmonic boundary data respectively. The complex value *val* is assigned to each  $i$ -th direction of the  $j$ -th node or element.

In case of scattering problems formulated in terms of total field, the sections *NODE\_RHS* and *TRAC\_RHS* are devoted to the definition of the known free field, see Section 2.2.3. The format to be used here is the same as in sections *DISP\_B* and *TRAC\_B*.

3. *Integral representation input file (problem.POSTGEO)*. In this file, the coordinate table of the interior points *NR* for which solution is computed by using the integral representation (2.5) is listed, see Fig.D.5. The IR is applied provided the boundary integral equation (BIE) has been solved on all the domain boundaries (and eventual interfaces).
4. *Input files for scattering problems with total field formulation (problem.GEO2 and problem.DAT2)*. These files contain the geometry and data (free field) of the planar free surface that appears in the right hand side of the BIE (2.24). The geometry file *problem.GEO2* defines the geometry of the discretized (truncated) free-surface. The format is the same as *problem.GEO*, but the keyword *Zone* refers to the region for which the integral is computed. The problem data file contains only the *DISP\_B* section of displacement free field.

#### D.1.4 Output files

COFFEE has four fixed output files. Two of them (respectively named *problem.DISP\_NODES.txt* and *problem.TRAC\_ELEM.txt*) collect the computation results, the other two contain information about the computation itself (*ERROR.err* and *STATUS.log*). If the integral representation has been required for a certain set of points (through the input file *problem.POSTGEO*),

In *problem.DISP\_NODES.txt*, for each node  $n$  the Cartesian component of the complex displacement are given in the following order ( $n = 1, NN$ ):

---

$n$	$\Re(u_x)$	$\Re(u_y)$	$\Re(u_z)$	$\Im(u_x)$	$\Im(u_y)$	$\Im(u_z)$
-----	------------	------------	------------	------------	------------	------------

---

---

**Problem**
 $\omega$ 

#

**Material properties** $\mu_1 \quad \nu_1 \quad \rho_1 \quad \beta_1^S \quad \beta_1^P$ 

...

 $\mu_{NZ} \quad \nu_{NZ} \quad \rho_{NZ} \quad \beta_{NZ}^S \quad \beta_{NZ}^P$ 

#

**DISP\_UNK****DIR**

i

j

...

#

**TRAC\_UNK****ZONE**

1

**DIR**

i

j

...

**ZONE****NZ**

...

#

**DISP\_B****DIR**i  $(\Re(val), \Im(val))$ 

j

...

#

**TRAC\_B****ZONE**

1

**DIR**i  $(\Re(val), \Im(val))$ 

j

...

**ZONE****NZ**

...

#

**NODE\_RHS**

#

**ELEM\_RHS**

#

---

**Figure D.4:** Format of the geometry input file problem.DAT.



---

```

Vertices
NR
Zone
1
x1    y1    z1
⋮
Zone
NZ
⋮
xNR  yNR  zNR
#

```

---

**Figure D.5:** Format of the geometry input file *problem.POSTGEO*. Coefficient *NR* is the number of nodes for which integral representation is computed.

In *problem.TRAC\_ELEM.txt*, the element tractions are given with the following convention ( $e = 1, NE$ ):

---

$e$	$\Re(t_x)$	$\Re(t_y)$	$\Re(t_z)$	$\Im(t_x)$	$\Im(t_y)$	$\Im(t_z)$
-----	------------	------------	------------	------------	------------	------------

---

During the computation, the most important information are collected in the file *STATUS.log*: the FMM octree geometry (number of levels, cells size), the GMRES parameters and its convergence history, the number of iterations and the CPU time per iteration and the residuum at the last iteration. In case of error during the computation, the file *ERROR.err* should contains the explication of the error nature and its localisation in the source code.

### D.1.5 Post-processing

The results can be easily exploited using Matlab and visualized by the help of scientific visualization software as for example the OpenGL-based software *medit 3.0* [123].

## D.2 CUSIM PROGRAM

### D.2.1 Introduction

The program *CUSIM* solves 3-D time-harmonic linear (visco-)elastodynamics problems by coupling the finite element method (FEM) and the fast multipole boundary element method (FMBEM) according to the simultaneous approach proposed in Section 3.6. Due to external constraints, we have chosen to integrate the FEM subroutines needed by the coupling algorithm in the program *COFFEE*, thus resulting in the hybrid Fortran 90-based code *CUSIM*. The preparation of input files and the analysis of output results are guided by two Matlab codes

called PRE-CUSIM and POST-CUSIM. Although computations can be performed independently with CUSIM (provided the input files are coherent and available in the right format), these pre- and post-processing programs are very useful for piloting the domain decomposition and the generation of the FEM and BEM mesh (that should perfectly match at the common interface). A diagram of the main steps of the program CUSIM are represented in Fig.D.6.

### D.2.2 Installation requirements.

For the compilation, CUSIM requires the same libraries and routines needed by COFFEE and detailed in Section D.1.2, i.e. MKL, GMRES and the Flexible-GMRES. The Makefile of CUSIM is almost the same of CX-COFFEE, see Fig.D.2. Only two Fortran files, *read\_FEM.f90* and *comp\_FEM.f90* are added to the object files list. These two files contain the FEM subroutines. After compilation under Linux platforms, the executable CUSIM can be easily launched from the prompt.

### D.2.3 Input files

CUSIM needs two input files for the BEM subdomain and one for the FEM subdomain. The input files required for the BEM subdomain are the geometry file *problem.GEO* and the data file *problem.DAT*. These two files are the same of those needed by COFFEE, and their format has been detailed in Section D.1.3. Referring to the example depicted in Fig.D.7, the geometry input file defines the discretized subdomain boundary  $\partial\Omega_B$ , whereas the data file describes the time-harmonic boundary data, i.e. prescribed tractions on the surface  $\Gamma_B$  and unknown displacements and efforts field across the common interface  $\Phi_{BF}$ .

The input file *problem.FEM.GEO* contains all characteristics of the FEM subdomain geometry and of the mesh. As shown in Fig.D.8, the file is composed of five sections separated by the symbol # :

- *FE Vertices.* In the first line, the number  $NN$  of mesh nodes and the number  $NM$  of materials in the FEM subdomain are listed. In each of the successive  $NN$  rows, after the three coordinates of the FEM  $i$ -th node, the local number of the corresponding BE-node  $N_B(i)$  on the matching grid is reported.
- *FE Tetrahedra.* The number of three-dimensional finite elements of the FEM volume mesh (for the moment limited to linear four-noded tetrahedra) is followed by the global  $NN \times 4$  connectivity table that defines each element through the list of its nodes. The total number of entries for each line is  $4+1$ , the last integer coefficient specifying the material type of the element.
- *FE Interface T3.* After the number  $NI$  of three-noded triangles that constitute the interface mesh, the connectivity table of the trace of interface tetrahedra that constitute the interface mesh on the FEM subdomain side is reported.

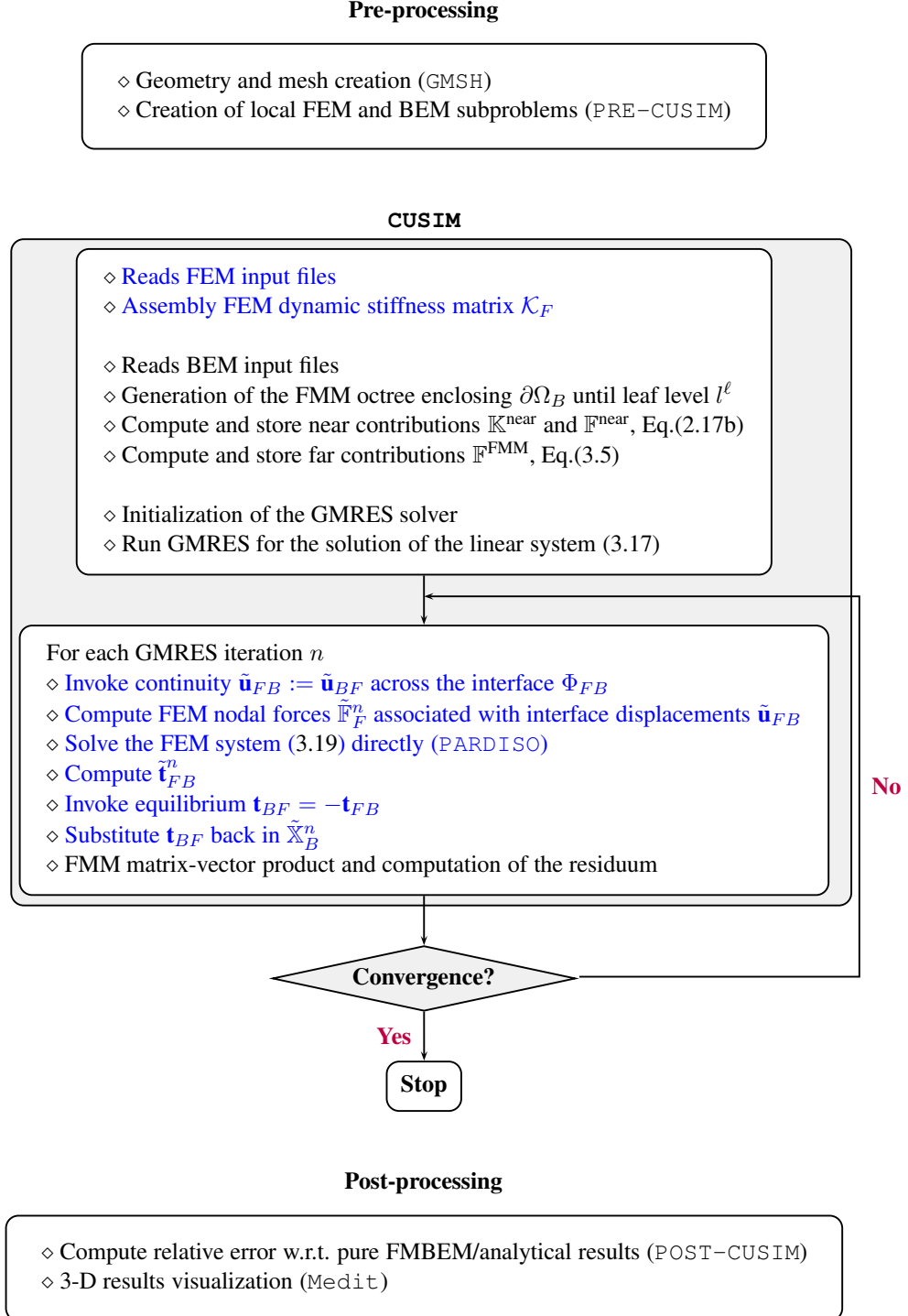


**Figure D.6:** Schematic description of the simultaneous coupling algorithm implemented in CUSIM, after a pre-processing step for the generation of the global mesh and of the local subproblems. The FEM steps are highlighted in blue whereas the BEM steps are in black.

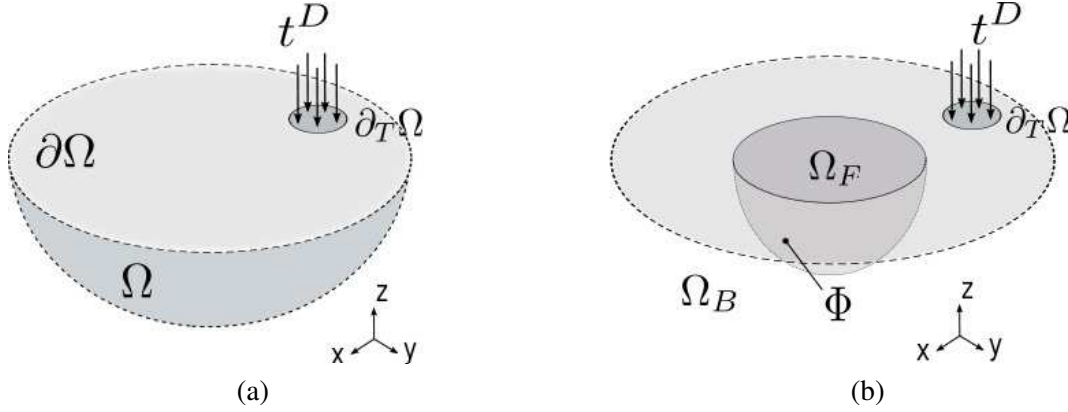


**Figure D.7:** Example of problem that can be solved by using the simultaneous FEM/FMBEM coupling. The original semi-infinite domain  $\Omega$  (a) is split into two non-overlapping subdomains  $\Omega_B$  (discretized by BEM) and  $\Omega_F$  (discretized by FEM) (b).

- **Interface tetrahedra list.** This section simply contains the vertical list of tetrahedra having at least one node on the interface  $\Phi$ .
- **Material properties.** The mechanical properties of the materials presents in the FEM subdomain are listed here: the shear modulus  $\mu$ , the Poisson's ration  $\nu$ , the mass density  $\rho$  and the Rayleigh coefficients required for the definition of the Rayleigh damping matrix.

**PRE-CUSIM.** A Matlab program called PRE-CUSIM has been written to drive the creation of the BEM and FEM local subproblems (Fig.D.7b) starting from the original unique problem defined on the domain  $\Omega$  (Fig.D.7a). The global mesh is generated with GMSH v.1.60.1, free software available with documentation at the web page [www.geuz.org/gmsh/](http://www.geuz.org/gmsh/). In GMSH, the geometry of the domain  $\Omega$  is defined by means of the file *problem.geo*<sup>1</sup>, whose format is described in Fig.D.10 for the example problem of Fig.D.7. The order used in the definition of *Circle*, *Line Loop* and *Ruled Surface* determines the orientation of the surface normal, as shown in Fig.D.9d. Indeed, GMSH will generate a mesh whose traces on each surface respect the normal orientation defined in the geometry file (the normal orientation of a mesh being determined by the node ordering, via the evaluation of a cross product). For an exhaustive description of the geometry file format we refer the reader to the GMSH documentation.

PRE-CUSIM requires the following information: the problem name, the number of materials in the FEM sub-domain, the possibility to store in text format certain geometry information that can be reused for successive computations (e.g. list of interface tetrahedra), the number characterizing each physical entity (defined in the last lines of Fig.D.10) and the problem data (circular frequency, material properties). The Rayleigh coefficients required for the definition of the FEM damping matrix are computed by the code starting from values of damping factor and

<sup>1</sup>Note: do not confuse the GMSH file *problem.geo* with the *problem.GEO* (capital *.GEO* extension) input file of COFFEE

---

```

FE Vertices
NN      NM
x1    y1    z1  NB(1)
:
:
xNN  yNN  zNN  NB(NNF)
#
FE Tetrahedra
NE
E1(1)  E1(2)  E1(3)  E1(4)  indM(1)
:
:
ENE(1)  ENE(2)  ENE(3)  ENE(4)  indM(NE)
#
FE Interface T3
NI
E=I1(1)  I1(2)  I1(3)
:
:
INE(1)  INE(2)  INE(3)  INE(4)
#
Interface tetrahedra list
1
:
:
NT
#
Material properties
μ1  ν1  ρ1  a1  b1
...
μNM  νNM  ρNM  aNM  bNM
#

```

---

**Figure D.8:** Format of the geometry input file *problem\_FEM.GEO*. *NN* is the number of FEM-mesh nodes, *NE* the number of finite elements (linear four-noded tetrahedra), *NM* the number of materials in the FEM subdomain, *NI* the number of nodes lying on the FE-BE interface  $\Phi$  and *NT* the number of tetrahedra having at least one node on  $\Phi$ . In the Material properties section, *a* and *b* are the coefficients required for the coherent definition of the damping Rayleigh matrix.

respecting the relations described in Sec.3.3.2. With this information, PRE-CUSIM reads the mesh of the original problem and the definition of the physical entities assigned to the various portion of surfaces or volumes. Then, it defines the local subproblems and creates the input files for the code CUSIM.

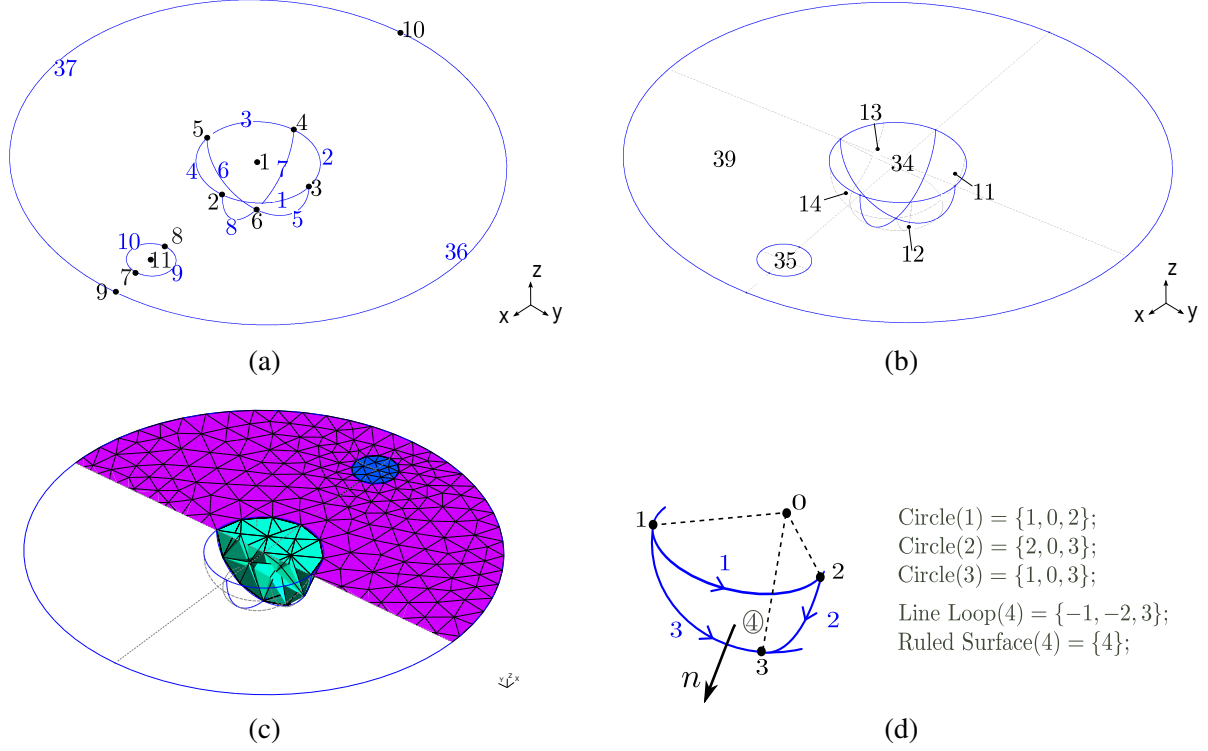


**Figure D.9:** Graphic visualization with the code *GMSH*: definition (a) of points number (black), circles number (blue), (b) of plane and ruled surfaces and (c) of the final mesh for the problem of Fig.D.7. The convention for orientation of loop lines and surface normals is shown in (d).

#### D.2.4 Output files

CUSIM produces two output text files containing the results (complex nodal displacements) in the FE- and in the BE- subdomains, called *resu\_dispFEM.txt* and *resu\_dispBEM.txt* respectively. For each node, the Cartesian components of displacement are given in the following order:

---

$n$	$\Re(u_x)$	$\Re(u_y)$	$\Re(u_z)$	$\Im(u_x)$	$\Im(u_y)$	$\Im(u_z)$
-----	------------	------------	------------	------------	------------	------------

---

where  $n = 1, NN_{FE}$  in *resu\_dispFEM.txt* and  $n = 1, NN_{BE}$  in *resu\_dispBEM.txt*.

#### D.2.5 Post-processing

The 3-D visualization of results can be exploited by means of different software such *GMSH* or the OpenGL-based software *medit 3.0* [123]. A Matlab function called *POST-CUSIM* has been written to read the CUSIM output files, re-combine the local FEM and BEM results in a global results set, prepare the *Medit* input files in the right format and eventually compute the relative error between results obtained using the simultaneous coupling with analytical results.

---

```
\\Mesh density coefficients
```

```
lcFE=.03;
```

```
lcBE=.03;
```

```
\\Geometry
```

```
rFE=.5;
```

```
rLOAD=.2;
```

```
dist=1.5;
```

```
rBE=2.;
```

```
Point(1) = {0, 0, 0, lcFE};
```

```
Point(2) = {rFE, 0, 0, lcFE};
```

```
Point(3) = {0, rFE, 0, lcFE};
```

```
Point(4) = {-rFE, 0, 0, lcFE};
```

```
Point(5) = {0, -rFE, 0, lcFE};
```

```
Point(6) = {0, 0, -rFE, lcFE};
```

```
Point(7) = {rLOAD+dist, 0, 0, lcBE};
```

```
Point(8) = {-rLOAD+dist, 0, 0, lcBE};
```

```
Point(11) = {dist, 0, 0, lcFE};
```

```
Circle(1) = {2, 1, 3};
```

```
Circle(2) = {3, 1, 4};
```

```
Circle(3) = {4, 1, 5};
```

```
Circle(4) = {5, 1, 2};
```

```
Circle(5) = {3, 1, 6};
```

```
Circle(6) = {6, 1, 5};
```

```
Circle(7) = {4, 1, 6};
```

```
Circle(8) = {6, 1, 2};
```

```
Circle(9) = {7, 11, 8};
```

```
Circle(10) = {8, 11, 7};
```

```
Line Loop(11) = {-7, -2, 5};
```

```
Ruled Surface(11) = {11};
```

```
Line Loop(12) = {-5, -1, -8};
```

```
Ruled Surface(12) = {12};
```

```
Line Loop(13) = {-3, 7, 6};
```

```
Ruled Surface(13) = {13};
```

```
Line Loop(14) = {8, -4, -6};
```

```
Ruled Surface(14) = {14};
```

```
Line Loop(32) = {1, 2, 3, 4};
```

```
Line Loop(33) = {9, 10};
```

```
Plane Surface(34) = {32};
```

```
Plane Surface(35) = {33};
```

```
Surface Loop(15) = {14, 11, 13, 12, 34};
```

```
Volume(31) = {15};
```

```
Point(9) = {rBE, 0, 0, lcBE};
```

```
Point(10) = {-rBE, 0, 0, lcBE};
```

```
Circle(36) = {9, 1, 10};
```

```
Circle(37) = {10, 1, 9};
```

```
Line Loop(38) = {36, 37};
```

```
Plane Surface(39) = {-32, 33, -38};
```

```
\\Definition of physical entities
```

```
Physical Surface(27) = {11, 12, 13, 14};
```

```
\\Interface  $\Phi_{FB}$ 
```

```
Physical Volume(28) = {31};
```

```
\\FEM volume
```

```
Physical Surface(29) = {35};
```

```
\\Load surface
```

```
Physical Surface(30) = {34};
```

```
\\FEM free-surface
```

```
Physical Surface(40) = {39};
```

```
\\BEM free-surface
```

---

**Figure D.10:** Format of the geometry GMSH input file problem.geo for the example of Fig.D.9. Comments are preceded by the symbol \\. Documentation for write this kind of file is available on the GMSH website.

### D.3 CUSEQ PROGRAM

#### D.3.1 Introduction

CUSEQ is a Matlab-based program that drives the iterative coupling between the FEM code *CESAR-LCPC* and the FMBEM solver *COFFEE*. The external FEM program should assemble the damped dynamic stiffness matrix, the known right-hand side and solve the FEM linear problem. In particular, using an existing FEM code is advantageous because different types of finite elements (e.g. beam elements) or anisotropic laws can be used within the FEM subdomain. The only condition to be respected is that the trace of the finite elements on the interface  $\Phi_{FB}$  must guarantee the conforming match with the BE subdomain discretization in three-noded triangles. For the reasons explained in Sec. 3.1.2, if the finite element model employs only four-noded tetrahedra, some FEM functions have been implemented in CUSEQ in order to have a higher flexibility than using the actual *CESAR* module *LINC*.

#### D.3.2 Installation requirements.

The program CUSEQ is a Matlab R2010a function and does not require specific packages nor libraries in itself. However, as it drives a sequential coupling between external codes, one should ensure that the external codes are well installed before use. For the specific installation requirements please refer to Section D.1 for *COFFEE* and to [160, 161] for *CESAR*.

#### D.3.3 Input data

CUSEQ does not require specific input files. However, the head of the main program *CUSEQ.M* should be modified to define the problem mechanical parameters, amplitude and circular frequency of the boundary data and the options for the computation (name of the FEM external code, etc).

#### D.3.4 Output data and post-processing

CUSEQ alternates the solution of local BEM and FEM subproblems by using *COFFEE* and *CESAR* (or own CUSEQ subroutines) respectively. Once the convergence of the iterative coupling algorithm is reached, the solution will be available for both subproblems separately, according to the program adopted. Thus, BEM results obtained with *COFFEE* are written in the files *problem.DISP\_NODES.txt* and *problem.TRAC\_ELEM.txt*. The nodal FEM displacement results are stored in the file *problem\_uFE.dat* with the following format:

---

$\Re(u_x)$	$\Re(u_y)$	$\Re(u_z)$	$\Im(u_x)$	$\Im(u_y)$	$\Im(u_z)$
------------	------------	------------	------------	------------	------------

---



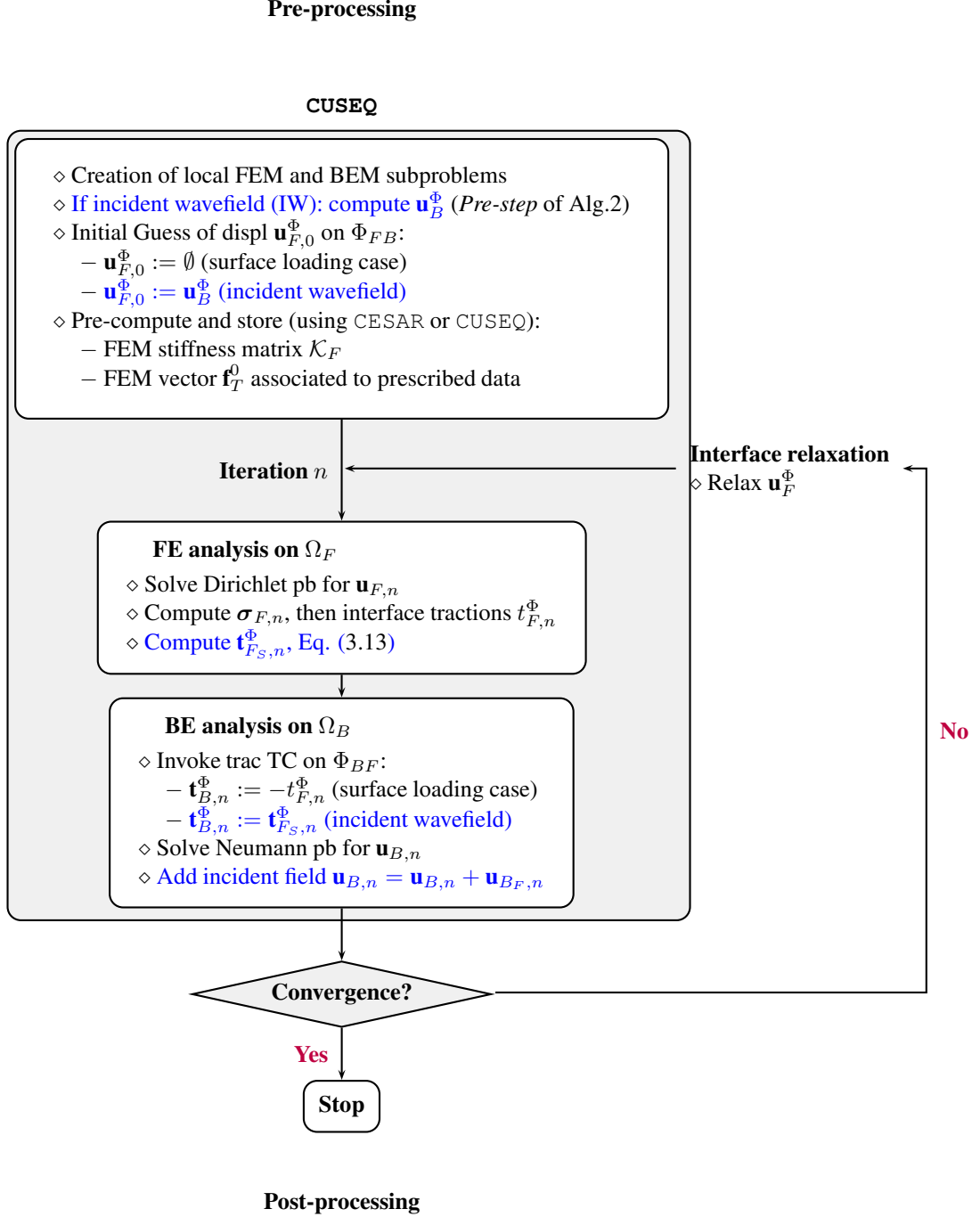


**Figure D.11:** Schematic description of the simultaneous coupling algorithm implemented in CUSEQ. If the FEM mesh is exclusively made of linear four-noded tetrahedra, the code CUSEQ can solve the FEM subproblem independently. Text in blue indicates steps followed by the algorithm in case of incident wavefield.



# References

- [1] Intel (R) Math Kernel Library User's Guide for the Linux Operating System, 2007.
- [2] N.A. Abrahamson. Spatial variation of multiple supports inputs. In *Proc of 1st US Seminar on Seismic Evaluation and Retrofit of Steel Bridges, A Caltrans and Univ. of California at Berkeley Seminar, San Francisco CA.*, 1993.
- [3] M. Abramowitz and I. Stegun. *Handbook of Mathematical Functions with Formulas, Graphs, and Mathematical Tables*. Dover Publications, 1964.
- [4] J.D. Achenbach. *Wave propagation in elastic solids*. North-Holland Publishing Company, 1975.
- [5] M Adam, G Pflanz, and G Schmid. Two- and three-dimensional modelling of half-space and train-track embankment under dynamic loading. *Soil Dyn. Earthquake Eng.*, 19:559–573, 2000.
- [6] M. Adam and O. von Estorf. Reduction of train-induced building vibrations by using open and filled trenches. *Comput. Struct.*, 83:11–24, 2005.
- [7] S. Ahmad, T.M. Al-Hussaini, and K.L. Fishman. Investigation on active isolation of machine foundations by open trenches. *J. Geotech. Eng.*, 122:454–461, 1996.
- [8] S. Ahmad and T.m. Alhussaini. Simplified design for vibration screening by open and in-filled trenches. *J. Geotech. Eng.*, 117:67–88, 1991.
- [9] K. Aki and K.L. Larner. Surface motion of a layered medium having an irregular interface due to incident plane sh waves. *J. Geophys. Res.*, 75:933–954, 1970.
- [10] K. Aki and P.G. Richard. *Quantitative seismology*, volume 1 and 2. Freeman, San Francisco, 2nd edition, 1980.
- [11] T.M. Al-Hussaini and S. Ahmad. Design of wave barriers for reduction of horizontal ground vibration. *J. Geotech. Eng.*, 117:616–636, 1991.
- [12] T.M. Al-Hussaini and S. Ahmad. Active isolation of machine foundations by in-filled trench barriers. *J. Geotech. Eng.*, 122:288–294, 1996.
- [13] T.M. Al-Hussaini, S. Ahmad, and J.M. Baker. Numerical and experimental studies on vibration screening by open and in-filled trench barriers. pages 241–250, 2000. Wave 2000 International Workshop, Bochum, Germany, Dec 13-15, 2000.
- [14] Z. Alterman and F.C. Zaral. Propagation of elastic waves in layered media by finite difference methods. *Bull. Seismol. Soc. Amer.*, 58:367–398, 1968.
- [15] L. Andersen and C. J. C. Jones. Coupled boundary and finite element analysis of vibration from railway tunnels - a comparison of two- and three-dimensional models. *J. Sound Vibr.*, 293:611–625, 2006.
- [16] L. Andersen, S. R. K. Nielsen, and S. Krenk. Numerical methods for analysis of structure and ground vibration from moving loads. *Comput. Struct.*, 85:43–58, 2007.
- [17] L. Andersen and S.R.K. Nielsen. Reduction of ground vibration by means of barriers or soil improvement along a railway track. *Soil Dyn. Earthquake Eng.*, 25:701–716, 2005.
- [18] S. Aoi and H. Fujiwara. 3d finite-difference method using discontinuous grids. *Bull. Seismol. Soc. Amer.*, 89:918–930, 1999.
- [19] L Auersch. Dynamic interaction of an infinite-plate and a half-space due to a harmonic point load. *Arch. Appl. Mech.*, 64:346–356, 1994.

- 
- [20] J. Aviles and F.J. Sanchez-Sesma. Foundation isolation from vibrations using piles as barriers. *J. Eng. Mech.*, 114:1854–1870, 1988.
  - [21] P.K. Banerjee, S. Ahmad, and K. Chen. Advanced application of bem to wave barriers in multi-layered 3-dimensional soil media. *Earthquake Eng. Struct. Dyn.*, 16:1041–1060, 1988.
  - [22] H. Bao, J. Bielak, O. Ghattas, F.L. Kallivokas, D.R. O'Hallaron, J.R. Shewchuk, and J. Xu. Large-scale simulation of elastic wave propagation in heterogeneous media on parallel computers. *Comp. Meth. Appl. Mech. Eng.*, 152:85–102, 1998.
  - [23] M. S. Bapat, L. Shen, and Y. J. Liu. Adaptive fast multipole boundary element method for three-dimensional half-space acoustic wave problems. *Eng. Anal. Bound. Elem.*, 33:1113–1123, 2009.
  - [24] JR Barber. Surface displacements due to a steadily moving point force. *J. Appl. Mech. ASME*, 63:245–251, 1996.
  - [25] P.-Y. Bard. Diffracted waves and displacement field over two-dimensional elevated topographies. *Geophysical. J. R. Astr. Soc.*, 71:111–120, 1982.
  - [26] P.Y. Bard and pp. Bouchon, M. The two dimensional resonance of sediment filled valleys. *Bull. Seismol. Soc. Amer.*, 75:519–541, 1985.
  - [27] P.Y. Bard, J.L. Chazelas, P. Guéguen, M. Kham, and Semblat J.F. *Assessing and managing earthquake risk*, chapter 5: Site-city interaction. Springer, 2005.
  - [28] A. Bayliss, C.I. Goldstein, and E. Turkel. On accuracy conditions for the numerical computation of waves. *J. Comput. Phys.*, 59:396–404, 1985.
  - [29] A. Bayliss and E. Turkel. Radiation boundary conditions for wave-like equations. *Comm. Pure Appl. Math.*, 33:707–725, 1980.
  - [30] M. Bebendorf and S. Rjasanow. Adaptive low-rank approximation of collocation matrices. *Computing*, 70:1–24, 2003.
  - [31] E. Bécache, S. Fauqueux, and P. Joly. Stability of perfectly matched layers, group velocities and anisotropic waves. *J. Comput. Phys.*, 188:399–433, 2003.
  - [32] P.M. Belotserkovskiy. On the oscillations of infinite periodic beams subjected to a moving concentrated force. *J. Sound Vibr.*, 193:705–712, 1996.
  - [33] F. Ben Belgacem. The mortar finite element method with lagrange multipliers. *Numerische Mathematik*, 84:173–197, 1999.
  - [34] Jean-Pierre Berenger. A perfectly matched layer for the absorption of electromagnetic waves. *J. Comput. Phys.*, 114:185–200, 1994.
  - [35] D.E. Beskos. Dynamic inelastic structural analysis by boundary element methods. *Archive of Computational Methods in Engineering*, 2:55–87, 1995.
  - [36] D.E. Beskos, B. Dasgupta, and I.G. Vardoulakis. Vibration isolation using open or filled trenches. part1: 2-d homogeneous soil. *Comput. Mech.*, 1:43–63, 1986.
  - [37] P. Bettess. *Infinite elements*. Penshaw Press (1992), 1992.
  - [38] G. Beylkin, R. Coifman, and V. Volkhlin. Fast wavelet transforms and numerical algorithms. *Commun. Pure Appl. Math.*, 44:141–183, 1991.
  - [39] J. Bielak. Earthquake ground motion and structural response in alluvial valleys. *J. Geotech. Geoenviron. Eng.*, 125:413–423, 1999.
  - [40] J. Bielak, O. Ghattas, and E.J. Kim. Parallel octree-based finite element method for large-scale earthquake ground motion simulation. *Comput. Model. Eng. Sci.*, 10:99–112, 2005.
  - [41] M.A. Biot. Theory of wave propagation of elastic waves in a fluid-saturated porous solid. i: Low-frequency range. *J. Acoust. Soc. Amer.*, 28:168–178, 1956.
  - [42] J.L. Bogdanoff, J.E. Goldberg, and A.J. Schiff. The effect of ground transmission time on the response of long structures. *Bull. Seismol. Soc. Amer.*, 55:627–640, 1965.
  - [43] T. Bohlen. Parallel 3-d viscoelastic finite difference seismic modelling. *Computers & Geosciences*, 28:887–

- 899, 2002.
- [44] M. Bonnet. *Boundary Integral Equation Methods for Solids and Fluids*. Wiley, 1999.
  - [45] M. Bonnet, G. Maier, and C. Polizzotto. Symmetric galerkin boundary element method. *Appl. Mech. Rev.*, 51:669–704, 1998.
  - [46] D.M. Boore and M.D. Zoback. Two-dimensional kinematical fault modeling of the pacoima dam strong-motion recordings of the february, 9, 1971, san fernando earthquake. *Bull. Seismol. Soc. Amer.*, 64:555–570, 1974.
  - [47] M. Bouchon. Effects of topography on surface motion. *Bull. Seismol. Soc. Amer.*, 63:615–622, 1973.
  - [48] M. Bouchon and F.J. Sánchez-Sesma. Boundary integral equations and boundary elements methods in elastodynamics. *Advances in Geophysics*, 48:157–189, 2007.
  - [49] T. Bourbié, O. Coussy, and B. Zinszner. *Acoustics of porous media*. Edition Technip, 1987.
  - [50] C.A. Brebbia, J.C.F. Telles, and L.C. Wrobel. *Boundary Element Techniques*. Springer, 1984.
  - [51] C.A. Brebbia and L.C. Wrobel. *The boundary element method for engineers*. Computer methods in fluids. London/New York: Pentech Press/Halstead Press, 1978.
  - [52] Dominik Brunner, Guenther Of, Michael Junge, Olaf Steinbach, and Lothar Gaul. A fast be-fe coupling scheme for partly immersed bodies. *Int. J. Num. Meth. Eng.*, 81:28–47, 2010.
  - [53] H.D. Bui, B. Loret, and M. Bonnet. Régularisation des équations intégrales de l'élastostatique et de l'élastodynamique. *C.R. Acad. Sci., Série 2, Mécanique, Physique, Chimie, Sciences de l'univers, Sciences de la Terre*, 300:633–636, 1985.
  - [54] A.J. Burton and G.F. Miller. The application of integral equation methods to the numerical solution of some exterior boundary-value problems. *Proc. Royal Soc. London*, 323:201–220, 1971.
  - [55] G.N. Bycroft. Forced vibrations of a circular plate on a semi-infinite elastic space and on an elastic stratum. *Phil. Trans. Royal Soc. London*, 248, Ser.A:327–368, 1956.
  - [56] X.-C. Cai and O.B. Widlund. Domain decomposition algorithms for indefinite elliptic problems. *SIAM J. Sci. Stat. Comp.*, 13:243–258, 1992.
  - [57] José M. Carcione. Wave propagation simulation in a linear viscoelastic medium. *Geophysical Journal*, 95:597–611, 1988.
  - [58] B. Carpentieri, I.S. Duff, L. Giraud, and Sylvand G. Combining fast multipole techniques and an approximate inverse preconditioner for large electromagnetism calculations. *SIAM J. Sci. Comput.*, 27:774–792, 2005.
  - [59] E. Celebi. Three-dimensional modelling of train-track and sub-soil analysis for surface vibrations due to moving loads. *Appl. Math. Comput.*, 179:209–230, 2006.
  - [60] E Celebi and G Schmid. Investigation of ground vibrations induced by moving loads. *Engineering Structures*, 27:1981–1998, 2005.
  - [61] S. Chaillat. *Fast Multipole Method for 3-D elastodynamic boundary integral equations. Application to seismic wave propagation*. PhD thesis, Ecole Nationale des Ponts et Chaussées, 2008.
  - [62] S. Chaillat, M. Bonnet, and J.-F. Semblat. A multi-level fast multipole BEM for 3-D elastodynamics in the frequency domain. *Comp. Meth. Appl. Mech. Eng.*, 197:4233–4249, 2008.
  - [63] S Chaillat, M. Bonnet, and J.F. Semblat. A new fast multi-domain bem to model seismic wave propagation and amplification in 3d geological structures. *Geophys. J. Int.*, 2009.
  - [64] S. Chaillat and H.D. Bui. Resolution of linear viscoelastic equations in the frequency domain using real Helmholtz boundary integral equations. *Comptes Rendus Mecanique*, 335:746–750, 2007.
  - [65] S. Chaillat, J.F. Semblat, and M. Bonnet. A preconditioned 3-d multi-region fast multipole solver for seismic wave propagation in complex geometries. *Commun. Comput. Phys.*, 11:594–609, 2012.
  - [66] E. Chaljub, D. Komatitsch, J.-P. Vilotte, Y. Capdeville, B. Valette, and G. Festa. Spectral-element analysis in seismology. *Advances in Geophysics*, 48:365–419, 2007.
  - [67] B. Chareyre, A. Cortis, E. Catalano, and E. Barthélemy. Pore-scale modeling of viscous flow and induced

- forces in dense sphere packings. *Transport in Porous Media*, pages 1–21, 2011.
- [68] W.C. Chew, H.Y. Chao, T.J. Cui, S. Ohnuki, Y.C. Pan, J.M. Song, S. Velamparambil, and J.S. Zhao. Fast integral equation solvers in computational electromagnetics of complex structures. *Eng. Anal. Bound. Elem.*, 27:803–823, 2003.
- [69] K. Chopra, Anil. *Dynamics of structures*. Prentice Hall, 2001.
- [70] R.M. Christensen. *Theory of viscoelasticity*. Dover Publications, 1982.
- [71] B. Cockburn, G.E. Karniadakis, and Chi-Wang Shu. *The Development of Discontinuous Galerkin Methods*, chapter 1, pages 3–50. Springer-Verlag Berlin, 2000.
- [72] HB Coda and WS Venturini. On the coupling of 3d bem and fem frame model applied to elastodynamic analysis. *Int. J. Solids Struct.*, 36:4789–4804, 1999.
- [73] HB Coda, WS Venturini, and MH Aliabadi. A general 3d bem/fem coupling applied to elastodynamic continua/frame structures interaction analysis. *Int. J. Num. Meth. Eng.*, 46:695–712, 1999.
- [74] R. Coifman, V. Rokhlin, and S. Wandzura. The fast multipole method for the wave equation: a pedestrian description. *IEEE Antennas and Propagation Magazine*, 35:7–12, 1993.
- [75] F. Collino, S. Ghanemi, and P. Joly. Domain decomposition method for harmonic wave propagation: a general presentation. *Comput. Meth. Appl. Mech. Eng.*, 184:171–172, 2000.
- [76] C. Comina and S. Foti. Surface wave tests for vibration mitigation studies. *J. Geotech. Geoenviron. Eng.*, 133:1320–1324, 2007.
- [77] M. Costabel. *Boundary Elements IX*, chapter Symmetric methods for the coupling of finite elements and boundary elements, pages 414–420. Springer-Verlag, Berlin, Heidelberg, 1987.
- [78] P.A. Cundall and O.D.L. Strack. A discrete numerical model for granular assemblies. *Geotechnique*, 29:47–65, 1979.
- [79] O. Czygan and O. von Estorff. Fluid-structure interaction by coupling bem and nonlinear fem. *Eng. Anal. Bound. Elem.*, 26:773–779, 2002.
- [80] P. Dangla, J.F. Semblat, H. Xiao, and N. Delépine. A simple and efficient regularization method for 3d bem : application to frequency-domain elastodynamics. *Bull. Seismol. Soc. Amer.*, 95:1916–1927, 2005.
- [81] E. Darve. The fast multipole method i: Error analysis and asymptotic complexity. *SIAM J. Numer. Anal.*, 38:98–128, 2000.
- [82] E Darve. The fast multipole method: Numerical implementation. *J. Comput. Phys.*, 160:195–240, 2000.
- [83] E Darve and P Have. Efficient fast multipole method for low-frequency scattering. *J. Comput. Phys.*, 197:341–363, 2004.
- [84] S.M. Day. Efficient simulation of constant  $q$  using coarse-grained memory variables. *Bull. Seismol. Soc. Amer.*, 88:1051–1062, 1998.
- [85] S.M. Day and C. Bradley. Memory-efficient simulation of anelastic wave propagation. *Bull. Seismol. Soc. Amer.*, 91:520–531, 2001.
- [86] S.M. Day and J.B. Minster. Numerical simulation of attenuated wavefields using a padé approximant method. *Geophys. J. Royal Astron. Soc.*, 78:105–118, 1984.
- [87] A. de La Bourdonnaye, C. Farhat, A. Macedo, F. Magoulès, and F.-X. Roux. A non-overlapping domain decomposition method for the exterior helmholtz problem. *Contemporary Mathematics*, 218:42–66, 1998.
- [88] N. Delépine, L. Lenti, G. Bonnet, and J. F. Semblat. Nonlinear viscoelastic wave propagation: an extension of nearly constant attenuation models. *J. Eng. Mech.*, 135:1305–1314, 2009.
- [89] L. Demkowicz and F. Ihlenburg. Analysis of a coupled finite-infinite element method for exterior helmholtz problems. *Numerische Mathematik*, 88:43–73, 2001.
- [90] A. Deraemaeker, I. Babuška, and P. Bouillard. Dispersion and pollution of the fem solution for the helmholtz equation in one, two and three dimensions. *Int. J. Num. Meth. Eng.*, 46:471–499, 1999.
- [91] B. (1990). Després. Décomposition de domaine et problème de helmholtz. *C.R. Acad. Sci. Paris*, 311:313–316, 1990.

- 
- [92] R. Dobry, I. Oweis, and A. Urzua. Simplified procedures for estimating the fundamental period of a soil profile. *Bull. Seismol. Soc. Amer.*, 66:1293–1321, 1976.
  - [93] C.R. Dohrmann. A preconditioner for substructuring based on constrained energy minimization. *SIAM J. Numer. Anal.*, 25(1):246–258, 2003.
  - [94] J. Dominguez. *Boundary Elements in Dynamics*. Computational Mechanics Publications, Southampton Boston, 1993.
  - [95] J. Dominguez and T. Meise. On the use of the bem for wave propagation in infinite domains. *Eng. Anal. Bound. Elem.*, 8, Issue 3:132–138, 1991.
  - [96] Jack Dongarra and Francis Sullivan. Guest editors introduction: The top 10 algorithms. *Computing in Science and Engineering*, 2:22–23, 2000.
  - [97] C.F. Du Toit. The numerical computation of bessel functions of the first and second kind for integer orders and complex arguments. *IEEE Trans. Antennas Propag.*, 38:1341–1349, 1990.
  - [98] M. Dumbser and M. Käser. An arbitrary high order discontinuous galerkin method for elastic waves on unstructured meshes ii: The three-dimensional isotropic case. *Geophys. J. Int.*, 167:319–336, 2006.
  - [99] M. Dumbser and M. Käser. Erratum: An arbitrary high order discontinuous galerkin method for elastic waves on unstructured meshes ii: The three-dimensional isotropic case. *Geophys. J. Int.*, 171:1324, 2007.
  - [100] M. Dumbser, M. Käser, and J. de la Puente. Arbitrary high order finite volume scheme for seismic wave propagation on unstructured meshes in 2d and 3d. *Geophys. J. Int.*, 171:665–694, 2007.
  - [101] M. El-Gebeily, W.M. Elleithy, and H. Al-Gahtani. Convergence of the domain decomposition finite element-boundary element coupling methods. *Comp. Meth. Appl. Mech. Eng.*, 191:4851–4867, 2002.
  - [102] Wael M. Elleithy, H.J. Al-Gahtani, and M. El-Gebeily. Iterative coupling of be and fe methods in elastostatics. *Eng. Anal. Bound. Elem.*, 25:685–695, 2001.
  - [103] Wael M. Elleithy and M. Tanaka. Interface relaxation algorithms for bem-bem coupling and fem-bem coupling. *Comp. Meth. Appl. Mech. Eng.*, 192:2977–2992, 2003.
  - [104] Wael M. Elleithy, M. Tanaka, and A. Guzik. Interface relaxation fem-bem coupling method for elasto-plastic analysis. *Eng. Anal. Bound. Elem.*, 28:849–857, 2004.
  - [105] K Emad and GD Manolis. Shallow trenches and propagation of surface-waves. *J. Eng. Mech.*, 111:279–282, 1985.
  - [106] H. Emmerich and M. Korn. Incorporation of attenuation into time-domain computations of seismic wave fields. *Geophysics*, 52:1252–1264, 1987.
  - [107] B. Engquist, , and A. Majda. Radiation boundary conditions for acoustic and elastic calculations. *Comm. Pure Appl. Math.*, 32:313–357, 1979.
  - [108] A. C. Eringen and E. S. Suhubi. *Elastodynamics, Vol. II-Linear Theory*. Academic Pres, 1975.
  - [109] E. Faccioli, F. Maggio, R. Paolucci, and A. Quarteroni. 2d and 3d elastic wave propagation by a pseudo-spectral domain decomposition method. *Journal of Seismology*, 1:237–251, 1997.
  - [110] C. Fohrat, M. Lesoinne, and K. Pierson. A scalable dual-primal domain decomposition method. *Numerical Linear Algebra with Applications*, 7:687–714, 2000.
  - [111] C. Fohrat, A. Macedo, and M. Lesoinne. A two-level domain decomposition method for the iterative solution of high frequency exterior helmholtz problems. *Numerische Mathematik*, 85:283–308, 2000.
  - [112] C. Fohrat and F.X. Roux. A method of finite tearing and interconnecting and its parallel solution algorithm. *Int. J. Num. Meth. Eng.*, 32:1205–1227, 1991.
  - [113] Y.T. Feng and D.R.J. Owen. Iterative solution of coupled fe/be discretizations for plate-foundation interaction problems. *Int. J. Num. Meth. Eng.*, 39, i.11:1889–1901, 1996.
  - [114] G. Festa and S. Nielsen. Pml absorbing boundaries. *Bull. Seismol. Soc. Amer.*, 93:891–903, 2003.
  - [115] M Fischer and L Gaul. Fast BEM-FEM mortar coupling for acoustic-structure interaction. *Int. J. Num. Meth. Eng.*, 62:1677–1690, 2005.
  - [116] Y. Fragakis and M. Papadrakakis. A unified framework for formulating domain decomposition methods

- in structural mechanics. Technical report, Institute of Structural Analysis & Seismic Research, National Technical University Athens, 2002.
- [117] S. François, G. Lombaert, and G. Degrande. Local and global shape functions in a boundary element formulation for the calculation of traffic induced vibrations. *Soil Dyn. Earthquake Eng.*, 25:839–856, 2005.
  - [118] A. Frangi and M. Bonnet. On the application of the fast multipole method to helmholtz-like problems with complex wavenumber. *Comput. Model. Eng. Sci.*, 58:271–296, 2010.
  - [119] A. Frangi and A. di Gioia. Multipole bem for the evaluation of damping forces on mems. *Comp. Mech.*, 37:24–31, 2005.
  - [120] A. Frangi, L. Ghezzi, and P. Faure-Ragani. Accurate force evaluation for industrial magnetostatics applications with fast bem-fem approaches. *Comput. Model. Eng. Sci.*, 15, n.1:41–48, 2006.
  - [121] V. Frayssé, L. Giraud, and Gratton. A set of flexible-gmres routines for real and complex arithmetics. Technical report, CERFACS Technical Report TR/PA/98/20, public domain software available on [www.cerfacs.fr/algor/Softs](http://www.cerfacs.fr/algor/Softs), 2001.
  - [122] V. Frayssé, L. Giraud, S. Gratton, and J. Langou. A set of gmres routines for real and complex arithmetics. Technical report, CERFACS Technical Report TR/PA/03/3, public domain software available on [www.cerfacs.fr/algor/Softs](http://www.cerfacs.fr/algor/Softs), 2007.
  - [123] P. Frey. Medit: An interactive mesh visualization software. Technical report, INRIA Rapport Technique n 0253, OpenGL software available on [www.ann.jussieu.fr/frey/software.html](http://www.ann.jussieu.fr/frey/software.html), 2001.
  - [124] H. Fujiwara. The fast multipole method for solving integral equations of three-dimensional topography and basin problems. *Geophys. J. Int.*, 140:198–210, 2000.
  - [125] A.P. Gaitanaros and D.L. Karabalis. Dynamic analysis of 3-d flexible embedded foundations by a frequency domain bem-fem. *Earthquake Eng. Struct. Dyn.*, 16:653–674, 1988.
  - [126] M.J. Gander, F. Magoules, and F. Nataf. Optimized schwarz methods without overlap for the helmholtz equations. *SIAM J. Sci. Comput.*, 24:38–60, 2002.
  - [127] G. Y. Gao, Z. Y. Li, Ch. Qiu, and Z. Q. Yue. Three-dimensional analysis of rows of piles as passive barriers for ground vibration isolation. *Soil Dyn. Earthquake Eng.*, 26:1015–1027, 2006.
  - [128] L. Gaul. The influence of damping on waves and vibrations. *Mechanical Systems And Signal Processing*, 13:1–30, 1999.
  - [129] L. Gaul and M. Junge. Simulation of elastic scattering with a coupled fmbem-fe approach. *Recent Advances in Boundary Element Method*, pages 131–145, 2009.
  - [130] Walter Gautschi. Computational aspects of the three-term recurrence relations. *SIAM Review*, 9:1, 1967.
  - [131] L. Geli, P.Y. Bard, and B. Jullien. The effect of topography on earthquake ground motion: A review and new results. *Bull. Seismol. Soc. Amer.*, 78:42–63, 1988.
  - [132] N. Geng, A. Sullivan, and L. Carin. Fast multipole method for scattering from 3-d pec targets situated in a half-space environment. *Microwave Opt. Technol. Lett.*, 21:399–405, 1999.
  - [133] N. Geng, A. Sullivan, and L. Carin. Multilevel fast-multipole algorithm for scattering from conducting targets above or embedded in a lossy half space. *IEEE Trans. Geosci. Remote Sens.*, 38:1561–1573, 2000.
  - [134] N. Geng, A. Sullivan, and L. Carin. Fast multipole method for scattering from an arbitrary pec target above or buried in a lossy half space. *IEEE Trans. Antennas Propag.*, 49:740–748, 2001.
  - [135] D. Givoli and J.B. Keller. Non-reflecting boundary conditions for elastic waves. *Wave Motion*, 12:261–279, 1990.
  - [136] D. Givoli and B. Neta. High-order non-reflecting boundary scheme for time-dependent waves. *J. Comput. Phys.*, 186:24–46, 2003.
  - [137] Dan Givoli. Non reflecting boundary conditions. *J. Comput. Phys.*, 94:1–29, 1991.
  - [138] R. Glowinski and P. Le Tallec. Augmented lagrangian interpretation of the nonoverlapping schwarz alternating method. In *Proc. Third Internat. Sympos. on Domain Decomposition Methods (Houston)*, SIAM, Philadelphia, PA, 1990.



- 
- [139] P. Gosselet and C. Rey. Non-overlapping domain decomposition methods in structural mechanics. *Archives of Computational Methods in Engineering*, 13, n.4:515–572, 2007.
  - [140] E. Grasso, S. Chaillat, J.F. Semblat, and M. Bonnet. Application of the multi-level time-harmonic fast multipole bem to 3-d visco-elastodynamics. *Eng. Anal. Bound. Elem.*, 36:744–758, 2012.
  - [141] R.W. Graves. Simulating seismic wave propagation in 3d elastic media using staggered-grid finite differences. *Bull. Seismol. Soc. Amer.*, 86:1091–1106, 1996.
  - [142] L. Greengard and V. Rokhlin. A fast algorithm for particle simulations. *J. Comput. Phys.*, 73:325–348, 1987.
  - [143] M.J. Grote. Nonreflecting boundary conditions for elastodynamic scattering. *J. Comput. Phys.*, 161:331–353, 1999.
  - [144] P. Guéguen, P.Y. Bard, and F.J. Chávez-Garcia. Site-city interaction in mexico city-like environments: An analytical study. *Bull. Seismol. Soc. Amer.*, 92:794–811, 2002.
  - [145] V. Guglielmetti, P. Grasso, A. Mahtab, and S. Xu. *Mechanized Tunnelling in Urban Areas*. Taylor & Francis, 2008.
  - [146] M. Guiggiani and A. Gigante. A general algorithm for multidimensional cauchy principal value integrals in the boundary element method. *J. Appl. Mech.*, 57:906–915, 1990.
  - [147] Nail A. Gumerov and R. Duraiswami. *Fast Multipole Methods for the Helmholtz Equation in Three Dimensions*. 2004.
  - [148] Nail A. Gumerov and Ramani Duraiswami. A broadband fast multipole accelerated boundary element method for the three dimensional Helmholtz equation. *J. Acoust. Soc. Amer.*, 125:191–205, 2009.
  - [149] W. Hackbusch. A sparse matrix arithmetic based on h-matrix. part i: Introduction to h-matrices. *Computing*, 62:89–108, 1999.
  - [150] W. Hackbusch and Z.P. Nowak. On the fast multiplication in the boundary element method by panel clustering. *Numerische Mathematik*, 54:463–491, 1989.
  - [151] T. Hagstrom and S.I. Hariharan. A formulation of asymptotic and exact boundary conditions using local operators. *Appl. Numer. Math.*, 27:403–416, 1998.
  - [152] I. Harari and T.J.R. Hughes. Finite element method for the helmholtz equation in an exterior domain: Model problems. *Comp. Meth. Appl. Mech. Eng.*, 87:59–96, 1991.
  - [153] G.D. Hatzigeorgiou and D.E. Beskos. Dynamic elastoplastic analysis of 3-d structures by the domain/boundary element method. *Comput. Struct.*, 80:339–347, 2002.
  - [154] G.D. Hatzigeorgiou. *Dynamic Inelastic Analysis with BEM: Results and Needs*, pages 193–206. Springer, 2009.
  - [155] D.L. Heckmann and S.L. Dvorak. Numerical computation of hankel functions of integer order for complex valued arguments. *Radio Science*, 36:1265–1270, 2001.
  - [156] R Hildebrand. Asymptotic analysis of hard wave barriers in soil. *Soil Dyn. Earthquake Eng.*, 23:143–158, 2003.
  - [157] W.G. Hoover, W.T. Ashurt, and R.J. Olness. Two-dimensional computer studies of crystal stability and fluid viscosity. *Journal of Chem. Phys.*, 60:4043–4047, 1974.
  - [158] G.C. Hsiao. The coupling of boundary element and finite element methods. *Z. Angew. Math. Mech.*, 70:493–503, 1990.
  - [159] Thomas J.R. Hughes. *The finite element method: linear static and dynamic finite element analysis*. Prentice-Hall, Englewood Cliffs, New Jersey, 1987.
  - [160] P. Humbert and A. Dubouchet. *CESAR-LCPC 3.3, manuel de formation*. Laboratoire Central des Ponts et Chaussées, 7 edition edition, 2001.
  - [161] P. Humbert, A. Dubouchet, G. Fezens, and D. Remaud. Cesar-lcpc, un progiciel de calcul dédié au génie civil. Technical Report Technical Report 256-257, Bul. des Laboratoires des Ponts et Chaussées, Paris, France, 2005.

- 
- [162] H.H. Hung and Y.-B. Yang. A review on ground-borne vibrations with emphasis on those induced by trains. Invited Review Paper Vol.25, No.1, pp. 1-16, Proc.Natl.Sci.Counc. ROC(A), 2001.
  - [163] H. E. M. Hunt. Modelling of rail vehicles and track for calculation of ground-vibration transmission into buildings. *J. Sound Vibr.*, 193:185–194, 1996.
  - [164] F. Ihlenburg and I. Babuška. Finite element solution of the helmholtz equation with high wave number, part i: The h-version of the fem. *Computers & Mathematics with Applications*, 30:9–37, 1995.
  - [165] P.C. Jennings. Distant motions from a building vibration test. *Bull. Seismol. Soc. Amer.*, 60:2037–2043, 1970.
  - [166] Semblat J.F., A.-M. Duval, and P. Dangla. Seismic site effects in a deep alluvial basin: numerical analysis by the boundary element method. *Computers & Geotechnics*, 29:573–585, 2002.
  - [167] C. J. C. Jones and J. R. Block. Prediction of ground vibration from freight trains. *J. Sound Vibr.*, 93:205–213, 1996.
  - [168] C. J. C. Jones and M. Petyt. Ground vibration due to a rectangular harmonic load. *J. Sound Vibr.*, 212:61–74, 1998.
  - [169] SH Ju. Finite element analyses of wave propagations due to a high-speed train across bridges. *Int. J. Num. Meth. Eng.*, 54:1391–1408, 2002.
  - [170] SH Ju and HT Lin. Analysis of train-induced vibrations and vibration reduction schemes above and below critical Rayleigh speeds by finite element method. *Soil Dyn. Earthquake Eng.*, 24:993–1002, 2004.
  - [171] N. Kamiya and H. Iwase. Bem and fem combination parallel analysis using conjugate gradient and condensation. *Eng. Anal. Bound. Elem.*, 20:319–326, 1998.
  - [172] N. Kamiya, H. Iwase, and E. Kita. Parallel implementation of boundary element method with domain decomposition. *Eng. Anal. Bound. Elem.*, 18:209–216, 1997.
  - [173] Norio Kamiya, Hidehito Iwase, and Eisuke Kita. Parallel computing for the combination method of bem and fem. *Eng. Anal. Bound. Elem.*, 18:223–229, 1997.
  - [174] H. Kanamori and Don L. Anderson. Importance of physical dispersion in surface wave and free oscillation problems: Review. *Review of Geophysics and Space Physics*, 15:115–112, 1977.
  - [175] A. Karlström. An analytical model for ground vibrations from accelerating trains. *J. Sound Vibr.*, 293:587–598, 2006.
  - [176] A. Karlström and A. Boström. An analytical model for train-induced ground vibrations from railways. *J. Sound Vibr.*, 292:221–241, 2006.
  - [177] A. Karlström and A. Boström. Efficiency of trenches along railways for trains moving at sub- or supersonic speeds. *Soil Dyn. Earthquake Eng.*, 27:625–641, 2007.
  - [178] M. Käser, M. Dumbser, J. de la Puente, and H. Igel. An arbitrary high order discontinuous galerkin method for elastic waves on unstructured meshes iii: Viscoelastic attenuation. *Geophys. J. Int.*, 168:224–242, 2007.
  - [179] SE Kattis, D Polyzos, and DE Beskos. Vibration isolation by a row of piles using a 3-D frequency domain BEM. *Int. J. Num. Meth. Eng.*, 46:713–728, 1999.
  - [180] E. Kausel. The thin-layer method in seismology and earthquake engineering. In *Wave Motion in Earthquake Engineering*. WIT Press, Southampton, UK, 2000.
  - [181] J.B. Keller and D. Givoli. Exact non-reflecting boundary conditions. *J. Comput. Phys.*, 82:172–192, 1989.
  - [182] K.R. Kelly, R.W. Ward, S. Treitel, and R.M. Alford. Synthetic seismograms; a finite-difference approach. *Geophysics*, 41:2–27, 1976.
  - [183] N. Khalili, M. Yazdchi, and S. Valliappan. Wave propagation analysis of two-phase saturated porous media using coupled finite-infinite element method. *Soil Dyn. Earthquake Eng.*, 18:533–553, 8 1999.
  - [184] M. Kham, J.F. Semblat, P.Y. Bard, and P. Dangla. Seismic site-city interaction: Main governing phenomena through simplified numerical models. *Bull. Seismol. Soc. Amer.*, 95:1934–1951, 2006.
  - [185] E. Kjartansson. Constant q-wave propagation and attenuation. *J. Geophys. Res.*, 84:4737–4748, 1979.
  - [186] A. Klawonn and O. B. Widlund. A domain decomposition method with lagrange multipliers and inexact

- solvers for linear elasticity. *SIAM J. Sci. Comput.*, 22:1199–1219, 2000.
- [187] R. Klein, H. Antes, and D. Le Le Houedec. Efficient 3d modelling of vibration isolation by open trenches. *Comput. Struct.*, 64:809–817, 1997.
  - [188] L. Knopoff. Q. *Review of Geophysics and Space Physics*, 2:625–660, 1964.
  - [189] S. Koc, J. Song, and WC Chew. Error analysis for the numerical evaluation of the diagonal forms of the scalar spherical addition theorem. *SIAM J. Numer. Anal.*, 36:906–921, 1999.
  - [190] D. Komatitsch, G. Erlebacher, D. Göddeke, and D. Michéa. High-order finite-element seismic wave propagation modeling with mpi on a large gpu cluster. *J. Comput. Phys.*, 229, 2010.
  - [191] D. Komatitsch and R. Martin. An unsplit convolutional perfectly matched layer improved at grazing incidence for the seismic wave equation. *Geophysics*, 72:155–167, 2007.
  - [192] D. Komatitsch and J.P. Voilotte. The spectral element method: an efficient tool to simulate the seismic response of 2d and 3d geological structures. *Bull. Seismol. Soc. Amer.*, 88:368–392, 1998.
  - [193] S.L. Kramer. *Geotechnical earthquake engineering*. Prentice-Hall International Series in Civil Engineering and Engineering Mechanics, 1996.
  - [194] J. Kristek, P. Moczo, and M. Galis. Stable discontinuous staggered grid in the finite-difference modelling of seismic motion. *Geophys. J. Int.*, 183:1401–1407, 2010.
  - [195] C. Lai and G.J. Rix. Simultaneous inversion of rayleigh phase velocity and attenuation for near-surface site characterization. Technical report, National Science Foundation and U.S. Geological Survey, Georgia Institute of Technology, 1998.
  - [196] H. Lamb. On the propagation of tremors over the surface of an elastic solid. *Phil. Trans. Royal Soc. London*, 203:1–42, 1904.
  - [197] U. Langer and O. Steinbach. Boundary element tearing and interconnecting methods. *Computing*, 71:205–228, 2003.
  - [198] U. Langer and O. Steinbach. Coupled boundary and finite element tearing and interconnecting methods. *Lecture Notes in Computational Science and Engineering*, 40, part I:83–97, 2005.
  - [199] Ulrich Langer, Günter Of, O. Steinbach, and W. Zulehner. Inexact fast multipole boundary element tearing and interconnecting methods. *Lecture Notes in Computational Science and Engineering*, 55, part II:405–412, 2007.
  - [200] D Le Houedec. Modelling and analysis of ground vibration problems: A review. In Topping, BHV, editor, *Civil And Structural Engineering Computing: 2001*, pages 475–485, 2001. 8th International Conference on Civil and Structural Engineering Computing/6th International Conference on Application of Artificial Intelligence to Civil and Struct Engn, EISENSTADT, AUSTRIA, SEP 19-21, 2001.
  - [201] D. Le Houedec and M. Maldonado. Isolation and vibration due to urban rail traffic. In BHV Topping, G Montero, and R Montenegro, editors, *Innovation in Computational Structures Technology*, pages 393–416, 2006. 8th International Conference on Computational Structures Technology, Las Palmas, SPAIN, SEP 12-15.
  - [202] D Le Houedec, S MALEK, and J PICARD. Efficiency of trenches and screens for surface-wave diffraction. *Journal De Physique*, 51:147–156, 1990.
  - [203] P. Le Tallec. Domain decomposition methods in computational mechanics. *Computational Mechanics Advances*, 1:121–220, 1994.
  - [204] P. Li and M. Schanz. Fundamental solutions for a partially saturated poroelastic continuum. *Proceedings in applied mathematics and mechanics*, 1:243–244, 2011.
  - [205] C.-C. Lin, E.C. Lawton, Caliendo J.A., and L.R. Anderson. An iterative finite-element-boundary element algorithm. *Comput. Struct.*, 59, n.5:899–909, 1996.
  - [206] P.L. Lions. On the schwarz alternating method. In *Proc. First Internat. Sympos. on Domain Decomposition Methods (Paris), France*, 1987.
  - [207] H.-P. Liu, D.L. Anderson, and H. Kanamori. Velocity dispersion due to anelasticity: Implications for

- seismology and mantle composition. *Geophys. J. Royal Astron. Soc.*, 47:41–58, 1976.
- [208] Z. Liu. Efficient evaluation of the half-space green's function for fast-multipole scattering models. *Microwave Opt. Technol. Lett.*, 29:388–392, 2001.
- [209] G. Lombaert, G. Degrande, B. Vanhauwere, B. Vandebricht, and S. Francois. The control of ground-borne vibrations from railway traffic by means of continuous floating slabs. *J. Sound Vibr.*, 297:946–961, 2006.
- [210] C. Lubich. Convolution quadrature and discretized operational calculus. i. *Numerische Mathematik*, 52:129–145, 1988.
- [211] J. Lysmer. Lumped mass method for rayleigh waves. *Bull. Seismol. Soc. Amer.*, 60:89–104, 1970.
- [212] J. Lysmer and L.A. Drake. *A finite element method for seismology*, volume 11, chapter Chapter 6, pages 181–216. Academic Press, New York, 1972.
- [213] J. Lysmer and Jr. Richart, F. E. Dynamic response of footings to vertical loading. *Journal of Soil Mechanics and Foundation Engineering Division*, 92, SM1:65–91, 1966.
- [214] Y. Ma, L. Loures, and G.F. Margrave. Seismic modeling with the reflectivity method. *CREWES Research Report*, 16, 2004.
- [215] Y. Maday, C. Mavriplis, and A.T. Patera. Nonconforming mortar element methods: application to spectral discretizations. *Domain Decomposition Methods*, Ch.31:392–418, 1988.
- [216] F. Mahmoudian and G.F. Margrave. A review of the finite-element method in seismic wave modelling. Technical report, CREWES Research Report, 2003.
- [217] J. Mandel. Balancing domain decomposition. *Communications in Numerical Methods in Engineering*, 9(3):233–291, 1993.
- [218] J. Mandel and B. Sousedik. Coarse spaces over the ages. 2010.
- [219] H.A. Mang, P. Torzicky, and Z.Y. Chen. On the mechanical inconsistency of symmetrization of unsymmetric coupling matrices for be/fem discretization of solids. *Comp. Mech.*, 4:301–308, 1989.
- [220] G.D. Manolis and D. Polyzos. *Recent Advances in Boundary Element Method*. Springer, 2009.
- [221] K.J. Marfurt. Accuracy of finite-difference and finite-element modeling of the scalar and elastic wave equations. *Geophysics*, 49:533–, 1984.
- [222] M. Margonari and M. Bonnet. Fast multipole method applied to elastostatic bem-fem coupling. *Comput. Struct.*, 83:700–717, 2005.
- [223] T.W. May and B.A. Bolt. The effectiveness of trenches in reducing seismic motion. *Earthquake Eng. Struct. Dyn.*, 10:195–210, 1982.
- [224] Messner. A regularized collocation boundary element method for linear poroelasticity. *Comput. Mech.*, 47:669–680, 2011.
- [225] K.C. Meza-Fajardo. *Numerical Simulation of Wave Propagation in Unbounded Elastic Domains using Spectral Element Method*. PhD thesis, Università degli Studi di Pavia, ROSE School, 2007.
- [226] P. Moczo and J. Kristek. On the rheological models used for time-domain methods of seismic wave propagation. *Geophysical Research Letter*, 32, 2005.
- [227] P. Moczo, J. Kristek, M. Galis, E. Chaljub, and V. Etienne. 3-d finite-difference, finite-element, discontinuous-galerkin and spectral-element schemes analysed for their accuracy with respect to p-wave to s-wave speed ratio. *Geophys. J. Int.*, 187:1645–1667, 2011.
- [228] P. Moczo, J. Kristek, M. Galis, P. Pazak, and M. Balazovjeh. The finite-difference and finite-element modeling of seismic wave propagation and earthquake motion. *Acta Physica Slovaca*, 57:177–406, 2007.
- [229] Peter Moczo and Pierre-Yves Bard. Wave diffraction, amplification and differential motion near strong lateral discontinuities. *Bull. Seismol. Soc. Amer.*, 83:85–106, 1993.
- [230] H. Mogi and H. Kawakami. Analysis of scattered waves on ground with irregular topography using the direct boundary element method and neumann series expansion. *Bull. Seismol. Soc. Amer.*, 97:1144–1157, 2007.
- [231] R. Mullen and T. Belytschko. Dispersion analysis of finite element semidiscretizations of the two-

- dimensional wave equation. *Int. J. Num. Meth. Eng.*, 18:11–29, 1982.
- [232] G. Müller. The reflectivity method: a tutorial. *J. Geophys.*, 58:1536174, 1985.
- [233] Antonio Munjiza. *The combined finite-discrete element method*. Wiley, 2004.
- [234] M.J. Nénning and M. Schanz. Infinite elements in a poroelastodynamic fem. *Proceedings in applied mathematics and mechanics* 10, 1:199–200, 2010.
- [235] K. Niino and N. Nishimura. Preconditioning based on calderon’s formulae for periodic fast multipole methods for helmholtz equation. *J. Comput. Phys.*, 231:66–81, 2012.
- [236] N. Nishimura. Fast multipole accelerated boundary integral equation methods. *Appl. Mech. Rev.*, 55:299–324, 2002.
- [237] G.S. O’Brien and C.J. Bean. A 3d discrete numerical elastic lattice method for seismic wave propagation in heterogeneous media with topography. *Geophysical Research Letter*, 31, 2004.
- [238] Emmanuel Olivi, Maureen Clerc, and Théodore Papadopoulos. Domain decomposition for coupling finite and boundary element methods in eeg. In *Proc. Biomag.*, 2010.
- [239] R. Paolucci. Shear resonance frequencies of alluvial valleys by rayleigh’s method. *Earthquake Spectra*, 15:503–521, 1999.
- [240] R. Paolucci and D. Spinelli. Ground motion induced by train passage. *J. Eng. Mech.*, 132, 2006.
- [241] Roberto Paolucci. Amplification of earthquake ground motion by steep topographic irregularities. *Earthquake Eng. Struct. Dyn.*, 31:1831–1853, 2002.
- [242] J. Park and E. Kausel. Numerical dispersion in the thin-layer method. *Comput. Struct.*, 82:607–625, 2004.
- [243] P.W. Partridge and C.A. Brebbia. *The dual reciprocity boundary element method*. Southampton: Computational Mechanics Publications, 1992.
- [244] A.T. Patera. A spectral element method for fluid dynamics: Laminar flow in a channel expansion. *J. Comput. Phys.*, 54:468–488, 1984.
- [245] G.D. Pavlatos and D.E. Beskos. Dynamic elastoplastic analysis by bem/fem. *Eng. Anal. Bound. Elem.*, 14:51–63, 1994.
- [246] A. Pecker. *Dynamique des sols*. Presses de l’Ecole Nationale des Ponts et Chaussées, 1984.
- [247] CL Pekeris. The seismic surface pulse. *Proceedings Of The National Academy Of Sciences Of The United States Of America*, 41:469–480, 1955.
- [248] C. Pescatore and R.J. Cole. A method for predicting the stability characteristics of three-term homogeneous recurrence relations. *J. Comput. Appl. Math.*, 6, n.3:197–199, 1980.
- [249] D.F. Pilkey. *Computation of a Damping Matrix for Finite Element Model Updating*. PhD thesis, Virginia Polytechnic Institute and State University, 1998.
- [250] E. Muhammad Rahman and Orr Trevor. Finite element modelling of ground vibrations due to tunnelling activities. *International Journal of Civil and Environmental Engineering*, 3:143–149, 2011.
- [251] J. Rahola. Diagonal forms of the translation operators in the fast multipole algorithm for scattering problems. 36:333–358, 1996.
- [252] Singiresu S. Rao. *The Finite Element Method in Engineering*. Elsevier, 4th edition, 2005.
- [253] Lord Rayleigh. On waves propagated along the plane surface of an elastic solid. *Proc. London Math. Soc.*, 1-17:4–11, 1885.
- [254] W.H. Reed and T.R. Hill. Triangular mesh methods for the neutron transport equation. Technical Report LA-UR-73-479, Los Alamos Scientific Laboratory, 1973.
- [255] E. Reinoso, L.C. Wrobel, and H. Power. Three-dimensional scattering of seismic waves from topographical structures. *Soil Dyn. Earthquake Eng.*, 16:41–61, 1997.
- [256] L Ricci, VH Nguyen, K Sab, D Duhamel, and L Schmitt. Dynamic behaviour of ballasted railway tracks: A discrete/continuous approach. *Comput. Struct.*, 83:2282–2292, 2005.
- [257] J.R. Rice, P. Tsompanopoulou, and E. Vavalis. Interface relaxation methods for elliptic differential equations. *Applied Numerical Mathematics*, 32:219–245, 2000.

- 
- [258] F.E. Jr. Richart, J.R. Hall, and R.D. Woods. *Vibrations of soils and foundations*. Prentice-Hall, Inc. Englewood cliffs, New Jersey, 1970.
  - [259] J.O. Robertsson, J.O. Blanch, and W. Symes. Viscoelastic finite-difference modeling. *Geophysics*, 59:1444–1456, 1994.
  - [260] V. Rokhlin. Rapid solution of integral equations of classical potential theory. *J. Comput. Phys.*, 60:187–207, 1985.
  - [261] V. Rokhlin. Diagonal forms of translation operators for the helmholtz equation. *Appl. Computat. Harmon. Analysis*, 1:82–93, 1993.
  - [262] Thomas Ruberg and Martin Schanz. Coupling finite and boundary element methods for static and dynamic elastic problems with non-conforming interfaces. *Comp. Meth. Appl. Mech. Eng.*, 198:449–458, 2008.
  - [263] J. Ryue, D.J. Thompson, P.R. White, and D.R. Thompson. Investigations of propagating wave types in railway tracks at high frequencies. *J. Sound Vibr.*, 315:157–175, 2008.
  - [264] Y. Saad. A flexible inner-outer preconditioned gmres algorithm. *SIAM J. Sci. Comput.*, 14:461–469, 1993.
  - [265] Y. Saad. *Iterative Methods for Sparse Linear Systems*. SIAM, 2nd edition, 2003.
  - [266] E.H. Saenger and T. Bohlen. Finite-difference modeling of viscoelastic and anisotropic wave propagation using the rotated staggered grid. *Geophysics*, 69:583–591, 2004.
  - [267] E.H. Saenger, N. Gold, and S.A. Shapiro. Modeling the propagation of elastic waves using a modified finite-difference grid. *Wave motion*, 31:77–92, 2000.
  - [268] F. Sánchez-Sesma. Diffraction of elastic waves by three-dimensional surface irregularities. *Bull. Seismol. Soc. Amer.*, 73:1621–1636, 1983.
  - [269] F. Sánchez-Sesma, R. Benites, and J. Bielak. The assessment of strong ground motion: what lies ahead? In *Paper No.2014, Eleventh World Conference on Earthquake Engineering*, 1996.
  - [270] F. Sánchez-Sesma and M. Campillo. Topographic effects for incident p, sv, and rayleigh waves. *Tectonophysics*, pages 113–125, 1993.
  - [271] K. Sarabandi and Il-S. Koh. Fast multipole representation of green’s function for an impedance half-space. *IEEE Trans. Antennas Propag.*, 52:296–301, 2004.
  - [272] M Schanz. A boundary element formulation in time domain for viscoelastic solids. *Communications In Numerical Methods In Engineering*, 15:799–809, 1999.
  - [273] M. Schanz. *Wave propagation in Viscoelastic and Poroelastic Continua. A Boundary Element Approach*. Lecture Notes in Applied and Computational Mechanics 2, 2001.
  - [274] M Schanz and H Antes. A new visco- and elastodynamic time domain boundary element formulation. *Comput. Mech.*, 20:452–459, 1997.
  - [275] M. Schanz, H. Antes, and T. Rüberg. Convolution quadrature boundary element method for quasi-static visco- and poroelastic continua. *Comput. Struct.*, 83:673–684, 2005.
  - [276] S. Schneider. Fe/fmbe coupling to model fluid-structure interaction. *Int. J. Num. Meth. Eng.*, 76:2137–2156, 2008.
  - [277] J.F. Semblat. Rheological interpretation of rayleigh damping. *J. Sound Vibr.*, 206(5):741–744, 1997.
  - [278] J.F. Semblat and J.J. Brioist. Efficiency of higher order finite elements for the analysis of seismic wave propagation. *J. Sound Vibr.*, 231:460–467, 2000.
  - [279] J.F. Semblat, M. Kham, and P.Y. Bard. Seismic wave propagation in alluvial basins and influence of site-city interaction. *Bull. Seismol. Soc. Amer.*, 98:2665–2678, 2008.
  - [280] J.F. Semblat, M. Kham, E. Parara, P.Y. Bard, K. Pitilakis, and D. Raptakis. Seismic wave amplification: Basin geometry vs soil layering. *Soil Dyn. Earthquake Eng.*, 25:529–538, 2005.
  - [281] J.F. Semblat, L. Lenti, and A. Gandomzadeh. A simple multi-directional absorbing layer method to simulate elastic wave propagation in unbounded domains. *Int. J. Num. Meth. Eng.*, 85:1543–1563, 2011.
  - [282] J.F. Semblat, L. Lenti, D. Jacqueline, J.-J. Leblond, and E. Grasso. Vibrations induites dans les sols par le trafic ferroviaire: expérimentations, modélisations et isolation. *Revue Francaise de Géotechnique*, 134-

- 135:23–36, 2011.
- [283] J.F. Semblat and M.P. Luong. Wave propagation through soils in centrifuge testing. *Journal of Earthquake Engineering*, 2:147–171, 1998.
  - [284] J.F. Semblat, R. Paolucci, and A.-M. Duval. Simplified vibratory characterization of alluvial basins. *C.R. Acad. Sci., Série Géosciences*, 335:365–370, 2003.
  - [285] J.F. Semblat and A. Pecker. *Waves and Vibrations in Soils: Earthquakes, Traffic, Shocks, Construction works*. IUSS Press, 2009.
  - [286] Kubilay Sertel and L. Volakis, John. Incomplete lu preconditioner for fmm implementation. *Microwave Opt. Technol. Lett.*, 26:265–267, 2000.
  - [287] Hung-Ta Lin Shen-Haw Ju. Analysis of train-induced vibrations and vibration reduction schemes above and below critical rayleigh speeds by fem. *Soil Dyn. Earthquake Eng.*, 24:993–1002, 2004.
  - [288] X. Sheng, C. J. C. Jones, and M. Petyt. Ground vibration generated by a harmonic load acting on a railway track. *J. Sound Vibr.*, 225:3–28, 1999.
  - [289] X. Sheng, C. J. C. Jones, and D. J. Thompson. Responses of infinite periodic structures to moving or stationary harmonic loads. *J. Sound Vibr.*, 282:125–149, 2005.
  - [290] X. Sheng, C. J. C. Jones, and D. J. Thompson. Prediction of ground vibration from trains using the wavenumber finite and boundary element methods. *J. Sound Vibr.*, 293:575–586, 2006.
  - [291] X.-Q. Sheng, J.-M. Jin, and J. Song. On the formulation of hybrid finite-element and boundary-integral methods for 3-d scattering. *IEEE Trans. Antennas Propag.*, 46, n.3:303–311, 1998.
  - [292] J.C. Simo and T.J.R. Hughes. *Computational Inelasticity*. Springer, 1998.
  - [293] W.D. Smith. The application of finite element analysis to body wave propagation problems. *Geophys. J. Royal Astron. Soc.*, 42:747–768, 1975.
  - [294] D. Soares. An optimised fem-bem time-domain iterative coupling algorithm for dynamic analyses. *Comput. Struct.*, 86:1839–1844, 2008.
  - [295] D. Soares, J.A.M. Carrer, and W.J. Mansur. Non-linear elastodynamic analysis by the bem: an approach based on the iterative coupling of the d-bem and td-bem formulations. *Eng. Anal. Bound. Elem.*, 29:761–774, 2005.
  - [296] Jr D. Soares, O. von Estorff, and W.J. Mansur. Iterative coupling of bem and fem for nonlinear dynamic analysis. *Comput. Mech.*, 34:67–73, 2004.
  - [297] C. Somigliana. Sopra l’equilibrio di un corpo elastico isotrope. *Il nuovo ciemento*, 1886.
  - [298] J. Song, Lu Cai-Cheng, and W.C. Chew. Multilevel fast multipole algorithm for electromagnetic scattering by large complex objects. *IEEE Trans. Antennas Propag.*, 45:1488–1493, 1997.
  - [299] J. Song and WC Chew. Error analysis for the truncation of multipole expansion of vector green’s functions. *IEEE Microwave and Wireless Components Letters*, 11:311–313, 2001.
  - [300] C.C. Spyrakos and Chaojin Xu. Seismic soil-structure interaction of massive flexible strip-foundations embedded in layered soils by hybrid bem-fem. *Soil Dyn. Earthquake Eng.*, 23:383–389, 2003.
  - [301] O. Steinbach and M. Windisch. Stable boundary element domain decomposition methods for the helmholtz equation. *Numerische Mathematik*, 118:171–195, 2011.
  - [302] Ernst P. Stephan. *Coupling of Boundary Element Methods and Finite Element Methods*, volume 1, pages 375–412. 2004.
  - [303] D. Thompson. Ch.3 - track vibration. In *Railway Noise and Vibration*, pages 29–95. Elsevier, Oxford, 2009.
  - [304] A. Toomey and C.J. Bean. Numerical simulation of seismic waves using a discrete particle scheme. *Geophys. J. Int.*, 141:595–604, 2000.
  - [305] A. Toselli and O. Widlund. *Domain Decomposition Methods - Algorithms and Theory*. Springer, 2005.
  - [306] J. Tromp, D. Komatitsch, and Q. Liu. Spectral-element and adjoint methods in seismology. *Communications in Computational Physics*, 3:1–32, 2008.
  - [307] S.V. Tsynkov. Numerical solution of problems on unbounded domains, a review. *Appl. Numer. Math.*,

- 27:465–532, 1998.
- [308] Eric E. Ungar, Douglas H. Sturz, and C.Hal Amick. Vibration control design of high technology facilities. *J. Sound Vibr.*, 1990.
  - [309] Jean Virieux. Sh-wave propagation in heterogeneous media: Velocity-stress finite-difference method. *Geophysics*, 49:11, 1984.
  - [310] O. von Estorff and M. Firuziaan. Coupled bem/fem approach for nonlinear soil/structure interaction. *Eng. Anal. Bound. Elem.*, 24:715–725, 2000.
  - [311] O von Estorff and C. Hagen. Iterative coupling of fem and bem in 3d transient elastodynamics. *Eng. Anal. Bound. Elem.*, 29:775–787, 2005.
  - [312] O. von Estorff and M.J. Prabucki. Dynamic response in the time domain by coupled boundary and finite elements. *Comput. Mech.*, 6:35–46, 1990.
  - [313] G.S. Warren and W.R. Jr. Scott. Numerical dispersion in the finite-element method using three-dimensional edge elements. *Microwave Opt. Technol. Lett.*, 18:423–429, 1998.
  - [314] K.-L. Wen. Nonlinear soil response in ground motions. *Earthquake Eng. Struct. Dyn.*, 26:599–608, 1994.
  - [315] O. Widlund. The development of coarse spaces for domain decomposition algorithms. In *Domain decomposition Methods in Science and Engineering XVIII*, 2009.
  - [316] Barbara Wohlmuth. A mortar finite element method using dual spaces for the lagrange multiplier. *SIAM J. Numer. Anal.*, 38(3), 2000.
  - [317] H.L. Wong and P.C. Jennings. Effects of canyon topography on strong ground motion. *Bull. Seismol. Soc. Amer.*, 65:1239–1257, 1975.
  - [318] D.M. Wood. *Soil Behaviour and Critical State Mechanics*. Cambridge University Press, 1991.
  - [319] R. Woods. Screening of surface waves in soils. Technical report, University of Michigan, 1968.
  - [320] J.-W. Wu and R. Lee. The advantages of triangular and tetrahedral edge elements for electromagnetic. *IEEE Trans. Antennas Propag.*, 45:1431–1437, 1997.
  - [321] YB Yang and HH Hung. A parametric study of wave barriers for reduction of train-induced vibrations. *Int. J. Num. Meth. Eng.*, 40:3729–3747, 1997.
  - [322] Y.B. Yang, H.H. Hung, and L.C. Hsu. Ground vibrations due to underground trains considering soil-tunnel interaction. *Interaction and Multiscale Mechanics*, 1:157–175, 2007.
  - [323] Y. Yasuda and T. Sakuma. Analysis of sound fields in porous materials using the fast multipole bem. In *37th International Congress and Exposition on Noise Control Engineering, Shanghai, China*, 2008.
  - [324] M. Yazdchi, N. Khalili, and S. Valliappan. Non-linear seismic behaviour of concrete gravity dams using coupled finite element-boundary element technique. *Int. J. Num. Meth. Eng.*, 44:101–130, 1999.
  - [325] K. Yoshida. *Applications of Fast Multipole Method to Boundary Integral Equation*. PhD thesis, Department of Global Environment Engineering, Kyoto University, Japan, 2001.
  - [326] A. Zerva. *Spatial Variation of Seismic Ground Motions: Modeling and Engineering Applications*. CRC Press, 2009.
  - [327] C. Zhao and S. Valliappan. A dynamic infinite element for three-dimensional infinite-domain wave problems. *Int. J. Num. Meth. Eng.*, 36:2567–2580, 1993.
  - [328] OC Zienkiewicz, Dw Kelly, and P Bettess. Coupling of finite-element method and boundary solution procedures. *Int. J. Num. Meth. Eng.*, 11:355–375, 1977.
  - [329] O.C. Zienkiewicz and T. Shiomi. Dynamic behaviour of saturated porous media. the generalized biot formulation and its numerical solution. *Int. J. Numer. Anal. Meth. Geomech.*, 8:71–96, 1984.
  - [330] O.C. Zienkiewicz and R.L. Taylor. *The Finite Element Method*. Butterworth-Heinemann, 2000.
  - [331] D.W. Zingg. Comparison of high-accurate finite-difference methods for linear wave propagation. *SIAM J. Sci. Comput.*, 22:476–502, 2000.